

Adam Mickiewicz University, Poznań

Faculty of Physics and Astronomy



Doctoral Dissertation

**Nonequilibrium transport and Kondo correlations
in nanoscale systems**

Anand Manaparambil

Supervised by
Prof. dr. hab. Ireneusz Weymann
Institute of Spintronics and Quantum Information,
Faculty of Physics and Astronomy,
Adam Mickiewicz University, Poznań, Poland.

Poznań, October 2024

Acknowledgements

I would like to express my deepest gratitude to Prof. Ireneusz Weymann for his outstanding guidance and support. His openness to my ideas, whether dumb or not, gave me the confidence to grow, and his patience in introducing me to unfamiliar concepts was truly invaluable. I am deeply thankful for the opportunities he provided and the trust he placed in me throughout this journey. Dr. Kacper Wrześniewski for his feedback on the dissertation, countless discussions regarding many aspects of physics, and most importantly for teaching me how to pronounce Polish words properly. I thank all members of the Department of Mesoscopic Physics for the friendly and welcoming atmosphere.

I have had the great opportunity to collaborate with many wonderful people during my PhD journey, and would like to thank them wholeheartedly here. I thank Prof. Andreas Weichselbaum for hosting my visit at the Brookhaven National Laboratory in USA and guiding me through the complicated calculations via numerous insightful discussions and exciting brainstorming sessions, both online and in-person, that I thoroughly enjoyed. I would like to extend my thanks to Prof. Jan von Delft for hosting my visits at the Ludwig-Maximilians Universitat - Munich, Germany and paving way to many inspiring and informative discussions. Many thanks to Prof. Cătălin Pașcu Moca for hosting me at the University of Oradea, Romania, for the scientific discussions and encouraging me to find the beauty in the theoretical methods beyond the numerical results. Lastly, I wish to acknowledge Prof. Gergely Zarand for hosting me at the Budapest University of Technology and Economics, Hungary and the friendly discussions.

Additionally, I would like to acknowledge Ms. Joanna Kubicka for navigating me through the bureaucracies and easing the troubles brought on by the language barrier.

And finally, I would like to thank my parents and my sister for being the pillars of support during the difficult times. Nishita, Alice, Marcin and all the friends with whom I was able to survive the pandemic and enjoy the beautiful city of Poznań.

The financial support obtained within the following projects is also acknowledged:

- National Science Centre of Poland, Opus Grant No: 2017/27/B/ST3/00621.
- National Science Centre of Poland, Opus Grant No: 2022/45/B/ST3/02826.
- National Science Centre of Poland, Preludium Grant No: 2021/41/N/B/ST3/02098.
- NAWA-STER co-financed project No: PPI/STE2020/1/00007/U/00001.
- University of Excellence, ID-UB action 003, No: 003/13/UAM/0016.



To the boundaries of knowledge.

Contents

List of articles constituting the dissertation

Abstract

I Introduction

1	Aim and Motivation	1
2	Model systems and basic theory	5
2.1	Quantum impurities and where to find them	5
2.2	Quantum impurity models	5
2.2.1	Single impurity Anderson model	6
2.2.2	Noninteracting case: resonant level model	7
2.2.3	Resonant level model: spectral function and electronic transport	8
3	The many-body physics of interacting quantum impurities	11
3.1	Numerical renormalization group	12
3.1.1	Renormalization group flow diagram	14
3.1.2	Spectral function	16
3.1.3	Linear response transport properties	16
4	Numerical methods for systems out of equilibrium	19
4.1	Hybrid numerical renormalization group - time-dependent density matrix renormalization group approach	19
4.1.1	The hybrid logarithmic-linear discretization scheme	20
4.1.2	Thermofield representation of the lead modes	21
4.1.3	Recombination of the leads	22
4.1.4	Initial state quench and time evolution	23
4.1.5	Steady-state and physical observables	24
4.2	Perturbation theory for strongly asymmetric systems	25

4.3	Nonequilibrium thermoelectric transport coefficients	28
5	Summary	31
6	Streszczenie (Summary in Polish)	35
	Bibliography	41
II	Articles constituting the dissertation	51
7	Linear response transport properties	53
7.1	Spin Seebeck effect of correlated magnetic molecules [A]	53
8	Nonequilibrium steady-state transport: Kondo correlations from both leads	71
8.1	Nonequilibrium spintronic transport through Kondo impurities [B]	71
8.2	Nonequilibrium steady-state thermoelectrics of Kondo-correlated quantum dots [C]	83
9	Nonequilibrium transport properties in the asymmetric coupling limit	101
9.1	Nonequilibrium Seebeck effect and thermoelectric efficiency of Kondo-correlated molecular junctions [D]	101
9.2	Spin-resolved nonequilibrium thermopower of asymmetric nanojunctions [E]	117
9.3	Giant tunnel magnetoresistance induced by thermal bias [F]	133
	Appendices	142
A	List of Scientific Achievements	143
A.1	Complete list of Publications	143
A.2	List of Seminars and Conferences	144
A.3	Experience in Scientific Projects	145
A.4	List of Research visits	145
A.5	List of Awards	146
A.6	Other Scientific Activities	146
B	Statements concerning the Author's contributions	147

List of articles constituting the dissertation

- [A] Anand Manaparambil & Ireneusz Weymann.
Spin Seebeck effect of correlated magnetic molecules
Sci. Rep., vol. 11, no. 9192, 28 Apr. 2021, pp. 1-15, doi: [10.1038/s41598-021-88373-7](https://doi.org/10.1038/s41598-021-88373-7).
- [B] Anand Manaparambil, Andreas Weichselbaum, Jan von Delft & Ireneusz Weymann.
Nonequilibrium spintronic transport through Kondo impurities. (Editor's Suggestion)
Phys. Rev. B, vol. 106, no. 12, 14 Sept. 2022, p. 125413, doi:[10.1103/PhysRevB.106.125413](https://doi.org/10.1103/PhysRevB.106.125413).
- [C] Anand Manaparambil, Andreas Weichselbaum, Jan von Delft & Ireneusz Weymann.
Nonequilibrium steady-state thermoelectrics of Kondo-correlated quantum dots.
arXiv, 4 Sept. 2024, doi:[10.48550/arXiv.2409.03102](https://doi.org/10.48550/arXiv.2409.03102).
- [D] Anand Manaparambil & Ireneusz Weymann.
Nonequilibrium Seebeck effect and thermoelectric efficiency of Kondo-correlated molecular junctions.
Phys. Rev. B, vol. 107, no. 8, 7 Feb. 2023, p. 085404, doi:[10.1103/PhysRevB.107.085404](https://doi.org/10.1103/PhysRevB.107.085404).
- [E] Anand Manaparambil & Ireneusz Weymann.
Spin-resolved nonequilibrium thermopower of asymmetric nanojunctions.
Phys. Rev. B, vol. 109, no. 11, 4 Mar. 2024, p. 115402, doi:[10.1103/PhysRevB.109.115402](https://doi.org/10.1103/PhysRevB.109.115402).
- [F] Anand Manaparambil & Ireneusz Weymann.
Giant tunnel magnetoresistance induced by thermal bias.
J. Magn. Magn. Mater., vol. 587, 1 Dec. 2023, p. 171272, doi:[10.1016/j.jmmm.2023.171272](https://doi.org/10.1016/j.jmmm.2023.171272).

Abstract

Quantum impurity systems can be designed at the nanoscale as semiconductor quantum dots, nanowires, adatoms or magnetic molecules embedded in tunnel junctions, or on a metallic surface as in scanning tunneling microscopy settings. Such systems can exhibit various quantum effects originating from the strong confinement of electrons into lower dimensions. More complex many-body phenomena can emerge when the impurity starts to interact with the rest of the system. The Kondo effect is one such fascinating many-body phenomenon originating from the strong electronic interactions between the impurity and the conduction band electrons. Many characteristic behaviors are exhibited by Kondo-correlated quantum impurity systems. Primarily, a resonance peak in the density of states of the impurity at the Fermi level, the so-called Kondo-Abrikosov-Suhl resonance, emerges which can also mediate the transport through the impurity resulting in a characteristic zero-bias conductance peak in Kondo systems. The Kondo resonance can also manifest in the thermoelectric transport properties, such as the Seebeck coefficient, if the system is not particle-hole symmetric. While there is a great understanding of such correlated states at equilibrium, describing the Kondo correlations out of equilibrium had been an open problem in the field of condensed matter physics. The works that make up this doctoral dissertation shed light on various scarcely explored nonequilibrium regimes of quantum transport in the presence of Kondo correlations.

In this dissertation, the author presents the results of theoretical and numerical investigations into the nonequilibrium electronic, spintronic and thermoelectric transport through quantum dots as well as magnetic molecules coupled to nonmagnetic or ferromagnetic leads. A particular emphasis is placed on addressing the nonlinear applied bias or temperature gradient effects on the transport through quantum dots in the presence of Kondo correlations. The calculations performed within this dissertation employed the state-of-the-art methods, such as a hybrid numerical renormalization group - time dependent density matrix renormalization group quench method, to describe the transport across the Kondo-correlated impurity systems in the nonequilibrium settings. Quantum dot systems in the strongly asymmetric coupling limit were studied by treating the weaker coupling as a perturbation on the strongly coupled subsystem. The results in this dissertation presents the first quantitatively accurate description of spintronic and thermoelectric transport in the nonequilibrium Kondo regime, establishing a valuable benchmark for future theoretical and experimental research efforts. These findings not only deepen our understanding of fundamental quantum phenomena but also pave the way for advancements in applications such as spintronic devices and energy-efficient technologies.

Part I

Introduction

Chapter 1

Aim and Motivation

The study of electronic, thermoelectric, and heat transport through nanoscale structures comes with their own unique set of challenges due to the role of quantum effects at these scales. Phenomena such as quantum confinement, electronic correlations, and complex many-body effects dominate the behavior of such systems, leading to transport properties that are highly non-trivial and distinct from those in bulk materials [1–5]. With the ongoing trend of device miniaturization, pushing technology toward the lower physical limits in size, it is essential to understand the quantum nature of these systems under various external conditions, including electric fields, magnetic fields, and temperature gradients [6, 7].

Quantum dot systems, in particular, have emerged as ideal platforms for studying nanoscale transport. These structures, which confine electrons in a quasi-zero-dimensional space, exhibit a range of fascinating effects, including quantized energy levels, Coulomb blockade, and, at low temperatures, the Kondo effect [2]. Owing to their tunable properties, quantum dots are of great interest for both fundamental physics and potential applications in quantum computing, thermoelectric energy conversion, and spintronics.

Despite the growing experimental progress in probing these systems, the theoretical description of transport through quantum dots and other nanoscale structures remains a challenge, particularly when strong electron correlations are involved. Many traditional approaches to quantum transport, such as Landauer’s formalism or various Green’s function methods [8–12], are effective in weakly interacting systems but fall short when applied to strongly correlated regimes, where interactions between electrons are no longer negligible. This is especially the case when studying many-body phenomena like the Kondo effect, which arises when a localized spin interacts with a sea of conduction band electrons at low temperatures, giving rise to correlated transport behavior.

To address the complexities of correlated systems, advanced numerical techniques such as the numerical renormalization group (NRG) [13, 14] and the density matrix renormalization group (DMRG) [15–17] methods have been developed. These methods offer non-perturbative frameworks capable of capturing strong electron correlations in equilibrium systems with great precision. In particular, the NRG has been instrumental in elucidating the low-energy properties of quantum dot systems, especially in the linear response regime where transport can be described near equilibrium. For example, it has successfully been

used to study the Kondo effect and Coulomb blockade phenomena, providing quantitative agreement with experimental results [18–20].

However, the non-equilibrium regime, where devices operate under applied voltages or thermal gradients, poses additional challenges [21–28]. Standard methods, such as the NRG, which are highly effective in equilibrium, often break down when describing out-of-equilibrium transport, where nonlinear effects become significant. Understanding transport in these regimes is crucial, as many modern nano-devices operate in far-from-equilibrium conditions. For instance, quantum dots functioning as thermoelectric generators or transistors need to be understood in conditions where significant energy exchange occurs between different parts of the system [29–31]. The goal of this thesis is therefore to fill the theoretical gap in understanding the nonlinear transport through strongly correlated nanostructures by employing hybrid methods that combine the strengths of various numerical approaches. The main objectives of the thesis can be summarized as follows:

- Adaptation and development of numerical techniques to describe the transport through Kondo-correlated systems in far-from-equilibrium settings.
- Investigations of the electronic, thermoelectric and spin-caloritronic signatures of the Kondo effect beyond the linear response regime.
- Providing quantitatively reliable theoretical predictions in the nonequilibrium regime to aid experimental exploration of Kondo systems.

For this purpose, I employ a method that integrates the numerical renormalization group (NRG) with the time-dependent density matrix renormalization group (tDMRG), an approach known as the NRG-tDMRG approach [32]. This hybrid method offers the advantage of treating both strong electron correlations under nonequilibrium conditions in a numerically exact manner.

Additionally, I incorporate an NRG-based perturbative approach [33, 34], which allows for the study of transport properties beyond linear response regime, providing a simpler framework for analyzing real-world devices that operate under finite biases or temperature gradients. This approach is particularly relevant for asymmetric experimental setups, such as single electron transistors, molecular junctions or adatoms under scanning tunneling microscope.

By employing these advanced numerical methods, this dissertation seeks to provide a deeper understanding of the behavior of quantum dot systems and other correlated nanostructures in nonlinear regimes, thereby addressing key open questions in the field of quantum transport.

The present doctoral dissertation consists of two parts. The part I comprising of six chapters acts as an introduction to the research problems under investigation. In chapter 2, I will introduce the physical systems and relevant physics that dictates the transport through nanostructures. The chapter 3 will be dedicated to renormalization group methods, particularly the NRG method, a quantitatively reliable non-perturbative method to describe such correlated systems. The nonequilibrium numerical methods

employed in the publications that make up this thesis will be introduced in chapter 4. The dissertation and the included publications are summarized in chapter 5 (in English) and chapter 6 (in Polish).

The part II consisting of three chapters, has the publications organized according to the numerical methods employed and consequently the parameter regimes under investigation. The chapter 7 presents results that used NRG to study the linear response transport properties of a large spin impurity coupled to ferromagnetic electrodes. The publications using the NRG-tDMRG method, that addressed nonequilibrium spintronic and thermoelectric transport through a quantum dot strongly coupled to two leads, are presented and summarized in chapter 8. The chapter 9 contains the publications that studied the transport in the strongly asymmetric coupling regime using the NRG-based perturbation approach. The publications in this chapter explore the thermoelectric, spin-caloritronic and tunnel magnetoresistance of asymmetrically coupled quantum dot systems. The first two parts of the dissertation are followed by an Appendix that contains the list of all scientific publications, awards and other scientific activities of the doctoral student achieved during the doctoral studies and co-author statements outlining the individual contributions to the publications constituting this dissertation.

Chapter 2

Model systems and basic theory

2.1 Quantum impurities and where to find them

The presence of magnetic impurities in physical systems that surprised the physicists dates back to the 1930s when the experiments on the low temperature resistivity of gold and gold metal alloys showed a distinctive uptick in the resistivity curve [35]. Though this went unexplained at the time, this behavior was later attributed to the presence of magnetic impurities in the system and came to be known as the Kondo effect [36]. With the advent of nanotechnology, it turned out that such quantum impurity systems can be constructed in artificial heterostructures [37]. Thus, from an experimental perspective, transport through such structures has been studied using various setups involving single electron transistors (SET) [38–43], nanowires [44–47], carbon nanotubes [48, 49], molecular magnets [50–52], adatoms [53–55] and other quantum impurity systems [56–60].

In this chapter, I will present some of the most important models used to describe the quantum impurity systems and some basic properties exhibited by them. More involved phenomena, such as the Kondo effect originating from the strong interactions, will be described in the next chapter along with the numerical techniques used to explore them.

2.2 Quantum impurity models

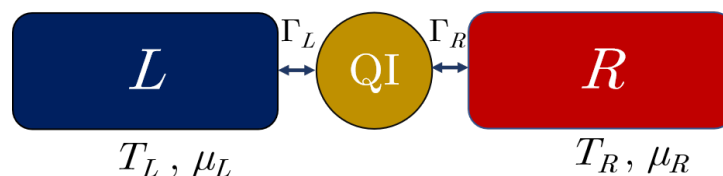


Figure 2.1: The schematic of a quantum impurity (QI) coupled to two leads [left (L) and right (R)] kept at temperatures T_L, T_R , and chemical potentials μ_L, μ_R , respectively.

The transport through impurities can be described according to various models that are valid for different parameter regimes. In this section, we discuss the theoretical models used to study the quantum impurities such as quantum dots or magnetic molecules coupled to electronic reservoirs. Figure 2.1 shows the schematic for a typical setup of quantum impurity coupled to leads kept at different temperatures T_L and T_R and chemical potentials μ_L and μ_R . The schematic in Fig. 2.1 can correspond to different experimental setups as mentioned in the previous section. The Hamiltonian that describes such a setup is as follows.

$$H = H_{\text{imp}} + H_T + H_{\text{leads}}, \quad (2.1)$$

where H_{imp} refers to the Hamiltonian of the quantum impurity, H_T is the tunneling Hamiltonian that describes the tunneling of electrons between the leads and the impurity and finally H_{leads} is the Hamiltonian of the leads. Though Eq. (2.1) is the general form of a quantum impurity Hamiltonian, effective models such as the s-d model, a.k.a the Kondo model, exist to represent specific parameter regimes. The Kondo Hamiltonian [2, 36] for a spin S coupled to a metallic reservoir takes the form,

$$H_{\text{Kondo}} = J \vec{S} \cdot \vec{s}(0) + \sum_{k\sigma} \varepsilon_k c_{k\sigma}^\dagger c_{k\sigma}. \quad (2.2)$$

Here, $\vec{S} \equiv [S_x, S_y, S_z]$ is the spin operator of the impurity, while $\vec{s}(0) = \frac{1}{2} \sum_{\sigma\sigma'} \sum_k c_{k\sigma}^\dagger \vec{\sigma}_{\sigma\sigma'} c_{k\sigma'}$ denotes the effective spin of the conduction band electrons near the impurity, with $\vec{\sigma} \equiv [\sigma_x, \sigma_y, \sigma_z]$ being the vector of the Pauli matrices and J is the Kondo coupling. As evident from the first term of the Hamiltonian, this model neglects the charge fluctuations from the impurity and thus can extract the physics originating purely from the spin processes. It is still interesting to note that, the spin-flip processes can result in a net charge transfer between the impurity and the lead, which can be further interpreted as a transfer of pseudofermions [2]. Moreover, to emphasize the historical significance, this is the first theoretical model by which Jun Kondo was able to explain the uptick of the resistivity curves in Ref. [35] using second order perturbation theory, hence the name Kondo model [36]. The Kondo Hamiltonian is a low energy effective Hamiltonian derivable from a much general single impurity Anderson model (SIAM) [61]. Consequently, the effective Kondo coupling J can be obtained from the SIAM parameters in the local moment regime. using the Schrieffer-Wolff transformation [2, 62].

2.2.1 Single impurity Anderson model

Figure 2.2 shows the energy level diagram for an interacting quantum dot, acting as the quantum impurity part, coupled to two leads as described by the Single Impurity Anderson Model. The quantum impurity part of the SIAM can thus be expressed as [61],

$$H_{\text{imp}} = \varepsilon_d (n_\uparrow + n_\downarrow) + U n_\uparrow n_\downarrow - g \mu_B B (n_\uparrow - n_\downarrow)/2, \quad (2.3)$$

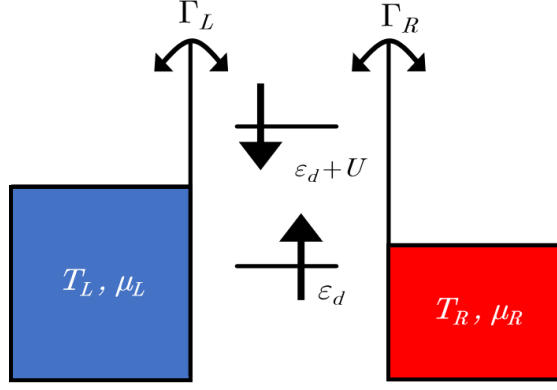


Figure 2.2: The energy level diagram for a SIAM with left and right leads kept at different chemical potentials and temperatures.

where $n_\sigma = d_\sigma^\dagger d_\sigma$ corresponds to the number operator for an electron with spin σ on the quantum dot with energy ε_d with the creation (annihilation) operators d_σ^\dagger (d_σ). The second term describes the Coulombic repulsion U when the quantum dot is doubly occupied, and the third term corresponds to the Zeeman splitting under the presence of a magnetic field B .

When the quantum dot is tunnel coupled to an electronic reservoir, the tunneling of electrons between the quantum dot and the lead is described by the tunneling Hamiltonian H_T of the form,

$$H_T = \sum_{\alpha k \sigma} v_{\alpha k \sigma} (d_\sigma^\dagger c_{\alpha k \sigma} + c_{\alpha k \sigma}^\dagger d_\sigma). \quad (2.4)$$

The $v_{\alpha k \sigma}$ are the tunnel matrix elements between an electron in the quantum dot level with spin σ and the conduction band electron with momentum k and spin σ on the lead $\alpha \in \{L, R\}$ defined by the lead creation (annihilation) operators $c_{\alpha k \sigma}^\dagger$ ($c_{\alpha k \sigma}$). The conduction band is treated as a Fermi sea of noninteracting electrons H_{leads} .

$$H_{\text{leads}} = \sum_{\alpha k \sigma} \varepsilon_{\alpha k \sigma} c_{\alpha k \sigma}^\dagger c_{\alpha k \sigma}. \quad (2.5)$$

Thus, the entire system can then be modelled using the total Hamiltonian $H_{\text{SIAM}} = H_{\text{imp}} + H_T + H_{\text{leads}}$.

2.2.2 Noninteracting case: resonant level model

In the absence of the Coulombic interaction ($U = 0$), the SIAM simplifies to the resonant level model (RLM). Since there is no interaction on the quantum dot, electrons with one particular spin do not influence the transport of its counterpart, resulting in the impurity orbital level being just a path for the conduction band electrons to tunnel through. One can directly identify this characteristic from their corresponding Green's functions.

For an RLM with a metallic reservoir, the retarded Green's function is defined as,

$$G_\sigma^r(t, t') = -i\Theta(t - t') \langle \{d_\sigma(t), d_\sigma^\dagger(t')\} \rangle. \quad (2.6)$$

Since the RLM consists of only quadratic terms, the explicit form of the retarded Green's function can be determined by the equations of motion technique [63]. In the frequency domain, the Greens function $G_\sigma^r(\omega)$ is of the form,

$$G_\sigma^r(\omega) = \frac{1}{\omega - \varepsilon_d + i\Gamma_\sigma}, \quad (2.7)$$

where Γ_σ is the level broadening, or more generally the hybridization function, which originates from the imaginary part of the self-energy correction due to the tunnel coupling, and is directly dependent on the tunneling matrix elements. For a flat conduction band with frequency independent couplings $v = v_{\alpha k \sigma}$ and in the wide band limit, the hybridization function for spin σ takes the form $\Gamma = \pi \rho_\sigma |v|^2$, where ρ_σ is the density of states for spin σ . In the next section, I will describe how such a hybridization term influences the physical observables in the system.

2.2.3 Resonant level model: spectral function and electronic transport

The spectral function $A_\sigma(\omega) = -\frac{1}{\pi} \text{Im}[G_\sigma^r(\omega)]$ is a physical observable directly derivable from the Green's functions. From the physical perspective, $A_\sigma(\omega)$ contains the relevant information about the local density of states of the quantum dot. The spectral function of the RLM, derived from the retarded Green's function in Eq. (2.7) comprises of a Lorentzian peak at the energy ε_d with the width determined by the hybridization function Γ ,

$$A_\sigma(\omega) = \frac{1}{\pi} \frac{\Gamma}{(\omega - \varepsilon_d)^2 + \Gamma^2}. \quad (2.8)$$

A direct consequence of coupling an impurity to electronic leads are the transport of electrons through the impurity energy level. The electronic current from a lead to the impurity can be determined by the rate of change of the occupation of the lead $\alpha \in \{L, R\}$, $N_\alpha = \sum_{k\sigma} c_{\alpha k \sigma}^\dagger c_{\alpha k \sigma}$,

$$I_\alpha = -e \langle \dot{N}_\alpha \rangle \equiv -\frac{ie}{\hbar} \langle [H, N_\alpha] \rangle. \quad (2.9)$$

N_α commutes with the noninteracting lead Hamiltonian H_{leads} and the impurity Hamiltonian H_{imp} . The only contribution to the current is from the term $\langle [H_T, N_\alpha] \rangle$. Thus, the total current across the impurity can be calculated from,

$$I = \frac{ie}{\hbar} \sum_{\alpha k \sigma} v_{\alpha k \sigma} \langle c_{\alpha k \sigma}^\dagger d_\sigma - \text{H.c.} \rangle. \quad (2.10)$$

These expectation values depend on the Green's functions and Fermi functions of the leads. A general expression of the current across an impurity is given by the Meir-Wingreen formula [63, 64]. But for systems with proportionate couplings, and in the noninteracting limit, Meir-Wingreen formula boils down

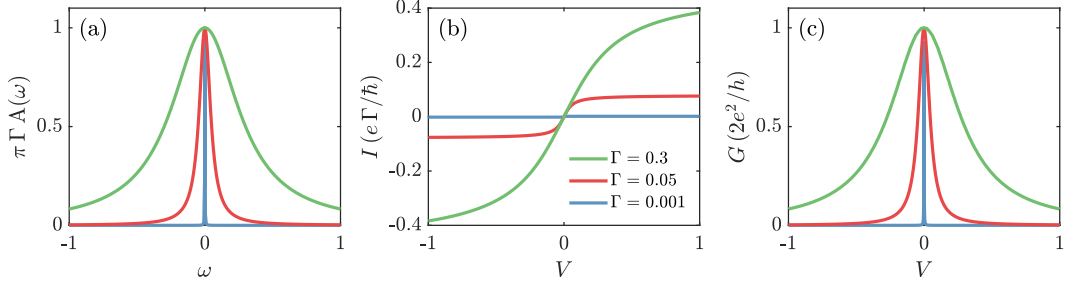


Figure 2.3: (a) The spectral function for the resonant level model at $\varepsilon_d = 0$, (b) the current-voltage characteristics and (c) the corresponding differential conductance $G = dI/dV$ as a function of the bias voltage V for different values of Γ and assuming temperature of the leads $T_L = T_R = 0.001 \Gamma$.

to a much simpler well-known expression, the Landauer-Buttiker formula [4, 65–67],

$$I = \frac{2e}{\hbar} \int d\omega [f_L(\omega) - f_R(\omega)] \mathbb{T}(\omega), \quad (2.11)$$

where $\mathbb{T}(\omega)$ is the transmission coefficient, $f_\alpha(\omega)$ is the Fermi function of lead α and the prefactor 2 corresponds to the number of spin channels. The transport across the quantum dot depends on the available electron density on the quantum dot, hence the transmission coefficient can be related to the spectral function as, $\mathbb{T}(\omega) = \pi \Gamma A(\omega)$ [64]. A more general form of transport is to have different couplings Γ_α to each lead α . In such a case, the transmission coefficient and spectral functions become of the form,

$$\mathbb{T}(\omega) = \pi \frac{4\Gamma_L \Gamma_R}{\Gamma} A(\omega) = \frac{4\Gamma_L \Gamma_R}{(\omega - \varepsilon_d)^2 + \Gamma^2}, \quad (2.12)$$

where $\Gamma = \Gamma_L + \Gamma_R$ is the total broadening of the resonant level due to the couplings to both leads. For temperatures $T \ll \Gamma$, potential bias V applied as $\mu_L = 0$ and $\mu_R = V$, the transport properties can directly scan the density of states of the quantum dot. Specifically, the differential conductance becomes $G(V) = dI/dV = \frac{2e^2}{\hbar} \mathbb{T}(\omega = V)$, and can thus be used experimentally to investigate the density of states of such systems. Figure 2.3(a) shows the spectral function of a RLM for different level broadenings Γ . The influence of the level broadening on the current-voltage characteristics is depicted in Fig. 2.3(b). The differential conductance as a function of V perfectly resembles the spectral function, and hence the density of states of the dot.

The physics of a quantum impurity becomes more complicated once we introduce the on-dot interaction $U \neq 0$. In the next chapter, we discuss the difficulties introduced by the interactions and the numerical methods available to tackle them.

Chapter 3

The many-body physics of interacting quantum impurities

When the ingenuity and the equations stop resulting in reliable solutions to the world around you, the physicists rely on their loyal calculating machines. In many of the cases, an efficiently adapted algorithm can provide solution to otherwise unsolvable analytical labyrinths. Particularly for the case of quantum many-body systems, the numerical techniques, such as the numerical renormalization group and the density matrix renormalization group constitute the state-of-the-art methods to study the physics originating from the strong electronic correlations in nanostructures.

The Kondo problem is one example of such a challenge that is very hard to deal with analytically. The perturbative treatment of the Kondo problem as done by Jun Kondo resulted in logarithmic divergences at low temperatures [36]. Though this logarithmic divergence was able to explain the rise in low-temperature resistivity of bulk metal alloys, having divergences in a theoretical description is often frowned upon in physics. A more systematic renormalization treatment of the conduction band done by P.W. Anderson [8], now known as the poor man's scaling, also ended up in logarithmic divergences of the renormalized couplings. But to their credit, both these works were able to identify an energy scale at the low temperatures where the logarithmic divergences dominate. This gave rise to the first definition of the Kondo energy scale or more commonly known as the Kondo temperature T_K ,

$$T_K \sim D \exp(-1/\rho J), \quad (3.1)$$

where D is the band half-width, ρ the density of states of the conduction band, and J the Kondo coupling.

As Sir Isaac Newton famously remarked, "*If I have seen further, it is by standing on the shoulders of giants*", K.G. Wilson in 1975, astutely recognized from the aforementioned works that the relevant physics of the Kondo problem occurs at low energies and had to be given greater importance. In his seminal work [13], Wilson's ingenious idea to deal with the persistent logarithmic divergences was to introduce them into the conduction band. More precisely, he introduced a logarithmic discretization of the conduction

band, strategically enhancing the significance of low-energy contributions. This worked wonders for the Kondo problem and related quantum impurity problems in general. Wilson's approach came to be known as the Numerical Renormalization Group method. It revolutionized the understanding of quantum impurity problems and earned him the Nobel prize in physics in 1982. In the next section, I will describe Wilson's NRG method in detail.

3.1 Numerical renormalization group

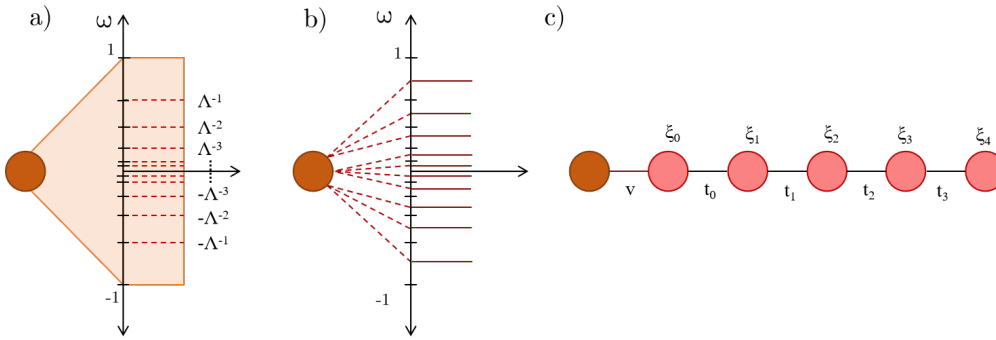


Figure 3.1: The schematic illustration of the NRG steps [14]. (a) The conduction band is separated into logarithmically spaced intervals I_k , (b) shows the conduction band after discretization where a single level represents the whole interval and (c) the semi-infinite Wilson chain after tridiagonalization with decaying couplings t_n and on-site energies ξ_n .

The Wilson's NRG is a non-perturbative method to study strongly correlated systems. Though NRG can be applied to various physical systems, the effectiveness of NRG in the study of quantum many-body systems is nothing short of impressive. In simple terms, NRG procedure can be summarized as follows,

- (i) Discretization of the continuum energy band,
- (ii) Tridiagonalization: transformation to tight-binding Wilson chain,
- (iii) Iterative diagonalization of the Hamiltonian,
- (iv) Truncating the high energy modes to resolve the low energy behavior.

I will describe the relevance of each step of the NRG here and then discuss how the common quantum impurity problems look through the lens of NRG. The fundamental concept behind NRG is a truncative iterative diagonalization with the assumption that the ground state of the total interacting Hamiltonian can be described by the low energy eigenstates of the intermediate Hamiltonians in the Wilson chain. For a quantum impurity coupled to an electronic reservoir, one can implement NRG with the following steps:

i) Discretization: We start by discretizing the conduction band logarithmically as shown in Fig. 3.1(a), typically described in NRG literature using the discretization parameter Λ . The logarithmically discretized intervals in the positive energy regime are defined as, $I_k = [\Lambda^{-k}, \Lambda^{-(k+1)}]$, where $k = [0, 1, 2, 3, \dots]$ and analogously for the negative energies. The half width of the conduction band is taken to be $D = 1$.

This logarithmic discretization is important to resolve the low-energy physics, especially in the case of such phenomena as the Kondo effect. From the point of view of the physics concerned, the logarithmic discretization, by design, gives more importance to the lower energy scales than the higher energies, resulting in the high resolving power of the NRG in the energy domain. In terms of the numerics, this scheme of discretization deals with the logarithmic divergences that come up in the analytical approaches at low energy scales, thus resulting in a more stable numerical results. Moreover, the scaling behaviors exhibited by various systems, such as the Kondo scaling, can be captured naturally by the way we describe the conduction band. Note that one can only discretize the conduction band till the Fermi level, thus NRG is not suitable to deal with the nonequilibrium phenomena resulting from different lead chemical potentials.

Once the conduction band is discretized, each interval is represented by a single energy ϵ_k . It is important to note that there is a certain degree of freedom associated with the choice of discretization schemes and associated energies ϵ_k , outlined by different schemes as in the references [14, 68, 69]. An additional factor of Λ^{-z} with $z \in [0, 1]$ known as the z-shift can also be used to improve the discretization artifacts in the NRG results by averaging over the data with different z-shifts [14]. After discretization, the impurity is coupled directly to each discretized interval I_k of the conduction band, via the couplings $v_{\alpha k \sigma} = \sqrt{\frac{\Gamma_\alpha}{\pi \rho}} \Lambda^{-k/2}$, that depend on the hybridization function Γ_α , width of the interval by Λ^{-k} and the band structure ρ near the discretized energy. The discretization of conduction band results in a transformation of the impurity coupled with a continuum bath to a star geometry of couplings, where the impurity is coupled to each and every discretized energy level on the conduction band [cf. Figs. 3.1(a,b)].

ii) Tridiagonalization:: One can transform the Hamiltonian with the discrete conduction band into a semi-infinite tight-binding chain, known as the Wilson chain for logarithmic discretization [13], as shown in Fig. 3.1(c). This can be accomplished by making use of the Lanczos method [70–72]. The transformed Hamiltonian constitutes the Hamiltonian of the NRG method with conduction band represented by the Wilson chain, which is given by,

$$H_{\text{NRG}} = H_{\text{imp}} + \sum_{\sigma} v_{\sigma} (f_{0\sigma}^{\dagger} d_{\sigma} + \text{H.c.}) + \sum_{n=0}^{\infty} \sum_{\sigma} \xi_n f_{n\sigma}^{\dagger} f_{n\sigma} + \sum_{n=0}^{\infty} \sum_{\sigma} t_n (f_{n\sigma}^{\dagger} f_{n+1\sigma} + \text{H.c.}), \quad (3.2)$$

where $f_{n\sigma}^{\dagger}$ ($f_{n\sigma}$) is the creation (annihilation) operator for an electron with spin σ on the n^{th} site of the Wilson chain. The impurity level described in H_{imp} is coupled to the zero-th site of the Wilson chain via the second term. The third term describes the on-site energies ξ_n of the n^{th} site of the Wilson chain, and the coupling between the sites is denoted by the hoppings t_n .

Starting from $H_0 = H_{\text{imp}} + \sum_{\sigma} v_{\sigma} (f_{0\sigma}^{\dagger} d_{\sigma} + \text{H.c.}) + \xi_0 f_{0\sigma}^{\dagger} f_{0\sigma}$, one can generate the full NRG Hamiltonian in Eq. (3.2) via the recursion relation,

$$H_{n+1} = \sqrt{\Lambda} H_n + \sum_{\sigma} \xi_{n+1} f_{n+1\sigma}^{\dagger} f_{n+1\sigma} + \sum_{\sigma} t_n (f_{n\sigma}^{\dagger} f_{n+1\sigma} + \text{H.c.}). \quad (3.3)$$

This relation adds one site to the impurity after another, thus essentially forming the full Wilson chain.

iii) *Iterative diagonalization*: Consequently, one can systematically diagonalize the Wilson chain Hamiltonian H_{NRG} by diagonalizing the impurity Hamilton H_{imp} first, then adding a subsequent site of the Wilson chain according to Eq. (3.3) followed by the diagonalization of the new effective total Hamiltonian H_n , and accordingly in an iterative fashion.

iv) *Truncation*: Introducing additional fermionic sites with $f_{n\sigma}^\dagger$ leads to a significant expansion of the Hilbert space. This is where one of the main assumptions of the NRG procedure comes in. Assuming that the ground state of the final Hamiltonian can be described by the low energy eigenstates of the intermediate Hamiltonians H_n , we truncate the Hilbert space by keeping a maximum number N_{keep} of lowest energy eigenstates after each iteration. This truncation of the Hilbert space at each iteration keeps the calculations numerically feasible for a finite chain length N . An improvement on the original NRG procedure, i.e., the full density matrix - numerical renormalization group (fdmNRG) [14, 73] has managed to make use of the discarded states during truncation. The truncated states along with the kept states of the last NRG iteration are used to generate the "full" density matrix. Taking the expectation values of the operators along this "full" density matrix allows the NRG procedure to minimize the loss of information by truncation.

In theory, one can extend the Wilson chain up to infinity in order to describe the entire energy regime of the system. From a practical perspective, one has to stop the iterative procedure at some point. One can make use of some special properties of the Wilson chain for this purpose. The exponential decay of the hoppings $t_n \sim \Lambda^{-n/2}$, results in a natural energy scale separation along the Wilson chain. Thus one can cut the Wilson chain at site N and still be able to resolve energies above $\sim \Lambda^{-(N-1)/2}$. A more rigorous argument is from the renormalization fixed points: Eq. (3.3), also known as the renormalization group transformation, transforms H_n into a rescaled effective Hamiltonian H_{n+1} . Beyond a certain n , the renormalization procedure does not bring any changes to the spectrum of H_n , thus converging the RG transformation into a fixed point of the renormalization group transformation. It is not guaranteed that a fixed point will always exist in the renormalization procedure. In some cases, a particular number of repeated applications of the renormalization group transformation may contain a fixed point. Therefore, in the case of impurity problems, one typically examines the spectra of the even and odd sites of the Wilson chain separately to identify these fixed points.

3.1.1 Renormalization group flow diagram

The energy spectra of the Hamiltonian evolves with every subsequent action of the RG transformation. This evolution or flow of the energy states is referred to as the RG flow in literature. The RG flow for a SIAM is presented in Fig. 3.2 with $N = 100$ sites of the Wilson chain and maximum number of kept states $N_{\text{keep}} = 1000$.

The SIAM has three RG fixed points. i) Free-orbital (FO) fixed point: this fixed point corresponds to an effective Hamiltonian with the impurity decoupled from the bath. ii) Local moment (LM) fixed point: an effective Hamiltonian with single occupation of the orbital level describes this fixed point. i.e., an impurity with orbital level below the Fermi level ($\epsilon_d = -U/2$ in our case), beyond the level broadening

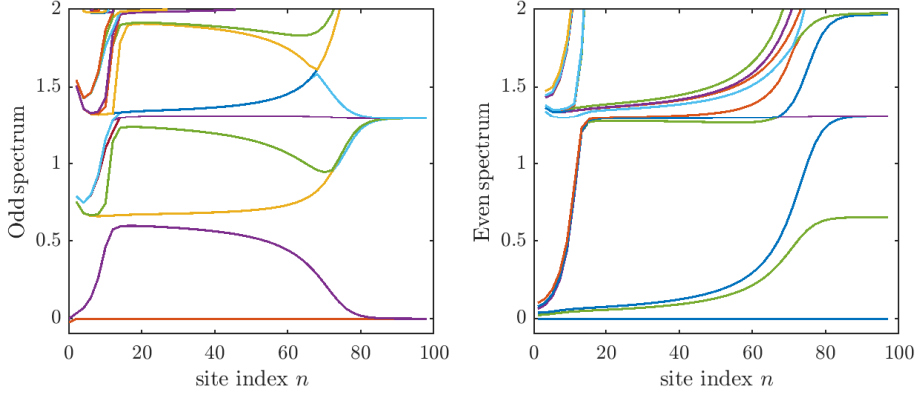


Figure 3.2: The renormalization group flow of the lowest energy eigenstates in the odd Wilson sites (left panel) and even Wilson sites (right panel) for a SIAM with $\Gamma = 0.001$, $U = 50\Gamma$, $\varepsilon_d = -U/2$ and standard NRG parameters $\Lambda = 2$, $N = 100$, $N_{\text{keep}} = 1000$. The SIAM parameters are in the units of band half-width $D = 1$.

($\varepsilon_d < -\Gamma$), and $U \gg \Gamma$ to avoid double occupancy. iii) Strong-coupling (SC) fixed point: corresponds to the impurity strongly coupled to the zero-th Wilson site. This effective coupling in the SC fixed point is so strong that the rest of the Wilson chain is essentially decoupled from the system.

One can identify these fixed points from the RG flow of the spectra presented in Fig. 3.2. Numerically, the fixed points are seen as a relatively stationary behavior of the spectra along the RG flow. For $5 < n < 10$, we have the FO fixed point as the impurity is relatively unperturbed by the Wilson chain. Around $20 < n < 60$, the system passes through the local moment fixed point. The strong coupling fixed point is reached for $n > 80$. The crossovers between the fixed points can be related to the corresponding energy-scales. Specifically, the system moves from FO to LM at energies around $\Gamma = 0.001 \approx \Lambda^{-10/2}$. The crossover from the LM to SC occurs at energies near the Kondo temperature. For a SIAM, the Kondo temperature T_K can be estimated analytically by the Haldane formula [74],

$$T_K = \sqrt{\frac{\Gamma U}{2}} \exp \left[\frac{\pi \varepsilon_d (\varepsilon_d + U)}{2\Gamma U} \right]. \quad (3.4)$$

Thus, for the system parameters in Fig. 3.2, the Kondo temperature is $T_K = 1.4 \times 10^{-11} \approx \Lambda^{-72/2}$, resulting in the crossover to the SC fixed point occurring at $n \approx 72$.

Moreover, the degeneracy of the ground state at the fixed points can also provide insights into the system. LM has two-fold degenerate ground state, corresponding to the degenerate spin states of the quantum dot. On the other hand, SC has a singlet ground state consisting of the strongly coupled impurity level and the zero-th Wilson site. This in turn sheds light onto the screening properties of the Kondo effect, since the singlet ground state of the combined impurity and zero-th site of the Wilson chain remains unaffected by the rest of the bath/chain under further RG transformations.

3.1.2 Spectral function

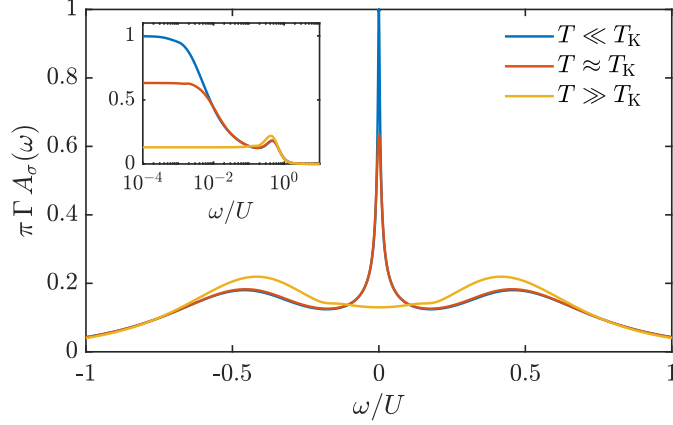


Figure 3.3: The spectral function $A_\sigma(\omega)$ of a SIAM with $\Gamma = 0.001$, $U = 10\Gamma$, $\varepsilon_d = -U/2$ and standard NRG parameters $\Lambda = 2$, $N = 100$, $N_{\text{keep}} = 1000$ with z -averaging over 4 different z -shifts. The parameters are in the unit of band half-width $D = 1$. The inset shows the same data in the logarithmic x axis.

The expectation values of any operator (pairs) defined on the Wilson chain can be readily calculated from the NRG spectra by using the Lehmann representation. Thus, the spectral function $A_\sigma(\omega) = -\frac{1}{\pi} \text{Im}(G_\sigma^r(\omega))$ can be obtained according to the operators in the definition of $G^r(\omega)$. Since the NRG spectrum is discrete, one obtains the spectral function as delta peaks binned in the energy domain. This discrete spectral weights are then broadened to obtain a smooth spectral function [75].

The spectral function for a SIAM at the particle-hole (p-h) symmetry point, $\varepsilon_d = -U/2$, calculated using NRG is shown in Fig. 3.3. The spectral function consists of two maxima at $\omega = \pm U/2$, known as the Hubbard peaks, which are broadened by the hybridization function Γ . With decreasing temperature, a resonance peak starts to emerge in the spectral function at the Fermi level. This resonance, widely known as the Kondo-Abrikosov-Suhl resonance or the Kondo resonance in short, is a characteristic feature of the many-body Kondo effect originating from strong electron-electron interactions in the low energy regime.

3.1.3 Linear response transport properties

In the linear response regime of potential bias V and temperature gradient ΔT , one can find the charge current I_C and the heat current I_Q to be as follows,

$$\begin{pmatrix} I_C \\ I_Q \end{pmatrix} = \sum_{\sigma} \begin{pmatrix} e^2 L_{0\sigma} & -e L_{1\sigma}/T \\ -e L_{1\sigma} & L_{2\sigma}/T \end{pmatrix} \begin{pmatrix} V \\ \Delta T \end{pmatrix}, \quad (3.5)$$

where,

$$L_{n\sigma} = -\frac{1}{h} \int d\omega \omega^n \frac{\partial f(\omega)}{\partial \omega} \mathbb{T}_{\sigma}(\omega). \quad (3.6)$$

Here, $L_n = \sum_{\sigma} L_{n\sigma}$, commonly referred to as the Onsager integrals, are determined from the transmission coefficient $\mathbb{T}_{\sigma}(\omega)$. From the NRG perspective, the spectral functions can be directly calculated from the

NRG spectra as discrete delta peaks, which in turn can be related to $\mathbb{T}(\omega)$. Thus, the Onsager integrals can be directly calculated by folding $\frac{\partial f(\omega)}{\partial \omega}$ onto the delta peaks of the spectral function $A(\omega)$ with appropriate weights [76].

Based on Eq. (3.5), one can define the linear response transport coefficients as,

$$G = e^2 L_0, \quad (3.7)$$

$$S = -\frac{1}{eT} \frac{L_1}{L_0}, \quad (3.8)$$

$$\kappa = \frac{1}{T} \left(L_2 - \frac{L_1^2}{L_0} \right), \quad (3.9)$$

where G is the differential conductance, S is the Seebeck coefficient and κ is the electronic contribution to the heat conductance.

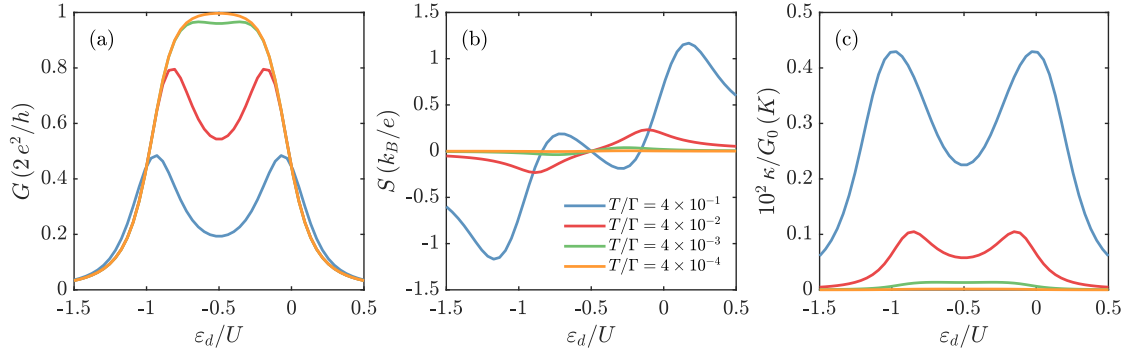


Figure 3.4: The linear response transport properties: (a) differential conductance G , (b) Seebeck coefficient S and (c) normalized electronic contribution to the heat conductance κ/G_0 for a SIAM with $\Gamma = 0.01$, $U = 0.1$ for different values of orbital energy ε_d with temperatures as indicated in the legends.

Figure 3.4 shows the linear response transport coefficients calculated for a SIAM with $\Gamma = 0.01$ and $U = 0.1$ for different values of temperatures. At high temperatures, the conductance shown in Fig. 3.4(a) shows peaks around $\varepsilon_d \approx 0, -U$ corresponding to the tunneling processes happening when the orbital level is close to the lead Fermi level. When the temperature is decreased, the conductance in the local moment regime $-U \lesssim \varepsilon_d \lesssim 0$ starts to increase, due to the Kondo effect. The conductance reaches the theoretical maxima for temperatures well below the Kondo temperature T_K . The uneven rise in the conductance for different values of orbital level ε_d are linked to the dependence of T_K on ε_d as in the Haldane formula mentioned in Eq. (3.4). The universal scaling of the Kondo resonance with respect to the Kondo temperature, and consequently the universality of the differential conductance $G(T/T_K)$, dictates the twin peak structure of $G(\varepsilon_d)$ seen in Fig. 3.4(a) for intermediate temperatures. T_K being a crossover energy scale, is only defined up to a prefactor of the order of 1. Alternative definitions of T_K make use of the spin susceptibility χ'' at zero temperature [2], half-width of the Kondo resonance or consequently the half-width of the zero-bias conductance peak $G(T_K) = G(0)/2$ [39].

The linear response Seebeck coefficient S shown in Fig. 3.4(b) can be related to the asymmetry of

the spectral function near $\omega = 0$. At the particle-hole symmetry point $\epsilon_d = -U/2$, the spectral function is symmetric with respect to $\omega = 0$ resulting in $S = 0$. Using the same argument, one can infer that S will remain antisymmetric across the p-h symmetry point. When the temperature is reduced, as Kondo resonance starts to form in the density of states of the impurity, and thus essentially altering the spectral function near $\omega = 0$, the Seebeck coefficient changes sign. This sign change in the Seebeck coefficient has been identified as a characteristic feature of the Kondo effect [77]. It is important to note that, unlike the T_K defined as the half-width of the conductance peak which follows the universal scaling, the temperature at which the Seebeck coefficient changes sign is not a universal Kondo energy scale. Rather a scaling akin to $G(0)/2$ was found to exist for the temperature at which S exhibits the largest magnitude in the Kondo regime [77].

The electronic contribution to the heat conductance κ does not show any signatures of the Kondo effect. Rather, κ contains significant values near $\epsilon_d \approx -U, 0$ corresponding to the energy transfer via the tunneling processes mediated by the quantum dot orbital.

The NRG calculations presented in this chapter are performed using the open-source Flexible DM-NRG code [78]. This code is used for the NRG calculations in the publications [A,B,D-F]. The NRG calculations for the publication [C] have been performed using the open-source QSpace tensor library available for Matlab [79].

Chapter 4

Numerical methods for systems out of equilibrium

The works that constitute this thesis primarily employ two methods to investigate the nonequilibrium behavior of the quantum impurity systems, i) a hybrid NRG-tDMRG thermofield quench method and ii) an NRG based perturbation method. In the following sections, I will describe these methods in more detail.

4.1 Hybrid numerical renormalization group - time-dependent density matrix renormalization group approach

The hybrid NRG-tDMRG method [32] can treat the system which has truly nonequilibrium correlations such as an interacting quantum dot coupled to leads kept under large and finite potential or thermal biases. A quantum impurity system described by a SIAM Hamiltonian as in Sec. 2.2.1 is considered as a model system in this chapter.

In short, employing the NRG-tDMRG to study the nonequilibrium transport of a quantum impurity system requires the separation of equilibrium and nonequilibrium energy modes of the leads and a thermofield treatment to map the leads into a particle-hole representation. The equilibrium lead modes together with the impurity are treated with NRG to generate a renormalized impurity (RI) ground state, which is quenched with the filled (empty) modes in the nonequilibrium regime of the particle-hole representation using tDMRG. These steps are explicitly presented in Fig. 4.1 for an impurity coupled to two metallic leads (L, R). Thus, the implementation of NRG-tDMRG can be separated into four parts, i) *the hybrid discretization scheme*, ii) *thermofield representation*, iii) *tridiagonalization and recombination of the lead modes* and iv) *initial state quench and time evolution*. Each step is further described in the following sections.

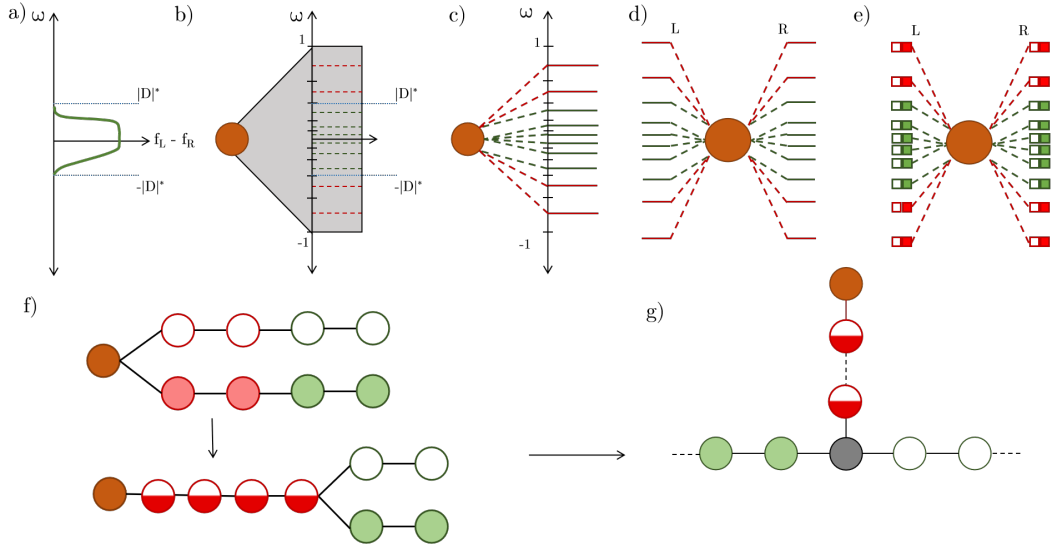


Figure 4.1: The NRG-tDMRG recipe: (a) the difference in lead Fermi distributions $f_L(\omega) - f_R(\omega)$ defining the transport window $[-D^*, D^*]$. (b,c) the hybrid discretization of the conduction band, i.e., linearly (logarithmically) discretized inside (outside) the transport window depicted as green (red) dashed lines. (d) the full system geometry after the discretization, i.e., the impurity coupled to each of the discretized modes in the left (L) and right (R) leads. (e) The schematic of the couplings after the thermofield treatment where the impurity is coupled to the filled particle modes (filled squares) and the empty hole modes (empty squares) in the enlarged Hilbert space. (f) The effective Wilson chains for the left-right recombined hole modes (empty circles) and particle modes (filled circles). The particles and holes outside the transport window are further recombined, represented as the half-filled red circles. (g) The initial state in the matrix product state (MPS) formalism with a renormalized impurity coupled to empty hole modes and filled particle modes ready for time evolution. Figure adapted from Ref. [32]

4.1.1 The hybrid logarithmic-linear discretization scheme

Unlike the discretization in NRG, where the entire conduction band is discretized logarithmically according to the discretization parameter Λ , the NRG-tDMRG employs a hybrid discretization scheme. The hybrid discretization scheme is based on the assumption that the high energy modes will essentially be in equilibrium whereas the lower energy modes can solely describe the nonequilibrium dynamics contributing to the transport. Thus, the regimes for the two discretizations are determined according to the transport window (TW) defined by the energy D^* at which the difference in Fermi functions $f_{L/R}(\omega)$ drops below a threshold value ε , i.e., $\max[f_L(D^*) - f_R(D^*)] < \varepsilon$. Resulting in the definition of D^* as

$$D^* = \mu + T \log(\varepsilon^{-1} - 1). \quad (4.1)$$

Beyond $\text{TW} \equiv [-D^*, D^*]$, the modes are in equilibrium as the difference in Fermi functions of the leads $|f_L(\omega) - f_R(\omega)|$ is essentially zero [cf. Fig. 4.1 (a-b)].

We discretize the energies outside the TW according to the discretization parameter Λ , Inside the TW, a linear discretization scheme according to the linear discretization parameter δ is performed as shown in Fig. 4.1 (b). For a smooth transition from the logarithmic discretization to the linear discretization, the energy intervals are determined by a function of the form

$$E(x) = \begin{cases} \delta \cdot x, & \text{for } |x| \leq D^*/\delta \\ \frac{\delta \cdot \sinh[\ln(\Lambda)(x \mp D^*/\delta)]}{\log(\Lambda)} \mp \delta \cdot D^*, & \text{for } x \gtrless \pm D^*/\delta, \end{cases}$$

where $x \in \mathbb{Z}$. This function thus generates a linearly discretized energy intervals for $E < |D^*|$ and logarithmically discretized intervals for $E > |D^*|$ with a continuous first derivative between the logarithmic and linear part. It is relevant to note that a z-shift akin to NRG discretization schemes also exist in the choice of discretizations here. As shown in Fig. 4.1 (c), each discretized interval $I_k = [E_k, E_{k+1}]$ has a representative energy ε_k determined as,

$$\varepsilon_k = \begin{cases} \frac{E_{k+1} - E_k}{\ln(E_{k+1}/E_k)}, & \text{if } |E_k|, |E_{k+1}| > D^* \\ \frac{1}{2}(E_{k+1} + E_k), & \text{elsewhere.} \end{cases}$$

The tunnel coupling between the impurity and a discretized mode k is given as $v_{\alpha\sigma k} = \sqrt{\Gamma_\alpha \delta_k / \pi}$, where δ_k is the size of the interval I_k .

The reliable timescales attained by the tDMRG time evolution are of the order of $1/D$ where D is the bandwidth. Since, the hybrid discretization scheme also changes the effective bandwidth for the tDMRG implementation from $D \rightarrow D^*$, it allows for the time evolution to reach longer timescales of the order of $1/D^*$. This is crucial in obtaining the steady-state value of the quantities of interest.

4.1.2 Thermofield representation of the lead modes

The conduction band discretized according to the prescription described in previous section is then subject to a thermofield treatment. Advantages of introducing a thermofield representation of the leads are manifold. First of all, it transforms the lead modes into a more useful physical representation with particle-like and hole-like modes. In this particle-hole picture, the finite temperature states can be represented as pure states, allowing for a "simple" initial state description for the quench and time evolution as will be discussed later. Additionally, the lead modes that decouple from the system can be described as simple product space in this description and can be omitted to improve computational efficiency. Moreover, the nonequilibrium parameters, such as the lead potential and the lead temperature, become embedded in the tunnel couplings of the transformed Hamiltonian in the thermofield description.

For the thermofield representation, the Hilbert space is doubled by introducing a decoupled auxiliary mode c_{q2} for every lead mode $c_{q1} = c_q$. Here, we use the composite index $q \equiv \{\alpha, k, \sigma\}$ for a concise representation. In the enlarged Hilbert space, spanned by $\{|0, 0\rangle_q, |0, 1\rangle_q, |1, 0\rangle_q, |1, 1\rangle_q\}$, we choose $|0, 1\rangle_q$ and $|1, 0\rangle_q$ to represent a pure state $|\Omega\rangle$ such that $\langle A \rangle = \langle \Omega | A | \Omega \rangle$ is the thermal expectation value of the operator A acting on the physical lead. Such a state $|\Omega\rangle$ can be represented as

$$|\Omega\rangle = \prod_q (\sqrt{1-f_q} |0, 1\rangle_q + \sqrt{f_q} |1, 0\rangle_q). \quad (4.2)$$

The choice of $|0, 1\rangle_q$ and $|1, 0\rangle_q$ is equally good as the choice of $|0, 0\rangle_q$ and $|1, 1\rangle_q$. The former choice has states with the same particle number resulting in the following Hilbert space rotation to retain particle number conservation. We rotate the Hilbert space in order to provide a product state representation of the thermal state

$$\begin{pmatrix} \tilde{c}_{q1} \\ \tilde{c}_{q2} \end{pmatrix} = \begin{pmatrix} \sqrt{1-f_q} & -\sqrt{f_q} \\ \sqrt{f_q} & \sqrt{1-f_q} \end{pmatrix} \begin{pmatrix} c_{q1} \\ c_{q2} \end{pmatrix}. \quad (4.3)$$

The new tilde basis has the modes defined as $\tilde{c}_{q1} |\Omega\rangle = \tilde{c}_{q2}^\dagger |\Omega\rangle = 0$, thus the modes corresponding to the index 1 and 2 can be interpreted as the holes and particles, respectively.

Thus, the rotation transforms the lead Hamiltonian in the enlarged Hilbert space as, $H_{\text{lead}} + H_{\text{aux}} = \sum_{qj} \epsilon_q c_{qj}^\dagger c_{qj} = \sum_{qj} \epsilon_q \tilde{c}_{qj}^\dagger \tilde{c}_{qj}$, where H_{aux} is the Hamiltonian of the auxiliary part corresponding to $j = 2$ in the original (non-tilde) basis. We set $\epsilon_{q2} = \epsilon_{q1} = \epsilon_q$ to avoid any couplings between the particle and hole modes after the rotation. More importantly, after the thermofield representation, the tunnel couplings in the tunneling Hamiltonian, $H_T = \sum_{qj} (\tilde{v}_{qj} d_{\alpha\sigma}^\dagger \tilde{c}_{qj} + \text{H.c.})$, will contain in itself the information about the nonequilibrium parameters, specifically, the temperature and potential of the leads via the Fermi functions as $\tilde{v}_{q1} = v_q \sqrt{1-f_q}$ and $\tilde{v}_{q2} = v_q \sqrt{f_q}$.

Since the tunnel couplings are now functions of the lead Fermi functions, we can decouple the particle and hole modes according to their respective weights $\sqrt{f_\alpha}$ and $\sqrt{1-f_\alpha}$. For energies outside the transport window, i.e., $\epsilon_k > D^* \implies f_\alpha(\epsilon_k) \approx 0$ and $\epsilon_k < -D^* \implies f_\alpha(\epsilon_k) \approx 1$. Thus,

$$\tilde{v}_{q1} \approx 0 \quad \text{if } \epsilon_k < -D^*, \quad (4.4)$$

$$\tilde{v}_{q2} \approx 0 \quad \text{if } \epsilon_k > D^*. \quad (4.5)$$

4.1.3 Recombination of the leads

After the thermofield treatment of the lead modes, we recombine both left and right leads into one effective lead. One can define an effective coupling to the recombined lead mode based on the couplings to the individual L, R modes. This is a standard trick used for describing the equilibrium transport across a single impurity coupled to two leads [14]. Since all the information about the nonequilibrium parameters is already embedded in the tunnel couplings after the thermofield treatment, such a recombination remains valid in this picture. The effective modes and couplings thus take the form,

$$\tilde{v}_{ki}^{\text{even}} = \sqrt{|\tilde{v}_{Lki}|^2 + |\tilde{v}_{Rki}|^2}, \quad (4.6)$$

$$\tilde{c}_{k\sigma i}^{\text{even}} = \frac{1}{\tilde{v}_{ki}^{\text{even}}} (\tilde{v}_{Lki} \tilde{c}_{Lk\sigma i} + \tilde{v}_{Rki} \tilde{c}_{Rk\sigma i}), \quad (4.7)$$

$$\tilde{c}_{k\sigma i}^{\text{odd}} = \frac{1}{\tilde{v}_{ki}^{\text{even}}} (-\tilde{v}_{Rki}^* \tilde{c}_{Lk\sigma i} + \tilde{v}_{Lki}^* \tilde{c}_{Rk\sigma i}). \quad (4.8)$$

This recombination decouples half of the lead modes from the system, resulting in only the "even"

modes contributing to the transport. Note that, we have to recombine the leads separately for the holes and particles in order to keep the simple product form of the thermal state $|\Omega\rangle$. The recombined particle and hole lead modes are tridiagonalized to form "Wilson-like" chains with couplings t_n [cf. Fig. 4.1 (f)]. "Wilson-like" in the sense that the couplings corresponding to only the higher-energy sites follow an exponential decay, while this trend of energy scale separation is absent at the farther end of the chain.

Beyond the transport window, the particle and hole modes do not introduce any dynamics in the system. Thus, the hole and particle modes in the high energy regime are combined to form one chain, resulting in the geometry described in Fig. 4.1 (f). The logarithmic part of the system is then treated using NRG to get the ground state $|\Phi\rangle_{\text{ini}}$. Thus, the whole system is described in MPS framework according to Fig. 4.1 (g), where the renormalized impurity in the MPS chain is coupled to one side by the "filled" particle modes and "empty" hole modes to the other side. As a consequence, the initial state can be described as

$$|\Psi_{\text{ini}}\rangle = |0\rangle \otimes |0\rangle \otimes |0\rangle \otimes \dots \otimes |0\rangle \otimes |\Phi_{\text{ini}}\rangle \otimes |1\rangle \otimes \dots \otimes |1\rangle \otimes |1\rangle. \quad (4.9)$$

4.1.4 Initial state quench and time evolution

Density Matrix Renormalization Group

The density matrix renormalization group (DMRG) method introduced by Steven White [15], inspired from the original Wilson's NRG paper [13], was aimed at solving a class of problems not suitable for NRG. In general terms, the DMRG procedure starts by considering two subsystems of the entire system, and slowly increasing the Hilbert space dimension by introducing additional parts of the full system, in theory, until the whole system is described. The truncation to manage the Hilbert space dimension during each step of the DMRG procedure is based on the low energy eigenstates in the reduced density matrix of the growing subsystem. Unlike NRG, where the final system is described by low energy eigenstates of the *intermediate Hamiltonians*, DMRG ground state is obtained from the low energy eigenstates of the reduced *density matrices* of the contained subsystems. Hence the name - density matrix renormalization group. By design, DMRG is best suited for treating 1-dimensional systems. Since, one can easily define two subsystems making a cut at any part of the 1-D system and increase the Hilbert space by moving parts of one subsystem to the next. In the case of Matrix Product State representations, this is accomplished by the singular value decomposition (SVD) of the combined tensors. For a finite size 1-D system, DMRG ground state is obtained by starting from an initial guess of the ground state and iteratively sweeping the system, while variationally approximating the initial guess to the ground state.

Though the initial applications of DMRG were as described above, various extensions like via projected entangled pair states (PEPS) for higher dimensional systems [80, 81], time-dependent DMRG (tDMRG) for quenches and/or time evolution of quantum systems [82, 83], open-system DMRG to study dissipative systems [84–86] and many others have come into the picture over time. Reader can refer to [17, 87] for detailed reviews on the DMRG method.

We use the time-dependent DMRG method to time evolve the initial state. More precisely, a second-

order Trotter time evolution [88, 89] as described below is employed.

Trotter time evolution

Having a system described by N sites and assuming only hopping between the neighboring sites, the time evolution of the state can be described according to the pairwise Hamiltonian $H_{n,n+1}$ acting on neighbouring sites n and $n + 1$. Thus, the total Hamiltonian has the form

$$H = \sum_{n=1}^{N-1} H_{n,n+1}. \quad (4.10)$$

Consequently, the MPS state can be time evolved by using the two-site matrix product operators as,

$$\exp(-iHt) = \prod_{n=1}^{N-1} \exp(-iH_{n,n+1}t). \quad (4.11)$$

The Trotter time evolution comes from splitting the time window t into N_t parts, thus implementing the full time evolutions by small timesteps $\delta t = t/N_t$. In the small timestep δt , the time evolution can be described by even Hamiltonians $H_{\text{even}} = \sum_{n=\text{even}} H_{n,n+1}$ and odd Hamiltonians $H_{\text{odd}} = \sum_{n=\text{odd}} H_{n,n+1}$ as,

$$\exp(-iH_{\text{odd}}\delta t) \exp(-iH_{\text{even}}\delta t) + O(\delta t^2), \quad (4.12)$$

with an error of the order of $O(\delta t^2)$. An improvement of this approach is called second-order Trotter time evolution, where the error scales as $O(\delta t^3)$. Here, the evolution is done according to

$$\exp(-\frac{i}{2}H_{\text{odd}}\delta t) \exp(-iH_{\text{even}}\delta t) \exp(-\frac{i}{2}H_{\text{odd}}\delta t) + O(\delta t^3). \quad (4.13)$$

Therefore, a second-order Trotter time evolution is used to time evolve the initial MPS state $|\Psi_{\text{ini}}\rangle$ in Eq. (4.9) according to the total Hamiltonian of the enlarged Hilbert space $\mathcal{H} = H + H_{\text{aux}}$. The coupling between the high energy part (Φ_{ini}) and the low energy part is quenched across a finite time window and is time evolved further to reach the nonequilibrium steady-state.

4.1.5 Steady-state and physical observables

The physical observables to be computed have to be defined in the MPS basis as operators, so that the dynamics can be extracted by taking expectation value over $|\Psi(t)\rangle$ after a set number of timesteps.

The observables of interest in transport are of course the current and occupation number $n_\sigma = d_\sigma^\dagger d_\sigma$ of the quantum dot. The current from lead α to the quantum dot defined as in Eq. (2.10) takes the form,

$$I_\alpha = \frac{2e}{\hbar} \sum_{k\sigma} \text{Im}(v_{\alpha k\sigma} \langle d_\sigma^\dagger c_{\alpha k\sigma} \rangle) = \frac{2e}{\hbar} \sum_{k\sigma} \sum_j \text{Im}(\tilde{v}_{\alpha k\sigma j} \langle d_\sigma^\dagger \tilde{c}_{\alpha k\sigma j} \rangle). \quad (4.14)$$

Weighing the contributions to the particle current from each mode by their respective energy defines

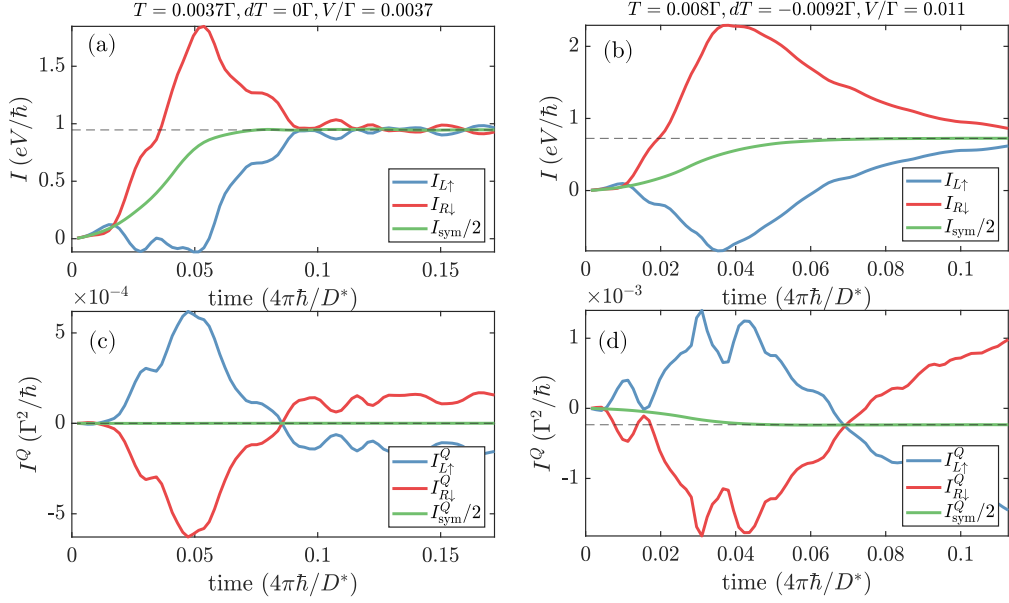


Figure 4.2: Representative dynamics of the particle current I (top row) and energy current I^Q (bottom row) calculated using NRGtDMRG for a SIAM with $\Gamma = 0.001$, $U = 12\Gamma$ and $\varepsilon_d = -U/3$ for different nonequilibrium parameters V and ΔT .

the energy current I^Q as,

$$I_{\alpha}^Q = \frac{2}{\hbar} \sum_{k\sigma} \sum_j \varepsilon_{k\sigma j} \text{Im}(\tilde{v}_{\alpha k\sigma j} \langle d_{\sigma}^{\dagger} \tilde{c}_{\alpha k\sigma j} \rangle). \quad (4.15)$$

Note that, a symmetrized particle (energy) current defined as $I_{\text{sym}}^{(Q)} = \frac{1}{2} (I_L^{(Q)} - I_R^{(Q)})$ converges to the steady-state before the individual currents (cf. Fig. 4.2). The NRG-tDMRG procedure was implemented in the MPS framework using the open-source QSpace tensor library for Matlab [79], with symmetries implemented using [90, 91].

The dynamics of the particle current and the heat current for NRG-tDMRG run for different nonequilibrium parameters is shown in Fig. 4.2. The charge current shows a transient behavior corresponding to the time window of the quench, and starts to oscillate around a finite steady-state value. This steady-state value can be extracted in various ways. In the work [B], the steady-state was obtained by averaging the dynamics over a number of oscillations. An improvement to this, by using linear prediction to obtain the $t \rightarrow \infty$ value, has been used in the most recent paper [C].

4.2 Perturbation theory for strongly asymmetric systems

In the absence of strong couplings, complex many-body phenomena do not emerge in quantum impurity systems. Rather, the transfer of electrons between the leads and the quantum dot via tunneling processes result in a net charge transfer giving rise to single-electron charging effects [92]. With the lowest-order perturbation theory in the tunneling Hamiltonian H_T , one can find the tunneling rates Γ between the quantum dot and a weakly coupled lead, thus providing an expression for the electronic current I [93].

Note that, introducing higher order contributions from the perturbation theory will result in co-tunneling processes containing approximated many-body features of the lowest order, thus the derivation in this section can only be considered accurate for very weak couplings where the sequential tunneling processes are solely responsible for the transport.

A smart way of setting up the system allows to abuse this perturbation formulation for the transport and reveal many-body features in the quantum dot [33, 94]. For this purpose, a special case of the Hamiltonian H_{SIAM} presented in the Sec. 2.2.1 is considered. The impurity is strongly coupled to the left lead ($\mu_L = 0, T_L = 0$, i.e., kept in equilibrium with the dot) where the coupling to the right lead (containing the nonequilibrium parameters $\mu_R = -eV, T_R = \Delta T$) is treated as a perturbation on this strongly coupled subsystem. This asymmetric model resembles many experimental setups to study quantum transport, such as scanning tunneling microscopy (STM) setups for molecular junctions [95–98], semiconductor quantum dot and single electron transistor (SET) setups [41, 99, 100], where the coupling to an individual lead can be easily tuned. In the case of STM, the weakly coupled lead corresponds to the tip of the scanning tunneling microscope and the coupling can be tuned by moving the tip away or closer to the impurity/molecule. For SET experiments, the coupling between the dot and a single electronic reservoir can be tuned by electrostatic gate voltages to control the tunnel barrier. Such easily relatable experimental setups proved to be an additional motivation to study transport in the strongly asymmetric coupling limit. It is relevant to emphasize that the perturbation is performed with respect to the tunnel matrix elements, thus choosing a nonlinear potential or temperature gradient characterizing the density of states in the weakly coupled lead is perfectly valid under this formulation.

The Hamiltonians for such an asymmetric setup consisting of a strongly coupled left subsystem H_L , weakly coupled to the right lead H_R via the tunneling Hamiltonian H_T can be written as,

$$H_L = \varepsilon_d \sum_{\sigma} n_{\sigma} + U n_{\uparrow} n_{\downarrow} + \sum_{k\sigma} \varepsilon_k c_{Lk\sigma}^{\dagger} c_{Lk\sigma} + t_L \sum_{k\sigma} (d_{\sigma}^{\dagger} c_{Lk\sigma} + c_{Lk\sigma}^{\dagger} d_{\sigma}), \quad (4.16)$$

$$H_T = t_R \sum_{k\sigma} (d_{\sigma}^{\dagger} c_{Rk\sigma} + c_{Rk\sigma}^{\dagger} d_{\sigma}), \quad (4.17)$$

$$H_R = \sum_{k\sigma} (\varepsilon_k - eV) c_{Rk\sigma}^{\dagger} c_{Rk\sigma}, \quad (4.18)$$

$$H_{\text{tot}} = H_L + H_T + H_R. \quad (4.19)$$

Here, the left subsystem L consists of the quantum dot with energy level ε_d , Coulombic repulsion U , strongly coupled to the left lead kept at $\mu_L = 0, T_L = 0$ with tunnel matrix elements $t_L = \sqrt{\Gamma_L/(\pi \rho_L)}$ between them. The temperature of the left lead is assumed to be much less than any other energy scale in the system, and thus for all practical purposes can be approximated to $T_L \approx 0$. The right lead kept at $\mu_R = -eV$ and $T_R = \Delta T$ is defined as the right subsystem. The two subsystems are weakly coupled via the tunnel coupling $t_R = \sqrt{\Gamma_R/(\pi \rho_R)}$ with $\Gamma_R \ll \Gamma_L$.

Assuming the left and right subsystems were initially decoupled and in equilibrium, one can define

their respective density matrices as,

$$\begin{aligned}\rho_L(i) &= \frac{1}{Z} \exp(-\beta E_i), \\ \rho_R(j) &= \frac{1}{Z} \exp(-\beta E_j).\end{aligned}\quad (4.20)$$

The transition rate $\Gamma_{i \rightarrow f}$ between an initial state of the system $|i\rangle$ with energy E_i and a final state of the system $|f\rangle$ with energy E_f can be expressed as,

$$\Gamma_{i \rightarrow f} = \frac{2\pi}{\hbar} |\langle f | H_T | i \rangle|^2 \delta(E_i - E_f). \quad (4.21)$$

Weighing by the occupation of the subsystems ρ_L and ρ_R , and summing over all the possible contributions of single electron charge transfer, one ends up at the tunneling rate $\Gamma_{L \rightarrow R}$ from the left to right of the form,

$$\Gamma_{L \rightarrow R} = \frac{2\pi}{\hbar} \sum_{i,j,i',j'} |t_R|^2 |\langle j', i' | \sum_{k,\sigma} c_{Rk\sigma}^\dagger d_\sigma | i, j \rangle|^2 \delta(E_i^N + E_j^{N_R} - E_{i'}^{N-1} - E_{j'}^{N_R+1}) \rho_L(i) \rho_R(j). \quad (4.22)$$

Here, i and j are the eigenstates of the N -particle initial density matrices described in Eq. (4.21), and i' and j' are the eigenstates after a single electron transfer. Making use of the diagonal form of the initial density matrices and transforming into the time domain,

$$\Gamma_{L \rightarrow R} = \frac{2\pi}{\hbar} t_R^2 \sum_{i,j,i',j'} \int_{-\infty}^{\infty} \frac{dt}{2\pi} \sum_{k\sigma} |\langle j' | c_{Rk\sigma}^\dagger | j \rangle|^2 \rho_R(j) |\langle i' | d_\sigma | i \rangle|^2 \rho_L(i) e^{i(\Delta E_{j,j'}^R + \Delta E_{i,i'}^L - eV)t}. \quad (4.23)$$

Absorbing the time evolution into the operators, $d_\sigma^\dagger(t) = e^{-iH_L t} d_\sigma^\dagger e^{iH_L t}$ and $c_{Rk\sigma}^\dagger(t) = e^{-iH_R t} c_{Rk\sigma}^\dagger e^{iH_R t}$, one can rewrite the above equation in the form of Green's functions as,

$$\Gamma_{L \rightarrow R} = \frac{1}{\hbar} t_R^2 \int_{-\infty}^{\infty} dt e^{-ieVt} \sum_{k\sigma} \langle d_\sigma^\dagger(t) d_\sigma(0) \rangle \langle c_{k\sigma}(t) c_{k\sigma}^\dagger(0) \rangle. \quad (4.24)$$

Here, the correlators correspond to the lesser and greater Green's functions on the left and right subsystems respectively as, $\langle d_\sigma^\dagger(t) d_\sigma(0) \rangle = -iG_{d,\sigma}^<(-t)$ and $\langle c_{k\sigma}(t) c_{k\sigma}^\dagger(0) \rangle = iG_{c_{Rk\sigma}}^>(t)$. Transforming back into the energy domain, one can rewrite

$$\Gamma_{L \rightarrow R} = \frac{1}{\hbar} t_R^2 \int d\omega \sum_{\sigma} G_{d\sigma}^<(\omega) G_{\psi_\sigma}^>(\omega + eV), \quad (4.25)$$

where $\psi_\sigma \equiv \sum_k c_{k\sigma}$, and $G_{d\sigma}^<(\omega)$ and $G_{\psi_\sigma}^>(\omega)$ are equilibrium Green's functions on H_L and H_R respectively, with $G_{d\sigma}^<(\omega) = 2\pi i f_L(\omega) \rho_{d\sigma}(\omega)$ and $G_{\psi_\sigma}^>(\omega) = -2\pi i (1 - f_R(\omega)) \rho_R$. The forward current I^F between L and R is then,

$$I^F = \frac{2\pi}{\hbar} |t_R|^2 \rho_{R\sigma} \int_{-\infty}^{\infty} d\omega f_L(\omega) [1 - f_R(\omega - eV)] \rho_{d\sigma}(\omega). \quad (4.26)$$

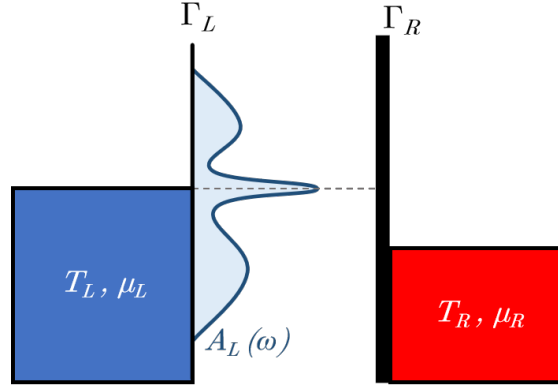


Figure 4.3: A quantum dot strongly coupled to the left lead with temperature $T_L = 0$ and chemical potential $\mu_L = 0$. The associated spectral function is depicted in the middle as $A_L(\omega)$. The right lead is kept at chemical potential $\mu_R = -eV$ and temperature $T_R = \Delta T$.

Similarly, the backward current also takes the form,

$$I^B = \frac{2\pi}{\hbar} |t_R|^2 \rho_{R\sigma} \int_{-\infty}^{\infty} d\omega [1 - f_L(\omega)] f_R(\omega - eV) \rho_{d\sigma}(\omega), \quad (4.27)$$

where $\rho_{R\sigma}$ is the spin-resolved density of states of the right lead and $\rho_{d\sigma}$ is the spin-resolved density of states of the quantum dot. For a flat band on the right lead $\rho_{R\sigma}$ is considered to be constant, hybridization function to the right lead $\Gamma_R = 2\pi\rho t_R^2$, and the density of states on the strongly coupled subsystem represented by the spectral function of the dot $A_L(\omega)$, the total current through spin channel σ can be calculated as $I_\sigma = I_\sigma^F - I_\sigma^B$,

$$I_\sigma(V, \Delta T) = \frac{\Gamma_{R\sigma}}{\hbar} \int_{-D}^D d\omega [f_L(\omega) - f_R(\omega - eV)] A_{L\sigma}(\omega). \quad (4.28)$$

The Fermi functions $f_\alpha(\omega) \equiv f(\omega, \mu_\alpha, T_\alpha)$ of the lead α are explicit functions of chemical potentials μ_α and lead temperature T_α .

A typical setup in the presence of Kondo correlations in the strongly coupled subsystem with $\Gamma_R \ll \Gamma_L$ is shown in Fig. 4.3.

4.3 Nonequilibrium thermoelectric transport coefficients

Having a large and finite V and/or ΔT , the definitions for the transport properties described in Sec. 3.1.3 do not necessarily translate into the nonequilibrium regime. In this section, I define a set of transport coefficients that is valid in the nonequilibrium regime once the nonequilibrium current $I(V, \Delta T)$ can be determined. Firstly, the definition of the differential conductance $G = (dI/dV)_{\Delta T} \equiv G(V, \Delta T)$ is applicable across the regimes and remains the same.

The classical definition of the Seebeck coefficient $S = -(V/\Delta T)_{I=0}$, is determined by the bias V required to compensate for the thermoelectric current I induced by the temperature gradient ΔT . Such a

definition only deals with a system with initial potential bias $V_{\text{ini}} = 0$ and thus $I_{\text{ini}} = 0$ initially. A direct extension of this definition is to consider a system with finite initial potential $V_{\text{ini}} = V$ and no temperature gradient $\Delta T_{\text{ini}} = 0$, which runs a current $I(V, 0) \neq 0$. When a temperature gradient ΔT is applied across the system, the contribution from the thermoelectric current changes $I(V, 0) \rightarrow I(V, \Delta T)$, which can be brought back to the original value by a change in the potential ΔV . Thus, the nonequilibrium Seebeck coefficient $S_n(V, \Delta T)$ can be defined analogous to the classic definition,

$$S_n(V, \Delta T) = - \left(\frac{\Delta V}{\Delta T} \right)_{I(V+\Delta V, \Delta T)=I(V, 0)}. \quad (4.29)$$

Further, a differential Seebeck coefficient $S_d(V, \Delta T)$ that acts as a response function on V and ΔT can be defined in the nonlinear regime as,

$$S_d(V, \Delta T) = - \left(\frac{dV}{d\Delta T} \right)_I \quad (4.30)$$

$$= - \left(\frac{\partial I}{\partial \Delta T} \right)_V / \left(\frac{\partial I}{\partial V} \right)_{\Delta T}, \quad (4.31)$$

where the numerator is the thermoelectric response of the current at constant V , and the denominator is the differential conductance at constant ΔT . Both of these quantities are experimentally accessible in the nonequilibrium regime and have been theoretically estimated for asymmetric quantum dot systems in the publications [D,E].

Chapter 5

Summary

The technological advances in the field of nanotechnology opened up a wide array of experimental platforms that are capable of exploring various aspects of quantum physics. Quantum dots, nanowires, nanotubes, superconducting qubits, molecular junctions and 2D materials like graphene are some notable platforms that are used to study various condensed matter phenomena originating from quantum effects. Due to the prominent role of quantum effects in such systems, various applications in quantum information technologies, cryogenics, thermoelectric cooling, energy harvesting, sensing technologies and many others have been proposed for such nanostructures that can rival their contemporary counterparts.

There exists a class of such nanostructures manufacturable using quantum dots, nanowires, single-electron transistors, molecular junctions or adatoms that can simulate quantum impurity systems. Such systems can confine the electrons into a quasi-zero-dimensional space to exhibit various interesting properties. Apart from the quantum confinement effects, electronic correlations and many-body effects give rise to more complex phenomena in these systems. The Kondo effect is such a many-body phenomena through which the conduction band electrons can screen the impurity spin. This results in a many-body correlated state known as the Kondo state, where the spatial correlations extend up to large length scales compared to the size of the impurity in such nanostructures. The spatial extension of such screening correlations of the Kondo effect is commonly referred to as the Kondo cloud. Many characteristic signatures are exhibited when Kondo correlations exist in a quantum dot system coupled to an electronic reservoir, such as a resonance peak in the quantum dot density of states at the Fermi level (Kondo-Abrikosov-Suhl resonance), zero-bias conductance peak in transport and a sign change in the Seebeck effect. Moreover, such Kondo-correlated systems show universal scaling behavior. This means that different experimental setups with Kondo correlations can be directly compared by rescaling the corresponding experimental data according to their respective Kondo energy scales.

Theoretical description of Kondo systems had been a daunting task for condensed matter physicists since the relevant physics comes from strong correlations at very low energies. Analytical approaches to describe the systems below the Kondo energy scale come with approximations of the relevant electronic correlations. A quantitatively reliable, numerically exact, controlled non-perturbative approach exists in the

name of numerical renormalization group. This had been the bread and butter for providing quantitatively reliable theoretical results for experiments in the Kondo regime. But NRG is an equilibrium method, and cannot describe systems out-of-equilibrium. Thanks to the advances in the experimental aspects of Kondo systems, there exists experimental setups that are capable of accurately studying far-from-equilibrium behavior in the Kondo regime. Thus, it is very relevant to describe the Kondo effect and its signatures under far-from-equilibrium conditions.

Thus, the main goal of this thesis is to describe Kondo systems in the scarcely explored regime of nonequilibrium. A controlled non-perturbative method combining the NRG and time dependent density matrix renormalization group is used to provide quantitatively accurate description of nonequilibrium transport across a Kondo-correlated quantum dot. A special case of strongly asymmetric coupling is treated with perturbation theory to investigate its spintronic properties, such as the tunnel magnetoresistance, thermoelectric and spin-caloritronic properties.

This thesis titled *Nonequilibrium transport and Kondo correlations in nanoscale systems* is presented as a series of publications [A-F]. The part I provides a concise introduction to the central concepts surrounding the thesis, main objectives and motivation for the research problem and the numerical techniques used to investigate them. The part II contains the publications that constitute this thesis, primarily organized based on the specific regimes of interest and the corresponding numerical methods employed to study them.

Chapter 7 consisting of the publication [A] is a linear response NRG study of a large spin magnetic molecule coupled to nonmagnetic/ferromagnetic leads. In this work, I investigated a magnetic molecule, modelled as an orbital level with an exchange interaction to a spin-1 magnetic core, coupled to nonmagnetic and ferromagnetic leads. This simplified effective model helps to unveil the dependence of the linear response transport properties on the internal parameters of the impurity such as the magnitude of the exchange interaction, ferromagnetic or antiferromagnetic nature of the exchange interaction and magnetic anisotropy, in addition to the various energy scales from the outside, such as the Kondo energy scale, ferromagnetic contact induced exchange field and temperature. This publication provided a detailed and exhaustive study of the competing energy scales and the corresponding characteristics on the differential conductance, Seebeck coefficient and spin-Seebeck coefficient. Some highlights of the results in this study include the competition between the Kondo effect and other energy scales reflecting in the sign changes of the Seebeck and the magnitude of the zero-bias conductance. The spin-Seebeck coefficient did not show any characteristic sign changes corresponding to the Kondo effect, but the regime of finite spin-Seebeck coefficient for an orbital level interacting with the magnetic core were shown to extend to lower temperatures than the spin-Seebeck effect exhibited by spin-1/2 impurities. Moreover, this publication unveiled various parameter regimes for the values of magnetic anisotropy and the exchange interactions, which can give rise to pronounced Seebeck and spin-Seebeck coefficients. Though, it is important to note that this did not result in any increase in the thermoelectric efficiency as the conductance was suppressed considerably for the relevant parameter regimes.

Chapter 8 consists of the publications [B,C] that deal with the nonequilibrium transport across a

quantum dot strongly coupled to two leads. The system studied in this chapter has Kondo-correlations mediated by conduction band electrons from both leads. The hybrid NRG-tDMRG method is employed to investigate the nonequilibrium steady-state transport properties of the quantum impurity systems. The publication [B] investigates how ferromagnetism of the leads influences the transport across the quantum dot. The results in this publication provided the first quantitatively accurate calculations for the spintronic transport through a Kondo-correlated quantum dot coupled to ferromagnetic leads. The Kondo energy scale in the applied bias was extracted from the zero-bias conductance peak and its dependence on the lead polarization was studied. In the absence of particle-hole symmetry, the differential conductance as a function of the applied bias showed a split-peak structure originating from the ferromagnetic contact induced exchange field. A particular value of magnetic field was shown to compensate for this exchange field splitting and to recover the zero-bias conductance peak.

The dependence of the transport properties on the individual lead temperatures and the associated thermoelectric transport is studied in paper [C]. This paper addressed a long-standing problem regarding the description of Kondo effect in the presence of nonlinear temperature gradients. In this work, the NRG-tDMRG method was extended to describe transport across a quantum dot strongly coupled to leads with independent temperatures. In the zero-bias regime, the differential conductance showed a radial behavior in the plane of left-right lead temperatures T_L, T_R . Far from intuitions, the points of half-maxima of the conductance, directly relatable to the Kondo energy scale, depicted a 'Kondo circle' in the T_L, T_R plane. This unveiled a dominance of second order contributions of the individual lead temperatures in the Kondo scaling regime, and indicated the presence of an effective equilibrium temperature that can replicate, with almost quantitative accuracy, the case with different lead temperatures. The sign changes in the thermoelectric current also showed a rough circle in the T_L, T_R plane. The points of sign change of thermopower having deviations from the circular behavior are not surprising as the point of sign change in the thermopower does not directly correspond to any energy scales under consideration. A polynomial fit was also provided for fitting any possible experimental data available for such systems. This paper further discusses the thermopower and its comparison to the effective equilibrium temperature values and heat conductance in the presence of finite temperature gradients.

Chapter 9 deals with a specific case of strong asymmetric coupling limit addressed in the publications [D-F]. In such a case, the quantum dot is strongly coupled to one lead and weakly coupled to the second lead. The transport properties are studied using the perturbation theory based approach described in chapter 4. Treating the strongly coupled part using NRG, this method includes all the processes between the strongly coupled lead and the quantum dot, but only the lowest order processes from the weakly coupled lead contribute to the transport. This special case is reflected in various experimental setups such as scanning tunneling spectroscopy, semiconductor quantum dots or single electron transistors.

The thermoelectric transport properties of a quantum dot asymmetrically coupled to two metallic leads are investigated in the publication [D]. The extensions of Seebeck coefficient to the nonequilibrium settings, such as the nonequilibrium Seebeck coefficient S_n and differential Seebeck coefficient S_d are

calculated for various nonequilibrium parameter regimes. Important findings of this publication constitutes new sign changes of S_n and S_d in the finite potential and temperature bias regime. This publication goes on to explore the thermoelectric efficiency of the asymmetric setup in the presence of nonequilibrium conditions, and found that depending on the parameters of the strongly coupled system, there exists different regimes of V and ΔT where the quantum dot system can output high thermoelectric efficiency. A more experimentally realizable system with capacitive couplings and voltage dependent orbital level was also investigated in this paper to aid experimental explorations.

An extension of the above work to the case of ferromagnetic leads was realized in publication [E]. Here, the nonequilibrium thermoelectric and spin-caloritronic properties under various configurations of the spin polarization on the leads have been investigated. This paper unveiled new sign changes in the nonequilibrium Seebeck coefficients originating from the competition between the Kondo effect and the ferromagnetic-contact induced exchange field. The setup mentioned above can also result in extremely large tunnel magnetoresistances in the presence of finite thermal bias. This scenario has been investigated and published in the short paper [F].

In conclusion, this doctoral dissertation presents the theoretical results on various aspects of transport in correlated systems exhibiting the Kondo effect in nonequilibrium conditions. The research utilized sophisticated numerical computational methods, including the hybrid NRG-tDMRG method, which enabled the inclusion of correlations in a rigorous manner and yielded quantitatively accurate results. The results presented in the six publications comprising the dissertation contributed to a deeper understanding of Kondo correlations beyond linear response and provided new results and predictions for the experimental investigation of such phenomena, thereby contributing to the development of spin-based nanoelectronics and caloritronics. Additionally, the obtained results offered insights into various potential applications of correlated quantum dot systems, including spintronic and thermoelectric applications.

Chapter 6

Streszczenie (Summary in Polish)

Postęp w dziedzinie nanotechnologii umożliwił implementację szerokiej gamy platform eksperymentalnych, które pozwalają badać najbardziej fundamentalne aspekty fizyki kwantowej. W tym kontekście, szczególne miejsce zajmują układy niskowymiarowe, takie jak kropki kwantowe, nanodruty, nanorurki, złącza molekularne czy też materiały dwuwymiarowe, takie jak grafen. Ze względu na dominującą rolę efektów kwantowych w takich układach, nanostruktury odgrywają również kluczową rolę, jeżeli chodzi o potencjalne zastosowania w nowoczesnych technologiach, w tym w technologiach kwantowych. W szczególności, obejmują one technologie związane z przechowywaniem i przetwarzaniem informacji, a także informację kwantową, nanoelektronikę, kriogenicę, technologie sensoryczne i energetyczne oraz wiele innych potencjalnych zastosowań, które są konkurencyjne w stosunku do ich współczesnych odpowiedników.

Ciekawą grupą nanostruktur są struktury quasi-zero-wymiarowe obejmujące kropki kwantowe, tranzystory jednoelektronowe, molekuly lub adatomy, które mogą symulować zachowanie układów domieszek kwantowych. W tego typu układach, oprócz efektów kwantowych prowadzących do dyskretnej struktury energetycznej, korelacje elektronowe i efekty wielociałowe mogą prowadzić do wystąpienia bardziej złożonych efektów fizycznych. Jednym z takich wielociałowych zjawisk jest efekt Kondo, w którym elektrony przewodnictwa ekranują spin domieszki kwantowej. W rezultacie powstaje wielociałowy stan skorelowany, znany jako stan Kondo, w którym korelacje przestrzenne rozciągają się na dużą skalę w porównaniu do rozmiaru domieszki w takich nanostrukturach. Przestrzenny rozkład korelacji spinowych w zjawisku Kondo jest często określany jako chmura Kondo.

W układzie kropki kwantowej sprzężonej z rezerwuarem elektronów, gdy występują korelacje Kondo, można zaobserwować wiele charakterystycznych cech, takich jak dodatkowy rezonans w gęstości stanów kropki kwantowej na poziomie Fermiego, tzw. rezonans Kondo-Abrikosova-Suhla, maksimum zero-napięciowego przewodnictwa, czy też zmianę znaku współczynnika Seebecka w funkcji temperatury. Co więcej, okazuje się, że skorelowane układy wykazujące istnienie efektu Kondo charakteryzują się uniwersalnym zachowaniem. Oznacza to, że różne eksperymentalne układy z korelacjami Kondo można bezpośrednio porównać, przeskalowując odpowiednie dane eksperymentalne zgodnie z odpowiednimi

skalami energii związanymi z efektem Kondo.

Dokładny, teoretyczny opis układów z korelacjami Kondo stanowił ogromne wyzwanie dla fizyków materii skondensowanej, ponieważ istotne zjawiska wynikają z silnych korelacji elektronowych przy bardzo niskich temperaturach. Analityczne podejścia do opisu tego typu zjawisk wymagają odpowiednich przybliżeń związanych z korelacjami elektronowymi, które nie dostarczają precyzyjnych wyników ilościowych. Istnieje jednak metoda nieperturbacyjna, znana jako numeryczna grupa renormalizacji (NRG), która jest ilościowo wiarygodna, numerycznie dokładna i kontrolowana. Metoda ta jest podstawowym narzędziem do otrzymania ilościowo wiarygodnych wyników, które mogą być bezpośrednio porównywane z wynikami doświadczalnymi dla układów w reżimie Kondo. Numeryczna grupa renormalizacji jest jednak metodą równowagową i nie opisuje układów poza równowagą. Okazuje się jednak, że dzięki postępom w eksperymentalnych badaniach układów Kondo, wiele doświadczeń jest przeprowadzanych w warunkach dalekich od równowagowych. Dlatego też niezwykle ważne jest dokładne opisanie zjawisk korelacyjnych, w tym efektu Kondo i jego zachowania, w takich warunkach. Głównym celem niniejszej dysertacji było właśnie przeprowadzenie ilościowo dokładnej analizy charakterystyk transportowych skorelowanych układów wykazujących zjawisko Kondo w warunkach nierównowagowych. W tym celu, zastosowana została hybrydowa metoda nieperturbacyjna, łącząca metodę NRG z zależną od czasu grupą renormalizacji macierzy gęstości (tDMRG), dla układu kropki kwantowej silnie sprzężonej do zewnętrznych elektrod metalicznych. Ponadto, rozpatrzono także przypadek silnie asymetrycznego złącza tunelowego z kropką kwantową, który został przeanalizowany przy pomocy metody NRG w oparciu o rachunek zaburzeń względem słabo sprzężonej elektrody. Metody te pozwoliły na dokładne przeanalizowanie właściwości transportowych badanych układów, z uwzględnieniem aspektów spintronicznych, termoelektrycznych i spinowo-kalorytronicznych.

Niniejsza dysertacja pt. „Transport nierównowagowy i korelacje Kondo w układach nanoskopowych” składa się z cyklu sześciu publikacji [A-F]. Część I rozprawy zawiera zwięzłe wprowadzenie do najważniejszych pojęć istotnych dla pracy doktorskiej, główne cele i motywację dla podjętego problemu badawczego oraz techniki numeryczne używane do badań. Część II zawiera publikacje, które składają się na dysertację, zorganizowane przede wszystkim w oparciu o konkretne obszary zainteresowania i odpowiadające im metody numeryczne stosowane w obliczeniach.

Rozdział 7, zawierający publikację [A], przedstawia wyniki badań własności termoelektrycznych w odpowiedzi liniowej przeprowadzonych przy użyciu metody NRG dla układu dużej molekuly magnetycznej sprzężonej z niemagnetycznymi lub ferromagnetycznymi elektrodami. Molekuła magnetyczna była modelowana poprzez jeden poziom orbitalny sprzężony wymiennie do rdzenia magnetycznego o spinie $S = 1$. Ten uproszczony model efektywny pozwolił określić zależności charakterystyk transportowych od wewnętrznych parametrów molekuly, takich jak wielkość sprzężenia wymiany, ferromagnetyczny lub antyferromagnetyczny charakter sprzężenia wymiany czy też wartość anizotropii magnetycznej. Ponadto, w układzie istotne były skale energii związane ze zjawiskiem Kondo, polem wymiany indukowanym przez sprzężenie z ferromagnetycznymi elektrodami oraz temperaturą. Publikacja [A] przedstawia szczegółowe

wyniki badań wykazujących konkurujący charakter powyższych efektów oraz ich wpływ na przewodnictwo różniczkowe, współczynnik Seebecka oraz spinowy współczynnik Seebecka. Kilka kluczowych rezultatów obejmuje stwierdzenie występowania współoddziaływania pomiędzy efektem Kondo a pozostałymi skalami energetycznymi, co odzwierciedla się w zmianach znaku współczynnika Seebecka i wielkości przewodnictwa liniowego. Ponadto, pokazano, że spinowy współczynnik Seebecka nie wykazywał charakterystycznych zmian znaku związanych z efektem Kondo. Natomiast w obszarze dodatnich wartości spinowego współczynnika Seebecka, wykazano, że obszar ten rozciąga się na znacznie niższe temperatury w stosunku do układów domieszek magnetycznych o spinie $S = 1/2$. Co więcej, w publikacji określono zakresy parametrów anizotropii magnetycznej i sprzężenia wymiany, które mogą prowadzić do znaczących wartości współczynnika Seebecka oraz jego spinowego odpowiednika. Warto jednak podkreślić, że obszary te nie były bezpośrednio związane ze wzrostem wydajności termoelektrycznej układu, ponieważ przewodnictwo było istotnie tłumione dla powyższych zakresów parametrów.

Rozdział 8 obejmuje publikacje [B,C], które dotyczą transportu nierównowagowego przez kropkę kwantową silnie sprzężoną z dwoma elektrodami. Układ badany w tym rozdziale posiada silne korelacje Kondo, które wynikają z ekranowania spinu kropki kwantowej poprzez elektrony przewodnictwa z obu elektrod. W badaniach zastosowano hybrydową metodę NRG-tDMRG, która pozwoliła uzyskać ilościowo dokładne wyniki w warunkach nierównowagowych przy ścisłym uwzględnieniu efektów korelacji elektronowych.

Publikacja [B] przedstawia badania pokazujące jak ferromagnetyzm elektrod wpływa na nierównowagowy transport przez kropkę kwantową. Wyniki zawarte w publikacji prezentują pierwsze, ilościowo dokładne dane dotyczących zależnego do spinu transportu przez skorelowaną kropkę kwantową wykazującą efekt Kondo, która jest sprzężona z ferromagnetycznymi elektrodami. Skala energetyczna charakterystyczna dla efektu Kondo została wyznaczona na podstawie zależności przewodności różniczkowej od napięcia, co umożliwiło zbadanie wpływu polaryzacji spinowej ferromagnetycznych elektrod. W przypadku braku symetrii elektron-dziura, przewodność różniczkowa w funkcji napięcia transportowego wykazała strukturę złożoną z rozszczepionego piku Kondo, wynikającego z obecności pola wymiany wywołanego przez ferromagnetyczne elektrody. Ponadto, w pracy pokazano, że odpowiednio przyłożone zewnętrzne pole magnetyczne może kompensować powyższe rozszczepienie przywracając maksimum anomalii zero-napięciowej przewodnictwa układu.

W publikacji [C] zbadano zależność własności transportowych od poszczególnych temperatur elektrod oraz związany z tym nierównowagowy transport termoelektryczny. Publikacja ta rozwiązała długotrwały problem opisu efektu Kondo w obecności nieliniowych gradientów temperatury. W pracy rozszerzono metodę NRG-tDMRG o możliwość opisu transportu przez kropkę kwantową silnie sprzężoną z elektrodami o niezależnych temperaturach. W przypadku zerowego napięcia transportowego przewodnictwo wykazało radialne zachowanie w płaszczyźnie temperatur lewej i prawej elektrody, T_L, T_R . Wbrew intuicji, punkty połowicznego maksimum przewodnictwa, bezpośrednio powiązane ze skalą energetyczną efektu Kondo, tworzyły tzw. 'okrąg Kondo' w płaszczyźnie T_L, T_R . Ujawniło to dominację wkładów drugiego rzędu

dla indywidualnych temperatur elektrod w zakresie skalowania zjawiska Kondo i wskazało na obecność efektywnej temperatury równowagowej, która może z niemal ilościową dokładnością odtworzyć przypadek z różnymi temperaturami elektrod. Ponadto, zmiany znaku widoczne w prądzie termoelektrycznym również ukazały zblizoną do okręgu strukturę w płaszczyźnie T_L, T_R . Odchylenia punktów zmiany znaku współczynnika Seebecka od zachowania opisanego okręgiem w płaszczyźnie T_L, T_R nie są zaskakujące, ponieważ punkty te nie są bezpośrednio związane z żadną z rozważanych skal energetycznych. W pracy przedstawiono również dopasowanie wielomianowe, które może być zastosowane do porównania z dostępnymi danymi eksperymentalnymi dla takich układów. Artykuł omawia ponadto zachowanie współczynnika Seebecka oraz jego porównanie z wartościami efektywnej temperatury równowagowej oraz przewodnictwa cieplnego w obecności skończonych gradientów temperatury.

Rozdział 9 dotyczy specyficznego przypadku silnie asymetrycznego złącza tunelowego, dla którego wyniki opisano w publikacjach [D-F]. W takim przypadku kropka kwantowa jest silnie sprzężona z jedną elektrodą i słabo sprzężona z drugą. Własności transportowe zostały zbadane za pomocą podejścia opartego na teorii zaburzeń, opisanego w rozdziale 9. Korzystając z metody NRG do wyznaczenia lokalnej gęstości stanów części silnie sprzężonej, można uwzględnić wszystkie procesy pomiędzy silnie sprzężoną elektrodą a kropką kwantową, podczas gdy do transportu przyczyniają się jedynie procesy najniższego rzędu z elektrodą słabo sprzężoną. Ten szczególny przypadek znajduje odzwierciedlenie w różnych układach eksperymentalnych, obejmujących spektroskopię skaningową adatomów czy też półprzewodnikowe kropki kwantowe bądź tranzystory jednoelektronowe z asymetrycznymi sprzężeniami do zewnętrznych elektrod.

W publikacji [D] przebadano własności transportu termoelektrycznego układu kropki kwantowej asymetrycznie sprzężonej z dwoma metalicznymi elektrodami. W pracy rozszerzono badania na współczynnik Seebecka w warunkach nierównowagowych, wyznaczając nieliniowy współczynnik Seebecka S_n oraz różniczkowy współczynnik Seebecka S_d , dla różnych zakresów parametrów. Kluczowe wyniki tej publikacji obejmują nowe zmiany znaku S_n i S_d w reżimie skończonej różnicy potencjałów oraz gradientu temperatury. W publikacji zbadano także efektywność termoelektryczną asymetrycznego układu w warunkach nierównowagowych i stwierdzono, że w zależności od parametrów silnie sprzężonego układu istnieją różne zakresy V i ΔT , w których układ kropki kwantowej może wykazywać wysoką efektywność termoelektryczną. Dodatkowo, aby uwzględnić parametry odpowiadające realnym nanostrukturom, w artykule przedstawiono wyniki termoelektrycznego transportu dla układu z pojemnościowymi sprzężeniami oraz zależnym od napięcia poziomem orbitalnym.

Rozszerzenie powyższej pracy na przypadek elektrod ferromagnetycznych zostało zrealizowane w publikacji [E]. W pracy tej zbadano własności termoelektryczne oraz ich spinowo zależne wielkości poza stanem równowagi zakładając różne konfiguracje polaryzacji spinowej w elektrodach. W artykule ujawniono nowe zmiany znaku widoczne w nierównowagowych współczynnikach Seebecka, wynikające z konkurencji pomiędzy efektem Kondo a polem wymiany indukowanym przez ferromagnetyczne elektrody. Opisany układ może również prowadzić do niezwykle dużych wartości tunelowego magnetooporu w obecności skończonego gradientu termicznego. To zjawisko zostało zbadane i opisane w artykule [F].

Podsumowując, niniejsza rozprawa doktorska przedstawia wyniki teoretycznych badań różnych aspektów transportu przez skorelowane układy wykazujące efekt Kondo w obszarze nierównowagowym. Badania przeprowadzono z wykorzystaniem nowoczesnych numerycznych metod obliczeniowych obejmujących hybrydową metodę NRG-tDMRG, co pozwoliło uwzględnić korelacje w sposób ścisły i uzyskać ilościowo dokładne rezultaty. Wyniki zaprezentowane w sześciu publikacjach stanowiących dysertację przyczyniły się do lepszego zrozumienia korelacji Kondo poza odpowiedzią liniową oraz dostarczyły nowych rezultatów i przewidywań do eksperymentalnego badania takich zjawisk, przyczyniając się tym samym do rozwoju spinowej nanoelektroniki i kalorytroniki. Ponadto, uzyskane rezultaty dostarczyły również wglądu w różne potencjalne zastosowania układów skorelowanych kropek kwantowych, obejmujące aplikacje spintroniczne czy też termoelektryczne.

Bibliography

- [1] C. W. J. Beenakker and H. van Houten. Quantum Transport in Semiconductor Nanostructures. In *Solid State Physics*, volume 44, pages 1–228. Academic Press, Cambridge, MA, USA, January 1991. doi: 10.1016/S0081-1947(08)60091-0.
- [2] Alexander Cyril Hewson. *The Kondo Problem to Heavy Fermions*. Cambridge Studies in Magnetism. Cambridge University Press, 1993. doi: 10.1017/CBO9780511470752.
- [3] Henrik Bruus, Karsten Flensberg, Henrik Bruus, and Karsten Flensberg. *Many-Body Quantum Theory in Condensed Matter Physics*. Oxford University Press, Oxford, England, UK, September 2004.
- [4] Supriyo Datta. *Quantum Transport: Atom to Transistor*. Cambridge University Press, Cambridge, England, UK, June 2005. ISBN 978-0-52163145-7. doi: 10.1017/CBO9781139164313.
- [5] Massimiliano Di Ventra. *Electrical Transport in Nanoscale Systems*. Cambridge University Press, Cambridge, England, UK, August 2008. ISBN 978-0-52189634-4. doi: 10.1017/CBO9780511755606.
- [6] Phaedon Avouris, Zhihong Chen, and Vasili Perebeinos. Carbon-based electronics. *Nat. Nanotechnol.*, 2:605–615, October 2007. ISSN 1748-3395. doi: 10.1038/nnano.2007.300.
- [7] Igor L. Markov. Limits on fundamental limits to computation. *Nature*, 512:147–154, August 2014. ISSN 1476-4687. doi: 10.1038/nature13570.
- [8] P. W. Anderson. A poor man’s derivation of scaling laws for the Kondo problem. *J. Phys. C: Solid State Phys.*, 3(12):2436, Dec 1970. ISSN 0022-3719.
- [9] P. Nozières. A “fermi-liquid” description of the Kondo problem at low temperatures. *J. Low Temp. Phys.*, 17(1):31–42, October 1974. ISSN 1573-7357. doi: 10.1007/BF00654541.
- [10] N. Andrei, K. Furuya, and J. H. Lowenstein. Solution of the Kondo problem. *Rev. Mod. Phys.*, 55(2):331–402, April 1983. ISSN 1539-0756. doi: 10.1103/RevModPhys.55.331.
- [11] P. B. Wiegmann. Exact solution of the s-d exchange model (Kondo problem). *J. Phys. C: Solid State Phys.*, 14(10):1463, April 1981. ISSN 0022-3719. doi: 10.1088/0022-3719/14/10/014.

- [12] Antoine Georges, Gabriel Kotliar, Werner Krauth, and Marcelo J. Rozenberg. Dynamical mean-field theory of strongly correlated fermion systems and the limit of infinite dimensions. *Rev. Mod. Phys.*, 68(1):13–125, January 1996. ISSN 1539-0756. doi: 10.1103/RevModPhys.68.13.
- [13] Kenneth G. Wilson. The renormalization group: Critical phenomena and the Kondo problem. *Rev. Mod. Phys.*, 47(4):773–840, Oct 1975. ISSN 1539-0756. doi: 10.1103/RevModPhys.47.773.
- [14] Ralf Bulla, Theo A. Costi, and Thomas Pruschke. Numerical renormalization group method for quantum impurity systems. *Rev. Mod. Phys.*, 80(2):395–450, Apr 2008. ISSN 1539-0756. doi: 10.1103/RevModPhys.80.395.
- [15] Steven R. White. Density matrix formulation for quantum renormalization groups. *Phys. Rev. Lett.*, 69(19):2863–2866, November 1992. ISSN 1079-7114. doi: 10.1103/PhysRevLett.69.2863.
- [16] Ulrich Schollwöck. The density-matrix renormalization group in the age of matrix product states. *Annals of Physics*, 326(1):96 – 192, 2011. ISSN 0003-4916. doi: 10.1016/j.aop.2010.09.012. January 2011 Special Issue.
- [17] Ulrich Schollwöck. The density-matrix renormalization group in the age of matrix product states. *Ann. Phys.*, 326(1):96–192, January 2011. ISSN 0003-4916. doi: 10.1016/j.aop.2010.09.012.
- [18] J. Martinek, M. Sindel, L. Borda, J. Barnaś, J. König, G. Schön, and J. von Delft. Kondo Effect in the Presence of Itinerant-Electron Ferromagnetism Studied with the Numerical Renormalization Group Method. *Phys. Rev. Lett.*, 91(24):247202, December 2003. ISSN 1079-7114. doi: 10.1103/PhysRevLett.91.247202.
- [19] Christopher J. Wright, Martin R. Galpin, and David E. Logan. Magnetic field effects in few-level quantum dots: Theory and application to experiment. *Phys. Rev. B*, 84(11):115308, September 2011. ISSN 2469-9969. doi: 10.1103/PhysRevB.84.115308.
- [20] T. A. Costi. Magnetic field dependence of the thermopower of Kondo-correlated quantum dots: Comparison with experiment. *Phys. Rev. B*, 100(15):155126, October 2019. ISSN 2469-9969. doi: 10.1103/PhysRevB.100.155126.
- [21] Yigal Meir, Ned S. Wingreen, and Patrick A. Lee. Low-temperature transport through a quantum dot: The Anderson model out of equilibrium. *Phys. Rev. Lett.*, 70(17):2601–2604, April 1993. ISSN 1079-7114. doi: 10.1103/PhysRevLett.70.2601.
- [22] R. Świrkowicz, J. Barnaś, and M. Wilczyński. Nonequilibrium Kondo effect in quantum dots. *Phys. Rev. B*, 68(19):195318, November 2003. ISSN 2469-9969. doi: 10.1103/PhysRevB.68.195318.
- [23] A. Rosch, J. Paaske, J. Kroha, and P. Wölfle. The Kondo Effect in Non-Equilibrium Quantum Dots: Perturbative Renormalization Group. *J. Phys. Soc. Jpn.*, 74(1):118–126, January 2005. ISSN 0031-9015. doi: 10.1143/JPSJ.74.118.

- [24] Antonius Dorda, Martin Ganahl, Sabine Andergassen, Wolfgang von der Linden, and Enrico Arrigoni. Thermoelectric response of a correlated impurity in the nonequilibrium Kondo regime. *Phys. Rev. B*, 94(24):245125, Dec 2016. ISSN 2469-9969. doi: 10.1103/PhysRevB.94.245125.
- [25] Miguel A. Sierra, Rosa López, and David Sánchez. Fate of the spin- $\frac{1}{2}$ Kondo effect in the presence of temperature gradients. *Phys. Rev. B*, 96(8):085416, Aug 2017. ISSN 2469-9969. doi: 10.1103/PhysRevB.96.085416.
- [26] Delia M. Fugger, Antonius Dorda, Frauke Schwarz, Jan von Delft, and Enrico Arrigoni. Nonequilibrium Kondo effect in a magnetic field: auxiliary master equation approach. *New J. Phys.*, 20(1):013030, January 2018. ISSN 1367-2630. doi: 10.1088/1367-2630/aa9fdc.
- [27] Ulrich Eckern and Karol I. Wysokiński. Two- and three-terminal far-from-equilibrium thermoelectric nano-devices in the Kondo regime. *New J. Phys.*, 22(1):013045, Jan 2020. ISSN 1367-2630. doi: 10.1088/1367-2630/ab6874.
- [28] Delia M. Fugger, Daniel Bauernfeind, Max E. Sorantin, and Enrico Arrigoni. Nonequilibrium pseudogap Anderson impurity model: A master equation tensor network approach. *Phys. Rev. B*, 101(16):165132, April 2020. ISSN 2469-9969. doi: 10.1103/PhysRevB.101.165132.
- [29] Robert S. Whitney. Most Efficient Quantum Thermoelectric at Finite Power Output. *Phys. Rev. Lett.*, 112(13):130601, April 2014. ISSN 1079-7114. doi: 10.1103/PhysRevLett.112.130601.
- [30] Björn Sothmann, Rafael Sánchez, and Andrew N. Jordan. Thermoelectric energy harvesting with quantum dots. *Nanotechnology*, 26(3):032001, Dec 2014. ISSN 0957-4484. doi: 10.1088/0957-4484/26/3/032001.
- [31] Holger Thierschmann, Rafael Sánchez, Björn Sothmann, Fabian Arnold, Christian Heyn, Wolfgang Hansen, Hartmut Buhmann, and Laurens W. Molenkamp. Three-terminal energy harvester with coupled quantum dots. *Nat. Nanotechnol.*, 10:854–858, October 2015. ISSN 1748-3395. doi: 10.1038/nnano.2015.176.
- [32] F. Schwarz, I. Weymann, J. von Delft, and A. Weichselbaum. Nonequilibrium Steady-State Transport in Quantum Impurity Models: A Thermofield and Quantum Quench Approach Using Matrix Product States. *Phys. Rev. Lett.*, 121(13):137702, Sep 2018. ISSN 1079-7114. doi: 10.1103/PhysRevLett.121.137702.
- [33] Szabolcs Csonka, Ireneusz Weymann, and Gergely Zarand. An electrically controlled quantum dot based spin current injector. *Nanoscale*, 4(12):3635–3639, May 2012. ISSN 2040-3364. doi: 10.1039/C2NR30399J.
- [34] Yuli V. Nazarov and Yaroslav M. Blanter. *Quantum Transport: Introduction to Nanoscience*. Cambridge University Press, Cambridge, England, UK, May 2009. ISBN 978-0-52183246-5. doi: 10.1017/CBO9780511626906.

- [35] W. J. de Haas, J. de Boer, and G. J. van den Berg. The electrical resistance of gold, copper and lead at low temperatures. *Physica*, 1(7):1115–1124, May 1934. ISSN 0031-8914. doi: 10.1016/S0031-8914(34)80310-2.
- [36] Jun Kondo. Resistance Minimum in Dilute Magnetic Alloys. *Prog. Theor. Phys.*, 32(1):37–49, Jul 1964. ISSN 0033-068X. doi: 10.1143/PTP.32.37.
- [37] Leo Kouwenhoven and Leonid Glazman. Revival of the Kondo effect. *Phys. World*, 14(1):33, January 2001. ISSN 2058-7058. doi: 10.1088/2058-7058/14/1/28.
- [38] D. Goldhaber-Gordon, Hadas Shtrikman, D. Mahalu, David Abusch-Magder, U. Meirav, and M. A. Kastner. Kondo effect in a single-electron transistor. *Nature*, 391(6663):156–159, Jan 1998. ISSN 1476-4687. doi: 10.1038/34373.
- [39] Sara M. Cronenwett, Tjerk H. Oosterkamp, and Leo P. Kouwenhoven. A Tunable Kondo Effect in Quantum Dots. *Science*, 281(5376):540–544, Jul 1998. ISSN 0036-8075. doi: 10.1126/science.281.5376.540.
- [40] Jörg Schmid, Jürgen Weis, Karl Eberl, and Klaus V. Klitzing. A quantum dot in the limit of strong coupling to reservoirs. *Physica B*, 256-258:182–185, December 1998. ISSN 0921-4526. doi: 10.1016/S0921-4526(98)00533-X.
- [41] D. Goldhaber-Gordon, J. Göres, M. A. Kastner, Hadas Shtrikman, D. Mahalu, and U. Meirav. From the Kondo Regime to the Mixed-Valence Regime in a Single-Electron Transistor. *Phys. Rev. Lett.*, 81(23):5225–5228, December 1998. ISSN 1079-7114. doi: 10.1103/PhysRevLett.81.5225.
- [42] F. Simmel, R. H. Blick, J. P. Kotthaus, W. Wegscheider, and M. Bichler. Anomalous Kondo Effect in a Quantum Dot at Nonzero Bias. *Phys. Rev. Lett.*, 83(4):804–807, July 1999. ISSN 1079-7114. doi: 10.1103/PhysRevLett.83.804.
- [43] C. H. L. Quay, John Cumings, S. J. Gamble, R. de Picciotto, H. Kataura, and D. Goldhaber-Gordon. Magnetic field dependence of the spin- $\frac{1}{2}$ and spin-1 Kondo effects in a quantum dot. *Phys. Rev. B*, 76(24):245311, December 2007. ISSN 2469-9969. doi: 10.1103/PhysRevB.76.245311.
- [44] Thomas Sand Jespersen, Martin Aagesen, Claus Sørensen, Poul Erik Lindelof, and Jesper Nygård. Kondo physics in tunable semiconductor nanowire quantum dots. *Phys. Rev. B*, 74(23):233304, December 2006. ISSN 2469-9969. doi: 10.1103/PhysRevB.74.233304.
- [45] S. Csonka, L. Hofstetter, F. Freitag, S. Oberholzer, C. Schönenberger, T. S. Jespersen, M. Aagesen, and J. Nygård. Giant Fluctuations and Gate Control of the g-Factor in InAs Nanowire Quantum Dots. *Nano Lett.*, 8(11):3932–3935, November 2008. ISSN 1530-6984. doi: 10.1021/nl802418w.
- [46] Henrik A. Nilsson, Philippe Caroff, Claes Thelander, Marcus Larsson, Jakob B. Wagner, Lars-Erik Wernersson, Lars Samuelson, and H. Q. Xu. Giant, Level-Dependent g Factors in InSb

- Nanowire Quantum Dots. *Nano Lett.*, 9(9):3151–3156, September 2009. ISSN 1530-6984. doi: 10.1021/nl901333a.
- [47] Andrey V. Kretinin, Ronit Popovitz-Biro, Diana Mahalu, and Hadas Shtrikman. Multimode Fabry-Pérot Conductance Oscillations in Suspended Stacking-Faults-Free InAs Nanowires. *Nano Lett.*, 10(9):3439–3445, September 2010. ISSN 1530-6984. doi: 10.1021/nl101522j.
- [48] Jesper Nygård, David Henry Cobden, and Poul Erik Lindelof. Kondo physics in carbon nanotubes. *Nature*, 408:342–346, November 2000. ISSN 1476-4687. doi: 10.1038/35042545.
- [49] Andrey V. Kretinin, Hadas Shtrikman, David Goldhaber-Gordon, Markus Hanl, Andreas Weichselbaum, Jan von Delft, Theo Costi, and Diana Mahalu. Spin- $\frac{1}{2}$ Kondo effect in an InAs nanowire quantum dot: Unitary limit, conductance scaling, and Zeeman splitting. *Phys. Rev. B*, 84(24):245316, December 2011. ISSN 2469-9969. doi: 10.1103/PhysRevB.84.245316.
- [50] Lam H. Yu and Douglas Natelson. The Kondo Effect in C60 Single-Molecule Transistors. *Nano Lett.*, 4(1):79–83, January 2004. ISSN 1530-6984. doi: 10.1021/nl034893f.
- [51] Gabriel González, Michael N. Leuenberger, and Eduardo R. Mucciolo. Kondo effect in single-molecule magnet transistors. *Phys. Rev. B*, 78(5):054445, August 2008. ISSN 2469-9969. doi: 10.1103/PhysRevB.78.054445.
- [52] G. D. Scott, Z. K. Keane, J. W. Ciszek, J. M. Tour, and D. Natelson. Universal scaling of nonequilibrium transport in the Kondo regime of single molecule devices. *Phys. Rev. B*, 79(16):165413, April 2009. ISSN 2469-9969. doi: 10.1103/PhysRevB.79.165413.
- [53] Nikolaus Knorr, M. Alexander Schneider, Lars Diekhöner, Peter Wahl, and Klaus Kern. Kondo Effect of Single Co Adatoms on Cu Surfaces. *Phys. Rev. Lett.*, 88(9):096804, February 2002. ISSN 1079-7114. doi: 10.1103/PhysRevLett.88.096804.
- [54] Markus Ternes, Andreas J. Heinrich, and Wolf-Dieter Schneider. Spectroscopic manifestations of the Kondo effect on single adatoms. *J. Phys.: Condens. Matter*, 21(5):053001, December 2008. ISSN 0953-8984. doi: 10.1088/0953-8984/21/5/053001.
- [55] Jindong Ren, Haiming Guo, Jinbo Pan, Yu Yang Zhang, Xu Wu, Hong-Gang Luo, Shixuan Du, Sokrates T. Pantelides, and Hong-Jun Gao. Kondo Effect of Cobalt Adatoms on a Graphene Monolayer Controlled by Substrate-Induced Ripples. *Nano Lett.*, 14(7):4011–4015, July 2014. ISSN 1530-6984. doi: 10.1021/nl501425n.
- [56] Jian-Hao Chen, Liang Li, William G. Cullen, Ellen D. Williams, and Michael S. Fuhrer. Tunable Kondo effect in graphene with defects. *Nat. Phys.*, 7:535–538, July 2011. ISSN 1745-2481. doi: 10.1038/nphys1962.

- [57] L. Riegger, N. Darkwah Oppong, M. Höfer, D. R. Fernandes, I. Bloch, and S. Fölling. Localized Magnetic Moments with Tunable Spin Exchange in a Gas of Ultracold Fermions. *Phys. Rev. Lett.*, 120(14):143601, April 2018. ISSN 1079-7114. doi: 10.1103/PhysRevLett.120.143601.
- [58] S. Seiro, L. Jiao, S. Kirchner, S. Hartmann, S. Friedemann, C. Krellner, C. Geibel, Q. Si, F. Steglich, and S. Wirth. Evolution of the Kondo lattice and non-Fermi liquid excitations in a heavy-fermion metal. *Nat. Commun.*, 9(3324):1–7, August 2018. ISSN 2041-1723. doi: 10.1038/s41467-018-05801-5.
- [59] A. S. Shankar, D. O. Oriekhov, Andrew K. Mitchell, and L. Fritz. Kondo effect in twisted bilayer graphene. *Phys. Rev. B*, 107(24):245102, June 2023. ISSN 2469-9969. doi: 10.1103/PhysRevB.107.245102.
- [60] Camiel van Efferen, Jeison Fischer, Theo A. Costi, Achim Rosch, Thomas Michely, and Wouter Jolie. Modulated Kondo screening along magnetic mirror twin boundaries in monolayer MoS₂. *Nat. Phys.*, 20:82–87, January 2024. ISSN 1745-2481. doi: 10.1038/s41567-023-02250-w.
- [61] P. W. Anderson. Localized Magnetic States in Metals. *Phys. Rev.*, 124(1):41–53, October 1961. doi: 10.1103/PhysRev.124.41. URL <https://link.aps.org/doi/10.1103/PhysRev.124.41>.
- [62] J. R. Schrieffer and P. A. Wolff. Relation between the Anderson and Kondo Hamiltonians. *Phys. Rev.*, 149(2):491–492, September 1966. ISSN 1536-6065. doi: 10.1103/PhysRev.149.491.
- [63] Hartmut Haug and Antti-Pekka Jauho. *Quantum Kinetics in Transport and Optics of Semiconductors*. Springer, Berlin, Germany. ISBN 978-3-540-73564-9.
- [64] Yigal Meir and Ned S. Wingreen. Landauer formula for the current through an interacting electron region. *Phys. Rev. Lett.*, 68(16):2512–2515, April 1992. ISSN 1079-7114. doi: 10.1103/PhysRevLett.68.2512.
- [65] Rolf Landauer. Electrical resistance of disordered one-dimensional lattices. *Philos. Mag.*, April 1970.
- [66] R. Landauer. Spatial variation of currents and fields due to localized scatterers in metallic conduction (and comment). *J. Math. Phys.*, 37(10):5259–5268, October 1996. ISSN 0022-2488. doi: 10.1063/1.531590.
- [67] M. Büttiker. Four-Terminal Phase-Coherent Conductance. *Phys. Rev. Lett.*, 57(14):1761–1764, October 1986. ISSN 1079-7114. doi: 10.1103/PhysRevLett.57.1761.
- [68] Vivaldo L. Campo, Jr. and Luiz N. Oliveira. Alternative discretization in the numerical renormalization-group method. *Phys. Rev. B*, 72(10):104432, September 2005. ISSN 2469-9969. doi: 10.1103/PhysRevB.72.104432.

- [69] Rok Žitko. Adaptive logarithmic discretization for numerical renormalization group methods. *Comput. Phys. Commun.*, 180(8):1271–1276, August 2009. ISSN 0010-4655. doi: 10.1016/j.cpc.2009.02.007.
- [70] Cornelius Lanczos. An iteration method for the solution of the eigenvalue problem of linear differential and integral operators. *J. Res. Nat. Bur. Stand.*, 45(4), 1950. doi: 10.6028/jres.045.026.
- [71] J. Cullum and R. Willoughby. *Lanczos Algorithms for Large Symmetric Eigenvalue Computations Vol. I Theory*, 1984. [Online; accessed 23. Sep. 2024].
- [72] Yousef Saad. *Iterative Methods for Sparse Linear Systems: Second Edition*. Society for Industrial and Applied Mathematics, April 2003. ISBN 978-0-89871534-7.
- [73] Walter Hofstetter. Generalized Numerical Renormalization Group for Dynamical Quantities. *Phys. Rev. Lett.*, 85(7):1508–1511, August 2000. ISSN 1079-7114. doi: 10.1103/PhysRevLett.85.1508.
- [74] FDM Haldane. Scaling theory of the asymmetric Anderson model. *Phys. Rev. Lett.*, 40(6):416–419, 1978.
- [75] Andreas Weichselbaum and Jan von Delft. Sum-Rule Conserving Spectral Functions from the Numerical Renormalization Group. *Phys. Rev. Lett.*, 99(7):076402, August 2007. ISSN 1079-7114. doi: 10.1103/PhysRevLett.99.076402.
- [76] I. Weymann and J. Barnaś. Spin thermoelectric effects in Kondo quantum dots coupled to ferromagnetic leads. *Phys. Rev. B*, 88(8):085313, August 2013. ISSN 2469-9969. doi: 10.1103/PhysRevB.88.085313.
- [77] T. A. Costi and V. Zlatić. Thermoelectric transport through strongly correlated quantum dots. *Phys. Rev. B*, 81(23):235127, Jun 2010. ISSN 2469-9969. doi: 10.1103/PhysRevB.81.235127.
- [78] *We used the open-access Budapest Flexible DM-NRG code, <http://www.phy.bme.hu/~dmnrg/>; O. Legeza, C. P. Moca, A. I. Tóth, I. Weymann, G. Zaránd, arXiv:0809.3143 (2008) (unpublished).*
- [79] Andreas Weichselbaum. QSpace - An open-source tensor library for Abelian and non-Abelian symmetries. *arXiv*, May 2024. doi: 10.48550/arXiv.2405.06632.
- [80] F. Verstraete and J. I. Cirac. Renormalization algorithms for Quantum-Many Body Systems in two and higher dimensions. *arXiv*, July 2004. doi: 10.48550/arXiv.cond-mat/0407066.
- [81] F. Verstraete, V. Murg, and J. I. Cirac. Matrix product states, projected entangled pair states, and variational renormalization group methods for quantum spin systems. *Adv. Phys.*, March 2008.
- [82] A. J. Daley, C. Kollath, U. Schollwöck, and G. Vidal. Time-dependent density-matrix renormalization-group using adaptive effective Hilbertspaces. *J. Stat. Mech.: Theory Exp.*, 2004 (04):P04005, April 2004. ISSN 1742-5468. doi: 10.1088/1742-5468/2004/04/P04005.

- [83] Steven R. White and Adrian E. Feiguin. Real-Time Evolution Using the Density Matrix Renormalization Group. *Phys. Rev. Lett.*, 93(7):076401, August 2004. ISSN 1079-7114. doi: 10.1103/PhysRevLett.93.076401.
- [84] Guifré Vidal. Efficient Classical Simulation of Slightly Entangled Quantum Computations. *Phys. Rev. Lett.*, 91(14):147902, October 2003. ISSN 1079-7114. doi: 10.1103/PhysRevLett.91.147902.
- [85] Michael Zwolak and Guifré Vidal. Mixed-State Dynamics in One-Dimensional Quantum Lattice Systems: A Time-Dependent Superoperator Renormalization Algorithm. *Phys. Rev. Lett.*, 93(20):207205, November 2004. ISSN 1079-7114. doi: 10.1103/PhysRevLett.93.207205.
- [86] Steven R. White. Minimally Entangled Typical Quantum States at Finite Temperature. *Phys. Rev. Lett.*, 102(19):190601, May 2009. ISSN 1079-7114. doi: 10.1103/PhysRevLett.102.190601.
- [87] U. Schollwöck. The density-matrix renormalization group. *Rev. Mod. Phys.*, 77(1):259–315, April 2005. ISSN 1539-0756. doi: 10.1103/RevModPhys.77.259.
- [88] H. F. Trotter. On the product of semi-groups of operators. *Proc. Amer. Math. Soc.*, 10(4):545–551, 1959. ISSN 0002-9939. doi: 10.1090/S0002-9939-1959-0108732-6.
- [89] Masuo Suzuki. Fractal decomposition of exponential operators with applications to many-body theories and Monte Carlo simulations. *Phys. Lett. A*, 146(6):319–323, June 1990. ISSN 0375-9601. doi: 10.1016/0375-9601(90)90962-N.
- [90] Andreas Weichselbaum. Non-abelian symmetries in tensor networks: A quantum symmetry space approach. *Ann. Phys.*, 327(12):2972–3047, December 2012. ISSN 0003-4916. doi: 10.1016/j.aop.2012.07.009.
- [91] Andreas Weichselbaum. X-symbols for non-Abelian symmetries in tensor networks. *Phys. Rev. Res.*, 2(2):023385, June 2020. ISSN 2643-1564. doi: 10.1103/PhysRevResearch.2.023385.
- [92] D. V. Averin and K. K. Likharev. Coulomb blockade of single-electron tunneling, and coherent oscillations in small tunnel junctions. *J. Low Temp. Phys.*, 62(3):345–373, February 1986. ISSN 1573-7357. doi: 10.1007/BF00683469.
- [93] Tero T. Heikkilä and Tero T. Heikkilä. *The Physics of Nanoelectronics*. Oxford University Press, Oxford, England, UK, January 2013. ISBN 978-0-19959244-9.
- [94] Patrycja Tulewicz, Kacper Wrześniewski, Szabolcs Csonka, and Ireneusz Weymann. Large Voltage-Tunable Spin Valve Based on a Double Quantum Dot. *Phys. Rev. Appl.*, 16(1):014029, Jul 2021. ISSN 2331-7019. doi: 10.1103/PhysRevApplied.16.014029.
- [95] V. Madhavan, W. Chen, T. Jamneala, M. F. Crommie, and N. S. Wingreen. Tunneling into a Single Magnetic Atom: Spectroscopic Evidence of the Kondo Resonance. *Science*, 280(5363):567–569, April 1998. ISSN 0036-8075. doi: 10.1126/science.280.5363.567.

- [96] T. Jamneala, V. Madhavan, W. Chen, and M. F. Crommie. Scanning tunneling spectroscopy of transition-metal impurities at the surface of gold. *Phys. Rev. B*, 61(15):9990–9993, April 2000. ISSN 2469-9969. doi: 10.1103/PhysRevB.61.9990.
- [97] Jiwoong Park, Abhay N. Pasupathy, Jonas I. Goldsmith, Connie Chang, Yuval Yaish, Jason R. Petta, Marie Rinkoski, James P. Sethna, Héctor D. Abruña, Paul L. McEuen, and Daniel C. Ralph. Coulomb blockade and the Kondo effect in single-atom transistors. *Nature*, 417:722–725, June 2002. ISSN 1476-4687. doi: 10.1038/nature00791.
- [98] Andrea Gemma, Fatemeh Tabatabaei, Ute Drechsler, Anel Zulji, Hervé Dekkiche, Nico Mosso, Thomas Niehaus, Martin R. Bryce, Samy Merabia, and Bernd Gotsmann. Full thermoelectric characterization of a single molecule. *Nat. Commun.*, 14(3868):1–6, June 2023. ISSN 2041-1723. doi: 10.1038/s41467-023-39368-7.
- [99] Wenjie Liang, Matthew P. Shores, Marc Bockrath, Jeffrey R. Long, and Hongkun Park. Kondo resonance in a single-molecule transistor. *Nature*, 417:725–729, June 2002. ISSN 1476-4687. doi: 10.1038/nature00790.
- [100] D. M. Zumbühl, C. M. Marcus, M. P. Hanson, and A. C. Gossard. Cotunneling Spectroscopy in Few-Electron Quantum Dots. *Phys. Rev. Lett.*, 93(25):256801, December 2004. ISSN 1079-7114. doi: 10.1103/PhysRevLett.93.256801.

Part II

Articles constituting the dissertation

Chapter 7

Linear response transport properties

7.1 Spin Seebeck effect of correlated magnetic molecules [A]



OPEN

Spin Seebeck effect of correlated magnetic molecules

Anand Manaparambil✉ & Ireneusz Weymann

In this paper we investigate the spin-resolved thermoelectric properties of strongly correlated molecular junctions in the linear response regime. The magnetic molecule is modeled by a single orbital level to which the molecular core spin is attached by an exchange interaction. Using the numerical renormalization group method we analyze the behavior of the (spin) Seebeck effect, heat conductance and figure of merit for different model parameters of the molecule. We show that the thermopower strongly depends on the strength and type of the exchange interaction as well as the molecule's magnetic anisotropy. When the molecule is coupled to ferromagnetic leads, the thermoelectric properties reveal an interplay between the spin-resolved tunneling processes and intrinsic magnetic properties of the molecule. Moreover, in the case of finite spin accumulation in the leads, the system exhibits the spin Seebeck effect. We demonstrate that a considerable spin Seebeck effect can develop when the molecule exhibits an easy-plane magnetic anisotropy, while the sign of the spin thermopower depends on the type and magnitude of the molecule's exchange interaction.

Thermoelectric properties of nanoscale systems have recently attracted a considerable attention^{1–5}. This is due to the fact that such systems are expected to offer much better thermoelectric efficiency as compared to their bulk counterparts^{6–8}. Moreover, it turns out that studying the behavior of thermoelectric coefficients can provide additional information about various correlations and quantum interference present in the system^{9–16}. One prominent example resulting from electronic correlations is the Kondo effect^{17,18} observed in quantum dots and molecules^{19,20}, for which the sign changes of the thermopower have been proposed as additional signatures and measures of the strength of Kondo correlations^{21–24}. In fact, thermoelectric properties of Kondo-correlated nanoscale junctions have been recently explored experimentally^{10,25,26}.

Interestingly, the thermoelectric phenomena of nanostructures have also been explored in the case of systems involving magnetic components. In fact, with the discovery of the spin Seebeck effect²⁷, a new field of interest, namely spin caloritronics, have started blossoming^{28–32}. It transpires that the interplay of charge, heat and spin gives rise to a rich behavior of the thermoelectric coefficients that are now spin-dependent^{33–35}. In correlated magnetic nanostructures, such as e.g. quantum dots coupled to ferromagnetic leads, the spin thermopower was shown to provide further information about an exchange field and its interactions with electronic correlations driving the Kondo effect^{36,37}. Moreover, the spin Seebeck effect has also been studied in the case of quantum dots subject to external magnetic field^{38–40}. An interesting situation occurs when the junction comprises a molecule of large spin, since the spin Seebeck effect is then additionally conditioned by intrinsic parameters of the molecule, such as an exchange interaction, magnetic anisotropy or the magnitude of the molecule's spin^{41,42}. In fact, the spin-dependent thermoelectric properties of large-spin molecular junctions have already been studied in the case of weak coupling to the contacts^{43–46}, whereas the system's behavior in the strongly correlated case remains to a large extent unexplored. This comprises the goal of this paper, which is to further extend the understanding of thermoelectricity in strongly correlated magnetic molecular systems.

We therefore undertake the studies of the Seebeck and spin Seebeck effects for a large-spin molecule, such as a single molecular magnet^{47–49}, embedded in a tunnel junction with either nonmagnetic or ferromagnetic contacts. The focus is on the linear response regime with respect to the applied potential and temperature gradients, which justifies the usage of the numerical renormalization group (NRG) method^{50,51} for the calculations. This method allows for obtaining very accurate results for the electrical and heat conductances as well as the Seebeck effect and the corresponding figure of merit in the full parameter space of the model. The molecule is assumed to possess an orbital level, through which transport takes place, which is exchange coupled to the spin of the molecule's internal core^{52–54}. First of all, we show that the Seebeck coefficient strongly depends on the type and strength of the exchange interaction. In particular, for antiferromagnetic exchange, we find an additional sign change of the thermopower as a function of temperature. Moreover, in the case of magnetic contacts, the interplay of Kondo screening with exchange field determines the thermoelectric response of the system. We

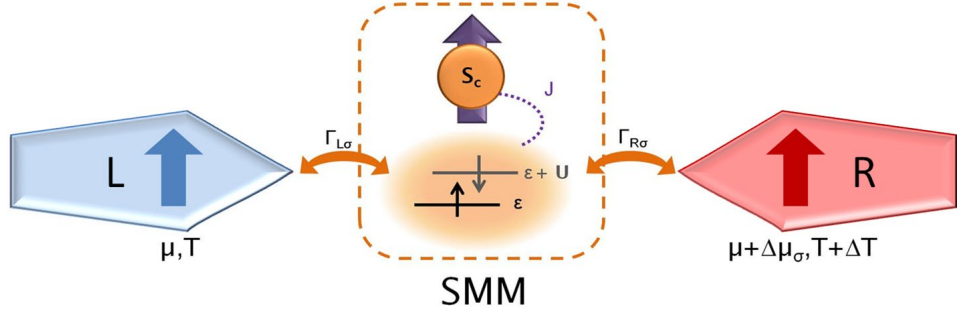


Figure 1. Schematic of the considered molecular junction. It consists of a magnetic molecule of spin $S = S_c + s$ tunnel-coupled to external leads, with spin-dependent coupling strengths, $\Gamma_{L\sigma}$ and $\Gamma_{R\sigma}$, for the left and right lead. S_c is the spin of the molecule's magnetic core, while s denotes the spin of electrons occupying the orbital level. The molecule is assumed to effectively possess one orbital level, through which transport takes place, that is exchange-coupled (with coupling strength J) to the molecule's core spin S_c . The orbital level is characterized by on-site energy ε and the Coulomb correlations U . There is a voltage ($\Delta\mu_\sigma$) and temperature (ΔT) gradient applied to the system. In the case of magnetic contacts, the voltage gradient may be spin-dependent. In considerations we assume $S_c = 1$, while $s = 1/2$ ($s = 0$) when the orbital level occupancy is odd (even).

consider two specific cases regarding the spin relaxation time in the leads^{35,36}. In the case of slow spin relaxation, a spin bias can be generated in the system, which gives rise to the spin Seebeck effect. On the other hand, for fast spin relaxation, the spin Seebeck effect does not develop, however, the thermoelectric coefficients still exhibit interesting spin-resolved properties due to spin dependence of tunneling processes. We believe that our study, by providing a comprehensive analysis of (spin) thermopower in the case of large-spin molecules, adds a new insight into the interplay of heat, charge and spin in magnetic molecules, contributing thus to further development of molecular spin caloritronics.

Results

The schematic of the studied system is presented in Fig. 1. A high-spin magnetic molecule, of spin $S = S_c + s$, is coupled to external magnetic leads, whose magnetizations point in the same direction. The molecule's easy axis is assumed to coincide with the direction of leads' magnetizations. It is further assumed that a single molecular energy level is active in transport and this orbital level is coupled through an exchange interaction J to the core spin S_c of the molecule. Thus, the Hamiltonian of the molecule reads as⁵²⁻⁵⁴,

$$\hat{H}_{\text{mol}} = \varepsilon \sum_{\sigma} \hat{n}_{\sigma} + U \hat{n}_{\uparrow} \hat{n}_{\downarrow} - J \hat{\mathbf{S}}_c \cdot \hat{\mathbf{s}} - D \hat{S}_z^2, \quad (1)$$

where ε and U denote the energy of the molecule's orbital level and Coulomb correlation energy between two electrons of opposite spin occupying that level. $\hat{n}_{\sigma} \equiv \hat{d}_{\sigma}^{\dagger} \hat{d}_{\sigma}$ is the occupation number operator for an electron of spin σ and $\hat{d}_{\sigma}^{\dagger}$ (\hat{d}_{σ}) is the corresponding creation (annihilation) operator. The spin operator for an electron occupying the orbital level is denoted by $\hat{\mathbf{s}} \equiv (1/2) \sum_{\sigma\sigma'} \hat{d}_{\sigma}^{\dagger} \boldsymbol{\sigma}_{\sigma\sigma'} \hat{d}_{\sigma'}$, where $\boldsymbol{\sigma} \equiv (\sigma^x, \sigma^y, \sigma^z)$ denotes the vector of the Pauli matrices, and $\hat{\mathbf{S}}_c$ is the operator for the core spin of the molecule. The two spins are coupled by the exchange interaction J , which can be either of ferromagnetic ($J > 0$) or antiferromagnetic ($J < 0$) type, depending on the sign of J . The molecule can be subject to magnetic anisotropy denoted by D and \hat{S}_z is the z th component of the molecule spin operator $\hat{\mathbf{S}} = \hat{\mathbf{S}}_c + \hat{\mathbf{s}}$. In calculations, we assume $S_c = 1$, while the spin of electrons on the orbital level is given by $s = 1/2$ or $s = 0$, depending on its occupancy. Consequently, the total molecule's spin is $S = 3/2$ for singly occupied orbital level or $S = 1$ in the case when the occupation is even.

The tunneling processes between the molecule and the leads are described by the following Hamiltonian

$$\hat{H}_{\text{tun}} = \sum_{qk\sigma} v_{qk\sigma} (\hat{c}_{qk\sigma}^{\dagger} \hat{d}_{\sigma} + \hat{d}_{\sigma}^{\dagger} \hat{c}_{qk\sigma}), \quad (2)$$

where $q = L$ for the left and $q = R$ for the right electrode, the operator $\hat{c}_{qk\sigma}^{\dagger}$ ($\hat{c}_{qk\sigma}$) creates (annihilates) an electron with energy $\varepsilon_{qk\sigma}$, momentum k and spin σ in the q -th lead, and $v_{qk\sigma}$ denotes the corresponding tunnel matrix elements. The leads are described within the non-interacting quasi-particle approximation by

$$\hat{H}_{\text{leads}} = \sum_{qk\sigma} \varepsilon_{qk\sigma} \hat{c}_{qk\sigma}^{\dagger} \hat{c}_{qk\sigma}. \quad (3)$$

Having defined the three parts of the Hamiltonian, the total Hamiltonian is given by, $\hat{H} = \hat{H}_{\text{mol}} + \hat{H}_{\text{tun}} + \hat{H}_{\text{leads}}$.

The tunnel coupling between the molecule and the leads gives rise to the broadening of the orbital level, which can be described by, $\Gamma_{q\sigma} = \pi \rho_{q\sigma} v_{q\sigma}^2$, where $\rho_{q\sigma}$ is the spin-dependent density of states at the Fermi level in the lead q and we assumed momentum-independent tunnel matrix elements $v_{qk\sigma} \equiv v_{q\sigma}$. We then define the full broadening function, which for spin σ can be written as, $\Gamma_{\sigma} = (1 + \eta p) \Gamma$, where $\Gamma = \Gamma_L + \Gamma_R$

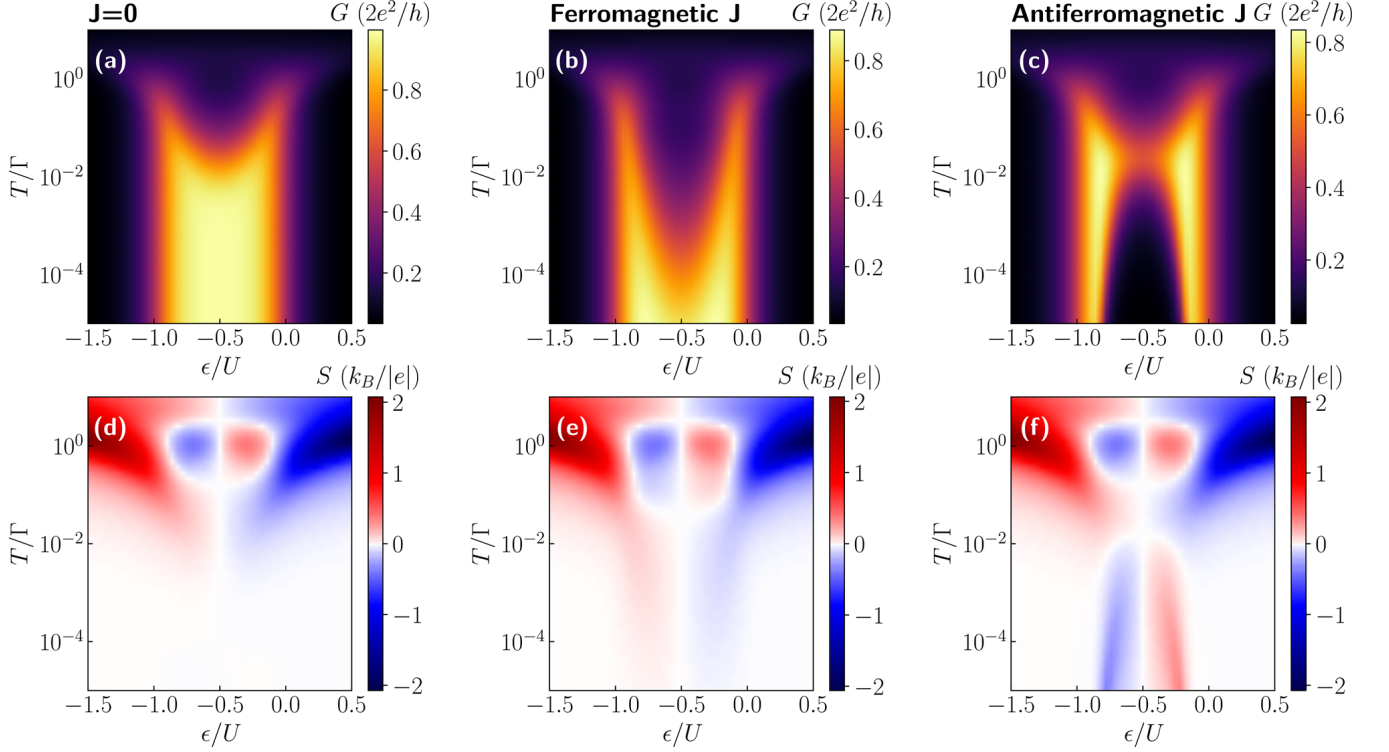


Figure 2. Conductance and thermopower of molecule in nonmagnetic junction. The linear conductance G and thermopower S as a function of the position of molecule's level ε and temperature T in the case of (a,d) $J = 0$, (b,e) ferromagnetic ($J = 10T_K$) and (c,f) antiferromagnetic ($J = -T_K$) exchange interaction, where $T_K = 0.0022$ is the Kondo temperature in the case of $\varepsilon = -U/2$, $J = 0$ and $p = 0$. The other parameters are: $\Gamma = 0.05$, $U = 0.5$, $D = 0$, in units of band halfwidth, and $p = 0$. The spin of the molecule is equal to $S = 3/2$.

and $\Gamma_q = \Gamma_{q\uparrow} + \Gamma_{q\downarrow}$, whereas p is the effective spin polarization of the left and right ferromagnetic lead, $p = (p_L + p_R)/2$, and $\eta = 1$ ($\eta = -1$) for spin-up (spin-down) electrons.

Thermopower in the case of nonmagnetic leads. We focus on the thermoelectric transport properties of the considered molecular junction in the linear response regime. The interesting thermoelectric phenomena happening across the magnetic molecule can be quantified using the transport coefficients, such as the electrical conductance G , the thermopower (Seebeck coefficient) S , as well as the thermal conductance κ and the thermoelectric figure of merit ZT . In the linear response regime, these quantities can be expressed in terms of Onsager integrals $L_{n\sigma}$ ⁵⁵

$$L_{n\sigma} = -\frac{1}{h} \int d\omega (\omega - \mu)^n \frac{\partial f}{\partial \omega} \mathcal{T}_\sigma(\omega), \quad (4)$$

where $\mathcal{T}_\sigma(\omega)$ is the energy-dependent transmission coefficient for the spin channel σ , f is the Fermi-Dirac distribution function and μ denotes the electrochemical potential. The electrical conductance G and the electronic contribution to the thermal conductance κ can be then found from

$$G = e^2 L_0 \quad \text{and} \quad \kappa = \frac{1}{T} \left(L_2 - \frac{L_1^2}{L_0} \right), \quad (5)$$

where e is the electron charge, T denotes the temperature and $L_n = \sum_\sigma L_{n\sigma}$. On the other hand, the thermopower S is defined as $S = -[\Delta V / \Delta T]_{J=0}$, on the condition of vanishing of the charge current J . Hence, S can be expressed in the form

$$S = -\frac{1}{|e|T} \frac{L_1}{L_0}. \quad (6)$$

Having defined G , S and κ , one can obtain the thermoelectric figure of merit $ZT \equiv GS^2T/\kappa$.

Let us first consider the case of nonmagnetic molecular junction. The linear conductance and the Seebeck coefficient as a function of the molecule's orbital level energy ε and temperature T are shown in Fig. 2. The first column shows the results for $J = 0$, while the second (third) column corresponds to the case of the ferromagnetic (antiferromagnetic) exchange interaction J . The case of $J = 0$ is shown just for reference and allows us to clearly reveal the effects stemming from the presence of large-spin molecule. To begin with, we consider the behavior of the linear conductance. The largest changes with lowering the temperature are visible when the orbital level is singly occupied, i.e. for $-U \lesssim \varepsilon \lesssim 0$. In this case, the Kondo effect can develop at sufficiently low temperatures,

such that $T \lesssim T_K$, where T_K is the Kondo temperature¹⁷. Once $T \ll T_K$, the conductance reveals a plateau as a function of ε of height $G = 2e^2/h$ in the case of $J = 0$ ^{18,20}. However, for magnetic molecules described by the Hamiltonian (1), the low-temperature behavior strongly depends on the type of exchange interaction J ⁵⁶. For ferromagnetic exchange, the Kondo effect always develops with lowering T , however, T_K becomes reduced compared to the case of $J = 0$. On the other hand, in the antiferromagnetic- J case, once $|J| \gtrsim T_K$, the spin on the orbital level strongly binds with the magnetic core spin, which results in the suppression of the conductance through the system. In this case, in the singly occupied orbital regime, one only observes a small enhancement (a local maximum) of G with decreasing T followed by its strong suppression⁵⁶.

The different scenarios discussed above give rise to a unique behavior of the Seebeck coefficient, which is presented in the bottom row of Fig. 2. The first observation is that, as expected^{9,12}, the thermopower changes sign with respect to the particle-hole symmetry point, $\varepsilon = -U/2$. Moreover, one can see that the behavior of S for $T \gtrsim \Gamma$ is hardly affected by the type of exchange interaction J . This is because in our considerations $|J| < \Gamma$ and the effects of finite J can be visible only when $T \lesssim |J|$. Let us anyway summarize the main features of the high-temperature behavior. One observes two pronounced maxima for $T \approx \Gamma$ in the case when the orbital level is either empty or doubly occupied. On the other hand, when moving to the Coulomb blockade regime where the orbital level is singly occupied, the thermopower changes sign and two local extrema develop antisymmetrically around $\varepsilon = -U/2$ for $T \approx \Gamma$ ^{21,36}. With lowering the temperature, distinct features appear, resulting from the interplay of the correlations driving the Kondo effect and the molecule's exchange interaction. First of all, one can note that in the case of $J = 0$, the regions of large $|S|$ extend from the empty and doubly occupied regimes for $T \approx \Gamma$ downwards to low temperatures in the single occupancy regime. For singly occupied orbital level, the thermopower exhibits then a sign change as a function of T , see Fig. 2d, which signals the relevance of the Kondo correlations²¹. A qualitatively similar behavior can be observed in the case of ferromagnetic exchange interaction J , see Fig. 2e, with the main difference associated with smaller temperatures at which the corresponding sign change occurs. This is associated with the fact that the sign change occurs at the onset of the Kondo correlations and, because the Kondo effect develops at much lower temperatures in the case of ferromagnetic J compared to the case of $J = 0$ (see Fig. 2a,b), one observes that the sign change in S is also shifted to lower temperatures. However, this shift is not proportional to the corresponding shift visible in the behavior of G . It is because while much smaller temperatures are needed for the full development of the Kondo effect in the case of ferromagnetic J , the temperature associated with the onset of the Kondo correlations only weakly decreases with J . This is why the crossover for $J > 0$ is only slightly shifted to lower temperatures compared to the case of $J = 0$, cf. Fig. 2d,e. Interestingly, qualitatively new features compared to the case of $J \geq 0$ can be observed in the case of antiferromagnetic exchange interaction, where an additional sign change at low temperatures is present, see Fig. 2f.

Further insight into the behavior of the thermoelectric properties can be obtained from the inspection of Fig. 3, which presents the temperature dependence of G , S , κ and ZT for different values of the exchange interaction J , as indicated. This figure is generated for the case when the orbital level is detuned from the particle-hole symmetry point, such that a considerable thermopower can be observed. In addition, the orbital level is assumed to be singly occupied ($\varepsilon = -U/3$), such that the system is in the local moment regime and the Kondo correlations are relevant at sufficiently low temperatures. Let us start with the analysis of the linear conductance. In the case of ferromagnetic J (see the solid lines in the figure), the enhancement of J results in a decrease of the Kondo temperature. In this case the ground state is always two-fold degenerate with total spin given by $S = S_c + 1/2$ and the Kondo effect develops irrespective of J , though T_K becomes very cryogenic with increasing J ⁵⁶. Consequently, we observe mainly quantitative changes in Fig. 3a, while qualitative behavior is the same. On the other hand, the situation is completely different in the case of antiferromagnetic exchange interaction $J < 0$, see the dashed lines in Fig. 3. Now, with increasing $|J|$, the ground state becomes $S = S_c - 1/2$, since the spin on the orbital level binds anti-ferromagnetically with the molecule's core spin. Because of that, the Kondo effect is quenched once the temperature becomes lower than the energy scale responsible for this antiferromagnetic state. As a result, the temperature dependence of conductance exhibits a nonmonotonic behavior⁵⁶, see Fig. 3a. We note that such behavior is similar to the two-stage Kondo effect observed in side-attached double quantum dots where the hopping induces an antiferromagnetic interaction between the dots⁵⁷.

The behavior of the conductance has a strong influence on the Seebeck coefficient. This is because the temperature dependence of conductance reflects the energy dependence of the transmission coefficient $\mathcal{F}(\omega)$ and, from the Sommerfeld expansion, the thermopower at low temperatures can be estimated from (note that temperature T is in units of energy)

$$S \approx -\frac{\pi^2}{3} \frac{k_B}{e} \frac{T}{\mathcal{F}(\omega)} \left. \frac{\partial \mathcal{F}(\omega)}{\partial \omega} \right|_{\omega=0}, \quad (7)$$

where $\mathcal{F}(\omega) = \sum_{\sigma} \mathcal{F}_{\sigma}(\omega)$. One can thus see that the thermopower is related to the monotonicity of the variation of the spectral function with energy. This is why in the case of ferromagnetic exchange interaction we only observe qualitative changes in S , see the solid lines in Fig. 3b. The enhancement of J suppresses then the Kondo temperature, which is seen in the behavior of S as a shift of the local minimum towards smaller temperatures. However, a completely different scenario develops for antiferromagnetic J , where an additional sign change occurs and S exhibits an extra maximum for temperatures corresponding to the energy scale at which $G(T)$ starts decreasing with lowering T , see the dashed curves in Fig. 3b.

Despite a spectacular impact of exchange interaction on the thermopower, its effect on the thermal conductance is less pronounced, see Fig. 3c. This is because κ is considerable only at energy scales corresponding to the coupling strength and Coulomb correlations and thus, as long as $|J| \ll \Gamma$, κ hardly depends on the type and magnitude of exchange interaction. On the other hand, the figure of merit ZT displays new peaks in the case of antiferromagnetic J , see Fig. 3d, which are associated with the above-discussed maxima emerging in the

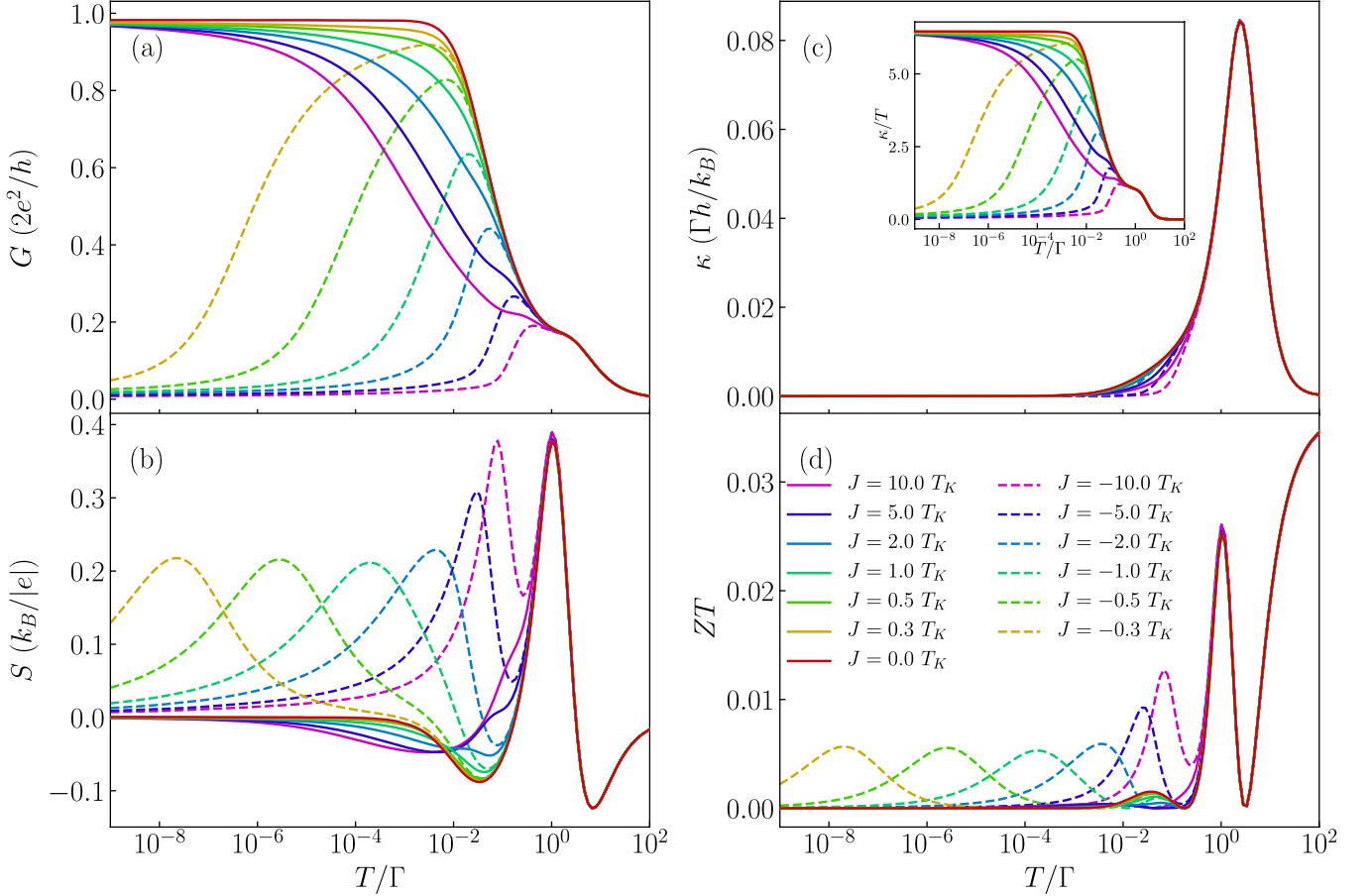


Figure 3. Dependence of thermoelectric coefficients on exchange interaction. (a) The conductance, (b) Seebeck coefficient, (c) heat conductance and (d) figure of merit as a function of temperature for selected values of exchange interaction J in the case of nonmagnetic contacts. The solid (dashed) lines correspond to the case of ferromagnetic (antiferromagnetic) exchange interaction. The inset in (c) presents the temperature dependence of κ/T . The parameters are the same as in Fig. 2 with $\varepsilon = -U/3$.

temperature dependence of S . We also note that the influence of J on κ is more visible when one plots κ/T , see the inset in Fig. 3c. It is nicely visible that the qualitative behavior of κ/T resembles that of the linear conductance, which is a direct consequence of the Wiedemann–Franz law. A similar behavior has been recently observed for T-shaped double quantum dots²³.

Effect of magnetic anisotropy. We now focus on elucidating the role of magnetic anisotropy on the thermoelectric properties of the considered molecular junction. We consider both an easy-axis ($D > 0$) and easy-plane ($D < 0$) types of magnetic anisotropy. First we note that in the case of ferromagnetic exchange interaction between the orbital level and molecule’s core spin the magnetic anisotropy has a very moderate influence on the thermoelectric properties. It does not lead to new qualitative behavior as long as $|D|$ is smaller than the corresponding Kondo temperature, therefore in the following we just analyze the case of antiferromagnetic exchange coupling J . The temperature dependence of the conductance and the Seebeck coefficient for this situation is shown in Fig. 4, where the left (right) column corresponds to the easy-plane (easy-axis) magnetic anisotropy case. This figure was generated for the same orbital level position as in Fig. 3, such that the orbital level is detuned from the particle-hole symmetry point, while the system stays in the local moment regime. In the absence of anisotropy the conductance displays a nonmonotonic dependence, characteristic of the antiferromagnetic exchange coupling. When an easy plane anisotropy arises in the system and the molecule possesses a half-integer spin, it results in a two-fold degenerate ground state of $S = 1/2$, such that the Kondo effect can be restored. This is clearly seen in Fig. 4a, where one observes an upturn of the conductance with lowering T . This in turn has a considerable impact on the Seebeck coefficient, which exhibits an additional sign change, see Fig. 4b. On the other hand, in the case of easy plane anisotropy, the low-temperature conductance again becomes increased with D , as can be seen in Fig. 4c. This is however just associated with a decreased exchange interaction between the molecule’s core spin and the spin of the orbital level, and not with the reinstatement of the Kondo effect. Consequently, while the Seebeck coefficient strongly depends on D , no additional sign changes are present. In fact, the maximum in S for $D = 0$ becomes suppressed with increasing D and smears out completely once $D \approx T_K$, see Fig. 4d.

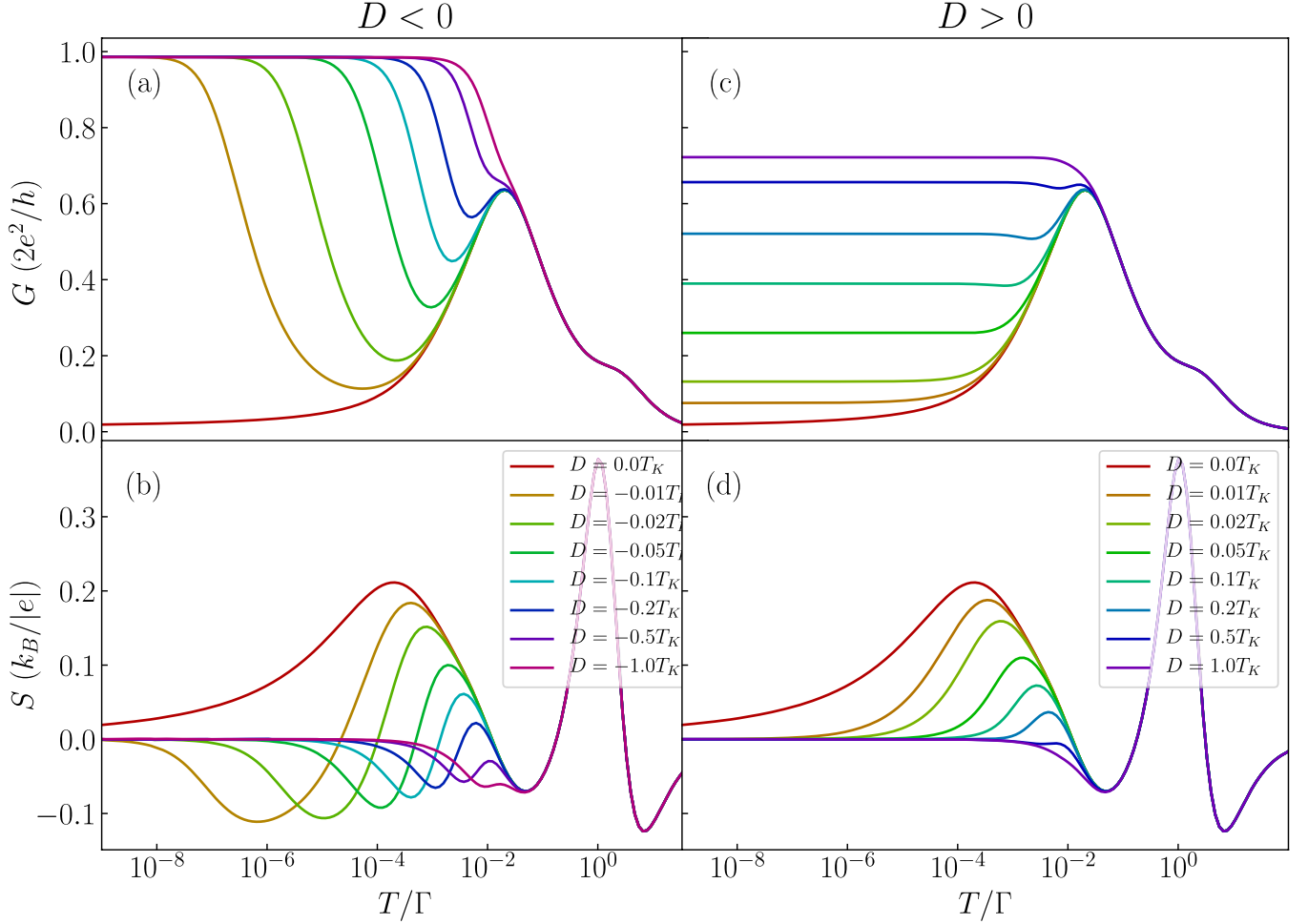


Figure 4. The effect of magnetic anisotropy in the case of molecule with nonmagnetic contacts. The temperature dependence of (a,c) the conductance and (b,d) the Seebeck coefficient in the case of antiferromagnetic exchange interaction $J = -T_K$ for selected values of magnetic anisotropy D . The left (right) column presents the case of easy-plane (easy-axis) type of magnetic anisotropy. The parameters are the same as in Fig. 2 with $\varepsilon = -U/3$.

Thermopower in the case of ferromagnetic leads. We now turn to the discussion of thermoelectric properties in the case of ferromagnetic electrodes. For the ferromagnetic contacts, we assume a moderate spin polarization^{58–60}, $p = 20\%$. In this section we assume that the spin relaxation in the contacts is relatively fast, such that no spin accumulation develops and the induced potential gradient does not depend on spin, $\Delta\mu_\uparrow = \Delta\mu_\downarrow$. In this regime, although the spin Seebeck effect does not develop, the spin-dependence of tunneling processes greatly modifies the thermoelectric transport properties of the system as compared to the nonmagnetic case. We also note that in the absence of spin accumulation the formulas for spin-dependent thermoelectric coefficients are the same as in case of nonmagnetic leads^{35,36}.

The linear conductance and the Seebeck coefficient as a function of ε and T calculated for different values of J are displayed in Fig. 5. In the behavior of the conductance one can clearly observe the signatures of an effective exchange field that develops in the molecule coupled to ferromagnetic electrodes^{54,61}. Such an exchange field, which within the perturbation theory at zero temperature and for $J = 0$ can be described as⁶¹,

$$\Delta\varepsilon_{\text{exch}} \approx \frac{2p\Gamma}{\pi} \log \left| \frac{\varepsilon}{\varepsilon + U} \right|, \quad (8)$$

results in a spin-splitting of the molecule's orbital level, when it is detuned from the particle-hole symmetry point of the model $\varepsilon = -U/2$. In the case of considered molecule, this field depends in a nontrivial way on the properties of the molecule, such as J , D and S_c , however, it still vanishes whenever $\varepsilon = -U/2$ ^{54,62}. If the exchange field splitting becomes larger than the Kondo temperature, it suppresses the Kondo resonance. As a consequence, the low-temperature conductance in the Coulomb blockade regime is generally decreased except for $\varepsilon = -U/2$, where a local maximum as a function of ε is present, see Fig. 5a. A similar conductance suppression can be seen in the case of ferromagnetic exchange interaction J presented in Fig. 5b. However, now the suppression of G is larger as compared to the case of $J = 0$, which is associated with a smaller Kondo temperature when $J > 0$. On the other hand, when J is antiferromagnetic, mainly quantitative changes can be observed in the conductance behavior, cf. Figs. 2c and 5c. Namely, the region of suppression of low-temperature conductance is now smaller, which is an

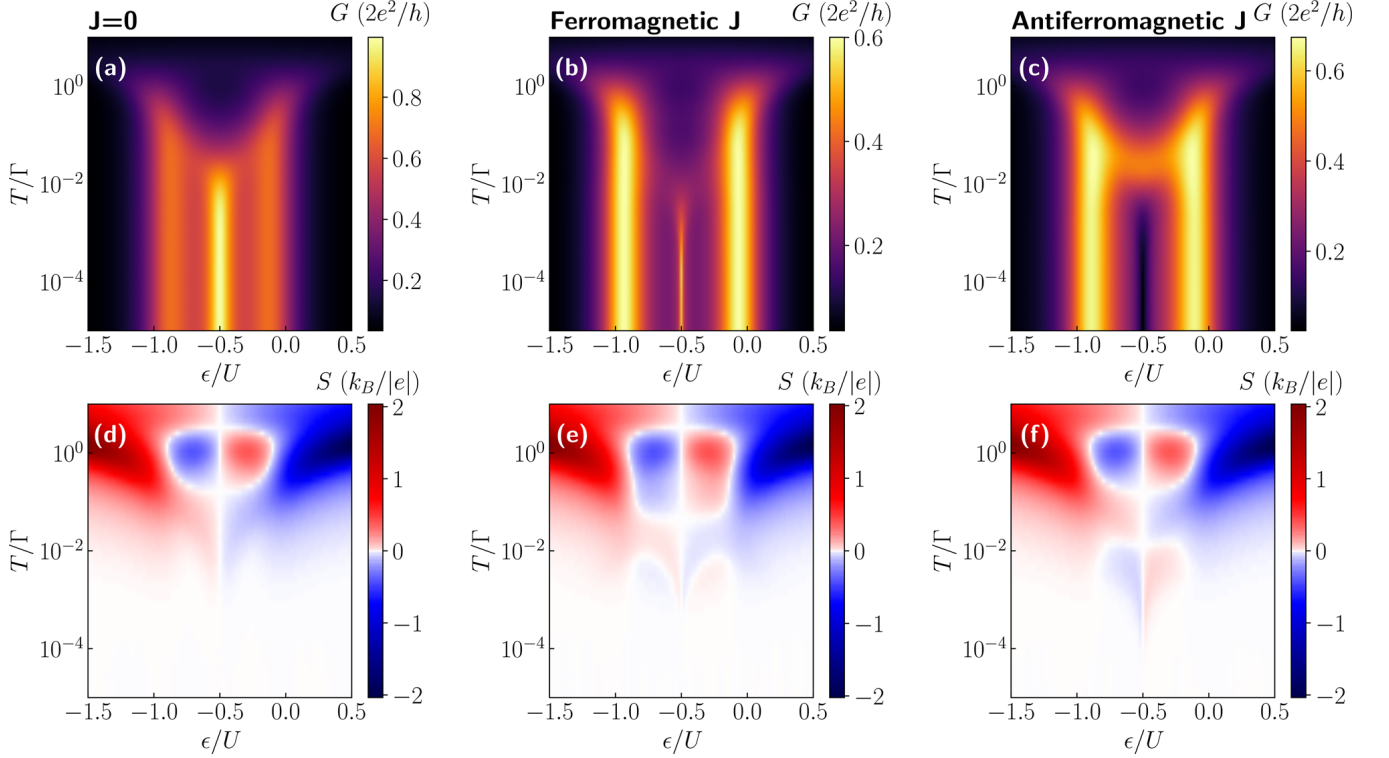


Figure 5. Conductance and thermopower of molecule in ferromagnetic junction. The linear conductance G and thermopower S as a function of the position of molecule's level ϵ and temperature T in the case of **(a,d)** $J = 0$, **(b,e)** ferromagnetic ($J = 10T_K$) and **(c,f)** antiferromagnetic ($J = -T_K$) exchange interaction. The other parameters are the same as in Fig. 2 with $p = 20\%$.

indication that the exchange field hinders the formation of an antiparallel spin state between the orbital level and the core spin. Because of that, the decrease of conductance due to that formation is correspondingly weakened. The signatures of the interplay of exchange field, Kondo correlations, and the molecule's exchange interaction are also visible in the behavior of the thermopower, which is presented in the bottom row of Fig. 5. One can see that the main changes are visible in the low-temperature behavior, which reveals the energy scale associated with the exchange field. More specifically, in the case of ferromagnetic exchange interaction, an additional sign change in S occurs as compared to the case of nonmagnetic leads, whereas for antiferromagnetic J the Seebeck coefficient becomes generally reduced, cf. Figs. 2 and 5.

To shed more light onto the thermoelectric behavior of the considered magnetic molecular junction, in Fig. 6 we present the temperature dependence of the conductance, Seebeck coefficient, heat conductance and figure of merit calculated for different values of exchange interaction, as indicated. This figure was determined for a relatively low value of detuning from the particle-hole symmetry point, $\epsilon = -0.48U$, such that the exchange field effects rather compete than surpass other energy scales, and the system's behavior is most interesting. First of all, one can note that below a certain temperature the conductance stops changing any more and retains its low-temperature value. This characteristic energy scale is set by the exchange field $\Delta\epsilon_{\text{exch}}$ —when this field is larger than thermal energy, it determines the transport behavior and no further dependence on lowering T is visible, see Fig. 6. The Seebeck effect becomes then suppressed and so does the figure of merit. This can be understood by referring to the Sommerfeld expansion: once the exchange field is the dominant energy scale the conductance becomes constant and so does the low-energy transmission coefficient. Consequently, $[\partial\mathcal{F}(\omega)/\partial\omega]_{\omega=0} \approx 0$ and thus $S \approx 0$. This explains why $S \approx 0$ and $ZT \approx 0$ for $T/\Gamma \lesssim \Delta\epsilon_{\text{exch}}/\Gamma \approx 10^{-4}$, see Fig. 6b,d.

Let us now focus on the most interesting behavior, which is present for temperatures of the order and larger than the exchange field, and let us start with the case of ferromagnetic exchange interaction $J > 0$. One can see that increasing J results in suppression of the low-temperature conductance, see Fig. 6a. This results from the fact that increasing J leads to lowering of T_K , and once $\Delta\epsilon_{\text{exch}} \gtrsim T_K$, the Kondo peak becomes suppressed. This is also visible in the thermopower and the figure of merit where a new maximum emerges at energy scale corresponding to the exchange field $T \approx \Delta\epsilon_{\text{exch}}$, see Fig. 6. While in the case of ferromagnetic exchange interaction mainly qualitative effects are visible, the case of antiferromagnetic exchange is completely different, see the dashed lines in Fig. 6. In this case, increasing $|J|$ gives rise to the suppression of the conductance due to the formation of an antiferromagnetic spin state between the molecule's orbital level and its magnetic core. When $|J|$ is relatively low, the exchange field wins over the antiferromagnetic interaction and only a small suppression of G as a function of T is present, see e.g. the curve for $J = -0.3T_K$ in Fig. 6a. However, further enhancement of $|J|$, stabilizes the antiferromagnetic state of the molecule and a full suppression of G is obtained once $J \lesssim -2T_K$. This behavior gives rise to a new maximum visible both in S and ZT . Moreover, while the maximum associated with the conductance drop as T is lowered moves to higher energies with decreasing J ($J < 0$), there is an extra maximum

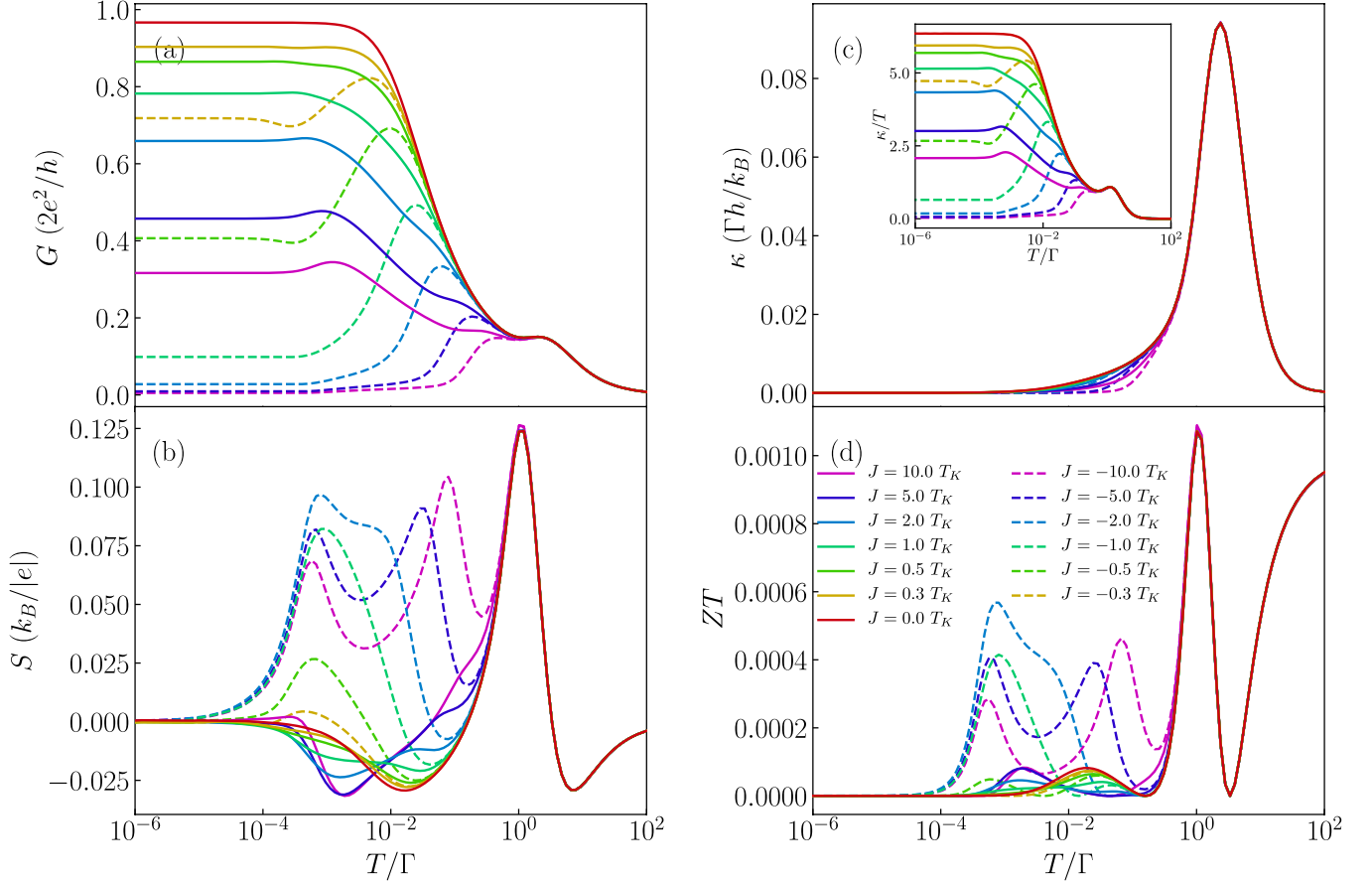


Figure 6. Dependence on exchange interaction in the case of ferromagnetic junction. (a) The conductance, (b) Seebeck coefficient, (c) heat conductance and (d) figure of merit as a function of temperature for selected values of exchange interaction J in the case of ferromagnetic leads. The solid (dashed) lines correspond to the case of ferromagnetic (antiferromagnetic) exchange interaction. The inset in (c) presents κ/T as a function of temperature. The parameters are the same as in Fig. 5 with $\varepsilon = -0.48U$.

visible just at the energy scale corresponding to $T \approx \Delta\varepsilon_{\text{exch}}$. As a consequence, the temperature dependence of the Seebeck coefficient displays an interesting triple-peak structure, see Fig. 6b.

To complete the picture, in Fig. 7 we present the temperature dependence of G and S calculated for different values of magnetic anisotropy. Similarly to the case of nonmagnetic leads, we display the data for antiferromagnetic exchange interaction, which shows the most interesting behavior. Let us first analyze the case of uniaxial anisotropy, which is presented in the right column of Fig. 7. One can see that finite anisotropy gives rise to an enhancement of the low-temperature conductance. This is a consequence of the fact that anisotropy breaks the symmetry of the antiferromagnetic state of the molecule responsible for the conductance suppression. This effect gives rise to a local maximum in the Seebeck coefficient that develops at the energy scale of the order of magnetic anisotropy, see Fig. 7d. The case when the molecule exhibits easy-plane type of anisotropy is shown in the left column of Fig. 7. Now, one can observe a very strong dependence of both G and S on the magnitude of magnetic anisotropy. First of all, the low- T conductance exhibits a nonmonotonic dependence on $D < 0$. Once the easy-plane anisotropy is present in the system and $|D| \lesssim 0.1T_K$, G becomes suppressed. However, this tendency becomes reversed when $D \lesssim -0.1T_K$, such that one observes an enhancement of G at low temperatures, see Fig. 7a. This is associated with the formation of a doublet ground state in the molecule in the case of considerable easy-plane anisotropy. Now, however, one witnesses a subtle interplay between the antiferromagnetic exchange interaction, the easy-plane magnetic anisotropy, the exchange field that splits the doublet state of the molecule and the Kondo correlations. The antiferromagnetic J gives rise to the suppression of G at low temperatures, which is however slightly hindered by the exchange field. On the other hand, turning on D ($D < 0$), results initially in a larger suppression of the conductance, nevertheless, increased values of $|D|$ eventually make the doublet state the ground state of the molecule, enhancing thus G due to the Kondo effect. Consequently, for sufficiently large $|D|$, the conductance shows a pronounced Kondo resonance, see Fig. 7a. The behavior of the conductance is clearly revealed in the temperature dependence of the Seebeck coefficient, which is shown in Fig. 7b. One can see that for values of D such that the conductance starts increasing, the thermopower exhibits a considerable maximum, which actually develops for $T \approx \Delta\varepsilon_{\text{exch}}$. With further increase of $|D|$, this maximum becomes however decreased and its position moves towards higher temperatures of the order of the Kondo temperature, see Fig. 7b. This large enhancement of the Seebeck coefficient is a result of interplay between the intrinsic properties of the molecule, such as its magnetic anisotropy, and the ferromagnetism of the leads. Unfortunately, this effect

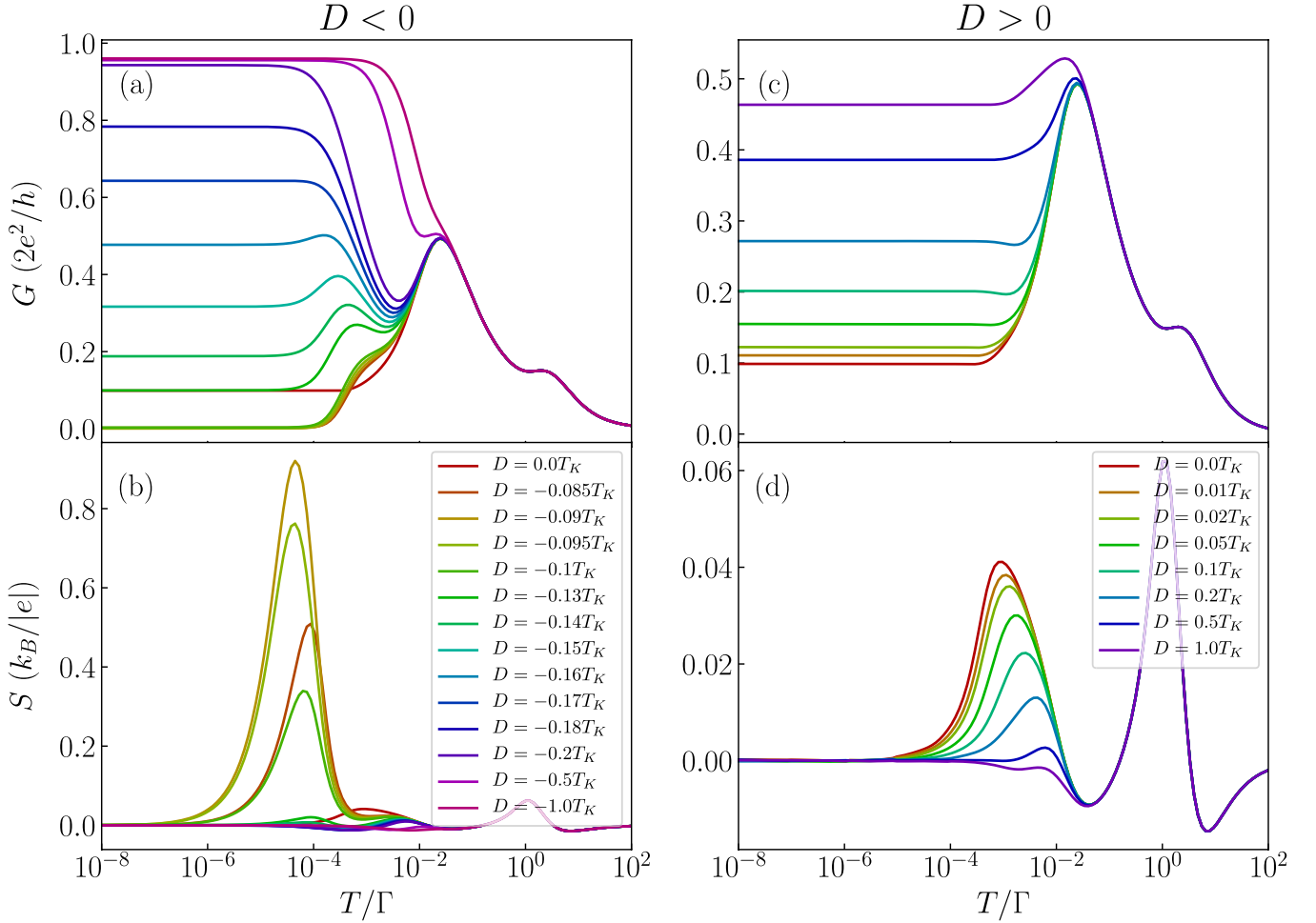


Figure 7. The effects of magnetic anisotropy in the case of ferromagnetic junction. The temperature dependence of (a,c) the conductance and (b,d) the Seebeck coefficient in the case of antiferromagnetic exchange interaction $J = -T_K$ for selected values of magnetic anisotropy D . The left (right) column presents the case of easy-plane (easy-axis) type of magnetic anisotropy. The parameters are the same as in Fig. 5 with $\varepsilon = -0.48U$.

is not associated with a particularly large figure of merit since the corresponding electrical conductance is then relatively low, see Fig. 7a.

Spin Seebeck effect. When the electrodes are ferromagnetic and are characterized by a long spin relaxation time, in addition to the charge current, a spin current can be generated in the system^{35,36}. The spin current I_S flows if there is a difference between chemical potentials for given spin direction, i.e. in the presence of a spin bias $\Delta\mu_\uparrow \neq \Delta\mu_\downarrow$. The development of spin bias is conditioned by the spin relaxation time in the contacts compared to the time of tunneling events. The case of fast spin relaxation was discussed in previous section, now, let us focus on the situation when the spin accumulation can build up in the leads, i.e. when the spin relaxation time is long. In such case, the spin Seebeck effect S_S can develop in the system. Assuming open circuit conditions, i.e. the vanishing of the spin and charge currents, it can be found from, $S_S = (S_\uparrow - S_\downarrow)/2$, where S_σ is the thermopower in the spin channel σ , which yields^{35,36}

$$S_S = -\frac{1}{2|e|T} \left(\frac{L_{1\uparrow}}{L_{0\uparrow}} - \frac{L_{1\downarrow}}{L_{0\downarrow}} \right). \quad (9)$$

On the other hand, the Seebeck coefficient in the case of finite spin bias is given by^{35,36}, $S = -\frac{1}{2|e|T} (L_{1\uparrow}/L_{0\uparrow} + L_{1\downarrow}/L_{0\downarrow})$, whereas the heat conductance can be expressed as, $\kappa = \frac{1}{T} \sum_\sigma (L_{2\sigma} - L_{1\sigma}^2/L_{0\sigma})$.

We would like to emphasize that in the case of ferromagnetic leads in the absence of spin accumulation, the Seebeck effect is due to a generated voltage difference that is not spin dependent. However, the tunneling processes themselves do depend on spin, therefore one then observes the spin-dependent Seebeck effect. On the other hand, when the spin accumulation is relevant in the leads, a spin bias becomes generated, which gives rise to the spin Seebeck effect. Such spin thermopower results from the spin splitting of the chemical potentials in the contacts and is associated with the corresponding spin current. Moreover, we would like to note that spin Seebeck effect due to electron transport is also referred to as the spin-dependent Seebeck effect, whereas the typical Seebeck effect in the case of magnetic contacts is referred to as spin-resolved Seebeck effect^{29,32}. However, in our paper we adopt the notion introduced by Świrkowicz et al.³⁵.

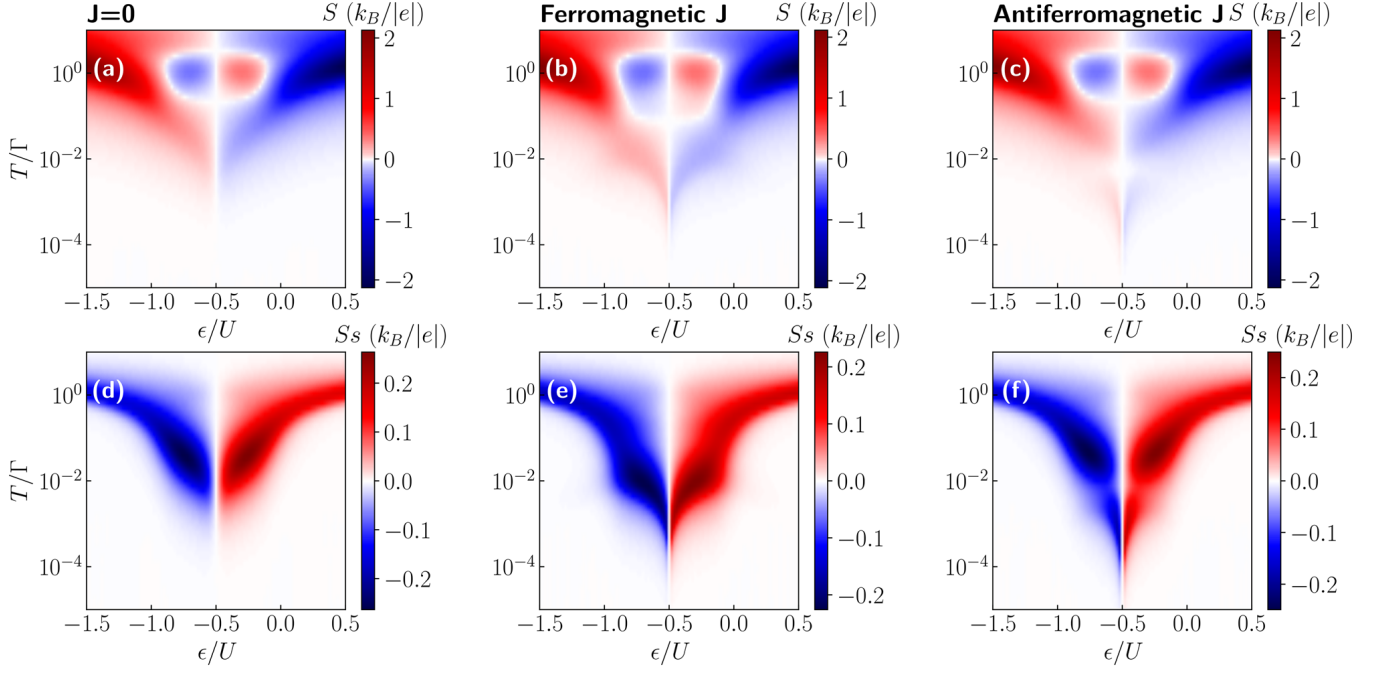


Figure 8. The spin Seebeck coefficient. (a–c) The Seebeck and (d–f) spin Seebeck coefficient as a function of temperature and orbital level position calculated for (a,d) $J = 0$ (b,e) ferromagnetic J and (c,f) antiferromagnetic J in the case of finite spin accumulation in the leads. The other parameters are the same as in Fig. 5.

The Seebeck and spin Seebeck coefficients as a function of temperature and the position of the molecule's orbital level calculated for different values of exchange interaction J are shown in Fig. 8. First of all, we note that the Seebeck effect at higher temperatures $T \approx \Gamma$ behaves generally very similarly as in the case of no spin accumulation in the leads, however, its low-temperature behavior is changed. While in the absence of spin accumulation, S exhibits an additional sign change for $-U \lesssim \epsilon \lesssim 0$ and $T \lesssim 0.01\Gamma$, in the case of long spin relaxation these features are not seen anymore. Instead, the Seebeck coefficient changes sign only once around $T \approx \Gamma$ and extends to low temperatures till it is quenched by the exchange field, see the first row of Fig. 8. On the other hand, the spin Seebeck effect displays completely different behavior. As can be seen, the only sign change occurs across the particle-hole symmetry point when tuning the position of the molecule's orbital level. Moreover, the overall behavior is reversed as compared to the Seebeck coefficient. In the regions where S is generally negative S_S is positive and vice versa. This is directly associated with the definition of S and S_S —while S captures the spin-resolved contributions due to hole and electron processes, S_S presents mainly the difference between the spin-dependent components. As can be seen in the bottom row of Fig. 8, the spin-up contribution dominates the thermopower for $\epsilon > -U/2$, while for $\epsilon < -U/2$ the spin-down thermopower is dominant. Such behavior is visible in all considered cases, namely, for $J = 0$ as well as for ferromagnetic and antiferromagnetic exchange interaction. However, there are some subtle differences. First of all, the spin Seebeck effect is finite for lower temperatures in the case of finite J , as compared to the case with $J = 0$. Moreover, while for ferromagnetic J , S_S exhibits a local maximum for $T \approx 0.01\Gamma$, for antiferromagnetic J , there is a small local minimum in the temperature dependence of spin Seebeck effect, see Fig. 8f.

The above-mentioned features are better visible in the temperature dependence of the thermopower and spin thermopower presented in Fig. 9. Moreover, it turns out that the above discussion is not fully complete, since one can now clearly observe that a sign change of both the Seebeck as well as spin Seebeck effect can develop, provided that the exchange interaction is sufficiently large. In the case of ferromagnetic exchange, a large minimum in S develops with increasing J at energy scale corresponding to the exchange field, see Fig. 9a. On the other hand, for the spin Seebeck effect a maximum forms at the same temperature for which S exhibits a minimum. An interesting behavior occurs for antiferromagnetic exchange interaction, when with increasing $|J|$, both the thermopower and spin thermopower change sign once $J \lesssim -T_K$. More specifically, S exhibits then a pronounced maximum, whereas a considerable minimum develops in S_S for $T \approx \Delta\epsilon_{\text{exch}}$, see Fig. 9. The sign change of the thermopower is associated with the fact that the exchange field effects, which determine the sign of S and S_S for low values of J , become overwhelmed by antiferromagnetic J , once the exchange interaction becomes sufficiently large, i.e. $|J| \gtrsim \Delta\epsilon_{\text{exch}}$.

To further understand the spin thermopower of magnetic molecules, we present the impact of magnetic anisotropy on the Seebeck and spin Seebeck effects for the case of antiferromagnetic exchange interaction in Fig. 10. First of all, for the case of uniaxial type of magnetic anisotropy, as shown in the right column of Fig. 10, there is a suppression in the minima (maxima) present in the Seebeck (spin Seebeck) effect with increasing anisotropy. This behavior is in fact similar to that observed in the case of no spin accumulation discussed in previous section. However, the case of an easy plane type of anisotropy presented in the left column of Fig. 10 shows far more interesting behavior. The thermopower and spin thermopower exhibit a change in sign around $T \approx \Delta\epsilon_{\text{exch}} \approx 10^{-4}$ for values of $D \lesssim -0.1T_K$. For temperatures $T \lesssim \Delta\epsilon_{\text{exch}}$, a considerable peak, positive (negative) for the spin

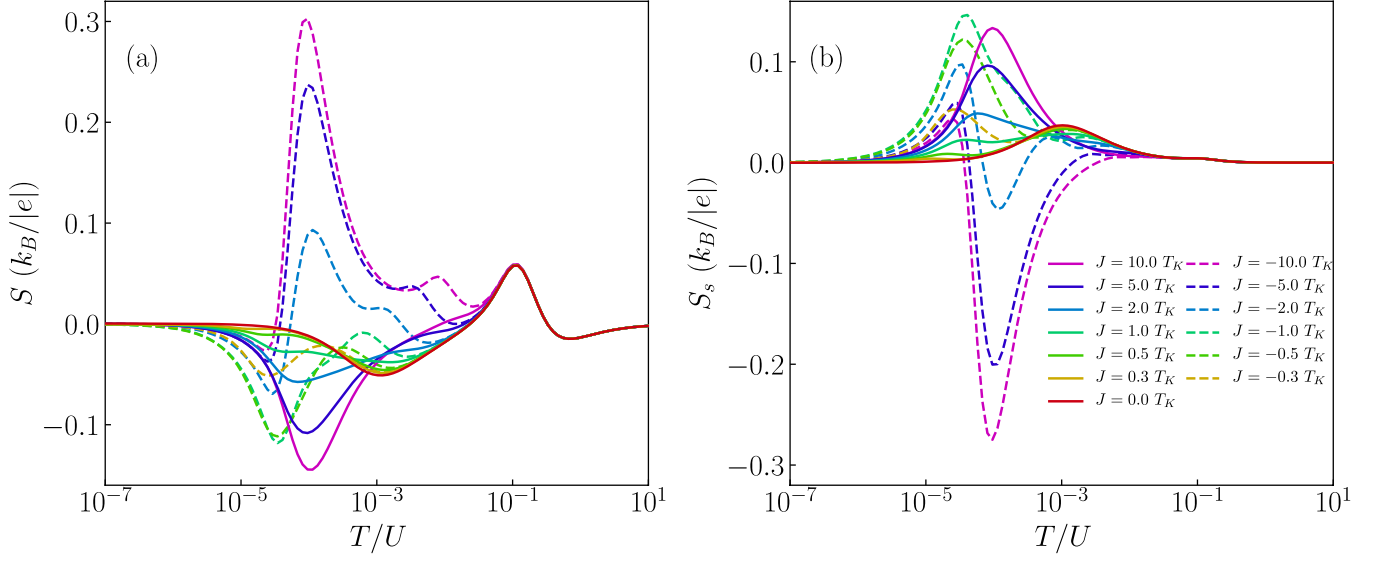


Figure 9. Spin thermopower for different values of exchange interaction. (a) The Seebeck and (b) spin Seebeck effect as a function of temperature for different values of exchange interaction J , as indicated. The parameters are the same as in Fig. 5 with $\varepsilon = -0.48U$.

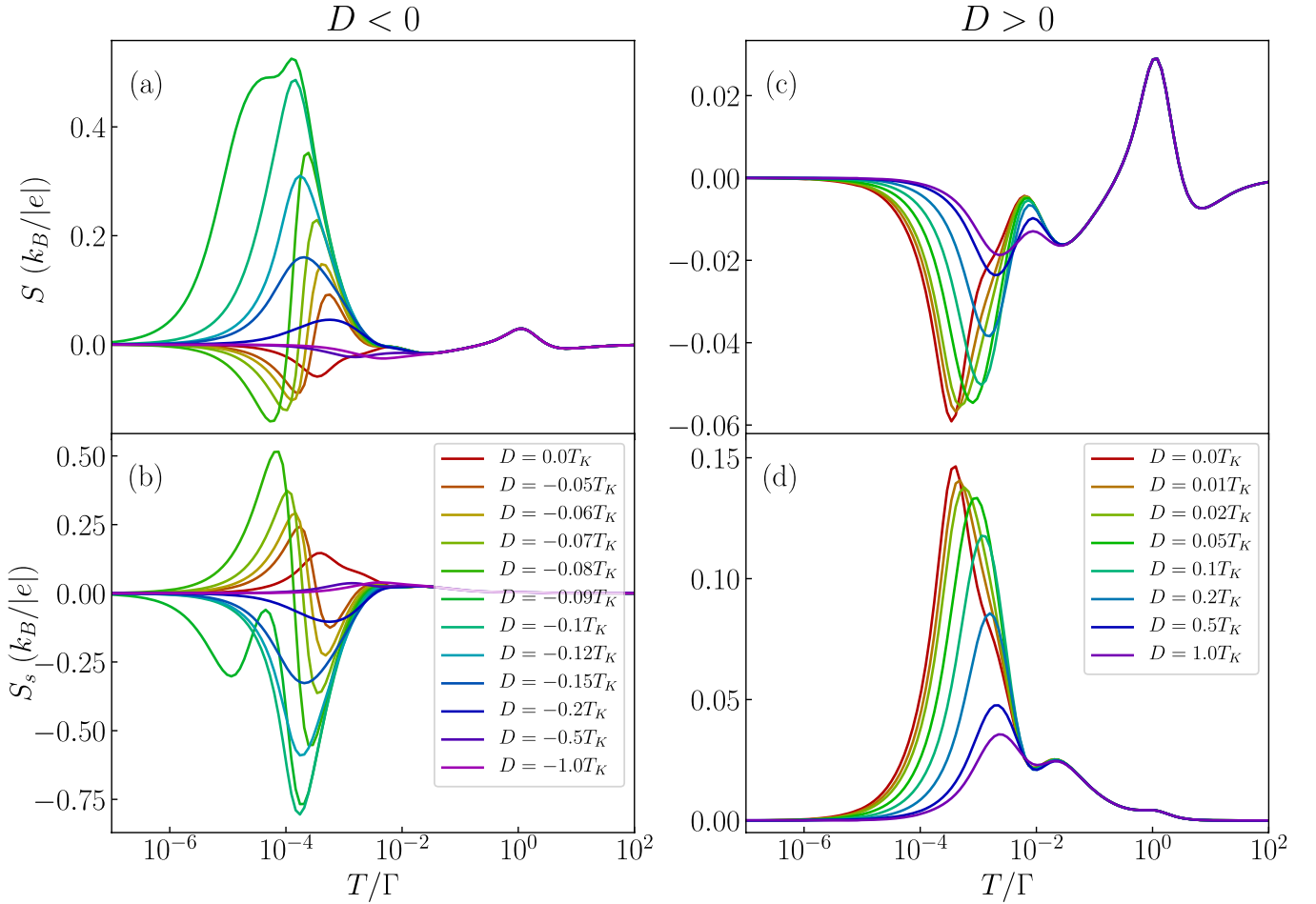


Figure 10. Spin thermopower for different values of magnetic anisotropy. The temperature dependence of (a,c) the thermopower and (b,d) the spin thermopower in the case of antiferromagnetic exchange interaction $J = -T_K$ for selected values of magnetic anisotropy D . The left (right) column presents the case of easy-plane (easy-axis) type of magnetic anisotropy. The parameters are the same as in Fig. 9.

Seebeck (Seebeck) effect, is formed. On the other hand, for $T \gtrsim \Delta\varepsilon_{\text{exch}}$ an additional maximum (minimum)

develops for S (S_S), see the left column of Fig. 10. Further increase in the magnitude of anisotropy D suppresses the local extrema in the thermopower, as seen in the case of no spin accumulation. Consequently, one observes a strong nonmonotonic dependence of the (spin) Seebeck effect on the value of the easy-plane anisotropy. Large values of S and S_S develop for such intrinsic parameters of the molecule that the temperature dependence of G is most spectacular, i.e. when the Kondo effect starts being restored with increasing $|D|$. However, once a plateau in G is formed at low temperatures due to the Kondo effect, which happens for considerable values of $D < 0$, the thermopower becomes suppressed, see Fig. 10.

Discussion

We have determined the thermoelectric properties of large-spin magnetic molecules attached to both nonmagnetic and ferromagnetic electrodes. Our analysis was focused on the strong correlation regime where the Kondo effect can emerge. To accurately address the system's behavior in this nonperturbative regime, we have employed the numerical renormalization group method, which allowed us to study the electrical and heat conductances, the Seebeck effect and the figure of merit in the full parameter space of considered molecular junction. In particular, we have considered the cases of both ferromagnetic and antiferromagnetic exchange interaction J between the orbital level of the molecule and its magnetic core. Moreover, we have also analyzed the effect of finite magnetic anisotropy of the molecule.

In the case of nonmagnetic contacts, we have shown that the behavior of the Seebeck effect strongly depends on the type of exchange interaction J . In the case of ferromagnetic exchange, we have shown that the Seebeck coefficient displays features qualitatively similar to the case of $J = 0$ (quantum dot case). However, due to a reduced Kondo temperature, the sign change in S occurs at a lower temperature and the thermopower was found to retain finite values extending to much lower T compared to the quantum dot case. Interestingly, in the case of antiferromagnetic exchange interaction, we have found a new sign change of the thermopower, at energy scale corresponding to the exchange interaction between the orbital level and molecule's core spin. Moreover, we have also determined the influence of finite magnetic anisotropy on the thermoelectric properties of magnetic molecule. Finite magnetic anisotropy gives rise to new qualitative features especially in the case of antiferromagnetic J , where a new sign change of thermopower occurs in the case of easy-plane magnetic anisotropy.

On the other hand, when the leads are ferromagnetic, depending on the spin relaxation time, spin accumulation may be generated in the contacts giving rise to the spin Seebeck effect. First, we have focused on the impact of the spin-resolved tunneling on the thermopower in the absence of spin accumulation. We have shown that in the case of ferromagnetic exchange interaction there is an additional sign change in the temperature dependence of the thermopower. On the other hand, the low-temperature Seebeck effect has been found to strongly depend on the position of the molecule's orbital level, which conditioned the strength of the exchange field in the molecule. Generally, the Seebeck effect becomes quenched once the temperature gets smaller than the corresponding exchange field.

Finally, we have assumed that the spin relaxation time in the leads is long, so that a spin bias can be generated in the system, resulting in the spin Seebeck effect. We have shown that for relatively low values of molecule's exchange interaction the spin Seebeck effect changes sign only when tuning the orbital level across the particle-hole symmetry point. This is associated with the fact, that the sign of the spin thermopower is conditioned by the sign of the exchange field, which changes only when crossing $\varepsilon = -U/2$. However, if the molecule's antiferromagnetic exchange interaction becomes larger than the Kondo temperature, the temperature dependence of the spin Seebeck effect can exhibit a sign change. This feature is associated with the interplay of exchange field, antiferromagnetic interaction between the orbital level and molecule's core spin and the Kondo correlations. A similarly nontrivial behavior have been observed in the case of finite easy-plane magnetic anisotropy. We have found that the spin Seebeck effect exhibits then a nonmonotonic dependence on the magnitude of anisotropy. This effect is related to a revival of the Kondo effect when the anisotropy becomes large enough to bring about the two-fold degenerate ground state of the molecule, i.e. when the easy-plane anisotropy wins over both the exchange field as well as the molecule's antiferromagnetic exchange interaction.

As far as the experimental progress is concerned, the field of molecular spin caloritronics is rather at its initial stage of development. The model studied here can however also describe quantum dots or impurities coupled to a large spin. It is therefore worth mentioning that, recently, there have been successful measurements of thermopower of Kondo-correlated quantum dots^{10,25,26}. Moreover, spin-resolved electronic transport properties of molecular junctions have already been extensively studied^{60,63-65}. Therefore, it seems that all the necessary ingredients are at hand and, with the state-of-the-art apparatus, it should be possible to explore the effects presented in this paper. We do hope that our work will foster further experimental efforts in this direction.

Methods. The thermoelectric properties of the system in the linear response regime can be characterized by the Onsager integrals, $L_{n\sigma}$, which depend on the spin-resolved transmission coefficient $\mathcal{T}_\sigma(\omega)$. The transmission coefficient $\mathcal{T}_\sigma(\omega)$ can be related to the spin-dependent spectral function $A_\sigma(\omega)$ using the relation

$$\mathcal{T}_\sigma(\omega) = \frac{4\Gamma_{L\sigma}\Gamma_{R\sigma}}{\Gamma_{L\sigma} + \Gamma_{R\sigma}}\pi A_\sigma(\omega), \quad (10)$$

where $A_\sigma(\omega) = -\text{Im}[G_\sigma^R(\omega)]/\pi$ and $G_\sigma^R(\omega)$ is the Fourier transform of the retarded Green's function of the molecule's orbital level, $G_\sigma^R(t) = -i\theta(t)\langle\{a_\sigma(t), a_\sigma^\dagger(0)\}\rangle$. The main task is thus to accurately determine the spectral function of the system. One of the most powerful methods in this regard is the Wilson's numerical renormalization group method^{50,51,66,67}, which allows for nonperturbative treatment of all correlations in the system. In this method one performs a discretization of the conduction band with discretization parameter Λ and, consecutively,

a tridiagonalization of the Hamiltonian describing such discretized system is performed. Eventually, one obtains the following NRG Hamiltonian⁵⁰

$$\hat{H}_{\text{NRG}} = \hat{H}_{\text{mol}} + \sum_{\sigma} \sqrt{\frac{2W\Gamma_{\sigma}}{\pi}} \left(\hat{d}_{\sigma}^{\dagger} \hat{f}_{0\sigma} + \hat{f}_{0\sigma}^{\dagger} \hat{d}_{\sigma} \right) + \sum_{\sigma} \sum_{n=0} \xi_n \left(\hat{f}_{n\sigma}^{\dagger} \hat{f}_{n+1\sigma} + \hat{f}_{n+1\sigma}^{\dagger} \hat{f}_{n\sigma} \right), \quad (11)$$

in which the molecule is coupled to the first site of the tight-binding chain with exponentially decaying hoppings ξ_n . Here, $\hat{f}_{n\sigma}^{\dagger}$ creates a spin- σ electron at the Wilson site n and W denotes the band halfwidth, which is used as energy unit $W \equiv 1$. This Hamiltonian is then solved in an iterative fashion by retaining a fixed number of states N_K . While the kept states are used to construct the statespace for the next iteration, the states that are discarded during calculation play a vital role in the problem as these states are used to construct the complete many-body basis of the full NRG Hamiltonian⁶⁸. The discarded states are then used for the calculation of quantities of interest with the aid of the full density matrix⁶⁹. In our calculations we have exploited the Abelian symmetries for the system's spin z th component and charge. We have used $\Lambda = 2$ and kept at least $N_K = 2000$ states in the iteration. Moreover, we have determined the Onsager transport coefficients from the raw NRG data without the need of broadening the Dirac delta peaks³⁶.

Received: 3 February 2021; Accepted: 9 April 2021

Published online: 28 April 2021

References

1. Giazotto, F., Heikkilä, T. T., Luukanen, A., Savin, A. M. & Pekola, J. P. Opportunities for mesoscopics in thermometry and refrigeration: Physics and applications. *Rev. Mod. Phys.* **78**, 217–274 (2006).
2. Szczech, J. R., Higgins, J. M. & Jin, S. Enhancement of the thermoelectric properties in nanoscale and nanostructured materials. *J. Mater. Chem.* **21**, 4037–4055 (2011).
3. Heremans, J. P., Dresselhaus, M. S., Bell, L. E. & Morelli, D. T. When thermoelectrics reached the nanoscale. *Nat. Nanotechnol.* **8**, 471–473 (2013).
4. Sánchez, D. & Linke, H. Focus on thermoelectric effects in nanostructures. *New J. Phys.* **16**, 110201 (2014).
5. Benenti, G., Casati, G., Saito, K. & Whitney, R. S. Fundamental aspects of steady-state conversion of heat to work at the nanoscale. *Phys. Rep.* **694**, 1–124 (2017).
6. Hicks, L. D. & Dresselhaus, M. S. Effect of quantum-well structures on the thermoelectric figure of merit. *Phys. Rev. B* **47**, 12727–12731 (1993).
7. Hicks, L. D. & Dresselhaus, M. S. Thermoelectric figure of merit of a one-dimensional conductor. *Phys. Rev. B* **47**, 16631–16634(R) (1993).
8. Mahan, G. D. & Sofo, J. O. The best thermoelectric. *Proc. Natl. Acad. Sci. U.S.A.* **93**, 7436–7439 (1996).
9. Beenakker, C. W. J. & Staring, A. A. M. Theory of the thermopower of a quantum dot. *Phys. Rev. B* **46**, 9667–9676 (1992).
10. Scheibner, R., Buhmann, H., Reuter, D., Kiselev, M. N. & Molenkamp, L. W. Thermopower of a Kondo spin-correlated quantum dot. *Phys. Rev. Lett.* **95**, 176602 (2005).
11. Reddy, P., Jang, S.-Y., Segalman, R. A. & Majumdar, A. Thermoelectricity in molecular junctions. *Science* **315**, 1568–1571 (2007).
12. Dubi, Y. & Di Ventra, M. Colloquium: Heat flow and thermoelectricity in atomic and molecular junctions. *Rev. Mod. Phys.* **83**, 131–155 (2011).
13. Trocha, P. & Barnaś, J. Large enhancement of thermoelectric effects in a double quantum dot system due to interference and Coulomb correlation phenomena. *Phys. Rev. B* **85**, 085408 (2012).
14. Thierschmann, H., Sánchez, R., Sothmann, B., Buhmann, H. & Molenkamp, L. W. Thermoelectrics with Coulomb-coupled quantum dots. *C. R. Phys.* **17**, 1109–1122 (2016).
15. Jaliel, G. *et al.* Experimental realization of a quantum dot energy harvester. *Phys. Rev. Lett.* **123**, 117701 (2019).
16. Kleeorin, Y. *et al.* How to measure the entropy of a mesoscopic system via thermoelectric transport. *Nat. Commun.* **10**, 1–8 (2019).
17. Kondo, J. Resistance minimum in dilute magnetic alloys. *Prog. Theor. Phys.* **32**, 37 (1964).
18. Hewson, A. C. *The Kondo Problem to Heavy Fermions* (Cambridge University Press, 1997).
19. Goldhaber-Gordon, D. *et al.* The Kondo effect in a single-electron transistor. *Nature (London)* **391**, 156–159 (1998).
20. Cronenwett, S., Oosterkamp, T. & Kouwenhoven, L. A tunable Kondo effect in quantum dots. *Science* **281**, 540 (1998).
21. Costi, T. A. & Zlatić, V. Thermoelectric transport through strongly correlated quantum dots. *Phys. Rev. B* **81**, 235127 (2010).
22. Tooski, S. B., Ramšak, A., Buřka, B. R. & Žitko, R. Effect of assisted hopping on thermopower in an interacting quantum dot. *New J. Phys.* **16**, 055001 (2014).
23. Wójcik, K. P. & Weymann, I. Thermopower of strongly correlated T-shaped double quantum dots. *Phys. Rev. B* **93**, 085428 (2016).
24. Nguyen, T. K. T. & Kiselev, M. N. Thermoelectric transport in a three-channel charge Kondo circuit. *Phys. Rev. Lett.* **125**, 026801 (2020).
25. Svilans, A. *et al.* Thermoelectric characterization of the Kondo resonance in nanowire quantum dots. *Phys. Rev. Lett.* **121**, 206801 (2018).
26. Dutta, B. *et al.* Direct probe of the Seebeck coefficient in a Kondo-correlated single-quantum-dot transistor. *Nano Lett.* **19**, 506–511 (2019).
27. Uchida, K. *et al.* Observation of the spin Seebeck effect. *Nature* **455**, 778–781 (2008).
28. Johnson, M. Spin caloritronics and the thermomagnetolectric system. *Solid State Commun.* **150**, 543–547 (2010).
29. Bauer, G. E. W., Saitoh, E. & van Wees, B. J. Spin caloritronics. *Nat. Mater.* **11**, 391–399 (2012).
30. Yu, H., Brechet, S. D. & Ansermet, J.-P. Spin caloritronics, origin and outlook. *Phys. Lett. A* **381**, 825–837 (2017).
31. Back, C. H., Bauer, G. E. W. & Zink, B. L. Special issue on spin caloritronics. *J. Phys. D Appl. Phys.* **52**, 230301 (2019).
32. Uchida, K.-I. Transport phenomena in spin caloritronics. *Proc. Jpn. Acad. Ser. B* **97**, 69–88 (2021).
33. Krawiec, M. & Wysokiński, K. I. Thermoelectric effects in strongly interacting quantum dot coupled to ferromagnetic leads. *Phys. Rev. B* **73**, 075307 (2006).
34. Dubi, Y. & Di Ventra, M. Thermospin effects in a quantum dot connected to ferromagnetic leads. *Phys. Rev. B* **79**, 081302 (2009).
35. Świrkowicz, R., Wierzbicki, M. & Barnaś, J. Thermoelectric effects in transport through quantum dots attached to ferromagnetic leads with noncollinear magnetic moments. *Phys. Rev. B* **80**, 195409 (2009).
36. Weymann, I. & Barnaś, J. Spin thermoelectric effects in Kondo quantum dots coupled to ferromagnetic leads. *Phys. Rev. B* **88**, 085313 (2013).
37. Weymann, I. Boosting spin-caloritronic effects by attractive correlations in molecular junctions. *Sci. Rep.* **6**, 1–10 (2016).
38. Rejec, T., Žitko, R., Mravlje, J. & Ramšak, A. Spin thermopower in interacting quantum dots. *Phys. Rev. B* **85**, 085117 (2012).

39. Costi, T. A. Magnetic field dependence of the thermopower of Kondo-correlated quantum dots: Comparison with experiment. *Phys. Rev. B* **100**, 155126 (2019).
40. Costi, T. A. Magnetic field dependence of the thermopower of Kondo-correlated quantum dots. *Phys. Rev. B* **100**, 161106 (2019).
41. Koch, J., von Oppen, F., Oreg, Y. & Sela, E. Thermopower of single-molecule devices. *Phys. Rev. B* **70**, 195107 (2004).
42. Wang, R.-Q., Sheng, L., Shen, R., Wang, B. & Xing, D. Y. Thermoelectric effect in single-molecule-magnet junctions. *Phys. Rev. Lett.* **105**, 057202 (2010).
43. Misiorny, M. & Barnaś, J. Spin-dependent thermoelectric effects in transport through a nanoscopic junction involving a spin impurity. *Phys. Rev. B* **89**, 235438 (2014).
44. Misiorny, M. & Barnaś, J. Effect of magnetic anisotropy on spin-dependent thermoelectric effects in nanoscopic systems. *Phys. Rev. B* **91**, 155426 (2015).
45. Niu, P., Liu, L., Su, X., Dong, L. & Luo, H.-G. Spin current generator in a single molecular magnet with spin bias. *J. Magn. Magn. Mater.* **465**, 9–13 (2018).
46. Hammar, H., Vasquez Jaramillo, J. D. & Fransson, J. Spin-dependent heat signatures of single-molecule spin dynamics. *Phys. Rev. B* **99**, 115416 (2019).
47. Gatteschi, D., Caneschi, A., Pardi, L. & Sessoli, R. Large clusters of metal ions: The transition from molecular to bulk magnets. *Science* **265**, 1054 (1994).
48. Gatteschi, D., Sessoli, R. & Villain, J. *Molecular Nanomagnets* (Oxford University Press, 2006).
49. Gatteschi, D. & Sessoli, R. Quantum tunneling of magnetization and related phenomena in molecular materials. *Angew. Chem. Int. Ed.* **42**, 268–297 (2003).
50. Wilson, K. G. The renormalization group: Critical phenomena and the Kondo problem. *Rev. Mod. Phys.* **47**, 773–839 (1975).
51. Bulla, R., Costi, T. & Pruschke, T. Numerical renormalization group method for quantum impurity systems. *Rev. Mod. Phys.* **80**, 395–450 (2008).
52. Elste, F. & Timm, C. Transport through anisotropic magnetic molecules with partially ferromagnetic leads: Spin-charge conversion and negative differential conductance. *Phys. Rev. B* **73**, 235305 (2006).
53. Timm, C. & Elste, F. Spin amplification, reading, and writing in transport through anisotropic magnetic molecules. *Phys. Rev. B* **73**, 235304 (2006).
54. Misiorny, M., Weymann, I. & Barnaś, J. Interplay of the Kondo effect and spin-polarized transport in magnetic molecules, adatoms, and quantum dots. *Phys. Rev. Lett.* **106**, 126602 (2011).
55. Onsager, L. Reciprocal relations in irreversible processes. II. *Phys. Rev.* **38**, 2265 (1931).
56. Misiorny, M., Weymann, I. & Barnaś, J. Temperature dependence of electronic transport through molecular magnets in the Kondo regime. *Phys. Rev. B* **86**, 035417 (2012).
57. Wójcik, K. P. & Weymann, I. Two-stage Kondo effect in t-shaped double quantum dots with ferromagnetic leads. *Phys. Rev. B* **91**, 134422 (2015).
58. Sahoo, S. *et al.* Electric field control of spin transport. *Nat. Phys.* **1**, 99–102 (2005).
59. Merchant, C. & Marković, N. Electrically tunable spin polarization in a carbon nanotube spin diode. *Phys. Rev. Lett.* **100**, 156601 (2008).
60. Gaass, M. *et al.* Universality of the Kondo effect in quantum dots with ferromagnetic leads. *Phys. Rev. Lett.* **107**, 176808 (2011).
61. Martinek, J. *et al.* Kondo effect in quantum dots coupled to ferromagnetic leads. *Phys. Rev. Lett.* **91**, 127203 (2003).
62. Misiorny, M., Weymann, I. & Barnaś, J. Influence of magnetic anisotropy on the Kondo effect and spin-polarized transport through magnetic molecules, adatoms, and quantum dots. *Phys. Rev. B* **84**, 035445 (2011).
63. Pasupathy, A. *et al.* The Kondo effect in the presence of ferromagnetism. *Science* **306**, 86–89 (2004).
64. Hauptmann, J., Paaske, J. & Lindelof, P. Electric-field-controlled spin reversal in a quantum dot with ferromagnetic contacts. *Nat. Phys.* **4**, 373–376 (2008).
65. Bordoloi, A., Zannier, V., Sorba, L., Schönenberger, C. & Baumgartner, A. A double quantum dot spin valve. *Commun. Phys.* **3**, 135 (2020).
66. Legeza, O., Moca, C. P., Toth, A. I., Weymann, I. & Zarand, G. Manual for the Flexible DM-NRG code, [arXiv:0809.3143](https://arxiv.org/abs/0809.3143). <http://www.phy.bme.hu/~dmnrg/> (2008).
67. Tóth, A. I., Moca, C. P., Legeza, Ö. & Zarand, G. Density matrix numerical renormalization group for non-Abelian symmetries. *Phys. Rev. B* **78**, 245109 (2008).
68. Anders, F. & Schiller, A. Real-time dynamics in quantum-impurity systems: A time-dependent Numerical Renormalization-Group approach. *Phys. Rev. Lett.* **95**, 196801. <https://doi.org/10.1103/PhysRevLett.95.196801> (2005).
69. Weichselbaum, A. & von Delft, J. Sum-rule conserving spectral functions from the numerical renormalization group. *Phys. Rev. Lett.* **99**, 76402 (2007).

Acknowledgements

This work was supported by the National Science Centre in Poland through the Project No. 2017/27/B/ST3/00621.

Author contributions

A.M. performed the calculations and prepared the figures. Both authors contributed to the manuscript preparation and results interpretation. I.W. coordinated the whole project.

Competing interests

The authors declare no competing interests.

Additional information

Correspondence and requests for materials should be addressed to A.M.

Reprints and permissions information is available at www.nature.com/reprints.

Publisher's note Springer Nature remains neutral with regard to jurisdictional claims in published maps and institutional affiliations.



Open Access This article is licensed under a Creative Commons Attribution 4.0 International License, which permits use, sharing, adaptation, distribution and reproduction in any medium or format, as long as you give appropriate credit to the original author(s) and the source, provide a link to the Creative Commons licence, and indicate if changes were made. The images or other third party material in this article are included in the article's Creative Commons licence, unless indicated otherwise in a credit line to the material. If material is not included in the article's Creative Commons licence and your intended use is not permitted by statutory regulation or exceeds the permitted use, you will need to obtain permission directly from the copyright holder. To view a copy of this licence, visit <http://creativecommons.org/licenses/by/4.0/>.

© The Author(s) 2021





Chapter 8

Nonequilibrium steady-state transport: Kondo correlations from both leads

8.1 Nonequilibrium spintronic transport through Kondo impurities

[B]

Nonequilibrium spintronic transport through Kondo impurities

Anand Manaparambil ^{1,*} Andreas Weichselbaum ² Jan von Delft ³ and Ireneusz Weymann ¹¹*Institute of Spintronics and Quantum Information, Faculty of Physics, Adam Mickiewicz University, Uniwersytetu Poznańskiego 2, 61-614 Poznań, Poland*²*Department of Condensed Matter Physics and Materials Science, Brookhaven National Laboratory, Upton, New York 11973-5000, USA*³*Arnold Sommerfeld Center for Theoretical Physics, Center for NanoScience, and Munich Center for Quantum Science and Technology, Ludwig-Maximilians-Universität München, 80333 Munich, Germany*

(Received 17 June 2022; revised 16 August 2022; accepted 17 August 2022; published 14 September 2022)

In this work we analyze the nonequilibrium transport through a quantum impurity (quantum dot or molecule) attached to ferromagnetic leads by using a hybrid numerical renormalization group–time-dependent density matrix renormalization group thermofield quench approach. For this, we study the bias dependence of the differential conductance through the system, which shows a finite zero-bias peak, characteristic of the Kondo resonance and reminiscent of the equilibrium local density of states. In the nonequilibrium settings, the resonance in the differential conductance is also found to decrease with increasing the lead spin polarization. The latter induces an effective exchange field that lifts the spin degeneracy of the dot level. Therefore, as we demonstrate, the Kondo resonance can be restored by counteracting the exchange field with a finite external magnetic field applied to the system. Finally, we investigate the influence of temperature on the nonequilibrium conductance, focusing on the split Kondo resonance. Our work thus provides an accurate quantitative description of the spin-resolved transport properties relevant for quantum dots and molecules embedded in magnetic tunnel junctions.

DOI: [10.1103/PhysRevB.106.125413](https://doi.org/10.1103/PhysRevB.106.125413)

I. INTRODUCTION

Charge and spin transport through nanostructures such as nanowires, quantum dots, and molecules have been under rigorous experimental and theoretical research worldwide. These studies are motivated primarily by the possible applications in spintronics, nanoelectronics, and spin caloritronics, as well as fascinating physics emerging at the nanoscale [1–4]. In particular, the high research interest in transport through artificial quantum impurity systems stems from the observation of the Kondo effect, a many-body phenomenon, in which the spin of a quantum impurity becomes screened by conduction electrons of attached electrodes [5–7]. Many studies, both experimental and theoretical ones, focused on providing a deep understanding of the interplay between the Kondo physics and other many-body phenomena, such as ferromagnetism [8,9] and superconductivity [10,11], have been carried out. In this regard, especially interesting in the context of spin nanoelectronics are quantum dots or molecules attached to ferromagnetic electrodes [12,13]. Besides the fact that such nanostructures allow for implementing devices with highly spin-resolved properties, they enable the exploration of the interplay between the itinerant ferromagnetism and the strong electron correlations [9,14–16]. In fact, the spintronic transport properties of ferromagnetic quantum impurity systems have been the subject of extensive investigations [8,9,14–

25]; however, their accurate quantitative description in truly nonequilibrium settings still poses a formidable challenge.

Reliable equilibrium and linear-response studies of transport through quantum impurity systems have been made possible by a robust nonperturbative numerical renormalization group (NRG) method [26,27]. Unfortunately, this method falls short when describing the nonequilibrium behavior. On the other hand, although nonequilibrium situations can be studied by various analytical methods, their main drawback is an approximate treatment of electron correlations. It is important to note that these disadvantages have been overcome by the time-dependent density matrix renormalization group (tDMRG) method [28], which, however, has the drawback that it can reliably study the system's behavior only for timescales of the order of $1/D$, where D is the half bandwidth of the conduction band. A reliable quantum quench approach to study the transport through quantum impurity systems out of equilibrium was recently proposed by Schwarz *et al.* [29]. This approach combines both the NRG and tDMRG methods and, in addition, makes use of the thermofield treatment [30] to efficiently describe the system.

In this paper, by employing the hybrid NRG-tDMRG thermofield quench approach [29], we provide an accurate theoretical investigation of the nonequilibrium transport through a quantum impurity interacting with ferromagnetic leads. In particular, we study the bias voltage dependence of the differential conductance, which exhibits a zero-bias peak, a characteristic feature of the Kondo effect, when the system is tuned to the particle-hole symmetry point. We show that the Kondo energy scale in the applied bias potential decreases

*anaman@amu.edu.pl

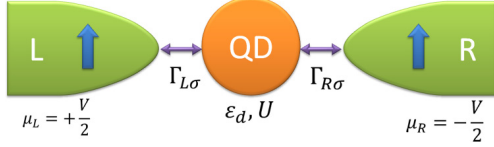


FIG. 1. Model system. A magnetic impurity (quantum dot or molecule), characterized by an orbital level of energy ε_d and Coulomb correlations U , is attached to two ferromagnetic contacts with spin-dependent coupling strengths $\Gamma_{L\sigma}$ and $\Gamma_{R\sigma}$, respectively. These leads are locally in equilibrium at a global temperature T , but with a voltage bias $V = \mu_L - \mu_R$ that is applied symmetrically across them.

with increasing the lead spin polarization. On the other hand, when we detune the system away from this symmetry point, we observe a splitting of the zero-bias peak for finite lead spin polarization, which can be attributed to the emergence of a local exchange field in the impurity. Furthermore, we study the behavior of this split Kondo peak under external parameters, such as applied magnetic field or temperature. We show that a particular value of the magnetic field can lead to the restoration of the Kondo resonance in the system. Moreover, we determine the temperature dependence of the differential conductance at the bias voltage corresponding to the split Kondo peak.

This paper is organized as follows. In Sec. II we describe the model and method used in calculations. The main results and their discussion are presented in Sec. III, where we first analyze the differential conductance at the particle-hole symmetry point and then study the effect of the finite exchange field on the transport behavior. We also examine the possibility to restore the Kondo effect using magnetic field and determine the temperature dependence. Finally, this paper is summarized in Sec. IV.

II. MODEL AND METHOD

The considered system consists of a quantum impurity (quantum dot or a molecule) attached to two ferromagnetic leads with spin-dependent couplings, subject to a voltage bias, as shown schematically in Fig. 1. More specifically, such a system can be described by a single-impurity Anderson model [31], in which the quantum impurity is modeled as

$$H_{\text{imp}} = \sum_{\sigma} \varepsilon_{d\sigma} n_{\sigma} + U n_{\uparrow} n_{\downarrow}, \quad (1)$$

where $n_{\sigma} = d_{\sigma}^{\dagger} d_{\sigma}$, where d_{σ}^{\dagger} creates an electron with spin $\sigma \in \{\uparrow, \downarrow\} \equiv \{+1, -1\}$ at the impurity; $\varepsilon_{d\sigma} \equiv \varepsilon_d - \frac{\sigma}{2} B$ denotes the energy of an impurity energy level, with B being the external magnetic field in units of $g\mu_B \equiv 1$; and U is the Coulomb repulsion experienced when the level is doubly occupied.

The leads attached to the impurity are assumed to be ferromagnetic metals and are characterized by the Fermi functions, $f_{\alpha}(\omega) = [e^{(\omega - \mu_{\alpha})/T} + 1]^{-1}$ (using units of $\hbar = k_B = e = 1$ throughout), where the index α refers to the leads, $\alpha \in \{L, R\} \equiv \{-1, +1\}$, and $\mu_{\alpha} = \alpha V/2$. The lead Hamiltonian

reads as follows:

$$H_{\text{lead}} = \sum_{\alpha k \sigma} \varepsilon_{\alpha k \sigma} c_{\alpha k \sigma}^{\dagger} c_{\alpha k \sigma}, \quad (2)$$

with $c_{\alpha k \sigma}^{\dagger}$ creating an electron in lead α with energy $\varepsilon_{\alpha k \sigma}$, momentum k , and spin σ . The quantum impurity is coupled to the leads according to the Hamiltonian H_{hyb} ,

$$H_{\text{hyb}} = \sum_{\alpha k \sigma} (v_{\alpha k \sigma} d_{\sigma}^{\dagger} c_{\alpha k \sigma} + \text{H.c.}). \quad (3)$$

The electronic transition between each lead mode $c_{\alpha k \sigma}$ and the impurity spin state σ is specified by the tunnel matrix elements $v_{\alpha k \sigma}$. This coupling between the lead and impurity induces an impurity-lead hybridization in the system, expressed by the hybridization function $\Gamma_{\alpha\sigma}(\omega) = \pi \sum_k |v_{\alpha k \sigma}|^2 \delta(\omega - \varepsilon_{\alpha k \sigma})$. Finally, the total Hamiltonian of the system reads

$$H_{\text{tot}} = H_{\text{imp}} + H_{\text{lead}} + H_{\text{hyb}}. \quad (4)$$

In this work we assume a constant hybridization function over the entire bandwidth $2D$ (we use $D := 1$ as the unit of energy throughout, unless specified otherwise). The hybridization function can thus be written as $\Gamma_{\alpha\sigma}(\omega) = \Gamma_{\alpha\sigma} \vartheta(D - |\omega|)$, with $\vartheta(\cdot)$ being the Heaviside step function and constant $\Gamma_{\alpha\sigma} = \pi \rho_{\alpha\sigma} |v_{\alpha\sigma}|^2$, where $\rho_{\alpha\sigma}$ is the spin-dependent density of states of lead α . Assuming that $v_{\alpha\sigma} \equiv v$ is independent of the spin or lead, it is then convenient to introduce the spin polarization p_{α} of the ferromagnetic contact α ,

$$p_{\alpha} = \frac{\rho_{\alpha\uparrow} - \rho_{\alpha\downarrow}}{\rho_{\alpha\uparrow} + \rho_{\alpha\downarrow}}. \quad (5)$$

The coupling strength can then be written as $\Gamma_{\alpha\sigma} = (1 + \sigma p_{\alpha}) \Gamma_{\alpha}$, with $\Gamma_{\alpha} = (\Gamma_{\alpha\uparrow} + \Gamma_{\alpha\downarrow})/2$. The total coupling strength for spin σ is given by $\Gamma_{\sigma} = \Gamma_{L\sigma} + \Gamma_{R\sigma}$. In the following we assume that the system is left-right symmetric, i.e., $\Gamma_L = \Gamma_R \equiv \Gamma/2$ and $p_L = p_R \equiv p$. Consequently, the computed electrical current through the impurity is independent of the sign of the applied bias voltage V , and therefore, it suffices to analyze $V \geq 0$.

The impurity parameters are fixed to

$$U = 0.012, \quad \Gamma = 0.001 \quad (6)$$

throughout this paper to ensure a well-defined Kondo regime well isolated from the finite bandwidth, with the impurity level position ε_d varied from particle-hole symmetric ($\varepsilon_d = -U/2$) to asymmetric ($\varepsilon_d = -U/3$).

We use a hybrid NRG-tDMRG thermofield quench method [29] to study the nonequilibrium behavior of the system. This initializes the leads in thermal equilibrium at their respective chemical potentials before they get dynamically coupled when smoothly turning on the coupling to the impurity. This method can treat the correlations exactly while sustaining the nonequilibrium conditions of a fixed chemical potential difference and fixed temperature in the leads. We define a transport window (TW) using the Fermi functions of the leads [$f_L(\omega) \neq f_R(\omega)$]. The energies outside the TW are assumed to be in equilibrium and are discretized logarithmically according to the logarithmic discretization parameter Λ , and energies inside the TW are assumed to be out of equilibrium and discretized linearly according to the linear discretization parameter δ .

A thermofield treatment is performed on the discrete energy levels which maps the system to a particle-hole representation. Moreover, in this particle-hole picture, the tunnel matrix elements turn out to be functions of the bias voltage V , thus containing information about the nonequilibrium settings. The particle and hole modes in the leads are recombined separately, leaving the impurity coupled with one set of effective particle modes and one set of effective hole modes. Then, NRG is applied to the logarithmically discretized part of the system, resulting in a renormalized impurity (RI), which is coupled to the linearly discretized part of the hole and particle chain. We represent the RI in the matrix product state (MPS) framework as one site of the MPS chain coupled to completely filled particle and completely empty hole modes in the linearly discretized sector. The system is then time evolved using a second-order Trotter time evolution, where the coupling between the RI and the lead modes is switched on over a finite time window. Further details of the method are presented in the Appendix.

III. RESULTS AND DISCUSSION

In the case of quantum dots or molecules attached to ferromagnetic contacts the transport properties are strongly dependent on the spin-resolved charge fluctuations between the impurity and ferromagnets. These fluctuations give rise to the level renormalization $\delta\varepsilon_\sigma$. Because, for $p > 0$, $\delta\varepsilon_\uparrow \neq \delta\varepsilon_\downarrow$, a spin splitting of the impurity level can be generated, $\Delta\varepsilon_{\text{exch}} \equiv \delta\varepsilon_\uparrow - \delta\varepsilon_\downarrow$, referred to as a ferromagnetic-contacted induced exchange field. Here the exchange field is defined such that $\Delta\varepsilon_{\text{exch}} > 0$ tends towards a *negative* impurity magnetization, which in terms of sign is contrary to the definition of B in Eq. (1). Hence, the effective total magnetic field experienced by the impurity is given by

$$B_{\text{tot}}^{\text{eff}} \simeq B - \Delta\varepsilon_{\text{exch}}. \quad (7)$$

The exchange field in the local moment regime can be estimated within the second-order perturbation theory, and it is given by [8]

$$\Delta\varepsilon_{\text{exch}}^p = \frac{2p\Gamma}{\pi} \text{Re}[\phi(\varepsilon_d) - \phi(\varepsilon_d + U)], \quad (8)$$

where $\phi(\varepsilon) = \Psi(\frac{1}{2} + \frac{i\varepsilon}{2\pi T})$, with $\Psi(z)$ being the digamma function. At $T = 0$, the formula for the exchange field simply becomes

$$\Delta\varepsilon_{\text{exch}}^p = p \underbrace{\frac{2\Gamma}{\pi} \ln \left| \frac{\varepsilon_d}{\varepsilon_d + U} \right|}_{\equiv \gamma(\Gamma, \frac{\varepsilon_d}{U})}. \quad (9)$$

The most important property of $\Delta\varepsilon_{\text{exch}}$ is its tunability with changing the position of the orbital level. As follows from the above formula, $\Delta\varepsilon_{\text{exch}}$ changes sign when crossing the particle-hole (p-h) symmetry point, $\varepsilon_d = -U/2$, at which it vanishes.

We begin our analysis with the study of the influence of the lead polarization on the nonequilibrium conductance of the system when the impurity energy level is tuned to $\varepsilon_d = -U/2$. We then proceed to examine the case when the system is detuned from the p-h symmetry point ($\varepsilon_d \neq -U/2$), where the exchange field can introduce spin splitting in the system.

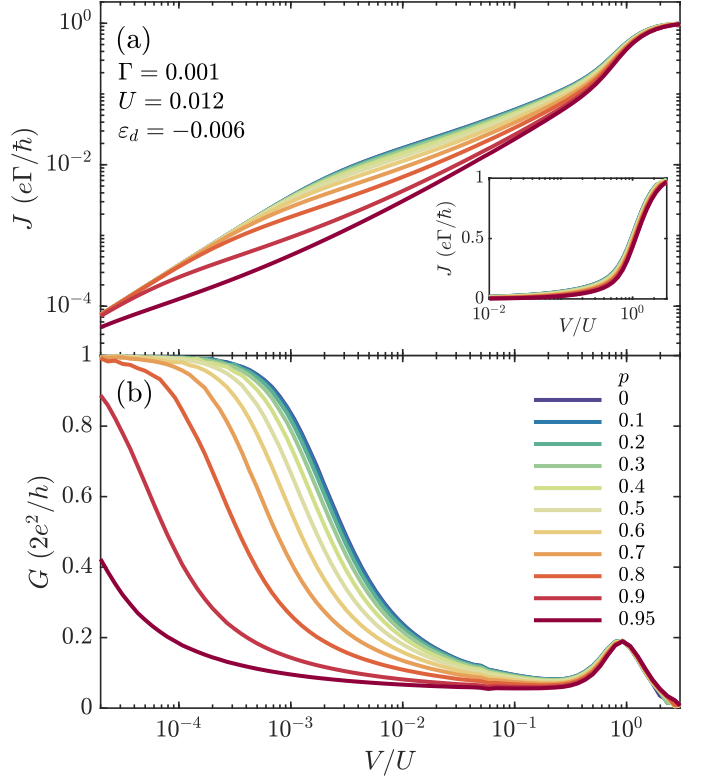


FIG. 2. The bias voltage dependence at $T = 0$ and particle-hole symmetry $\varepsilon_d = -U/2$ of (a) the mean current J on a log-log scale (inset lin-log) and (b) the corresponding differential conductance G on a lin-log scale. The various curves are for different values of the lead spin polarization p , as indicated.

We also analyze the influence of temperature and applied magnetic field on the split Kondo resonance observed in the differential conductance out of the p-h symmetry point.

A. Conductance at the p-h symmetry point

The mean current $J(V)$ and the corresponding differential conductance $G(V)$ through the system calculated at the particle-hole symmetry point ($\varepsilon_d = -U/2$) for different values of the lead spin polarization p are presented in Fig. 2. For this we always evaluate the symmetrized current as discussed in Sec. A2 [see Eq. (A4)]. For $p = 0$, we observe a zero-bias conductance peak, characteristic of the Kondo effect [6,7]. However, when p is finite, the Kondo temperature is found to decrease with increasing lead spin polarization. This was predicted to affect the Kondo temperature of the system at equilibrium using the poor man's scaling method [8]:

$$T_{K,p} \equiv \sqrt{\frac{\Gamma U}{2}} \exp \left\{ \frac{\pi \varepsilon_d (\varepsilon_d + U)}{2\Gamma U} \frac{\text{arctanh}(p)}{p} \right\}. \quad (10)$$

The decrease in the Kondo energy scale with spin polarization can be understood by realizing that by construction with Eq. (5), increasing polarization reduces the hybridization of the suppressed spin orientation. As such, this decreases the rate of spin-flip cotunneling processes responsible for the Kondo effect.

To quantitatively elucidate the influence of p on the Kondo effect, we define the Kondo energy scale V_K in the applied bias

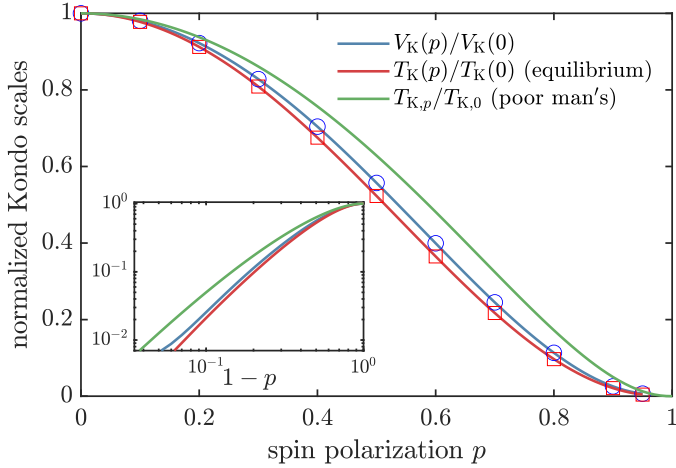


FIG. 3. Comparison of the Kondo energy scale V_K in the applied bias potential at $\varepsilon_d = -U/2$ [Eq. (6)] with the corresponding equilibrium values of T_K obtained from NRG calculations and the theoretical prediction for T_K (denoted by $T_{K,p}$) using the poor man's scaling approach, Eq. (10). The Kondo energy scales are normalized with their corresponding values at $p = 0$, with $T_{K,0} = 2.2 \times 10^{-5}$ and $V_K(0) = 3.6 \times 10^{-5} = 1.64 T_{K,0}$, and $T_K(0) = 2.6 \times 10^{-5} = 1.18 T_{K,0}$.

voltage as the half-maximum point of the conductance curve, i.e., $G(V_K)/G(0) = \frac{1}{2}$ at $T = B = 0$. In Fig. 3 we present the dependence of V_K obtained from our NRG-tDMRG numerical calculations along with the Kondo temperature $T_{K,p}$ estimated from Eq. (10) using the poor man's scaling and $T_K(p)$ calculated using the equilibrium NRG [32] from the temperature dependence of the linear conductance based on the definition $G(T_K)/G(0) = \frac{1}{2}$. Our nonequilibrium data corroborate the general tendency to decrease the Kondo energy scale with increasing spin polarization p . However, Fig. 3 also demonstrates some deviations: V_K is slightly larger than the equilibrium T_K but smaller than the Kondo temperature predicted by the analytical formula (10), after normalizing the Kondo energy scales with respect to their respective values at $p = 0$.

B. Effect of finite exchange field

We now discuss the behavior of the differential conductance in the case when the energy level is away from the p-h symmetry point ($\varepsilon_d = -U/3$) but still in the local moment regime where strong electron correlations play a vital role. The solid lines in Fig. 4(a) show the bias dependence of the conductance with an increase in the lead spin polarization p , computed at zero external magnetic field. We observe a finite zero-bias peak that gets suppressed when p grows. This effect can be attributed to the emergence of exchange field in the system [see Eq. (8)]. The exchange field introduces a spin splitting of the orbital level, which suppresses the Kondo resonance, once $|\Delta\varepsilon_{\text{exch}}| \gtrsim T_K, V_K$. The color-coded arrows in Fig. 4(a) indicate the magnitude of the exchange field for the corresponding spin polarizations obtained from Eq. (8) with $T = 0$. When the exchange field energy approaches the Kondo energy scale of the system, $|\Delta\varepsilon_{\text{exch}}| \approx T_K$, the zero-bias conductance becomes suppressed. When the spin polarization increases further, the differential conductance starts to develop

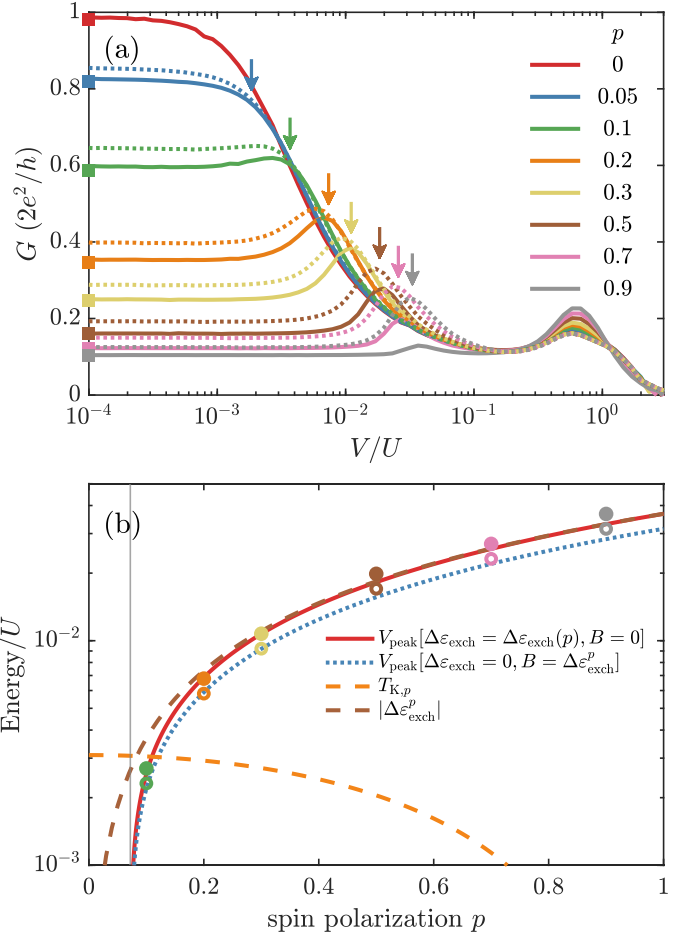


FIG. 4. (a) The differential conductance G as a function of the bias voltage in the case when the orbital level is detuned from the particle-hole symmetry point (solid lines) using $\varepsilon_d = -U/3$ [Eq. (6)] for different values of the spin polarization p as indicated in the legend. To check the continuity from the equilibrium regime, the corresponding NRG results for the linear-response conductance are marked by the color-matched squares on the left vertical axis. For comparison, we also show curves, where the macroscopic spin polarization was turned off and replaced, instead, by the corresponding local magnetic field $B = \Delta\varepsilon_{\text{exch}}^p$ (dotted curves). Here the value for $\Delta\varepsilon_{\text{exch}}^p$ was determined by Eq. (8) at $T = 0$, and its absolute value is indicated by the color-coded arrows. For $p = 0$, we obtain $T_{K,0} = 3.7 \times 10^{-5}$, $V_K = 6 \times 10^{-5} = 1.62 T_{K,0}$ for the voltage bias where the differential conductance drops to half its zero-bias value. (b) The solid (open) circles maps the location of the split Kondo peak from the solid (dotted) curves in (a), denoted by V_{peak} , tracked as a function of spin polarization p . Solid lines in (b) present the extrapolation using a linear fit of the squared data for the smallest polarizations (first three data points), thus fitting $V_{\text{peak}} = a_0 \gamma \sqrt{p^2 - p_0^2}$ with $\Delta\varepsilon_{\text{exch}} = \gamma p$, where $\gamma = 0.4413 \Gamma$ [see Eq. (9)], and the fit parameters $a_0 = 1.001$, $p_0 = 0.072$ (vertical line). Similarly, the fit of the open symbols (dotted line) results in $a_0 = 0.860$, $p_0 = 0.070$.

a peak around $V \equiv V_{\text{peak}} \approx |\Delta\varepsilon_{\text{exch}}|$, which is reminiscent of the splitting of the local density of states (LDOS) vs frequency in the presence of a sufficiently strong local magnetic field. To be specific, the peak in the differential conductance presented in Fig. 4(a) emerges for $p \gtrsim 0.1$. For this value of spin polarization, we can find that $T_{K,p} = 3.66 \times 10^{-5}$, $|\Delta\varepsilon_{\text{exch}}^p| \approx$

$4.4 \times 10^{-5} = 1.2 T_{K,p}$. Increasing the polarization further, the peak at $V \approx |\Delta \varepsilon_{\text{exch}}|$ persists while the conductance overall diminishes.

The dotted lines in Fig. 4(a) correspond to the case in which the system has no exchange field (i.e., $p = 0$) but an external magnetic field is applied, whose magnitude equals the exchange field calculated from Eq. (8) according to the spin polarizations mentioned in Fig. 4(a). This comparison shows two major differences between the exchange field and the magnetic field. First, a strong enough exchange field suppresses the split Kondo peak in the differential conductance significantly more strongly and leaves only a residual conductance derived from the hybridization side peak energies $V \simeq \varepsilon_d$ [note the log scale in Fig. 4(a)]. This is mainly attributed to the fact that the Kondo scale gets reduced with increasing spin polarization (see Fig. 3), such that the ratio $|\Delta \varepsilon_{\text{exch}}|/T_K$ is enhanced for the presence of an exchange field when compared to a local magnetic field. Second, the location of the split Kondo peak for finite p occurs at slightly higher voltages than for the case of a local magnetic field. The latter effect may be attributed to $B \approx \Delta \varepsilon_{\text{exch}}$ representing a lowest-order estimate. The explicit dependence of V_{peak} on the spin polarization p in the two above-discussed cases is shown in Fig. 4(b). For comparison, we also present the p dependence of $\Delta \varepsilon_{\text{exch}}$ and $T_{K,p}$ estimated from the respective analytical formulas. We can see that, indeed, the split Kondo peak emerges when $|\Delta \varepsilon_{\text{exch}}| \gtrsim T_{K,p}$. Moreover, by comparing $\Delta \varepsilon_{\text{exch}}$ and $T_{K,p}$, we can find that these two energy scales become equal for $p = 0.0834$. Keeping in mind that this is an approximate estimate, our numerical results corroborate this tendency very well. The split Kondo peak shows a slightly nonlinear behavior around low spin polarizations. We fit the V_{peak}^2 data against p^2 to

unveil any behavior of the form $V_{\text{peak}} \sim \sqrt{p^2 - p_0^2}$. Both the fits for the exchange field and the corresponding magnetic field give essentially the same value of $p_0 \simeq 0.071$, indicated by the gray vertical line in Fig. 4(b). The prefactor of the fit is exactly 1 (1.001) within numerical accuracy in the presence of polarization, with $V_{\text{peak}} \simeq \sqrt{(\Delta \varepsilon_{\text{exch}}^p)^2 - (\gamma p_0)^2}$ [see Eq. (9)]. This is also clearly seen in Fig. 4(b) in that the fit exactly coincides with $\Delta \varepsilon_{\text{exch}}$ for larger p . In the case of a substitute local magnetic field $B = \Delta \varepsilon_{\text{exch}}^p$ but unpolarized leads, the fit reads $V_{\text{peak}} \simeq 0.860 \sqrt{(\Delta \varepsilon_{\text{exch}}^p)^2 - (\gamma p_0)^2}$. This systematically offsets the peaks with the dashed data in Fig. 4(a) by a constant factor of 0.860 towards slightly smaller values of the bias voltage yet leads to the disappearance of the split peak at around the same polarization p_0 . On the semilog scale in Fig. 4(b) this change in the prefactor simply shifts the fits vertically relative to each other, as also reflected in the data for the full polarization range.

The symbols on the left vertical axis in Fig. 4(a) correspond to the linear-response data obtained by NRG, which is equivalent to the differential conductance for $V \rightarrow 0$. As also seen in later figures, while we have good overall consistency [e.g., see the inset in Fig. 6(b) below], there are minor quantitative differences in the NRG-tDMRG results compared with the linear-response NRG results. These are attributed to the different parametrization and discretization schemes. Specifically,

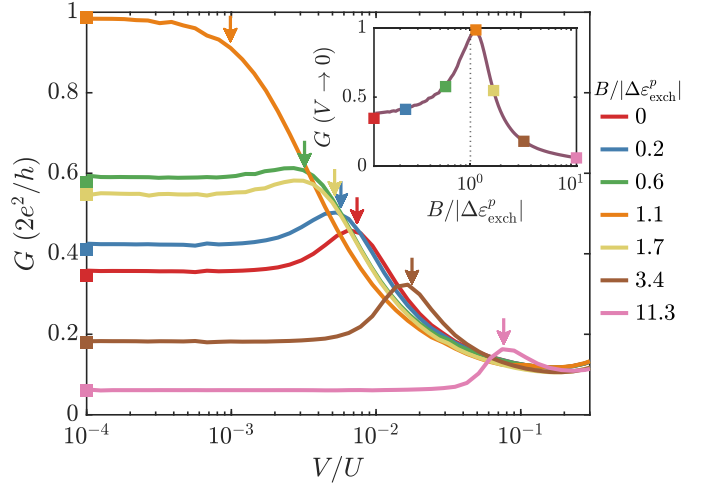


FIG. 5. The differential conductance G as a function of the bias voltage calculated at fixed $p = 0.2$ for different values of external magnetic field as indicated using $\varepsilon_d = -U/3$ [Eq. (6)], thus with $\Delta \varepsilon_{\text{exch}}^p = -0.0882\Gamma$ [Eq. (9)]. The color-matched arrows indicate $|B_{\text{tot}}^{\text{eff}}|$ as defined in Eq. (7). The corresponding NRG results for the linear-response conductance are shown by the color-matched squares on the left vertical axis. The inset shows the behavior of $G(B, V \rightarrow 0)$ as a function of the magnetic field B , with a significantly denser set of data points from NRG-tDMRG (line) and the symbols from NRG as in the main panel. The maximum of $G(B)$ occurs at $B_{\text{max}} = 1.12 \Delta \varepsilon_{\text{exch}}^p$.

linear conductance within linear response in NRG can be obtained strictly at $V = 0^+$ [33]. In contrast, the NRG-tDMRG approach always must assume a small, but finite, voltage in the presence of finite level spacing with the objective being to numerically compute a steady-state current via a real-time simulation.

C. The influence of magnetic field

In Fig. 5 we study the influence of external magnetic field on the split Kondo peak exhibited by the system detuned out of the p-h symmetry point assuming the lead spin polarization $p = 0.2$. We observe a full restoration of the zero-bias Kondo resonance by an applied magnetic field with a magnitude that can counterbalance the spin splitting induced by the exchange field; see the curve for $B = 1.1 |\Delta \varepsilon_{\text{exch}}^p|$ in Fig. 5. However, a further increase in magnetic field is shown to suppress the zero-bias peak again. This behavior qualitatively matches the experimental results discussed in Fig. 2 in Ref. [14]. As seen from the color-coded arrows in Fig. 5, the position of the split Kondo resonance corresponds to $V \approx |B_{\text{tot}}^{\text{eff}}|$, as defined in Eq. (7). The revival of the Kondo resonance can be distinctly observed from the inset in Fig. 5, where $G(V \rightarrow 0)$ exhibits a maximum around $B_{\text{max}} \simeq |\Delta \varepsilon_{\text{exch}}^p|$ such that $B_{\text{tot}}^{\text{eff}} \simeq 0$ [Eq. (7)]. More precisely, from the inset in Fig. 5, $B_{\text{max}} = 1.12 |\Delta \varepsilon_{\text{exch}}^{p=0.2}|$, with the small difference being primarily attributed to the perturbative nature of the analytic formula (8). The prefactor approximately coincides with a similar scale factor already encountered in Fig. 4(b), where $B = |\Delta \varepsilon_{\text{exch}}^p|$ also underestimated the peak position by an approximate factor of $1/0.860 = 1.16$.

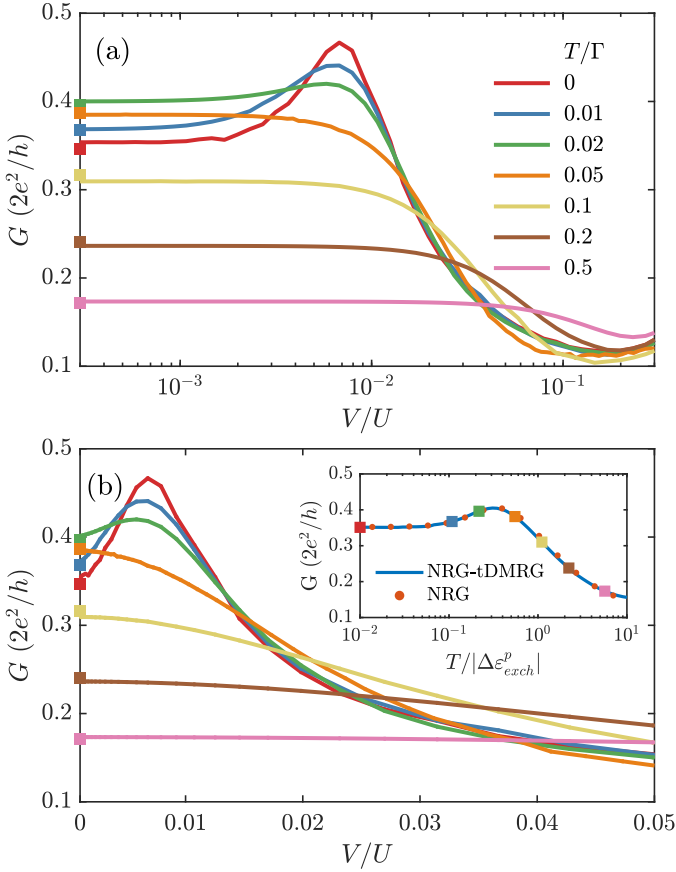


FIG. 6. The bias voltage dependence of the differential conductance G for fixed $p = 0.2$ and $B = 0$ calculated for different temperatures as indicated in the legend, using $\varepsilon_d = -U/3$ [Eq. (6)]. (a) presents $G(V)$ on the logarithmic scale, while (b) shows the same data on the linear scale with a focus on the low-bias behavior. The linear-response NRG results are shown by the color-matched squares on the left axis. The inset in (b) compares the linear-response conductance as a function of the temperature of our hybrid scheme (using $V = 10^{-3}$ T) with NRG results, where the large square symbols of the latter are identical to the ones in the main panels.

D. Temperature dependence of the split Kondo peak

In this section we analyze the effect of finite temperature on the split Kondo resonance. Figure 6 shows the bias voltage dependence of the differential conductance for various temperatures calculated for $\varepsilon_d = -U/3$ and $p = 0.2$. One can see that increasing T results in the suppression of the split Kondo peak, which completely disappears once the thermal energy exceeds the induced exchange splitting. Increasing temperature still further suppresses the differential conductance. The suppression of the split Kondo peak is accompanied by a weak increase in the conductance at zero bias for temperatures corresponding to the splitting of the LDOS due to the exchange field, as seen in the inset in Fig. 6(b). This can be used to estimate the temperature where the splitting in the differential conductance disappears. The split Kondo peak can survive up to a maximum temperature T_{\max} defined as the temperature at which $G(V \rightarrow 0, T) = G(V = V_{\text{peak}}, T)$. For the spin polarization $p = 0.2$, we estimate $T_{\max} = 2.06 \times 10^{-2} \Gamma = T_{K,0.2}$.

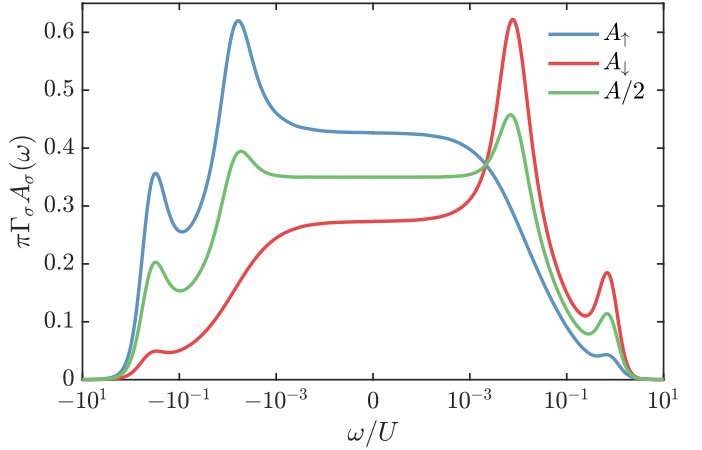


FIG. 7. The energy dependence of the equilibrium zero-temperature normalized spectral function $\pi\Gamma_\sigma A_\sigma(\omega)$ calculated for $\varepsilon_d = -U/3$, $p = 0.2$, and $B = 0$ [Eq. (6)]. Note the logarithmic energy scale.

The $V \rightarrow 0$ differential conductance is equivalent to linear response in thermal equilibrium. The latter is readily obtained with NRG, with a direct comparison shown in the inset in Fig. 6(b). Overall, we observe good quantitative agreement. The points corresponding to the temperatures plotted in the main panels are marked by the same color-matched squares. Since linear response can be efficiently obtained with NRG, a denser set of data points is permitted in the inset.

The weak increase in the linear-response conductance for a finite temperature can be explained by examining the energy dependence of the equilibrium local density of states, i.e., the impurity spectral function, assuming that this LDOS changes only weakly at low temperatures $T \lesssim \max(T_K, |\Delta\varepsilon_{\text{exch}}|)$. The linear-response conductance $G = \sum_\sigma G_\sigma$ is obtained from the spectral function using $G_\sigma(T) = \frac{\pi e^2}{h} \int_{-D}^D d\omega \Gamma_\sigma A_\sigma(\omega) [-f'(\omega)]$ [33], where $A_\sigma(\omega) = -\frac{1}{\pi} \text{Im} G_\sigma(\omega)$ is the spin-resolved spectral function based on the retarded impurity Green's function $G_\sigma(\omega)$ and $f'(\omega)$ is the derivative of the Fermi function at temperature T . Now if the exchange field due to polarization is sufficiently strong, $|\Delta\varepsilon_{\text{exch}}| \gtrsim T_K$, it will already split the spin-averaged LDOS at equilibrium, as shown for $p = 0.2$ in Fig. 7. When temperature is increased, the transport window widens and thus encompasses more weight from the split peaks. Assuming that the LDOS changes only weakly by turning on a small temperature $T \lesssim \max(T_K, |\Delta\varepsilon_{\text{exch}}|)$, the contributions from the peak in the spectral function around $\omega \approx |\Delta\varepsilon_{\text{exch}}|$ will increase the linear-response conductance up to $T \lesssim |\Delta\varepsilon_{\text{exch}}|$, where it reaches a maximum before it starts to decrease.

An explicit temperature dependence of the split Kondo peak conductance for a few selected values of spin polarization is shown in Fig. 8. Figure 8 is determined at finite bias voltage $V(p) \approx |\Delta\varepsilon_{\text{exch}}^p|$, i.e., at the voltage corresponding to the location of the split Kondo peak V_{peak} shown in Fig. 4. As seen by the vertical markers in Fig. 8, V agrees well with $|\Delta\varepsilon_{\text{exch}}^p|$ for large polarization p but clearly starts to differ for smaller p , given that there is no peak at finite V for $p \lesssim 0.0834$. By starting from the peak conductance,

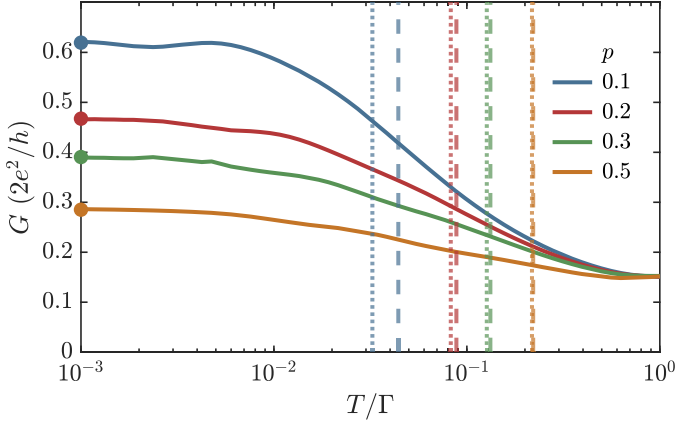


FIG. 8. The temperature dependence of the differential conductance G at fixed bias voltage $V = V_{\text{peak}}$ corresponding to the maximum of the split Kondo peak in Fig. 4(a) calculated for different spin polarizations using $\varepsilon_d = -U/3$ [Eq. (6)], where the circles on the left axis replicate the peak in the zero-temperature data in Fig. 4. The color-matched vertical dotted lines mark the peak bias voltage $V(p)$ at which conductance is calculated, whereas the dashed lines indicate $|\Delta\varepsilon_{\text{exch}}^p|$. These are roughly located where the peak conductance is reduced by about half relative to a background conductance due to the hybridization side peaks at energy ε_d .

we can now clearly see in Fig. 8 the decrease in the remaining Kondo resonance as the temperature increases. The logarithmic decrease in the split Kondo peak conductance at higher temperatures was experimentally observed in Fig. 3(a) of Ref. [9]. In the case of $p = 0.1$, the split Kondo peak just emerged, with $|\Delta\varepsilon_{\text{exch}}^{p=0.1}| \approx T_K$, as can be observed from Fig. 4 and the vertical blue lines in Fig. 8. Hence, we can see a slight nonmonotonic behavior arising from the interplay between the Kondo effect and the exchange field. More generally, we can infer from Figs. 6 and 8, for the split Kondo regime, i.e., sufficiently strong polarization p with $|\Delta\varepsilon_{\text{exch}}| > T_K$, that G_V vs T (G_T vs V) will exhibit a nonmonotonic behavior if $T < |\Delta\varepsilon_{\text{exch}}|$ ($V < |\Delta\varepsilon_{\text{exch}}|$) but a monotonic decay if $T \gtrsim |\Delta\varepsilon_{\text{exch}}|$ ($V \gtrsim |\Delta\varepsilon_{\text{exch}}|$). We also note that the temperature dependence of the nonequilibrium differential conductance at $V \approx |\Delta\varepsilon_{\text{exch}}|$ does not show a universal dependence. This can be understood by realizing that the system is then out of the Kondo regime.

IV. SUMMARY

In this paper we have studied the nonequilibrium spin-resolved transport through a quantum dot coupled to ferromagnetic leads while treating the correlations exactly. We showed that when the dot level is at the particle-hole symmetry point, the Kondo resonance can be observed for any value of spin polarization p , but the Kondo energy scale in the bias potential V_K reduces with increasing spin polarization. However, when the dot level is detuned out of the particle-hole symmetry point, we observed the emergence of an exchange field $\Delta\varepsilon_{\text{exch}}$ in the system, which splits the zero-bias conductance peak when it is comparable to or larger than the Kondo energy scale. A finite value of magnetic field $B \approx |\Delta\varepsilon_{\text{exch}}|$ was able to restore the Kondo resonance in such a system. More-

over, we determined the temperature dependence of the split Kondo peak and showed that the character of this dependence depends on the ratio of exchange field to the Kondo energy scale. Our work provides benchmark results for nonequilibrium spintronic transport through quantum impurity systems in the presence of ferromagnetic leads.

ACKNOWLEDGMENTS

This work was supported by the Polish National Science Centre from funds awarded through Decisions No. 2017/27/B/ST3/00621 and No. 2021/41/N/ST3/02098. We would also like to acknowledge the support from the project ‘‘Initiative of Excellence - Research University’’ from funds awarded through Decision No. 003/13/UAM/0016. A.W. was supported by the U.S. Department of Energy, Office of Science, Basic Energy Sciences, Materials Sciences and Engineering Division.

APPENDIX: THE HYBRID NRG-tDMRG THERMOFIELD QUENCH APPROACH

This Appendix provides more details of the hybrid NRG-tDMRG thermofield quench method [29] used to calculate the spin-resolved transport properties of the system in nonequilibrium settings.

1. Thermofield treatment of the leads

To describe the leads we use the thermofield approach [30,34,35], in which an auxiliary Hilbert space, equivalent to the lead Hilbert space but decoupled from the system, is introduced to the lead Hamiltonian, effectively doubling the Hilbert space. This allows us to simplify the computational problem since the decoupled modes of thermal leads can be expressed as simple product states. More importantly, the thermofield approach enables the description of the thermal states as pure states, which can then be time evolved within the matrix product state framework.

A pure state $|\Omega\rangle$ is defined on this enlarged space such that the thermal expectation value of an observable A in the original physical Hilbert space can be obtained from the enlarged space using $\langle A \rangle = \langle \Omega | A | \Omega \rangle$, where the state $|\Omega\rangle$ is defined as

$$|\Omega\rangle = \prod_q (\sqrt{1-f_q}|0,1\rangle_q + \sqrt{f_q}|1,0\rangle_q). \quad (\text{A1})$$

Here the composite index corresponds to $q \equiv \{\alpha, k, \sigma\}$, $f_q \equiv f_\alpha(\varepsilon_{\alpha k \sigma})$, and the Fock states $|0,1\rangle_q$ and $|1,0\rangle_q$, which act as the basis for the new Hilbert space, are defined as $c_{q1}|0,1\rangle_q = c_{q2}^\dagger|0,1\rangle_q = c_{q1}^\dagger|1,0\rangle_q = c_{q2}|1,0\rangle_q = 0$. We define the modes \tilde{c}_{qj} in a rotated basis such that $|\tilde{0}, \tilde{1}\rangle_q = \sqrt{1-f_q}|0,1\rangle_q + \sqrt{f_q}|1,0\rangle_q$, using the transformation

$$\begin{pmatrix} \tilde{c}_{q1} \\ \tilde{c}_{q2} \end{pmatrix} = \begin{pmatrix} \sqrt{1-f_q} & \sqrt{f_q} \\ \sqrt{f_q} & \sqrt{1-f_q} \end{pmatrix} \begin{pmatrix} c_{q1} \\ c_{q2} \end{pmatrix}. \quad (\text{A2})$$

With this transformation, the initial pure product state $|\Omega\rangle$ is such that $\tilde{c}_{q1}|0,1\rangle_q = \tilde{c}_{q2}^\dagger|0,1\rangle_q = 0$, which essentially results in one set of modes ($j=2$) being fully occupied, while the rest ($j=1$) are empty. The fully filled (empty) states in the new basis resemble the particle (hole) description of the lead Hamiltonian. The particles and holes will be recombined later

for the NRG part of the calculations but will be treated separately for the tDMRG time evolution, as described later.

2. The hybrid NRG-tDMRG time evolution

The hybrid NRG-tDMRG approach we employ combines the strong assets of both NRG and DMRG, namely, the ability of NRG to resolve logarithmic energy scales and the ability of DMRG to describe nonequilibrium situations at energy scales close to the bandwidth. One fundamental difference between the two methods is that while NRG is fundamentally based on logarithmic discretization, DMRG studies have found incredible success based on a linear discretization of the lead energy continuum. The energy scales that distinguish the regimes of implementation of these methods are denoted by the transport window (TW), which is determined by the difference in the electrochemical potentials of the leads, $f_L(\omega) \neq f_R(\omega)$. Assuming that the lead levels far from the TW are essentially in equilibrium, we implement a logarithmic discretization scheme outside the transport window in order to later treat them with the aid of the NRG. On the other hand, the energies inside the TW are discretized linearly to be compatible with the DMRG formalism. The discretized energy intervals are denoted by E_k and are defined as

$$E_k(x) = \begin{cases} \delta x, & |x| \leq D^*/\delta, \\ \frac{\delta \sinh[\ln(\Lambda)(x \mp D^*/\delta)]}{\log(\Lambda)} \mp \delta D^*, & x \lesseqgtr \pm D^*/\delta, \end{cases}$$

where δ and Λ are the linear and logarithmic discretization parameters, respectively. The energy levels outside the TW are treated using the numerical renormalization group method, giving rise to a renormalized impurity (RI) with a reduced effective bandwidth $2D^*$. As a result of the thermofield transformation in the linear sector, the system can be effectively described as a renormalized impurity coupled to two chains, corresponding to the tridiagonalized chains of the particle and hole modes.

The Hamiltonians, H_{lead} and H_{hyb} , transform according to the aforementioned rotation as

$$\begin{aligned} \mathcal{H}_{\text{lead}} &= H_{\text{lead}} + H_{\text{aux}} = \sum_{qj} \varepsilon_q c_{qj}^\dagger c_{qj} = \sum_{qj} \varepsilon_q \tilde{c}_{qj}^\dagger \tilde{c}_{qj}, \\ H_{\text{hyb}} &= \sum_{qj} (\tilde{v}_{qj} d_\sigma^\dagger \tilde{c}_{qj} + \text{H.c.}), \end{aligned} \quad (\text{A3})$$

where $j \in \{1, 2\}$ and the transformed couplings $\tilde{v}_{q1} = v_q \sqrt{1 - f_q}$ and $\tilde{v}_{q2} = v_q \sqrt{f_q}$. After the transformation, we recombine the particles and holes in the logarithmically discretized regime through another tridiagonalization in order to apply NRG. Furthermore, we recombine the transformed left and right lead modes so that one set of modes decouples from the system, which is common in the case of equilibrium NRG studies [27].

We perform a second-order Trotter time evolution on the initial state of the system, $|\psi_{\text{ini}}\rangle = |\phi_{\text{ini}}\rangle \otimes |\Omega\rangle$, during which the coupling between the linear and logarithmic sectors is switched on over a finite time interval. Here $|\phi_{\text{ini}}\rangle$ is the initial state of the RI, and $|\Omega\rangle$ is the pure product state of the linear sector. We calculate the symmetrized current

$$J = J_L - J_R \quad (\text{A4})$$

at each time step of the system's evolution, where J_L (J_R) is defined as the current flowing from the left (right) lead to the impurity and $J_\alpha = \sum_\sigma J_{\alpha\sigma}$. The system is time evolved until the relevant observables start to fluctuate around a mean value and a nonequilibrium steady state is reached. We evaluate our main quantity of interest—the current—as the mean of the symmetrized current over a finite time interval where the system shows steady-state behavior. The averaging time window is chosen by scanning through the current dynamics to find the one with least error around the mean value. The corresponding differential conductance $G = dJ(V)/dV$ is calculated from the mean symmetrized current. Both NRG and tDMRG calculations are implemented in the matrix product state framework [36]. In calculations we assume $\Lambda = 2.5$ and $\delta = 0.0625D^*$.

-
- [1] I. Žutić, J. Fabian, and S. Das Sarma, Spintronics: Fundamentals and applications, *Rev. Mod. Phys.* **76**, 323 (2004).
- [2] G. E. W. Bauer, E. Saitoh, and B. J. van Wees, Spin caloritronics, *Nat. Mater.* **11**, 391 (2012).
- [3] D. D. Awschalom, L. C. Bassett, A. S. Dzurak, E. L. Hu, and J. R. Petta, Quantum spintronics: Engineering and manipulating atom-like spins in semiconductors, *Science* **339**, 1174 (2013).
- [4] A. Hirohata, K. Yamada, Y. Nakatani, I.-L. Prejbeanu, B. Diény, P. Pirro, and B. Hillebrands, Review on spintronics: Principles and device applications, *J. Magn. Magn. Mater.* **509**, 166711 (2020).
- [5] A. C. Hewson, *The Kondo Problem to Heavy Fermions*, Cambridge Studies in Magnetism (Cambridge University Press, Cambridge, 1993).
- [6] D. Goldhaber-Gordon, H. Shtrikman, D. Mahalu, D. Abusch-Magder, U. Meirav, and M. A. Kastner, Kondo effect in a single-electron transistor, *Nature (London)* **391**, 156 (1998).
- [7] S. M. Cronenwett, T. H. Oosterkamp, and L. P. Kouwenhoven, A tunable Kondo effect in quantum dots, *Science* **281**, 540 (1998).
- [8] J. Martinek, Y. Utsumi, H. Imamura, J. Barnaś, S. Maekawa, J. König, and G. Schön, Kondo Effect in Quantum Dots Coupled to Ferromagnetic Leads, *Phys. Rev. Lett.* **91**, 127203 (2003).
- [9] A. N. Pasupathy, R. C. Bialczak, J. Martinek, J. E. Grose, L. A. K. Donev, P. L. McEuen, and D. C. Ralph, The Kondo effect in the presence of ferromagnetism, *Science* **306**, 86 (2004).
- [10] A. Yazdani, B. A. Jones, C. P. Lutz, M. F. Crommie, and D. M. Eigler, Probing the local effects of magnetic impurities on superconductivity, *Science* **275**, 1767 (1997).
- [11] K. J. Franke, G. Schulze, and J. I. Pascual, Competition of superconducting phenomena and Kondo screening at the nanoscale, *Science* **332**, 940 (2011).
- [12] P. Seneor, A. Bernand-Mantel, and F. Petroff, Nanospintronics: When spintronics meets single electron physics, *J. Phys.: Condens. Matter* **19**, 165222 (2007).
- [13] J. Barnaś and I. Weymann, Spin effects in single-electron tunnelling, *J. Phys.: Condens. Matter* **20**, 423202 (2008).
- [14] K. Hamaya, M. Kitabatake, K. Shibata, M. Jung, M. Kawamura, K. Hirakawa, T. Machida, T. Taniyama, S. Ishida, and Y.

- Arakawa, Kondo effect in a semiconductor quantum dot coupled to ferromagnetic electrodes, *Appl. Phys. Lett.* **91**, 232105 (2007).
- [15] J. R. Hauptmann, J. Paaske, and P. E. Lindelof, Electric-field-controlled spin reversal in a quantum dot with ferromagnetic contacts, *Nat. Phys.* **4**, 373 (2008).
- [16] M. Gaass, A. K. Hüttel, K. Kang, I. Weymann, J. von Delft, and Ch. Strunk, Universality of the Kondo Effect in Quantum Dots with Ferromagnetic Leads, *Phys. Rev. Lett.* **107**, 176808 (2011).
- [17] J. Martinek, M. Sindel, L. Borda, J. Barnaś, J. König, G. Schön, and J. von Delft, Kondo Effect in the Presence of Itinerant-Electron Ferromagnetism Studied with the Numerical Renormalization Group Method, *Phys. Rev. Lett.* **91**, 247202 (2003).
- [18] R. López and D. Sánchez, Nonequilibrium Spintronic Transport through an Artificial Kondo Impurity: Conductance, Magnetoresistance, and Shot Noise, *Phys. Rev. Lett.* **90**, 116602 (2003).
- [19] Y. Utsumi, J. Martinek, G. Schön, H. Imamura, and S. Maekawa, Nonequilibrium Kondo effect in a quantum dot coupled to ferromagnetic leads, *Phys. Rev. B* **71**, 245116 (2005).
- [20] R. Świrkowicz, M. Wilczyński, M. Wawrzyniak, and J. Barnaś, Kondo effect in quantum dots coupled to ferromagnetic leads with noncollinear magnetizations, *Phys. Rev. B* **73**, 193312 (2006).
- [21] I. Weymann and L. Borda, Underscreened Kondo effect in quantum dots coupled to ferromagnetic leads, *Phys. Rev. B* **81**, 115445 (2010).
- [22] R. Žitko, J. S. Lim, R. López, J. Martinek, and P. Simon, Tunable Kondo Effect in a Double Quantum Dot Coupled to Ferromagnetic Contacts, *Phys. Rev. Lett.* **108**, 166605 (2012).
- [23] K. P. Wójcik and I. Weymann, Two-stage Kondo effect in T-shaped double quantum dots with ferromagnetic leads, *Phys. Rev. B* **91**, 134422 (2015).
- [24] I. Weymann, R. Chirla, P. Trocha, and C. P. Moca, SU(4) Kondo effect in double quantum dots with ferromagnetic leads, *Phys. Rev. B* **97**, 085404 (2018).
- [25] A. Bordoloi, V. Zannier, L. Sorba, C. Schönenberger, and A. Baumgartner, A double quantum dot spin valve, *Commun. Phys.* **3**, 135 (2020).
- [26] K. G. Wilson, The renormalization group: Critical phenomena and the Kondo problem, *Rev. Mod. Phys.* **47**, 773 (1975).
- [27] R. Bulla, T. A. Costi, and T. Pruschke, Numerical renormalization group method for quantum impurity systems, *Rev. Mod. Phys.* **80**, 395 (2008).
- [28] U. Schollwöck, The density-matrix renormalization group in the age of matrix product states, *Ann. Phys. (NY)* **326**, 96 (2011).
- [29] F. Schwarz, I. Weymann, J. von Delft, and A. Weichselbaum, Nonequilibrium Steady-State Transport in Quantum Impurity Models: A Thermofield and Quantum Quench Approach Using Matrix Product States, *Phys. Rev. Lett.* **121**, 137702 (2018).
- [30] I. de Vega and M.-C. Bañuls, Thermofield-based chain-mapping approach for open quantum systems, *Phys. Rev. A* **92**, 052116 (2015).
- [31] P. W. Anderson, Localized magnetic states in metals, *Phys. Rev.* **124**, 41 (1961).
- [32] We used the open-access FLEXIBLE DM-NRG code, <http://www.phy.bme.hu/~dmnrg/>; O. Legeza, C. P. Moca, A. I. Tóth, I. Weymann, G. Zaránd, [arXiv:0809.3143](https://arxiv.org/abs/0809.3143).
- [33] Y. Meir, N. S. Wingreen, and P. A. Lee, Transport through a Strongly Interacting Electron System: Theory of Periodic Conductance Oscillations, *Phys. Rev. Lett.* **66**, 3048 (1991).
- [34] S. M. Barnett and B. J. Dalton, Liouville space description of thermofields and their generalisations, *J. Phys. A* **20**, 411 (1987).
- [35] A. Das, Topics in finite temperature field theory, in *Quantum Field Theory - A 20th Century Profile*, edited by A. N. Mitra (Hindustan Book Agency, New Delhi, 2000), pp. 383–411.
- [36] A. Weichselbaum, Tensor networks and the numerical renormalization group, *Phys. Rev. B* **86**, 245124 (2012).

8.2 Nonequilibrium steady-state thermoelectrics of Kondo-correlated quantum dots [C]

Nonequilibrium steady-state thermoelectrics of Kondo-correlated quantum dots

Anand Manaparambil,^{1,*} Andreas Weichselbaum,² Jan von Delft,³ and Ireneusz Weymann¹¹*Institute of Spintronics and Quantum Information,
Faculty of Physics, Adam Mickiewicz University,
Uniwersytetu Poznańskiego 2, 61-614 Poznań, Poland*²*Department of Condensed Matter Physics and Materials Science,
Brookhaven National Laboratory, Upton, New York 11973-5000, USA*³*Arnold Sommerfeld Center for Theoretical Physics, Center for NanoScience,
and Munich Center for Quantum Science and Technology,
Ludwig-Maximilians-Universität München, 80333 Munich, Germany*

(Dated: September 26, 2024)

The transport across a Kondo-correlated quantum dot coupled to two leads with independent temperatures and chemical potentials is studied using a controlled non-perturbative, and in this sense exact numeric treatment based on a hybrid numerical renormalization group combined with time-dependent density matrix renormalization group (NRG-tDMRG). We find a peak in the conductance at finite voltage bias vs. the temperature gradient $\Delta T = T_R - T_L$ across left and right lead. We then focus predominantly on zero voltage bias but finite ΔT far beyond linear response. We reveal the dependence of the characteristic zero-bias conductance on the individual lead temperatures. We find that the finite- ΔT data behaves quantitatively similar to linear response with an effective equilibrium temperature derived from the different lead temperatures. The regime of sign changes in the Seebeck coefficient, signaling the presence of Kondo correlations, and its dependence on the individual lead temperatures provide a complete picture of the Kondo regime in the presence of finite temperature gradients. The results from the zero-bias conductance and Seebeck coefficient studies unveil an approximate ‘Kondo circle’ in the T_L/T_R plane as the regime within which the Kondo correlations dominate. We also study the heat current and the corresponding heat conductance vs. finite ΔT . We provide a polynomial fit for our numerical results for the thermocurrent as a function of the individual lead temperatures which may be used to fit experimental data in the Kondo regime.

I. INTRODUCTION

Strong electronic correlations in a magnetic impurity coupled to electronic reservoirs result in a many-body screening phenomenon, mediated by the conduction band electrons, known as the Kondo effect [1]. The Kondo effect manifests itself in the density of states of the impurity as a narrow resonance peak around the Fermi level widely known as the Kondo-Abrikosov-Suhl resonance [2, 3]. This Kondo resonance that increases the low temperature resistivity of bulk metal alloys [4] has been found to be present in various classes of nanostructures, involving single electron transistors [5–10], nanowires [11–14], carbon nanotubes [15, 16], molecular magnets [17–19], adatoms [20–22] and other quantum impurity systems [23–27]. Such nanostructures are very tunable and act as a robust platform to explore various aspects of the Kondo effect [6, 28]. Moreover, the transport properties of Kondo-correlated impurity systems carry characteristic signatures of the Kondo effect, which emerge at low temperatures near the Kondo energy scale. Particularly, the zero-bias peak in the differential conductance [5, 6] and a sign change in the Seebeck coefficient at low energies [29–33] signify the presence of Kondo correlations in the system. The characteristic density of states present in the quantum dots makes them a class of

prospective systems to work as efficient energy-harvesters [34–42]. Various proposals, such as the charge Kondo effect [43], multi-quantum dot setups [44, 45], including the case of asymmetric couplings to the leads [46, 47], have pointed towards a considerable thermoelectric efficiency of quantum-dot based heat engines. Thermoelectric quantum dot devices have also demonstrated promising applications in sensing [46, 48] and cooling technologies [49–51].

An accurate description of the Kondo effect relies on the exact treatment of electronic correlations at low energy scales. Though many theoretical methods, including the Bethe-Ansatz [52, 53], perturbation theory [54], Fermi liquid theory [55] and the dynamical mean field theory [56], can tackle the Kondo problem and contribute to the qualitative understanding of the phenomenon at low energies, all of them rely on approximating the electronic correlations to describe the energies near the Kondo energy scale. The numerical renormalization group method (NRG) [57, 58], considered to be the best at tackling the Kondo problem, can provide quantitatively accurate description of the Kondo effect, but only up to linear response studies near equilibrium [29].

Notable theoretical attempts to describe the nonequilibrium transport through a Kondo impurity had employed nonequilibrium Greens function (NEGF) [59–61], renormalized perturbation theory (RPT) [62], generalized Fermi liquid theory [63–66], perturbative approaches [47, 67], auxiliary master equation approach

* anaman@amu.edu.pl

(AMEA) [48, 68, 69], non-crossing approximation (NCA) [70, 71] and slave-boson mean field theory (SBMFT) [60]. Though each method has its own virtues and provides theoretical insights at various limits, a complete picture of the whole nonequilibrium Kondo regime had remained elusive. A hybrid method, incorporating both numerical renormalization group and time-dependent density matrix renormalization group (tDMRG) method based on a thermofield quench approach (NRG-tDMRG), has achieved the feat of describing the nonequilibrium transport through a Kondo-correlated system with exact treatment of correlations [72]. Until now, this method has been employed to address the electronic transport under finite potential bias [72] and spintronic transport in the presence of ferromagnetism in the leads [73]. In this work, we extend the NRG-tDMRG method to describe the nonequilibrium Kondo effect in the presence of finite temperature gradients. In particular, we consider a quantum dot symmetrically coupled to two metallic leads held at different temperatures that can be tuned independently. The choice of symmetric couplings to the leads allows for the Kondo correlations to develop over both the leads, uncovering the influence of the individual lead temperatures on the Kondo effect. The dynamics of the electronic and heat currents are calculated using NRG-tDMRG and their nonequilibrium steady state values are extracted using linear prediction across a finite time window. We characterize the Kondo regime as a function of the individual lead temperatures using the zero-bias conductance and the Seebeck coefficient of the system. We find that transport in the presence of a nonlinear temperature gradient can be qualitatively described by linear response results with an effective equilibrium temperature. Our results demonstrate that the Kondo correlations persist as a circle when depicted in the individual lead temperatures.

Our work provides the first quantitatively accurate results for the thermoelectric transport coefficients of Kondo-correlated quantum dot in far-from-equilibrium settings. The paper is organized as follows: Sec. II describes the system Hamiltonian and the transport properties under study. In Sec. III, we discuss the results from NRG-tDMRG calculations. We begin by discussing a noninteracting system in Sec. III A, and then moving on to the interacting system described by the single impurity Anderson model in Sec. III B. The influence of temperature gradient on the zero-bias transport properties is discussed in Sec. III B 1. The differential conductance at zero-bias and for a finite potential bias in the presence of different lead temperatures is discussed in Sec. III B 2. The thermoelectric current, Seebeck coefficient and heat transport properties are discussed in Sec. III B 3. Finally, the paper is summarized in Sec. IV.

II. MODEL AND METHOD

A. Hamiltonian

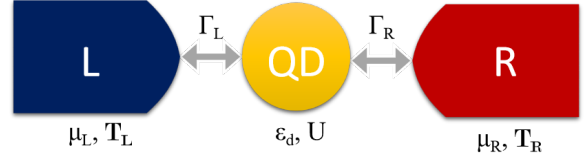


FIG. 1. The schematic of a quantum dot with orbital level ε_d and Coulomb repulsion U coupled to the left ($\alpha = L$) and right ($\alpha = R$) metallic lead with hybridization function Γ_α . Each lead is held at different temperature T_α and chemical potential $\mu_\alpha = \pm V/2$.

Our system consists of a quantum dot strongly coupled to two metallic leads. The Hamiltonian of such a system can be described as

$$H = H_{\text{imp}} + H_{\text{lead}} + H_{\text{tun}}, \quad (1)$$

where H_{imp} is the impurity part of the Hamiltonian described by a single impurity Anderson model (SIAM) with orbital energy ε_d and Coulomb interaction U . H_{imp} takes the form

$$H_{\text{imp}} = \varepsilon_d(n_\uparrow + n_\downarrow) + U n_\uparrow n_\downarrow, \quad (2)$$

where $n_\sigma = d_\sigma^\dagger d_\sigma$ is the number operator, with d_σ (d_σ^\dagger) being the annihilation (creation) operator for a dot electron with spin σ . The leads are modeled as noninteracting particles

$$H_{\text{lead}} = \sum_\alpha H_\alpha = \sum_{\alpha k \sigma} \varepsilon_{\alpha k} c_{\alpha k \sigma}^\dagger c_{\alpha k \sigma}, \quad (3)$$

with $c_{\alpha k \sigma}$ ($c_{\alpha k \sigma}^\dagger$) denoting the annihilation (creation) operator for an electron in the lead α with energy $\varepsilon_{\alpha k}$ and spin σ . Finally, the tunneling Hamiltonian H_{tun} describes the coupling of the quantum dot to the leads

$$H_{\text{tun}} = \sum_{\alpha k \sigma} (v_{\alpha k} d_\sigma^\dagger c_{\alpha k \sigma} + \text{H.c.}), \quad (4)$$

where $v_{\alpha k}$ is the tunneling matrix element between the k th mode in the lead α and the quantum dot. The dot hybridizes with the leads with the coupling strength given by, $\Gamma_\alpha = \pi \rho_\alpha |v_{\alpha k}|^2$, where ρ_α denotes the density of states of the lead α , which is assumed to be flat $\rho_\alpha \equiv 1/2D$, with D being the band halfwidth which is used as the unit of energy, hence $D = 1$. In the following, without loss of generality, we assume that the system is symmetric $\Gamma_L = \Gamma_R = \Gamma$. We set

$$\Gamma = 0.001, \quad U = 12\Gamma, \quad \varepsilon_d = -U/3, \quad (5)$$

unless specified otherwise. The bias voltage V is applied symmetrically as $\mu_L = -\mu_R = V/2$ and the left and

right lead temperatures T_L, T_R can be controlled independently.

To accurately take into account correlation effects at truly nonequilibrium settings, we employ a hybrid NRG-tDMRG method in the matrix product state (MPS) framework [72, 73]. This method consists of a logarithmic-linear discretization scheme of the conduction bands, a thermofield treatment, followed by a recombination of the leads modes, and finally the time evolution by the second-order Trotter decomposition to reach the nonequilibrium steady-state. The resolution of the method in the energy domain is conditioned by the number of intervals within the transport window. The steady state values as $t \rightarrow \infty$ of heat and charge currents are found from linear prediction of finite time dynamics (cf. App. B).

Since the hybrid NRG-tDMRG approach involves a linear discretization within the transport window and then the time evolution in this discretized basis by tDMRG, for realistic calculations in the case of a finite thermal bias, this sets the limit on the difference in the temperatures of the left and right leads to be around two orders of magnitude. More detailed description of the method is presented in App. A.

B. Transport coefficients

The charge current $J_{\alpha\sigma}$ from the lead α to the quantum dot in the spin channel σ is given by

$$\begin{aligned} J_{\alpha\sigma} &= e \langle \dot{N}_{\alpha\sigma} \rangle = -\frac{i e}{\hbar} \langle [N_{\alpha\sigma}, H] \rangle \\ &= \frac{e}{\hbar} \sum_k \text{Im} (v_{\alpha k} \langle d_{\sigma}^{\dagger} c_{\alpha k \sigma} \rangle). \end{aligned} \quad (6)$$

Here, $N_{\alpha\sigma} = \sum_k c_{\alpha k \sigma}^{\dagger} c_{\alpha k \sigma}$ is the occupation number in the lead α . Similarly, the energy current J_{α}^E from the lead α to the quantum dot can be described based on the lead Hamiltonian H_{α} as

$$\begin{aligned} J_{\alpha}^E &= \langle \dot{H}_{\alpha} \rangle = -\frac{i}{\hbar} \langle [H_{\alpha}, H] \rangle \\ &= \frac{1}{\hbar} \sum_{k\sigma} \varepsilon_{\alpha k} \text{Im} (v_{\alpha k} \langle d_{\sigma}^{\dagger} c_{\alpha k \sigma} \rangle). \end{aligned} \quad (7)$$

In the case of $V = 0$, the energy current can be considered as the heat current $J^Q \equiv J^E$. We note that since the symmetrized charge (heat) current $J^{(Q)}(t)$ converges faster than the current contributions from the individual leads, $J_{\alpha\sigma}^{(Q)}(t)$, it is more efficient to find the steady-state value of the total current $J^{(Q)}(t)$,

$$J^{(Q)}(t) = \sum_{\sigma} \frac{1}{2} [J_{L\sigma}^{(Q)}(t) - J_{R\sigma}^{(Q)}(t)]. \quad (8)$$

More details about estimating $J^{(Q)}(t)$ and the steady state $J^{(Q)}$ can be found in App. B.

The differential electronic conductance G and the electronic contribution to the heat conductance κ are respectively defined as

$$\begin{aligned} G &= \left(\frac{dJ}{dV} \right)_{T_L, T_R}, \\ \kappa &= \left(\frac{J^Q}{\Delta T} \right)_V. \end{aligned} \quad (9)$$

The Seebeck coefficient S estimates the potential V required to compensate for the induced thermoelectric current J under a finite temperature gradient ΔT and it is defined as

$$S = - \left(\frac{V}{\Delta T} \right)_{J=0}. \quad (10)$$

For the transport across an impurity coupled to metallic leads in the linear response regime, these transport coefficients can be estimated as a function of the Onsager integrals, $L_n = -\frac{1}{\hbar} \int d\omega (\omega - \mu)^n \frac{\partial f}{\partial \omega} \mathcal{T}(\omega)$, where $\mathcal{T}(\omega)$ is the transmission coefficient of the impurity and it is essentially equivalent to the equilibrium spectral function $A(\omega)$ [74]. The linear response transport coefficients can thus take the form [29]

$$\begin{aligned} G_0 &= e^2 L_0, \\ S_0 &= -\frac{1}{eT} \frac{L_1}{L_0}, \\ \kappa_0 &= \frac{1}{T} \left(L_2 - \frac{L_1^2}{L_0} \right). \end{aligned} \quad (11)$$

III. RESULTS AND DISCUSSION

In this section, we present and discuss the NRG-tDMRG results for the nonequilibrium transport through a quantum dot in the presence of temperature gradients. The details of the NRG-tDMRG calculations are described in App. A where the method specific parameters are provided in App. A 4. First, the results for a noninteracting impurity under finite potential bias and temperature gradient are compared with exact results in Sec. III A. On the other hand, the nonequilibrium transport across an interacting impurity in the presence of a finite temperature gradient is discussed in Sec. III B.

A. Noninteracting case: Resonant Level Model

As a benchmark for the nonequilibrium calculations, we consider the noninteracting resonant level model (RLM), i.e., essentially the Anderson model with $U = 0$. For this case, the current flowing through the system can be solved exactly [74]

$$J(V, \Delta T) = \frac{2e}{\hbar} \int d\omega \mathcal{T}(\omega) [f_L(\omega) - f_R(\omega)], \quad (12)$$

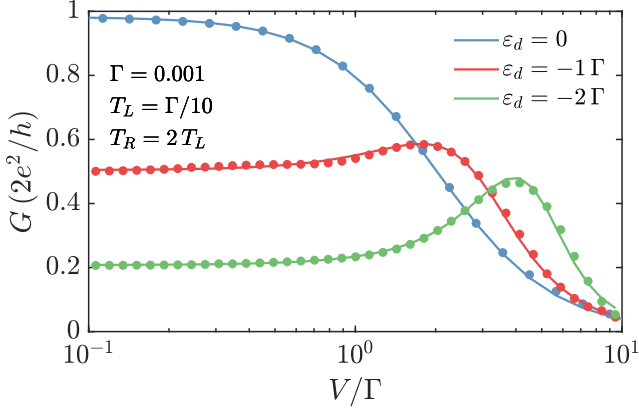


FIG. 2. The differential conductance for the resonant level model ($U = 0$) vs. potential bias V for fixed $\Delta T \sim T$ (see model parameters to the left) and orbital energies ε_d as indicated in the legend. NRG-tDMRG data (dots) is compared to exact analytic curves for continuum (lines) as a consistency check.

where $\mathcal{T}(\omega)$ denotes the transmission coefficient, which can be related to the quantum dot spectral function $A(\omega)$, $\mathcal{T}(\omega) = \pi\Gamma A(\omega)$. For the noninteracting quantum dot, the spectral function can be found exactly through the equation of motion for the Green's function. The transmission coefficient is then given by $\mathcal{T}(\omega) = \Gamma^2 / (\Gamma^2 + (\omega - \varepsilon_d)^2)$, where $f_\alpha(\omega) = 1 / \{1 + \exp[(\omega - \mu_\alpha) / T_\alpha]\}$ is the Fermi-Dirac distribution function of lead α with $k_B \equiv 1$. The differential conductance $G(V)$ calculated using NRG-tDMRG method for a noninteracting quantum dot with different orbital level energies ε_d in the presence of finite potential and temperature gradients is shown in Fig. 2. The differential conductance $G(V)$ has a peak around $V = 2\varepsilon_d$, which is attributed to the Lorentzian peak in $A(\omega)$ located at $\omega = \varepsilon_d$. The shift in the differential conductance peak from the Lorentzian peak originates from the symmetric nature of applied bias $\mu_L = -\mu_R = V/2$, resulting in the transport window (TW) $[f_L(\omega) - f_R(\omega)]$ inside the integral in Eq. (12) scanning the peak mainly around $\omega = 2V$. It is important to note that the both temperatures (T_L, T_R) smear out the transport window and can thus only broaden the conductance peak. The exact analytical calculations (lines) in Fig. 2 agree perfectly with the NRG-tDMRG data (dots), affirming that this technique can capture the nonequilibrium transport primarily originating from the nonlinear dependence of the lead Fermi distributions on V and T .

B. Interacting case: Single Impurity Anderson Model

In the presence of finite U , the nonequilibrium transport across the quantum dot becomes highly nontrivial and cannot be boiled down to an analytical description without sufficient approximations [60, 65]. But, the lin-

ear response description of transport across an interacting quantum dot in equilibrium can very well be calculated using the definitions in Eq. (12) once the spectral function $A(\omega)$ is obtained. The equilibrium spectral function $A(\omega)$ of a SIAM with finite U can be calculated using NRG with extreme precision, and thus it will be used as the benchmark for the calculation of linear response coefficients. The NRG data discussed in this section have been calculated using the QSpace tensor library for Matlab [75–77] with discretization parameter $\Lambda = 2$, iteration number $N = 60$ and the maximum number of states kept N_K after each iteration as 2^{10} .

1. Influence of finite temperature gradient

We first introduce the finite temperature gradient across a SIAM by keeping the left lead temperature at $T_L = 0.01\Gamma$ and changing the right lead temperature from $T_R = 0.01\Gamma$ to $T_R = 0.5\Gamma$. The electric current $J(V, T_L, T_R)$ and heat current $J^Q(V, T_L, T_R)$ across the SIAM using (5) is calculated for bias voltages close to linear response $V_0 \approx 0.005\Gamma$ using the NRG-tDMRG method. Thus the differential conductance $G(T_L, T_R) \equiv G(V = 0, T_L, T_R)$ can be estimated as

$$G(T_L, T_R) = \frac{1}{2V_0} \left(J(V_0) - J(-V_0) \right) \Big|_{T_L, T_R}. \quad (13)$$

The choice of linear response bias voltage V_0 is such that any nonlinear behavior of $G(V)$ can be avoided, allowing us to treat the estimated currents as linear in V . Since the bias values $V = \pm V_0$ are effectively in the linear response regime, the charge (heat) current $J^{(Q)}$ at zero bias can be calculated according to the linear response expansion as,

$$J^{(Q)}(T_L, T_R) = \frac{1}{2} \left(J^{(Q)}(V_0) + J^{(Q)}(-V_0) \right) \Big|_{T_L, T_R}. \quad (14)$$

The electronic contribution to the heat conductance according to Eq. (9) can thus be $\kappa(T_L, T_R) = J^Q(T_L, T_R) / (T_R - T_L)$. The information about $J(T_L, T_R)$ and $G(T_L, T_R)$ at $V = 0$ is sufficient to calculate the Seebeck coefficient S for the respective parameters. Moreover, the linear response in V allows the current for small voltages to be expressed as $J(V) = J(0) + V G$ for constant T_L and T_R . Thus the Seebeck coefficient S from its definition in Eq. (10) can be estimated as,

$$S(T_L, T_R) = -\frac{1}{T_R - T_L} \frac{J(T_L, T_R)_{V=0}}{G(T_L, T_R)_{V=0}}. \quad (15)$$

The transport coefficients for a quantum dot in the presence of finite temperature gradient calculated using NRG-tDMRG are shown in Fig. 3. The differential conductance G seen in Fig. 3(a) shows the evolution of the zero-bias conductance peak as a function of the orbital energy ε_d . The red dots in Fig. 3(a) display the NRG-tDMRG data for $T_L = T_R = 0.01\Gamma$, which match exactly with the equilibrium NRG data (red curve) for

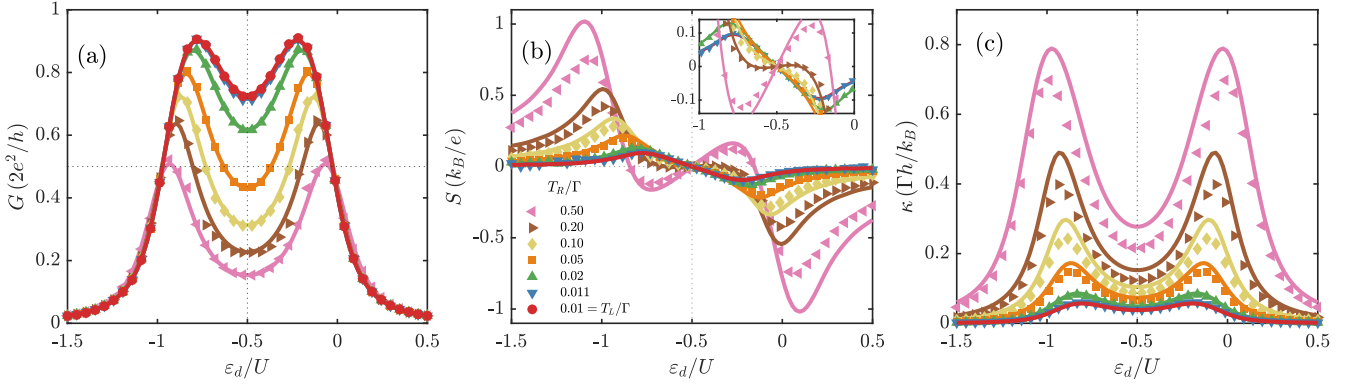


FIG. 3. (a) Differential conductance G , (b) Seebeck coefficient S , and (c) heat conductance κ of an interacting quantum dot [SIAM using parameters (5) except for ε_d which is varied here] vs. orbital level position ε_d in the linear response regime with respect to the bias voltage. The left lead is kept at temperature $T_L = 0.01\Gamma$ throughout, while the right lead temperatures are specified with the legend in (b). The colored symbols are the nonequilibrium data from the NRG-tDMRG calculations and the solid lines present the equilibrium NRG data with the same parameters but calculated for an effective global temperature $T_{\text{eff}} = T_{\text{rms}}$. Numerically, the determination of S and κ require a finite temperature difference ΔT . Hence, no red dots are shown for the case $T_L = T_R$ in (b) and (c). The limiting case $\Delta T \rightarrow 0$, however, is reflected in the small $\Delta T/T \sim 0.1$ data set (blue triangles), which already agrees well with the equilibrium NRG data for $\Delta T = 0$ (red line).

G_0 computed with a global temperature $T = 0.01\Gamma$. The large conductance inside the local moment regime, $-U \lesssim \varepsilon_d \lesssim 0$, is a characteristic feature of the Kondo resonance and the thermal fluctuations from the leads with temperature $T = 0.01\Gamma$ limit the conductance from reaching the unitary value of $G_0 = 2e^2/h$.

The Kondo temperature T_K in the local moment regime is analytically given by the improved Haldane formula from Fermi liquid theory [64]

$$T_K = \sqrt{\frac{\Gamma U}{2}} \exp\left[\frac{\pi \varepsilon_d (\varepsilon_d + U)}{2\Gamma U} + \frac{\pi \Gamma}{2U}\right]. \quad (16)$$

Since the Kondo temperature represents a crossover scale, it is only defined up to a prefactor of order one. Hence, alternatively from a data or experimental point of view, the Kondo temperature can be estimated by the temperature at which the zero-bias conductance drops by half. Below, we will refer to this as $T_{K'}$, where based on our data for the parameters in Eq. (5), $T_{K'} \simeq 1.05 T_K$ [cf. Fig. 4(c) and caption].

For the SIAM parameters in Eq. (5), we have $T_K = 0.042\Gamma$ [as compared to the lowest value at $\varepsilon_d = -U/2$, $T_K = 0.025\Gamma$]. Thus, in the local moment regime, the $G(\varepsilon_d)$ curves in Fig. 3(a) show minima at $\varepsilon_d = -U/2$ corresponding to the lowest T_K . We proceed to heat up the right lead (T_R), as specified in the legends of Fig. 3. With increasing T_R , the differential conductance in the local moment regime decreases as the Kondo resonance dies off with increasing thermal fluctuations from the hotter lead. The equilibrium NRG cannot account for different lead temperatures, but one can still define an effective global temperature T_{eff} at equilibrium as the root mean square value of the left and right lead temperatures

$$T_{\text{eff}} = T_{\text{rms}} = \sqrt{\frac{1}{2}(T_L^2 + T_R^2)}. \quad (17)$$

The significance of the root mean square value will be discussed in the next section, Sec. III B 2. For the sake of the discussion here, it is sufficient to note that $T_{\text{rms}} \rightarrow T$ when $T_R \rightarrow T_L$.

In Fig. 3 we show that a striking agreement exists between the nonequilibrium NRG-tDMRG results at finite thermal bias (colored symbols) and the equilibrium NRG results with an effective global temperature T_{rms} defined as the root mean square value of the lead temperatures. Implying that the dependence on the individual lead temperatures mimics the dependence of equilibrium Kondo resonance width with a global temperature T_{rms} . This is consistent with the low temperature limit from the perturbation theory and slave-boson mean field theory results of Ref. [60]. Moreover, the NRG-tDMRG results are valid for higher temperatures due to the exact treatment of correlations. It is also interesting to note that this effective T_{rms} equivalence extends even into the mixed valence and empty/filled orbital regimes ($\varepsilon_d \lesssim -U$, $\varepsilon_d \gtrsim 0$). Furthermore, the experimental works for the thermoelectrics in the Kondo regime show a good agreement with our results. Figure 2 of Ref. [30], showing the differential conductance and thermocurrent with $\Delta T/T \approx 0.3$ for different T near the Kondo regime, behaves in a very similar way to the results presented here. On the other hand, the experimental data for the Seebeck coefficient shown in Fig. 4 of Ref. [31] were related to the linear response NRG results. We note that in this case, the corresponding temperature gradients, though not precisely determined due to the experimental conditions, reached $\Delta T/T \approx 2/3$ which is well beyond linear response theory. The qualitative agreement obtained with linear-response NRG, nevertheless, we attribute to the T_{rms} equivalence discussed in this paper. A more quantitative agreement can be obtained using $T = T_{\text{rms}}$

in the NRG calculations, provided that the temperatures of the individual leads are known. Of course, deep in nonequilibrium, i.e., much beyond linear response, one needs to resort to out-of-equilibrium approaches such as NRG-tDMRG.

The linear response Seebeck coefficient S_0 of a quantum dot as a function of the global temperature has been shown to change sign with the onset of the Kondo correlations [29–31, 60]. On the other hand, the nonlinear temperature gradient dependence of S in the Kondo regime is largely unknown. Here, with our NRG-tDMRG method, we are able to provide first accurate data on it, which are presented in Fig. 3(b). The red curve represents the equilibrium case where $T_{\text{rms}} = T_L = T_R = 0.01\Gamma$. Note that the calculation of S from NRG-tDMRG requires a finite temperature gradient according to Eq. (15) and thus nonequilibrium data is absent for the $T_L = T_R$ case. The representative linear response results from NRG-tDMRG are presented in the case of $T_R = 0.011\Gamma$ (blue triangles) and agree well with the equilibrium results from NRG. The Seebeck coefficient remains antisymmetric across the particle-hole symmetry point $\varepsilon_d = -U/2$ and has a non-zero value in the local-moment regime, as expected for finite temperatures below T_K .

When the right lead temperature is increased, i.e. with a finite thermal bias, the Seebeck coefficient becomes reduced and starts to change sign in the local moment regime around $T_R = 0.2\Gamma$, indicating the destruction of the Kondo resonance. Interestingly and quite unexpectedly, the comparison to the equilibrium NRG results with a global temperature T_{rms} gives a reasonably good agreement in the local moment regime. The sign change in equilibrium $S_0(T)$ occurs at higher temperatures than T_K , which is also reflected in our finite ΔT results. However, outside the local moment regime, where the Kondo correlations do not emerge, the Seebeck coefficient increases in magnitude (no sign changes) with the increase in T_R and, correspondingly, with T_{rms} . In this regime, the effective linear response results show growing deviations from the nonequilibrium results with increasing temperature gradient.

Finally, for the sake of completeness, we examine the heat conductance κ as a function of ε_d in Fig. 3(c). The heat conductance is dominated by the contribution associated with charge fluctuations, which are most active at resonances. As can be seen, κ generally has two peaks corresponding to the proximity of the resonant levels to the Fermi energy at $\varepsilon_d \approx 0$ and $\varepsilon_d \approx -U$. With a finite thermal bias, κ shows deviations from the linear response T_{rms} calculations that increase with raising the temperature gradient.

2. The Kondo circle

In this section, we discuss how the Kondo effect depends on the individual lead temperatures. For this, we choose the orbital level $\varepsilon_d = -U/3$, for the system to

be in the local moment regime, but far enough from the particle-hole symmetry point to develop sufficient thermopower S .

Figure 4(a) presents the zero-bias differential conductance G as a function of the independent left and right lead temperatures. The conductance G has its maximum as $T_L, T_R \rightarrow 0$ and decays radially in the $T_L - T_R$ plane. In particular, we focus on the temperatures in the scaling regime, i.e. around $T = T_K$, where the conductance $G_0(T)$ is known to exhibit universal behavior. The black [white] dashed curves denote circles of radii $\sqrt{2}T_K$, where T_K is estimated from Eq. (16) [$\sqrt{2}T_{K'}$, where $T_{K'}$ is estimated as the half-width of the linear-response conductance $G_0(T_{\text{rms}})$]. Though the Kondo temperature $T_{K'} \approx 1.05T_K$ from the numerical NRG data provides a more accurate approximation of the Kondo energy scale than the analytical formula, for the sake of generality and ease of estimation, we will stick to T_K as the definition of Kondo temperature in this paper. Therefore, the half-width of the conductance peak lying on the $T_{K'}$ circle is an immediate consequence from the definition of T_{rms} and its correspondence to the nonlinear ΔT in the local moment regime [cf. Fig. 3(a)]. The horizontal cross-sections in panel (b) show how the conductance decays as a function of the right lead temperature T_R , where the temperature on the left lead T_L determines the peak value of the conductance curve. The $G(T_R)$ curve lies below the linear response $G_0(T_R = T_L = T)$ curve for $T_R < T_L$ and coincides with the linear response results at $T_L = T_R$ to remain above the linear response data for $T_R > T_L$. Due to the left-right symmetry in the system, the previous arguments hold true even if one swaps T_L and T_R . The conductance data $G(T_L, T_R)$ is plotted against the rescaled T_{rms} temperature in the panel (c). The rescaled data lies perfectly on top of the linear response $G_0(T_{\text{rms}})$ curve. This is a useful result, especially for the experimental exploration of the Kondo regime. In experiments, where one do not reach the truly linear response regime [30–33], T_{rms} can provide reliable theoretical estimations from equilibrium NRG calculations to accurately identify the parameter space of the Kondo regime in T_L and T_R separately.

In general, the zero-bias conductance peak along with the Kondo resonance is known to get smeared with increasing thermal fluctuations [6, 8]. The influence of the individual lead temperatures on the whole $G(V)$ curve beyond linear response bias voltage regime is less trivial and is shown in Fig. 5(a). The lower plane in Fig. 5(a) presents the $G(V)$ calculations for a cold left lead temperature $T_L \approx 0.1T_K$ and with increasing the right lead temperatures $T_R > T_L$. For small temperatures $T_R \ll T_K$, the conductance peak remains sharp in the finite V regime but with an increase in T_R around $T_R \approx 0.2T_K$ the Kondo peak starts to get smeared out in V . This behavior is clearly seen in $G(V)$ curves for different T_R presented in Fig. 5(b), where the increase in T_R suppresses the conductance at zero bias and smears the zero-bias conductance peak further into the finite V

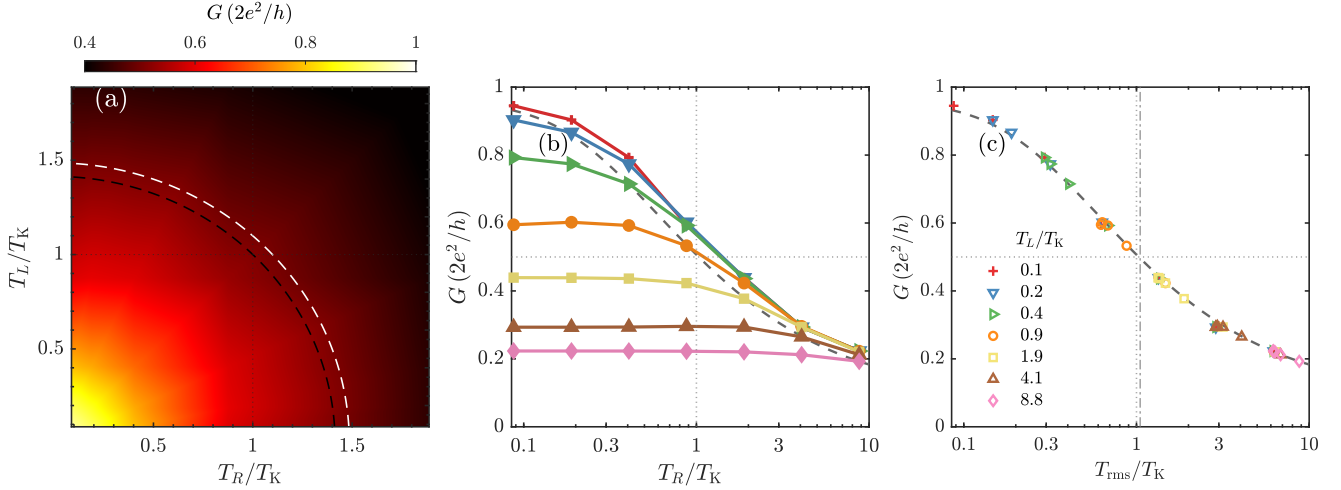


FIG. 4. (a) The differential conductance G through the quantum dot with orbital energy $\varepsilon_d = -U/3$ as in (5) as a function of the left and right lead temperatures, T_L and T_R , in the linear response regime $V \rightarrow 0$. The black dashed curve shows a circle of radius $\sqrt{2}T_K$ corresponding to $T_{rms} = T_K$ [cf. Eq. (16)], while the white dashed line shows $T_{rms} = T_K'$ estimated as the half-width of the zero-bias conductance peak from the NRG data versus effective temperature. The colored symbols in (b) present horizontal cross-sections of (a) for different values of T_L , as shown with panel (c) vs. T_R on a logarithmic scale. For comparison, the black dashed line displays the linear response NRG results of G vs. $T_R = T_L \equiv T$. Panel (c): Data in (b) replotted against the effective global temperature T_{rms} in Eq. (17). This is again contrasted with the equilibrium NRG data (black dashed line) where the vertical dash-dotted line denotes the half-width of equilibrium conductance $T_K' \simeq 1.05 T_K$.

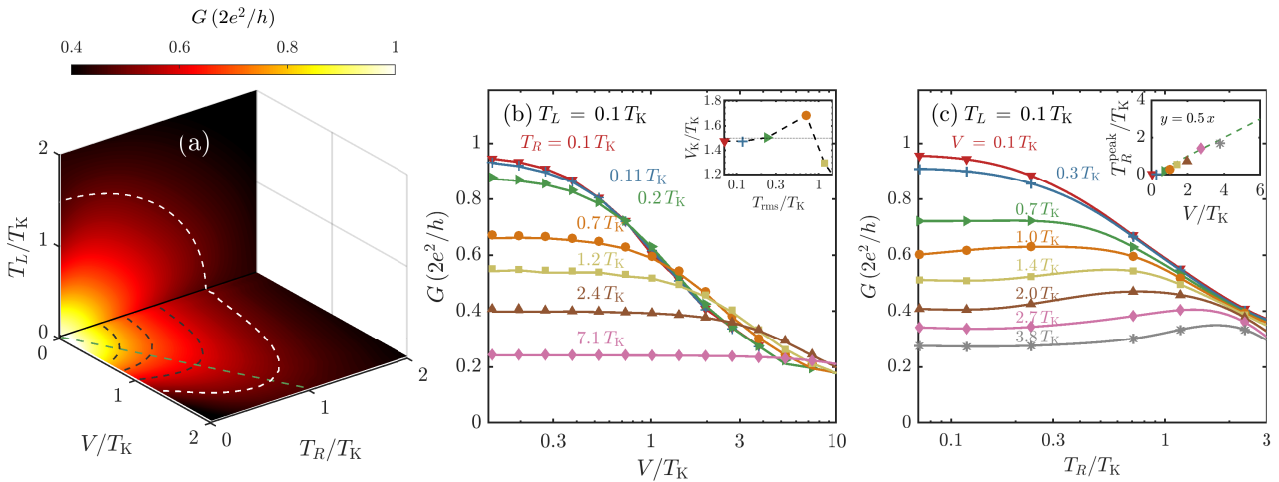


FIG. 5. (a) The differential conductance G through a quantum dot [SIAM using (5)] vs. T_L , T_R and a finite potential bias V . The data in the vertical plane is the same as in Fig. 4 (a), the horizontal plane is calculated with $T_L = 0.1 T_K$ and for different T_R as specified in the legends of panel (b). The black [white] dashed lines on the horizontal plane show the contours of constant conductance $G = (0.8, 0.7, 0.6)$ [$G = 0.5$]. The green dashed line indicates $T_R = V/2$, cf. inset to panel (c). Panel (b) shows the cross-sections (symbols) of the horizontal plane in panel (a) for a fixed right lead temperature as indicated by the colored labels. The solid lines show the corresponding $G(V)$ calculations for an effective global lead temperature $T_{rms} = T_L = T_R$. The inset in panel (b) tracks V_K , the Kondo scale in the applied bias, defined as $G(V_K) = 0.5$. Panel (c) shows the differential conductance $G(T_R)$ from the horizontal plane in panel (a) for a finite potential difference V , as indicated by the colored labels. Lines represent spline interpolations of the semilog-x data used to estimate the peak position T_R^{peak} . Inset shows T_R^{peak} vs. V , which approximately follows $T_R^{peak} = V/2$ (green dashed line).

regime.

Furthermore, we observe in our simulations that any configuration of the lead temperatures $G(V)_{T_L, T_R}$ can be approximated by a $G(V)_{T_{rms}, T_{rms}}$ curve with global tem-

perature T_{rms} [cf. solid lines in Fig. 5(b)]. The Kondo energy scale in the applied bias V_K , defined as the bias at which the conductance drops to one-half $G(V_K) = 1/2$, is a characteristic energy scale of the nonequilibrium Kondo

effect and behaves differently from T_K . The inset in Fig. 5(b) shows the dependence of V_K on T_{rms} . At low temperatures $T \ll T_K$, we recover the Fermi liquid theory prediction for the Kondo energy scales $V_K/T_K \approx 3/2$ [64, 72, 73, 78]. It can be seen that V_K increases with T_{rms} , corresponding to the smearing of the Kondo resonance with thermal fluctuations up to $T_{\text{rms}} \approx T_K$. Beyond which the Kondo resonance is considerably destroyed by the thermal fluctuations, such that $G(V)$ fails to attain the definition of V_K for temperatures around $T_{\text{rms}} \approx 1.3 T_K$ [cf. Fig. 5(b)].

Figure 5(c) shows the influence of the right lead temperature T_R on the differential conductance $G(T_R)_{T_L, V}$ with a constant T_L and finite potential bias V . For very small potential biases $V \ll T_K$, the differential conductance G monotonously decreases with increasing T_R , closely resembling the true zero-bias conductance curve in Fig. 4(b). In the case of a large potential bias $V \gtrsim T_K$, the $G(T_R)$ curves show maxima roughly located at a finite right lead temperature $T_R^{\text{peak}} \approx V/2$ [cf. inset of Fig. 5(c)]. This nonmonotonous behavior of $G(T_R)_{T_L, V}$ for $V > T_K$ can be attributed to the splitting of the Kondo resonance in the presence of large potential biases. Due to the bias configuration in our system, $\mu_{L/R} = \pm V/2$, the peaks of the split-Kondo resonance will be located at the respective lead potentials $\mu_{L/R}$ for $V \gtrsim T_K$, resulting in the additional feature in $G(T_R)$ around $T_R = V/2$.

3. Thermoelectrics of the Kondo circle

Instead of diving directly into the Seebeck coefficient, we first look at the thermoelectric current driven by the finite thermal bias in Fig. 6. The panel (a) shows the NRG-tDMRG results for the charge current as a function of both the left and right lead temperatures. The current $J(T_L, T_R)_{V=0}$ is antisymmetric across the $T_L = T_R$ line, as the temperature gradient changes sign across this line. In addition, there exists another sign change roughly as a circle in the T_L, T_R plane corresponding to the onset of Kondo correlations. The current at zero bias, computed as $J(T_L, T_R)_{V=0} = \frac{1}{2} (J(V_0) + J(-V_0))|_{T_L, T_R}$ from the data for small $\pm V_0$ [cf. Eq. (13)], can be fitted by the polynomial expression up to order n as in

$$J(T_L, T_R)_{V=0} = \Gamma \frac{T_L - T_R}{T_{\text{rms}}} p_n(x \equiv \frac{T_L}{T_K}, y \equiv \frac{T_R}{T_K}), \quad (18)$$

where

$$p_n(x, y) = \sum_{k=1}^n \sum_{i=0}^k a_{k,i} x^i y^{k-i}, \quad (19)$$

$$a_{k,i} = a_{k, k-i}. \quad (20)$$

Having $V = 0$, the current needs to be antisymmetric under inversion $T_L \leftrightarrow T_R$. This is taken care of by the leading factor $T_L - T_R$ on the RHS. The remaining polynomial $p_n(\frac{T_L}{T_K}, \frac{T_R}{T_K})$ thus must be symmetric

under inversion. This constrains the polynomial terms to Eq. (20). The denominator T_{rms} keeps the prefactor in check for large ΔT . i.e., the ratio $\frac{T_L - T_R}{T_{\text{rms}}} \rightarrow \sqrt{2}$ as $T_R \rightarrow \infty$. Thus providing a much more consistent weights for the data points with large ΔT used in the variational fitting. We note that a clean polynomial fit of the form $(T_L - T_R) p_n(\frac{T_L}{T_K}, \frac{T_R}{T_K})$ can still provide an acceptable fit for the current, but including the denominator T_{rms} considerably improves the fit at low T . At first glance, Eq. (18) only seems to account for the first order in ΔT . But, the first order polynomial terms T_L, T_R together with the $T_L - T_R$ prefactor makes up the $(T_L - T_R)^2 \equiv \Delta T^2$ dependence, the polynomial terms T_L^2, T_R^2 and $T_L T_R$ have encoded in it the information of the ΔT^3 dependence, and accordingly for the higher order dependences in ΔT . Thus the polynomial fit contains, but is not limited to, the perturbative expansion of J on ΔT .

The polynomial coefficients are determined by minimizing the cost function

$$C = \sum_i \left| J(T_L, T_R)|_i - \Gamma \frac{(T_L - T_R)}{T_{\text{rms}}} |_i p_n(x_i, y_i) \right|^2, \quad (21)$$

where the sum runs over all data points i with $T_L \neq T_R$. The quality of the fit is then estimated by the error measure $\delta_{\text{fit}} = \sqrt{\min(C)}$. The fit in Fig. 6 used $n = 4$ with coefficients

$$\begin{aligned} (a_{10}) &= (2.7874) \\ (a_{20}, a_{21}) &= (-1.0856, -0.9690) \\ (a_{30}, a_{31}) &= (0.1363, 0.1418) \\ (a_{40}, a_{41}, a_{42}) &= (-0.0068, -0.0091, -0.0060) \end{aligned} \quad (22)$$

n	$\delta_{\text{fit}}/\bar{J}$
1	0.9690
2	0.0051
3	0.0010
4	0.0002

TABLE I. The degree n of the polynomial used for the fit and corresponding error δ_{fit} relative to \bar{J} the largest value of thermoelectric current inside the Kondo circle.

The thermoelectric current from the polynomial fit Eq. (18) is shown in Figs. 6(b,c). The polynomial fit accurately recovers the regions of sign change in Fig. 6(a). The error measure of the fits presented in Table I shows that increasing order of the polynomial improves the fit quality. The fit converges at higher orders of the polynomial, indicated by the decreasing magnitude of the polynomial coefficients for the higher order terms [cf. Eq. (22)].

The estimation of S from Eq. (15) relies on the induced thermocurrent being small enough to be compensated by

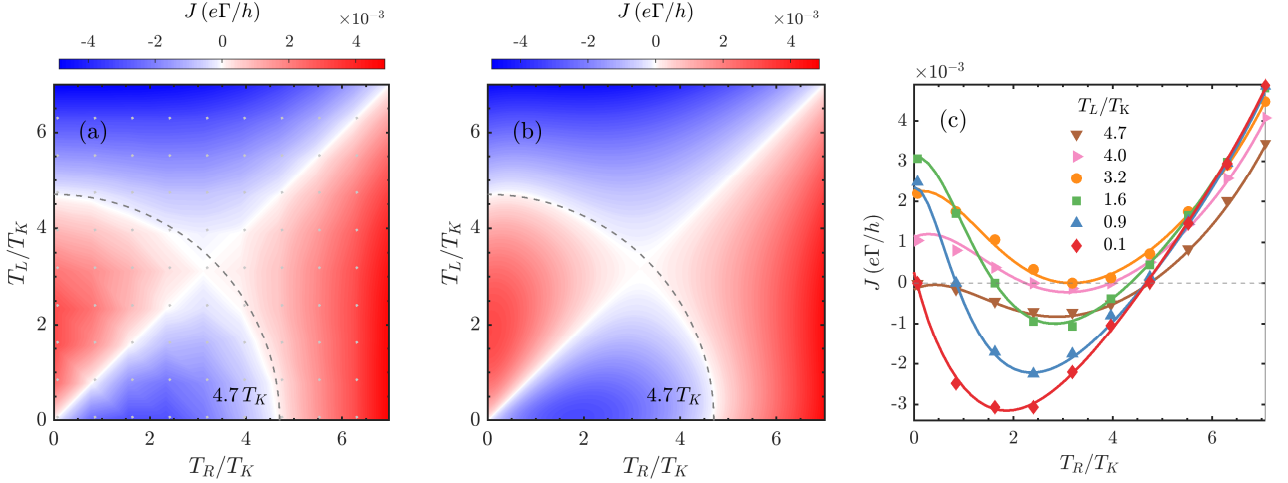


FIG. 6. (a) Thermoelectric current J through a quantum dot [SIAM using (5)] vs. T_L and T_R at $V = 0$ (computed as the average current for $V = \pm 10^{-2} T_K$). The data points located at the white dots are interpolated by the smooth color shading (cf. color bar). Panel (b) same as panel (a), but showing the polynomial fit of its data points based on Eq. (18) instead. Panel (c) shows horizontal cuts of the polynomial fit (lines) in panel (b) with their corresponding data points (symbols) from panel (a).

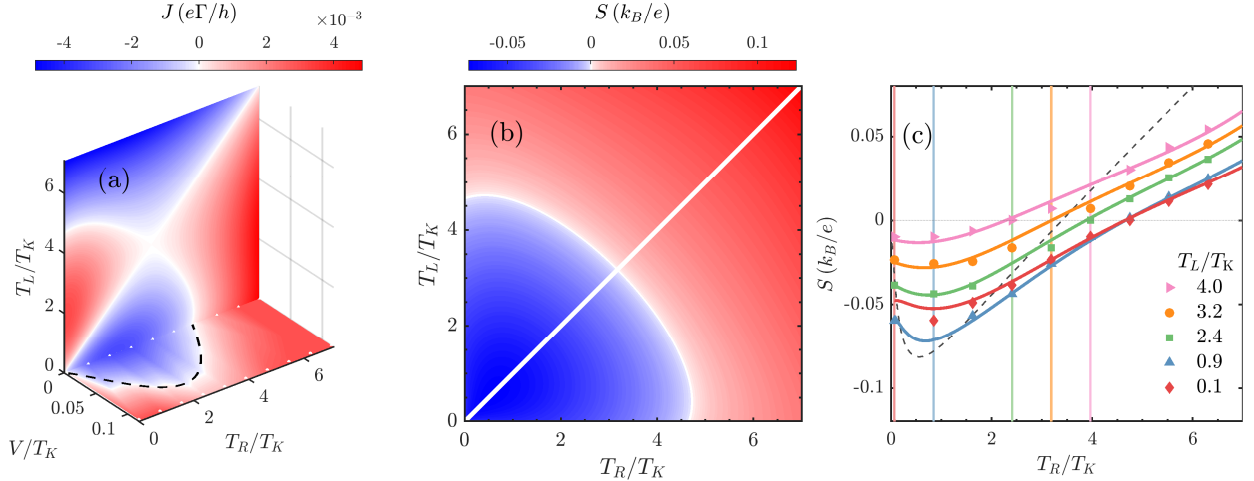


FIG. 7. (a) Thermoelectric current J through a quantum dot [SIAM using (5)] vs. T_L , T_R and for very small potential biases V . The black dashed curve shows the voltage V required to compensate the thermocurrent according to a linear response expansion with G_0 . The grid of NRG-tDMRG data in V is represented as white dots on the V, T_R plane. (b) The Seebeck coefficient $S = -V/\Delta T = -J/(G \Delta T)$ (assuming linear response in G) for the same parameters as in panel (a). Panel (c) shows the horizontal cross-sections of the panel (b) comparing S calculated from the fit [cf. Eq. (18)] (solid line) and S estimated from $J(T_L, T_R)_{V=0}$ from NRG-tDMRG (colored symbols). For comparison, the black dashed curve shows the linear response NRG calculations for S_0 with $T_L = T_R$. The colored vertical lines denote the corresponding left lead temperature T_L for each $S(T_R)$ curve.

a linear response bias V . In Fig. 7(a) we show the extension of the density plot in Fig. 6(a) towards the third dimension in the bias voltage V . The lower plane in V, T_R is calculated for $T_L \approx 0.1 T_K$ [brown curve in Fig. 6(c)], which contains the largest value of thermocurrent data in the Kondo regime. The points of zero current in the lower plane show that a bias voltage $V < V_0$ is sufficient to compensate for the induced thermocurrent. The zero

current (white) in the interpolated colormap from the NRG-tDMRG data for finite $V = \pm V_0$ coincides with the bias estimated from the linear response expansion (black dashed curve) of the current with the linear response conductance $G_0(T_{\text{rms}})$, further corroborating the choice of the linear response V_0 . Thus, Fig. 7(b) depicts the Seebeck coefficient S estimated for the full scaling regime in T_L, T_R plane. From the sign changes of the

thermoelectric current $J(T_L, T_R)$ in Fig. 6, only the sign change corresponding to the Kondo correlations survive for $S(T_L, T_R)$. This region of the sign change in the Seebeck coefficient now fully represents the temperature regime in which the Kondo correlations survive. The Kondo regime is roughly a circle in the T_L, T_R plane, slightly squeezed in the $T_L = T_R$ direction. It is important to note that the radius of the Kondo regime in the T_L, T_R plane determined by the points of sign change in S does not show any universal scaling with respect to T_K . The equilibrium NRG studies of S_0 have already demonstrated that the temperature at which $S_0(T)$ shows the maximum negative value in the Kondo regime scales with the Kondo temperature T_K . But the temperature at which S_0 changes sign, denoting the onset of Kondo correlations, does not exhibit such scaling with respect to T_K [29].

The quantitative behavior of $S(T_L, T_R)_{V=0}$ is shown in Fig. 7(c). The Seebeck coefficient S estimated from the NRG-tDMRG calculations (colored symbols) of the thermoelectric current $J(T_L, T_R)_{V=0}$ in Fig. 6 and S estimated from the polynomial fit for the thermoelectric current (solid lines) as in Eq. (18) with a constant T_L are plotted as a function of T_R . Near the equilibrium temperature $T_R \rightarrow T_L$, the NRG-tDMRG results approach the linear response NRG estimations of S_0 . We note that, since $T_L = T_R$ induces no thermoelectric current, the extraction of the linear response S_0 using NRG-tDMRG from the chosen T_L, T_R grid of datapoints is not possible [cf. Eq. (15)], and hence no datapoints from NRG-tDMRG are shown for the case of $T_L = T_R$ in Fig. 7(c). The polynomial fit for the thermoelectric current from Eq. (18) is unrestrained and can provide an approximation of the linear response S_0 for $T_L \rightarrow T_R$. $S(T_R \rightarrow T_L)$ estimated from the fit shows slight quantitative difference from the true linear response S_0 obtained from NRG, presumably stemming from the absence of very small ΔT in the data used for fitting. In general, for a constant T_L in the Kondo regime, $S(T_R)$ starts from a negative value for $T_R \rightarrow 0$ and shows a minima at temperature T_R of the order of T_K . With further increase in the temperature, $S(T_R)$ grows gradually until changing its sign denoting the total destruction of the Kondo resonance.

The comparison of $S(T_L, T_R)$ rescaled by the effective temperature T_{rms} and the linear response $S_0(T)$ from NRG is presented in Fig. 8. Unlike the differential conductance $G(T_{\text{rms}})$, the rescaled $S(T_{\text{rms}})$ data do not fully resemble the linear response $S_0(T)$ behavior, with increasing deviations for large temperature gradients. We observe that the deviation of $S(T_{\text{rms}})$ depends on the minima of the linear response S_0 . We define T_p as the temperature, at which S_0 has a negative peak. When the cold lead temperature is larger than T_p , $S(T_{\text{rms}})$ lies closer to the linear response S_0 . But for the case of a cold lead temperature below T_p , left lead temperature $T_L \approx 0.1 T_K$ in our case [cf. red diamonds in Fig. 8], $S(T_{\text{rms}})$ shows the largest deviations from the linear re-

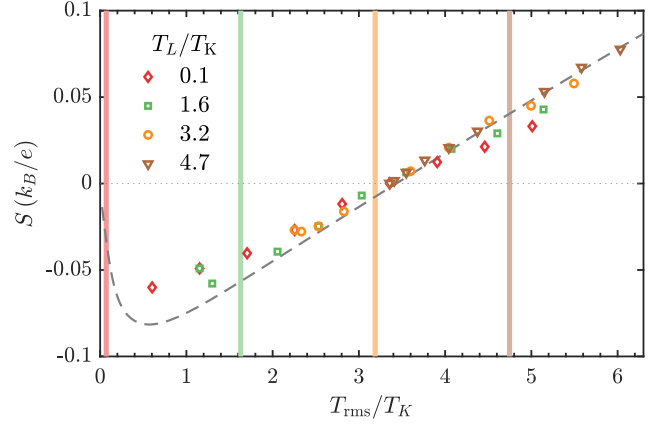


FIG. 8. The Seebeck coefficient $S(T_L, T_R)$ (colored symbols) with a fixed T_L (vertical colored lines) plotted against the effective temperature T_{rms} . The dashed line shows the equilibrium NRG data for $S_0(T_L = T_R = T_{\text{rms}})$.

sponse S_0 .

From the data in Fig. 8 we can conclude that the magnitude of the Seebeck coefficient is not enhanced when compared to linear response S_{lin} under zero-bias conditions even with nonlinear temperature gradients. Furthermore, the data in Fig. 8 shows rather small values $|S| \lesssim 1$ for the Seebeck coefficient in the Kondo regime. This is in contrast, for example, to Fig. 3 where the Seebeck coefficient can reach values an order of magnitude higher $|S| \gtrsim 1$ just outside the local moment regime. Based on these findings, let us briefly comment here on how to potentially enhance the thermoelectric response in the Kondo regime [42]. It was suggested that an asymmetric coupling to the leads together with a finite potential bias can improve the thermoelectric response in the Kondo regime, as suggested in Ref. [46]. While the NRG-tDMRG method is well-suited to handle such systems, a thorough investigation of this scenario necessitates a detailed study of its own and thus is beyond the scope of the present work.

Lastly, we analyze the heat current and heat conductance in the presence of a finite temperature gradient. The heat current J^Q across the quantum dot coupled to leads with temperatures T_L and T_R is shown in Fig. 9(a). Unlike the Seebeck coefficient, there exist no sign change in the heat conductance characterizing the Kondo resonance. Thus, the heat current shows only one sign change corresponding to the change in the sign of the temperature gradient $T_L - T_R$. The electronic contribution to the heat conductance κ calculated for the cross sections in panel (a) is presented in panel (b). It can be seen that for a constant T_L , κ is enhanced with increase in T_R . When reaching $T_R = T_L$, the heat conductance smoothly crosses the linear response κ_0 .

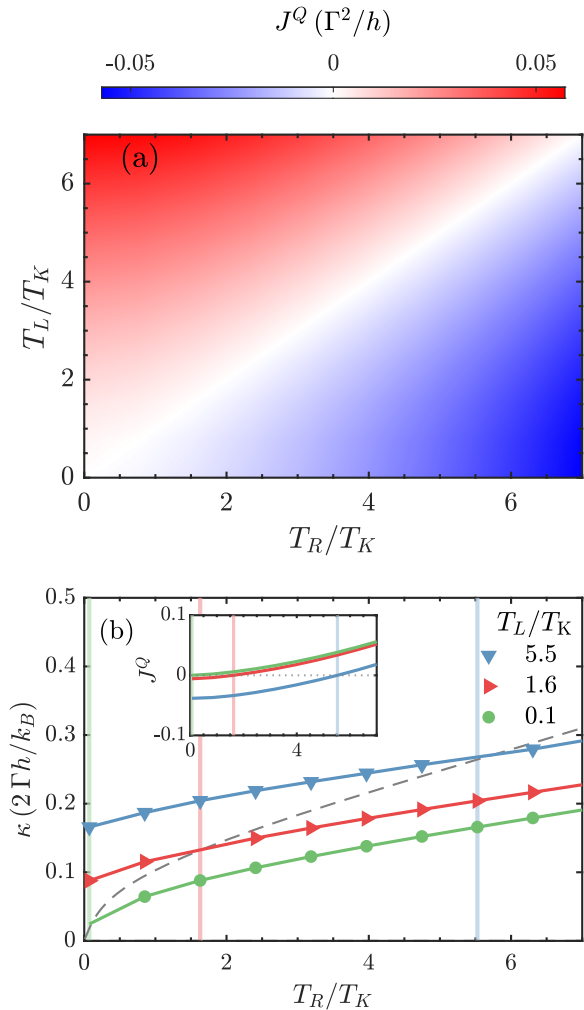


FIG. 9. (a) The heat/energy current J^Q through a quantum dot [SIAM using (5)] as a function of the left lead temperature T_L and the right lead temperature T_R . (b) shows the heat conductance κ for different values of T_L , as indicated. The dashed line corresponds to the equilibrium NRG results for κ_0 ($T = T_L = T_R$). The inset presents the horizontal cross sections of panel (a) used for the estimation of κ in panel (b).

IV. SUMMARY

In this work we have provided accurate quantitative results for the thermoelectric transport properties of a Kondo-correlated quantum dot subject to nonlinear temperature and voltage gradients. The calculations have been performed with the aid of numerical renormalization group–time-dependent density matrix renormalization group method. First of all, we have demonstrated that the thermoelectric behavior of the system, involving charge and heat currents as well as the Seebeck coefficient, can be qualitatively described by an effective global temperature T_{rms} . Moreover, a detailed investigation of the zero-bias conductance with respect to the

individual lead temperatures unveiled the Kondo regime as a circle in the plane of left-right lead temperatures, further affirming the qualitative agreement with T_{rms} . The thermoelectric current also showed characteristic sign changes crossing over to the Kondo regime, as a slightly distorted circle with the deviations occurring at large temperature gradients. Moreover, we have provided a qualitative expression to fit the thermoelectric current as a function of the left and right lead temperatures. Finally, we have discussed the heat current and conductance near the Kondo regime, which were mostly determined by the contribution from charge fluctuations, hardly revealing characteristics of the Kondo resonance.

The thermoelectrics in the presence of finite temperature gradients at zero bias voltage did not show any enhancement of the thermoelectric properties originating from the nonlinear contributions in the Kondo regime. However, investigating the nonequilibrium regime of asymmetrically coupled Kondo-correlated systems [46] is a promising direction where NRG-tDMRG can yield reliable insights. This complex scenario warrants a dedicated study of its own which goes beyond the scope of the present work and thus is left for the future.

V. ACKNOWLEDGEMENTS

This work was supported by the Polish National Science Centre from funds awarded through Decision No. NCN 2022/45/B/ST3/02826. A.M. acknowledges Brookhaven National Laboratory for hosting a research visit that contributed significantly to this work and is grateful to the NAWA-STER program for financial support provided for the visit through Decision no. PPI/STE2020/1/00007/U/00001. A.W. was supported by the U.S. Department of Energy, Office of Science, Basic Energy Sciences, Materials Sciences and Engineering Division. This work was funded in part by the Deutsche Forschungsgemeinschaft under Germany’s Excellence Strategy EXC-2111 (Project No. 390814868). We acknowledge helpful discussions with Kacper Wrzeźniewski during the development of this work.

VI. DATA AVAILABILITY STATEMENT

The datasets generated and analyzed for this work are publicly available on Zenodo at <https://doi.org/10.5281/zenodo.13773063>.

Appendix A: The Hybrid NRG-tDMRG method

We use a hybrid NRG-tDMRG method to study the nonequilibrium dynamics of the quantum dot coupled to leads with finite thermal and potential bias. Below, we

provide more details about this method and its extension to finite thermal gradients.

1. Hybrid discretization scheme

Primarily, we separate the conduction band into modes that can be treated in equilibrium and out-of-equilibrium. i.e., the modes with $f_L(\omega) - f_R(\omega) = 0$ correspond to the modes that are at equilibrium and $f_L(\omega) - f_R(\omega) \neq 0$ are the modes that are out of equilibrium, where $f_\alpha(\omega)$ is the Fermi function for the lead α . For simplicity, we keep the largest $|\omega|$ that satisfies $f_L(\omega) - f_R(\omega) \neq 0$ as our effective bandwidth D^* and define the transport window as $[-D^*, D^*]$ (essentially including more equilibrium modes into the tDMRG part, which is easier to handle and provides a more accurate description than moving more nonequilibrium modes into the NRG part). The energies outside $|D^*|$ are discretized logarithmically according to the discretization parameter Λ and the energies inside $|D^*|$ are discretized linearly according to the discretization parameter δ . In this discretized setting, the coupling between the quantum dot energy level ε_d to a discretized mode in the lead α with momentum k is given as $v_q = \sqrt{\Gamma_\alpha \delta_k / \pi}$, where δ_k is the size of the corresponding interval in the discretized band.

2. Thermofield treatment

We go on to describe the modes in this log-lin discretized band under a thermofield description. This entails the introduction of an auxiliary decoupled Hilbert space akin to the physical Hilbert space. For a mode c_{q1} in the physical Hilbert space, where $q \equiv \alpha, k, \sigma$ is a composite index, we introduce an auxiliary mode c_{q2} , where the index 2 denotes that the mode is in the auxiliary Hilbert space. This enlarged Hilbert space is rotated by,

$$\begin{pmatrix} \tilde{c}_{q1} \\ \tilde{c}_{q2} \end{pmatrix} = \begin{pmatrix} \sqrt{1-f_q} & -\sqrt{f_q} \\ \sqrt{f_q} & \sqrt{1-f_q} \end{pmatrix} \begin{pmatrix} c_{q1} \\ c_{q2} \end{pmatrix}, \quad (\text{A1})$$

such that in the rotated tilde Hilbert space, the modes $\tilde{c}_{q1} |\Omega\rangle = \tilde{c}_{q2}^\dagger |\Omega\rangle = 0$ can be interpreted as holes (1) and particles (2), where $|\Omega\rangle = \prod_q (\sqrt{1-f_q} |0, 1\rangle_q + \sqrt{f_q} |1, 0\rangle_q)$ is a pure state that can represent the thermal expectation value of an operator A on the physical lead as $\langle A \rangle = \langle \Omega | A | \Omega \rangle$.

In the rotated Hilbert space, the lead Hamiltonian becomes,

$$\mathcal{H}_{\text{lead}} = H_{\text{lead}} + H_{\text{aux}} = \sum_{qj} \varepsilon_q c_{qj}^\dagger c_{qj} = \sum_{qj} \varepsilon_q \tilde{c}_{qj}^\dagger \tilde{c}_{qj}. \quad (\text{A2})$$

We set $\varepsilon_{q2} = \varepsilon_{q1}$ to keep the total lead Hamiltonian $\mathcal{H}_{\text{lead}}$ diagonal. Similarly, the tunneling Hamiltonian in the rotated Hilbert space can be described as,

$$H_{\text{tun}} = \sum_{qj} (\tilde{v}_{qj} d_{\alpha\sigma}^\dagger \tilde{c}_{qj} + \text{H.c.}), \quad (\text{A3})$$

where the couplings $\tilde{v}_{q1} = v_q \sqrt{1-f_q}$ and $\tilde{v}_{q2} = v_q \sqrt{f_q}$ become functions of the Fermi-Dirac distribution functions and, thus, encompass the information about the nonequilibrium parameters, such as the temperature and potential bias on the leads.

3. Recombination of the leads and tridiagonalization

Outside the transport window $[-D^*, D^*]$, the impurity is coupled to only half of the lead modes. Since, $f_\alpha \rightarrow 1$ results in the hole coupling $\tilde{v}_{q1} \rightarrow 0$ and $f_\alpha \rightarrow 0$ results in the particle coupling $\tilde{v}_{q2} \rightarrow 0$. This essentially means that both the high energy particle modes and the low energy hole modes decouple from the impurity. Whereas for the energies inside the transport window, we use a different approach to simplify the structure. Then, a single impurity coupled to two leads can be described using an effective model with an impurity coupled to a single recombined lead and such a recombination of the leads results in half of the modes being decoupled from the system. This results in the quantum impurity being coupled to a set of hole lead modes and another set of particle lead modes. In next step, we proceed to tridiagonalize these particle and lead modes separately, resulting in two chains that are coupled to the impurity, one from the hole modes and another from the particle modes. In these chains, we can identify two sectors, the sector from the high energy modes that lies closest to the impurity on the chain exhibiting properties of a Wilson chain, i.e., energy scale separation and couplings that decay as $t_n \sim \Lambda^{-n}$.

4. NRG treatment of high energy modes and time evolution

Since the modes outside the transport window are essentially in equilibrium, we recombine the holes and particles in the high energy sector for a more physically accurate description. This results in our impurity being coupled to an effective Wilson chain corresponding to the high energy sector, which is then further coupled to the separate hole and particle chains. We treat the recombined high energy modes using the numerical renormalization group method and extract the ground state of the high energy sector as $|\phi_{\text{ini}}\rangle$. $|\phi_{\text{ini}}\rangle$ will act as the initial state for the high energy part of the chain, where the low energy hole modes are kept empty and the particle modes filled. Thus, our initial state for the time evolution $|\psi_{\text{ini}}\rangle$ becomes

$$|\psi_{\text{ini}}\rangle = |0\rangle \otimes |0\rangle \otimes \dots \otimes |0\rangle \otimes |\phi_{\text{ini}}\rangle \otimes |1\rangle \otimes \dots \otimes |1\rangle \otimes |1\rangle. \quad (\text{A4})$$

We time evolve $|\psi_{\text{ini}}\rangle$ using the second-order Trotter time evolution with a quench on the coupling between the high energy and low energy sector over a finite time window.

The NRG-tDMRG calculations for the SIAM in this paper are performed with parameters $\Lambda = 2.5$, $\delta/D^* = 0.01$, $N_{\text{keep}} = 900$ kept states in the effective NRG basis of the renormalized impurity, and a truncation tolerance of $\epsilon_{\text{SVD}} = 10^{-5}$ for the tDMRG sweeps. The observables are calculated for 100 tDMRG sweeps with the first 20 sweeps dedicated for the quench.

5. Charge and heat current

The particle current or the charge current J_α from the lead α to the quantum dot can be described as,

$$J_{\alpha\sigma} = e \langle \dot{N}_\sigma \rangle = -\frac{i}{\hbar} \langle [N_\sigma, H] \rangle$$

$$J_{\alpha\sigma} = \frac{e}{\hbar} \sum_k \text{Im} (v_{\alpha k} \langle d^\dagger c_{\alpha k} \rangle) \quad (\text{A5})$$

$$\equiv \frac{e}{\hbar} \sum_k \sum_j \text{Im} (\tilde{v}_{qj} \langle d^\dagger \tilde{c}_{qj} \rangle). \quad (\text{A6})$$

Similarly, the energy current J_α^E from the lead α to the quantum dot can be described based on the lead Hamiltonian as,

$$J_\alpha^E = \langle \dot{H}_\alpha \rangle = -\frac{i}{\hbar} \langle [H_\alpha, H] \rangle$$

$$= \frac{2e}{\hbar} \sum_{k\sigma} \sum_j \varepsilon_q \text{Im} (\tilde{v}_{qj} \langle d^\dagger \tilde{c}_{qj} \rangle). \quad (\text{A7})$$

The symmetrized current $J_\sigma(t)$ converges faster than the individual lead currents $J_{\alpha\sigma}$,

$$J_\sigma(t) = \frac{1}{2} (J_{L\sigma}(t) - J_{R\sigma}(t)) \quad (\text{A8})$$

Appendix B: Extracting steady state observables via linear prediction

The particle current shows a transient behavior during the quench window and starts to oscillate around a steady-state value. This steady state is extracted using linear regression. We start by generating a kernel for the oscillating part based on the training window

$$y_{n+1} = \underbrace{\begin{bmatrix} a_1 & a_2 & \cdots & a_n \end{bmatrix}}_K \begin{bmatrix} x_1 \\ x_2 \\ \vdots \\ x_n \end{bmatrix}, \quad (\text{B1})$$

where the kernel K estimates the next data point y_{n+1} based on the previous n data points $\{x_1, x_2, \dots, x_n\}$. We estimate K as the least squared approximation of the data points in the training window. The spectral decomposition of the kernel has the information about the oscillating behavior of the data. In particular, we isolate the eigenvector with the real eigenvalue (corresponding

to the non-oscillating part) to estimate the steady state current at $t \rightarrow \infty$

$$J(t \rightarrow \infty) = \frac{\|\vec{e}_0\|}{\sqrt{\varepsilon_0}}, \quad (\text{B2})$$

where \vec{e}_0 is the eigenvector corresponding to the real eigenvalue ε_0 . Figure 10 shows the charge current (a,b,c) and the heat current (d,e,f) dynamics of a SIAM using (5) obtained from NRG-tDMRG. The steady state value estimated from linear prediction is shown as the horizontal dashed line.

Appendix C: Effective Kondo energy scale

Analytical dependence of the Kondo energy scale on the temperature gradient has been discussed in Ref. [60] by using the perturbation theory and slave-boson mean-field theory. According to the perturbation theory, the Kondo energy scale depends on the temperature gradient as,

$$\tilde{T}_K^{\text{PT}}(\Delta T) = \sqrt{T_K^2 + \left(\frac{\Delta T}{2}\right)^2} - \frac{\Delta T}{2}, \quad (\text{C1})$$

where \tilde{T}_K is defined as the energy scale at which the second-order term dominates in the perturbation expansion of the conductance in the Kondo model [Eq. (11) and Eq. (13) from the Ref.[60]]. Nevertheless, throughout this paper, T_K denotes the intrinsic Kondo temperature of the system as defined in Eq. (16).

From the NRG-tDMRG calculations, an effective temperature of $T_{\text{rms}} = T_K$ in the $T_L - T_R$ plane represents a circle of the form $T_L^2 + T_R^2 = 2T_K^2$. To compare with the results from perturbation theory, we consider $T_L = T$ and $T_R = T + \Delta T$. Thus, we can define the energy scale $\tilde{T}_K(\Delta T)$ for a fixed ΔT ,

$$G(T, T + \Delta T)|_{T=\tilde{T}_K} = G_0/2, \quad (\text{C2})$$

i.e., as the temperature T at which $G(T, T + \Delta T)$ reaches the half maximum of the conductance peak G_0 at $T = \Delta T = 0$. By definition then, \tilde{T}_K reduces with increasing ΔT towards zero, and becomes undefined for sufficiently large $\Delta T > T_K$ once $G(T, T + \Delta T) < G_0/2$ for all T . In this sense, $\tilde{T}_K \rightarrow 0$ does not indicate a small physical Kondo scale, per se, but rather the disappearance of the Kondo physics. Based on the Kondo circle $T_L^2 + T_R^2 = 2T_K^2$ [cf. Sec. III B 2], Eq. (C2) provides an analytical expression for \tilde{T}_K

$$\tilde{T}_K(\Delta T) = \sqrt{T_K^2 - \left(\frac{\Delta T}{2}\right)^2} - \frac{\Delta T}{2}. \quad (\text{C3})$$

This expression for $\tilde{T}_K(\Delta T)$ is very similar to the perturbation theory result, except for the difference in sign of the ΔT^2 term under the square root.

The temperature \tilde{T}_K defined on the Kondo circle and the Kondo temperature \tilde{T}_K^{PT} from the perturbation theory show good agreement for small ΔT [cf. Fig. 11]. With

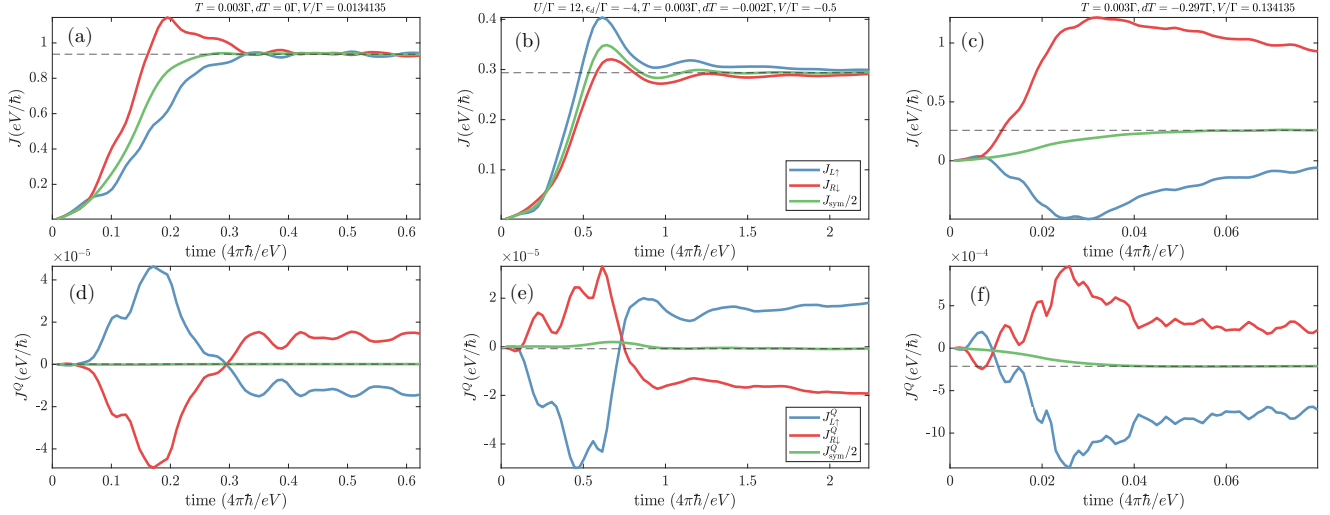


FIG. 10. The finite time dynamics of (a,b,c) charge current J and (d,e,f) heat current J^Q across a SIAM for representative values of the applied potential and temperature gradients. The horizontal dashed line shows the steady state value obtained from linear prediction.

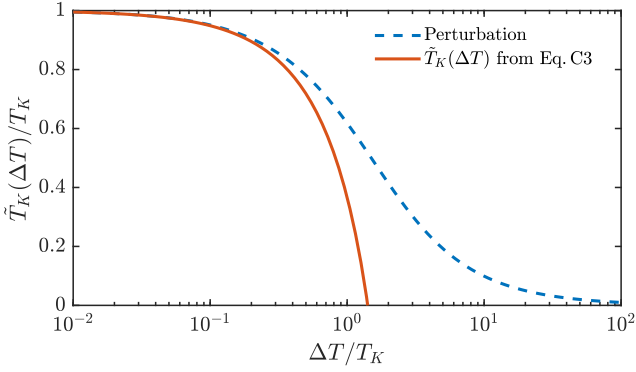


FIG. 11. The Kondo energy scale in Eq. (C3) as a function of the temperature gradient ΔT compared to the perturbation theory (Eq. (C1)) results from Ref. [60].

increasing ΔT , \tilde{T}_K decays faster than \tilde{T}_K^{PT} and proceed to become undefined beyond $\Delta T = \sqrt{2}T_K$.

- [1] A. C. Hewson, *The Kondo Problem to Heavy Fermions*, Cambridge Studies in Magnetism (Cambridge University Press, 1993).
- [2] H. Suhl, Dispersion Theory of the Kondo Effect, *Phys. Rev.* **138**, A515 (1965).
- [3] A. A. Abrikosov and A. A. Migdal, On the theory of the Kondo effect, *J. Low Temp. Phys.* **3**, 519 (1970).
- [4] W. J. de Haas, J. de Boer, and G. J. van den Berg, The electrical resistance of gold, copper and lead at low temperatures, *Physica* **1**, 1115 (1934).
- [5] D. Goldhaber-Gordon, H. Shtrikman, D. Mahalu, D. Abusch-Magder, U. Meirav, and M. A. Kastner, Kondo effect in a single-electron transistor, *Nature* **391**, 156 (1998).
- [6] S. M. Cronenwett, T. H. Oosterkamp, and L. P. Kouwenhoven, A Tunable Kondo Effect in Quantum Dots, *Science* **281**, 540 (1998).
- [7] J. Schmid, J. Weis, K. Eberl, and K. V. Klitzing, A quantum dot in the limit of strong coupling to reservoirs, *Physica B* **256-258**, 182 (1998).
- [8] D. Goldhaber-Gordon, J. Göres, M. A. Kastner, H. Shtrikman, D. Mahalu, and U. Meirav, From the Kondo Regime to the Mixed-Valence Regime in a Single-Electron Transistor, *Phys. Rev. Lett.* **81**, 5225 (1998).
- [9] F. Simmel, R. H. Blick, J. P. Kotthaus, W. Wegscheider, and M. Bichler, Anomalous Kondo Effect in a Quantum Dot at Nonzero Bias, *Phys. Rev. Lett.* **83**, 804 (1999).
- [10] C. H. L. Quay, J. Cumings, S. J. Gamble, R. d. Picciotto, H. Kataura, and D. Goldhaber-Gordon, Magnetic field dependence of the spin- $\frac{1}{2}$ and spin-1 Kondo effects in a quantum dot, *Phys. Rev. B* **76**, 245311 (2007).
- [11] T. S. Jespersen, M. Aagesen, C. Sørensen, P. E. Lindelof, and J. Nygård, Kondo physics in tunable semiconductor nanowire quantum dots, *Phys. Rev. B* **74**, 233304 (2006).

- [12] S. Csonka, L. Hofstetter, F. Freitag, S. Oberholzer, C. Schönenberger, T. S. Jespersen, M. Aagesen, and J. Nygård, Giant Fluctuations and Gate Control of the g -Factor in InAs Nanowire Quantum Dots, *Nano Lett.* **8**, 3932 (2008).
- [13] H. A. Nilsson, P. Caroff, C. Thelander, M. Larsson, J. B. Wagner, L.-E. Wernersson, L. Samuelson, and H. Q. Xu, Giant, Level-Dependent g Factors in InSb Nanowire Quantum Dots, *Nano Lett.* **9**, 3151 (2009).
- [14] A. V. Kretinin, R. Popovitz-Biro, D. Mahalu, and H. Shtrikman, Multimode Fabry-Pérot Conductance Oscillations in Suspended Stacking-Faults-Free InAs Nanowires, *Nano Lett.* **10**, 3439 (2010).
- [15] J. Nygård, D. H. Cobden, and P. E. Lindelof, Kondo physics in carbon nanotubes, *Nature* **408**, 342 (2000).
- [16] A. V. Kretinin, H. Shtrikman, D. Goldhaber-Gordon, M. Hanl, A. Weichselbaum, J. von Delft, T. Costi, and D. Mahalu, Spin- $\frac{1}{2}$ Kondo effect in an InAs nanowire quantum dot: Unitary limit, conductance scaling, and Zeeman splitting, *Phys. Rev. B* **84**, 245316 (2011).
- [17] L. H. Yu and D. Natelson, The Kondo Effect in C60 Single-Molecule Transistors, *Nano Lett.* **4**, 79 (2004).
- [18] G. González, M. N. Leuenberger, and E. R. Mucciolo, Kondo effect in single-molecule magnet transistors, *Phys. Rev. B* **78**, 054445 (2008).
- [19] G. D. Scott, Z. K. Keane, J. W. Ciszek, J. M. Tour, and D. Natelson, Universal scaling of nonequilibrium transport in the Kondo regime of single molecule devices, *Phys. Rev. B* **79**, 165413 (2009).
- [20] N. Knorr, M. A. Schneider, L. Diekhöner, P. Wahl, and K. Kern, Kondo Effect of Single Co Adatoms on Cu Surfaces, *Phys. Rev. Lett.* **88**, 096804 (2002).
- [21] M. Ternes, A. J. Heinrich, and W.-D. Schneider, Spectroscopic manifestations of the Kondo effect on single adatoms, *J. Phys.: Condens. Matter* **21**, 053001 (2008).
- [22] J. Ren, H. Guo, J. Pan, Y. Y. Zhang, X. Wu, H.-G. Luo, S. Du, S. T. Pantelides, and H.-J. Gao, Kondo Effect of Cobalt Adatoms on a Graphene Monolayer Controlled by Substrate-Induced Ripples, *Nano Lett.* **14**, 4011 (2014).
- [23] J.-H. Chen, L. Li, W. G. Cullen, E. D. Williams, and M. S. Fuhrer, Tunable Kondo effect in graphene with defects, *Nat. Phys.* **7**, 535 (2011).
- [24] L. Riegger, N. Darkwah Oppong, M. Höfer, D. R. Fernandes, I. Bloch, and S. Fölling, Localized Magnetic Moments with Tunable Spin Exchange in a Gas of Ultracold Fermions, *Phys. Rev. Lett.* **120**, 143601 (2018).
- [25] S. Seiro, L. Jiao, S. Kirchner, S. Hartmann, S. Friedemann, C. Krellner, C. Geibel, Q. Si, F. Steglich, and S. Wirth, Evolution of the Kondo lattice and non-Fermi liquid excitations in a heavy-fermion metal, *Nat. Commun.* **9**, 1 (2018).
- [26] A. S. Shankar, D. O. Oriekhov, A. K. Mitchell, and L. Fritz, Kondo effect in twisted bilayer graphene, *Phys. Rev. B* **107**, 245102 (2023).
- [27] C. van Efferen, J. Fischer, T. A. Costi, A. Rosch, T. Michely, and W. Jolie, Modulated Kondo screening along magnetic mirror twin boundaries in monolayer MoS₂, *Nat. Phys.* **20**, 82 (2024).
- [28] L. Kouwenhoven and L. Glazman, Revival of the Kondo effect, *Phys. World* **14**, 33 (2001).
- [29] T. A. Costi and V. Zlatić, Thermoelectric transport through strongly correlated quantum dots, *Phys. Rev. B* **81**, 235127 (2010).
- [30] A. Svilans, M. Josefsson, A. M. Burke, S. Fahlvik, C. Thelander, H. Linke, and M. Leijnse, Thermoelectric Characterization of the Kondo Resonance in Nanowire Quantum Dots, *Phys. Rev. Lett.* **121**, 206801 (2018).
- [31] B. Dutta, D. Majidi, A. García Corral, P. A. Erdman, S. Florens, T. A. Costi, H. Courtois, and C. B. Winkelmann, Direct Probe of the Seebeck Coefficient in a Kondo-Correlated Single-Quantum-Dot Transistor, *Nano Lett.* **19**, 506 (2019).
- [32] P. Gehring, J. K. Sowa, C. Hsu, J. de Bruijkere, M. van der Star, J. J. Le Roy, L. Bogani, E. M. Gauger, and H. S. J. van der Zant, Complete mapping of the thermoelectric properties of a single molecule, *Nat. Nanotechnol.* **16**, 426 (2021).
- [33] C. Hsu, T. A. Costi, D. Vogel, C. Wegeberg, M. Mayor, H. S. J. van der Zant, and P. Gehring, Magnetic-Field Universality of the Kondo Effect Revealed by Thermocurrent Spectroscopy, *Phys. Rev. Lett.* **128**, 147701 (2022).
- [34] L. D. Hicks and M. S. Dresselhaus, Effect of quantum-well structures on the thermoelectric figure of merit, *Phys. Rev. B* **47**, 12727 (1993).
- [35] G. D. Mahan and J. O. Sofo, The best thermoelectric., *Proc. Natl. Acad. Sci. U.S.A.* **93**, 7436 (1996).
- [36] J. P. Heremans, C. M. Thrush, and D. T. Morelli, Thermopower enhancement in lead telluride nanostructures, *Phys. Rev. B* **70**, 115334 (2004).
- [37] J. R. Szczech, J. M. Higgins, and S. Jin, Enhancement of the thermoelectric properties in nanoscale and nanostructured materials, *J. Mater. Chem.* **21**, 4037 (2011).
- [38] J. P. Heremans, M. S. Dresselhaus, L. E. Bell, and D. T. Morelli, When thermoelectrics reached the nanoscale, *Nat. Nanotechnol.* **8**, 471 (2013).
- [39] S. Hershfield, K. A. Muttalib, and B. J. Nartowt, Non-linear thermoelectric transport: A class of nanodevices for high efficiency and large power output, *Phys. Rev. B* **88**, 085426 (2013).
- [40] D. Sánchez and H. Linke, Focus on thermoelectric effects in nanostructures, *New J. Phys.* **16**, 110201 (2014).
- [41] G. Benenti, G. Casati, K. Saito, and R. S. Whitney, Fundamental aspects of steady-state conversion of heat to work at the nanoscale, *Phys. Rep.* **694**, 1 (2017).
- [42] D. Sánchez and R. López, Nonlinear phenomena in quantum thermoelectrics and heat, *C. R. Phys.* **17**, 1060 (2016).
- [43] S. Andergassen, T. A. Costi, and V. Zlatić, Mechanism for large thermoelectric power in molecular quantum dots described by the negative- U Anderson model, *Phys. Rev. B* **84**, 241107 (2011).
- [44] G. Gómez-Silva, P. A. Orellana, and E. V. Anda, Enhancement of the thermoelectric efficiency in a T-shaped quantum dot system in the linear and nonlinear regimes, *J. Appl. Phys.* **123**, 085706 (2018).
- [45] R. Santiago Cortes-Santamaria, J. A. Landazabal-Rodríguez, J. Silva-Valencia, E. Ramos, M. S. Figueira, and R. Franco Peñaloza, Universality and the thermoelectric transport properties of a double quantum dot system: Seeking for conditions that improve the thermoelectric efficiency, *SciPost Phys. Core* **7**, 058 (2024).
- [46] D. Pérez Daroca, P. Roura-Bas, and A. A. Aligia, Enhancing the nonlinear thermoelectric response of a correlated quantum dot in the Kondo regime by asymmetrical coupling to the leads, *Phys. Rev. B* **97**, 165433 (2018).
- [47] A. Manaparambil and I. Weymann, Nonequilibrium Seebeck effect and thermoelectric efficiency of Kondo-correlated molecular junctions, *Phys. Rev. B* **107**, 085404

- (2023).
- [48] A. Dorda, M. Ganahl, S. Andergassen, W. von der Linden, and E. Arrigoni, Thermoelectric response of a correlated impurity in the nonequilibrium Kondo regime, *Phys. Rev. B* **94**, 245125 (2016).
- [49] F. Giazotto, T. T. Heikkilä, A. Luukanen, A. M. Savin, and J. P. Pekola, Opportunities for mesoscopes in thermometry and refrigeration: Physics and applications, *Rev. Mod. Phys.* **78**, 217 (2006).
- [50] S.-Y. Hwang, B. Sothmann, and D. Sánchez, Superconductor–quantum dot hybrid coolers, *Phys. Rev. B* **107**, 245412 (2023).
- [51] X. Zeng, D. Zhang, L. Ye, L. Cao, R.-X. Xu, X. Zheng, and M. Di Ventra, Kondo cooling in quantum impurity systems, *Phys. Rev. B* **109**, 115423 (2024).
- [52] N. Andrei, K. Furuya, and J. H. Lowenstein, Solution of the Kondo problem, *Rev. Mod. Phys.* **55**, 331 (1983).
- [53] P. B. Wiegmann, Exact solution of the s-d exchange model (Kondo problem), *J. Phys. C: Solid State Phys.* **14**, 1463 (1981).
- [54] P. W. Anderson, A poor man’s derivation of scaling laws for the Kondo problem, *J. Phys. C: Solid State Phys.* **3**, 2436 (1970).
- [55] P. Nozières, A “fermi-liquid” description of the Kondo problem at low temperatures, *J. Low Temp. Phys.* **17**, 31 (1974).
- [56] A. Georges, G. Kotliar, W. Krauth, and M. J. Rozenberg, Dynamical mean-field theory of strongly correlated fermion systems and the limit of infinite dimensions, *Rev. Mod. Phys.* **68**, 13 (1996).
- [57] K. G. Wilson, The renormalization group: Critical phenomena and the Kondo problem, *Rev. Mod. Phys.* **47**, 773 (1975).
- [58] R. Bulla, T. A. Costi, and T. Pruschke, Numerical renormalization group method for quantum impurity systems, *Rev. Mod. Phys.* **80**, 395 (2008).
- [59] R. Van Roermund, S.-y. Shiau, and M. Lavagna, Anderson model out of equilibrium: Decoherence effects in transport through a quantum dot, *Phys. Rev. B* **81**, 165115 (2010).
- [60] M. A. Sierra, R. López, and D. Sánchez, Fate of the spin- $\frac{1}{2}$ Kondo effect in the presence of temperature gradients, *Phys. Rev. B* **96**, 085416 (2017).
- [61] U. Eckern and K. I. Wysokiński, Two- and three-terminal far-from-equilibrium thermoelectric nano-devices in the Kondo regime, *New J. Phys.* **22**, 013045 (2020).
- [62] A. Kaminski, Yu. V. Nazarov, and L. I. Glazman, Universality of the Kondo effect in a quantum dot out of equilibrium, *Phys. Rev. B* **62**, 8154 (2000).
- [63] A. Oguri, Fermi-liquid theory for the Anderson model out of equilibrium, *Phys. Rev. B* **64**, 153305 (2001).
- [64] C. Mora, C. P. Moca, J. von Delft, and G. Zaránd, Fermi-liquid theory for the single-impurity Anderson model, *Phys. Rev. B* **92**, 075120 (2015).
- [65] A. Oguri and A. C. Hewson, Higher-order Fermi-liquid corrections for an Anderson impurity away from half filling: Nonequilibrium transport, *Phys. Rev. B* **97**, 035435 (2018).
- [66] Y. Teratani, K. Tsutsumi, K. Motoyama, R. Sakano, and A. Oguri, Thermoelectric transport and current noise through a multilevel Anderson impurity: Three-body Fermi-liquid corrections in quantum dots and magnetic alloys, arXiv [10.48550/arXiv.2404.05947](https://arxiv.org/abs/10.48550/arXiv.2404.05947) (2024), 2404.05947.
- [67] S. Csonka, I. Weymann, and G. Zarand, An electrically controlled quantum dot based spin current injector, *Nanoscale* **4**, 3635 (2012).
- [68] D. M. Fugger, A. Dorda, F. Schwarz, J. von Delft, and E. Arrigoni, Nonequilibrium Kondo effect in a magnetic field: auxiliary master equation approach, *New J. Phys.* **20**, 013030 (2018).
- [69] D. M. Fugger, D. Bauernfeind, M. E. Sorantin, and E. Arrigoni, Nonequilibrium pseudogap Anderson impurity model: A master equation tensor network approach, *Phys. Rev. B* **101**, 165132 (2020).
- [70] N. S. Wingreen and Y. Meir, Anderson model out of equilibrium: Noncrossing-approximation approach to transport through a quantum dot, *Phys. Rev. B* **49**, 11040 (1994).
- [71] M. H. Hettler, J. Kroha, and S. Hershfield, Nonequilibrium dynamics of the Anderson impurity model, *Phys. Rev. B* **58**, 5649 (1998).
- [72] F. Schwarz, I. Weymann, J. von Delft, and A. Weichselbaum, Nonequilibrium Steady-State Transport in Quantum Impurity Models: A Thermofield and Quantum Quench Approach Using Matrix Product States, *Phys. Rev. Lett.* **121**, 137702 (2018).
- [73] A. Manaparambil, A. Weichselbaum, J. von Delft, and I. Weymann, Nonequilibrium spintronic transport through Kondo impurities, *Phys. Rev. B* **106**, 125413 (2022).
- [74] H. Haug and A.-P. Jauho, [Quantum Kinetics in Transport and Optics of Semiconductors](https://doi.org/10.1007/978-3-662-56678-2) (Springer, Berlin, Germany).
- [75] A. Weichselbaum, Non-abelian symmetries in tensor networks: A quantum symmetry space approach, *Ann. Phys.* **327**, 2972 (2012).
- [76] A. Weichselbaum, X-symbols for non-Abelian symmetries in tensor networks, *Phys. Rev. Res.* **2**, 023385 (2020).
- [77] A. Weichselbaum, QSpace - An open-source tensor library for Abelian and non-Abelian symmetries, arXiv [10.48550/arXiv.2405.06632](https://arxiv.org/abs/10.48550/arXiv.2405.06632) (2024), 2405.06632.
- [78] M. Filippone, C. P. Moca, A. Weichselbaum, J. von Delft, and C. Mora, At which magnetic field, exactly, does the Kondo resonance begin to split? A Fermi liquid description of the low-energy properties of the Anderson model, *Phys. Rev. B* **98**, 075404 (2018).

Chapter 9


Nonequilibrium transport properties in the asymmetric coupling limit

9.1 Nonequilibrium Seebeck effect and thermoelectric efficiency of Kondo-correlated molecular junctions [D]

Nonequilibrium Seebeck effect and thermoelectric efficiency of Kondo-correlated molecular junctions

Anand Manaparambil^{✉*} and Ireneusz Weymann[✉]

Institute of Spintronics and Quantum Information, Faculty of Physics, Adam Mickiewicz University, Uniwersytetu Poznańskiego 2, 61-614 Poznań, Poland

 (Received 14 October 2022; revised 18 January 2023; accepted 23 January 2023; published 7 February 2023)

We theoretically study the nonequilibrium thermoelectric transport properties of a strongly-correlated molecule (or quantum dot) embedded in a tunnel junction. Assuming that the coupling of the molecule to the contacts is asymmetric, we determine the nonlinear current driven by the voltage and temperature gradients by using the perturbation theory. However, the subsystem consisting of the molecule strongly coupled to one of the contacts is solved by using the numerical renormalization group method, which allows for accurate description of Kondo correlations. We study the temperature gradient and voltage dependence of the nonlinear and differential Seebeck coefficients for various initial configurations of the system. In particular, we show that in the Coulomb blockade regime with singly occupied molecule, both thermopowers exhibit sign changes due to the Kondo correlations at nonequilibrium conditions. Moreover, we determine the nonlinear heat current and thermoelectric efficiency, demonstrating that the system can work as a heat engine with considerable efficiency, depending on the transport regime.

DOI: [10.1103/PhysRevB.107.085404](https://doi.org/10.1103/PhysRevB.107.085404)

I. INTRODUCTION

Thermoelectric properties of nanoscale systems have become a subject of extensive studies [1–5]. This is because such structures, due to their reduced dimensions, allow for obtaining thermal response much exceeding that obtained in bulk materials [6]. In this regard, a special role is played by zero-dimensional systems, such as molecules or quantum dots, in which discrete energy spectrum is relevant for efficient energy filtering and obtaining considerable figure of merit. Thermopower of such systems has already been explored theoretically [7–14], both in the weak- and strong-coupling regimes, as well as experimentally [15–19]. A special attention has been paid to strong electron correlation regime, where the Kondo effect can emerge at sufficiently low temperatures [20,21]. This is due to the fact that the analysis of the temperature dependence of the Seebeck effect can provide additional information about the Kondo correlations in the system [10,16,17]. In particular, sign changes of linear thermopower as a function of temperature were shown to indicate the onset of the Kondo correlations in the system [16,17]. From theoretical side, accurate description of thermoelectric phenomena in the strong correlation regime requires using sophisticated numerical methods, therefore such considerations have been mostly limited to the linear response regime [10,22–26], while much less attention has been paid to the far-from-equilibrium regime [12,14,27].

The goal of this paper is therefore to shed more light on the nonequilibrium thermoelectric characteristics in systems where Kondo correlations are crucial. For that, we

consider a molecule (or a quantum dot) asymmetrically attached to external contacts. Such system's geometry allows us to incorporate strong electron correlation effects in far-from-equilibrium conditions in a very accurate manner. The electronic correlations give rise to the development of the Kondo phenomenon, which arises due to the strong coupling to one of the contacts, whereas the second contact, serves as a weakly coupled probe. In such scenario, we can make use of the numerical renormalization group (NRG) method [28–30] to solve the strongly-coupled subsystem, while the nonequilibrium current flowing through the whole system, triggered by voltage and/or temperature gradients, is evaluated based on the perturbation theory with respect to the weakly attached electrode. We show that with this method we can determine the thermoelectric effects at large and finite temperature and potential gradient without losing the Kondo correlations. We also note that accurate quantitative calculation of nonequilibrium thermoelectric transport in the case of *symmetrically-coupled* systems poses a great challenge that could be addressed by recently developed hybrid approach involving time-dependent density matrix renormalization group and NRG [31,32].

For the system considered here, we first study the voltage dependence of the differential conductance, demonstrating suppression of the zero-bias Kondo peak with increasing the temperature gradient. We then focus on the analysis of nonequilibrium and differential Seebeck effects, analyzing at the beginning the case of finite temperature gradient within linear response in applied voltage. Furthermore, we examine the behavior of the thermopower in the nonlinear voltage and temperature gradient regime, predicting new sign changes associated with Kondo correlations. We also calculate the heat currents and the power generated by the device as well as

*anaman@amu.edu.pl

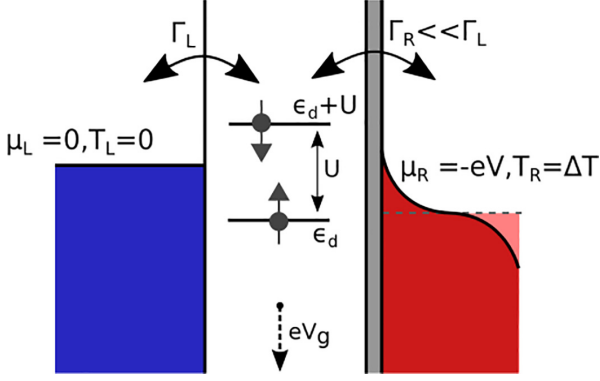


FIG. 1. The schematic of the considered system. It consists of a molecule (or a quantum dot) characterized by an orbital level of energy ε_d and Coulombic repulsion U . The molecule is strongly coupled to the left lead with coupling strength Γ_L , while the coupling to the right contact Γ_R is much weaker. V_g stands for the gate voltage, which can be used to tune the position of the orbital level. μ_L (μ_R) and T_L (T_R) denote the chemical potential and temperature of the left (right) lead, respectively. The left contact is grounded and kept at a constant temperature $T_L = 0$, while the right contact is subject to voltage bias V and temperature gradient ΔT .

the corresponding thermoelectric efficiency, revealing regimes of large efficiency depending on the transport regime. Finally, assuming realistic junction parameters, we consider the thermoelectric transport properties including the voltage dependence of the molecule's orbital level.

The paper is organized as follows. In Sec. II, we discuss the model and method used in the calculations along with the definitions for thermopower in out-of-equilibrium settings. The main results and discussions are presented in Sec. III, which begins with the analysis of the electronic transport under a finite potential bias and temperature gradient. The nonequilibrium thermoelectric coefficients are then studied, first at zero bias, and then generalized to the finite bias and temperature conditions. We also determine the behavior of the nonequilibrium heat current and the thermoelectric efficiency of the system under various parameter regimes. Finally, the paper is summarized in Sec. IV.

II. THEORETICAL FRAMEWORK

A. Model and Hamiltonian

The considered system consists of a molecule (or a quantum dot) asymmetrically coupled to two metallic leads, as schematically shown in Fig. 1. The molecule is described by an orbital level of energy ε_d and Coulomb correlations denoted by U . This orbital level may correspond to the lowest unoccupied orbital level (LUMO level) of the molecule. Transport through the system can be induced and controlled by applying a finite bias voltage V and/or a temperature gradient ΔT across the leads. We assume that the left contact is grounded and kept at a constant temperature T , while the right contact is subject to V and ΔT , see Fig. 1. The temperature T is assumed to be much smaller than the characteristic energy scale of the Kondo effect, i.e., in practical calculations we set $T \rightarrow 0$. Moreover, it is assumed that the coupling to the left lead (Γ_L) is much stronger than the coupling to the right

electrode (Γ_R). Such an asymmetry is frequently present in various molecular junctions [33–37], it can be also generated in artificial heterostructures comprising, e.g., a quantum dot [38–40]. Furthermore, it can be also encountered in studies of adatoms with scanning tunneling spectroscopy. Under this assumption, we determine the current flowing through the system using the perturbation theory in Γ_R , while the subsystem consisting of molecule strongly coupled to the left lead is treated exactly with the aid of the numerical renormalization group method [28–30]. In other words, we include the lowest-order processes between the molecule and the right electrode, while the tunneling processes between the molecule and the left lead are taken into account in an exact manner.

The Hamiltonian of the molecule coupled to the left lead can be expressed as [41]

$$H_L = \varepsilon_d n + U n_\uparrow n_\downarrow + \sum_{k\sigma} \varepsilon_{Lk\sigma} c_{Lk\sigma}^\dagger c_{Lk\sigma} + \sqrt{\frac{\Gamma_L}{\pi \rho_L}} \sum_{k\sigma} (d_\sigma^\dagger c_{Lk\sigma} + c_{Lk\sigma}^\dagger d_\sigma), \quad (1)$$

where the first two terms model the orbital level with energy ε_d and Coulomb correlations U , with $n = n_\uparrow + n_\downarrow$, $n_\sigma = d_\sigma^\dagger d_\sigma$, and d_σ^\dagger (d_σ) being the creation (annihilation) operator for spin- σ electrons on the orbital level. The creation (annihilation) operator for an electron of spin σ , momentum k , and energy $\varepsilon_{\alpha k\sigma}$ in the lead α is denoted by $c_{\alpha k\sigma}^\dagger$ ($c_{\alpha k\sigma}$). The third term in Eq. (1) describes the left lead in the free quasiparticle approximation, while the last term models the tunneling processes between the molecule and left lead. The density of states of the lead α is described by ρ_α . Here we use the wide-band approximation under which the couplings are energy independent. On the other hand, the Hamiltonian of the right contact can be written as [42]

$$H_R = \sum_{k\sigma} \varepsilon_{Rk\sigma} c_{Rk\sigma}^\dagger c_{Rk\sigma} - eV \sum_{k\sigma} c_{Rk\sigma}^\dagger c_{Rk\sigma}, \quad (2)$$

where V is the applied bias voltage and e stands for the elementary charge. Then, the tunneling processes between the left and right part of the system can be described by the following tunneling Hamiltonian [42]:

$$H_T = \sqrt{\frac{\Gamma_R}{\pi \rho_R}} \sum_{k\sigma} (d_\sigma^\dagger c_{Rk\sigma} + c_{Rk\sigma}^\dagger d_\sigma). \quad (3)$$

Thus, the total Hamiltonian is given by a sum of three terms, the strongly coupled left part H_L , the weakly coupled right lead H_R , and the term accounting for tunneling between both parts, H_T . $H = H_L + H_R + H_T$. In what follows, to determine the thermoelectric transport properties, we perform a perturbation expansion in H_T .

B. Nonequilibrium transport coefficients

1. Electric current

The assumption of the weak coupling Γ_R to the right subsystem allows us to perform a perturbative expansion in H_T . In the lowest-order perturbation theory, the electric current $I(V, \Delta T)$ at voltage bias V and temperature gradient ΔT can

be expressed as [38,40]

$$I(V, \Delta T) = -\frac{2e\Gamma_R}{\hbar} \int_{-\infty}^{\infty} d\omega A_L(\omega) \times [f_L(\omega) - f_R(\omega - eV)], \quad (4)$$

where $A_L(\omega)$ is the local density of states (spectral function) of the left subsystem and $f_\alpha(\omega)$ denotes the Fermi-Dirac distribution function of the lead α , $f_\alpha(\omega) = [1 + \exp(\omega/T_\alpha)]^{-1}$, with $T_L = 0$ and $T_R = \Delta T$, cf. Fig. 1, and $k_B \equiv 1$. The factor of 2 in Eq. (4) results from the spin degrees of freedom.

The spectral function $A_L(\omega)$ of the left subsystem is calculated by using the numerical renormalization group method [28–30]. This method is well suited to account for electron correlations in a very accurate manner, and especially those giving rise to the Kondo effect [21]. The spectral function can be related to the imaginary part of the molecule's orbital level retarded Green's function $G_\sigma^r(\omega)$, $A_L(\omega) = \sum_\sigma A_{L\sigma}(\omega)$, with $A_{L\sigma}(\omega) = -\text{Im}G_\sigma^r(\omega)/\pi$, where $G_\sigma^r(\omega)$ is the Fourier transform of $G_\sigma^r(t) = -i\Theta(t)\langle\{d_\sigma(t), d_\sigma^\dagger(0)\}\rangle$. Within the NRG, we first determine the eigenspectrum of H_L and then calculate $A_L(\omega)$ in the Lehmann representation.

2. Seebeck coefficient

A special emphasis in this paper is put on the nonequilibrium behavior triggered by a large temperature and/or voltage gradient. The Seebeck coefficient (or thermopower) is the thermoelectric property that quantifies the voltage induced by a thermal gradient across a conductor, and is defined as

$$S = -\left(\frac{V}{\Delta T}\right)_{I=0}, \quad (5)$$

under the assumption that the current I through the system vanishes, $I = 0$.

In the linear response regime, the Seebeck coefficient S_{lin} can be reliably described by using the Onsager integrals, $L_n = -\frac{1}{\hbar} \int d\omega \omega^n f'(\omega) \mathcal{T}(\omega)$, involving the transmission coefficient, $\mathcal{T}(\omega) \propto \Gamma_R A_L(\omega)$, where $f'(\omega)$ is the derivative of the Fermi function [43],

$$S_{\text{lin}} = -\frac{1}{eT} \frac{L_1}{L_0}. \quad (6)$$

This basic definition of the Seebeck coefficient can be directly extended to the nonequilibrium case by considering that only the current generated by the thermal gradient must vanish. Assume, for example, that a system with potential bias V exhibits a current I flowing through it. When an additional temperature gradient ΔT is applied, a new current $I_{\text{tot}} = I + I_{\text{th}}$ will flow through the system, where I_{th} is the additional current induced by the thermal gradient. One can then define a nonequilibrium (nonlinear) Seebeck coefficient $S_n(V, \Delta T)$ as [12,39,44–48]

$$S_n(V, \Delta T) = -\left(\frac{\Delta V}{\Delta T}\right)_{I(V+\Delta V, \Delta T)=I(V,0)}, \quad (7)$$

where ΔV is the change in potential bias required to suppress the current induced by the thermal gradient ΔT .

Additionally, in the nonlinear response regime, one can also define a differential Seebeck coefficient $S_d(V, \Delta T)$

as [49]

$$S_d(V, \Delta T) = -\left(\frac{dV}{d\Delta T}\right)_I = -\left(\frac{\partial I}{\partial \Delta T}\right)_V / \left(\frac{\partial I}{\partial V}\right)_{\Delta T}, \quad (8)$$

where $(\frac{\partial X}{\partial Y})_Z$ describes the partial derivative of X with respect to Y , while keeping Z constant. The differential Seebeck effect is related to the ratio of the thermal response at finite voltage to differential conductance at finite temperature gradient. We note that in the linear response regime with respect to the bias voltage, S_d becomes comparable to the linear response Seebeck coefficient given by Eq. (6).

3. Heat current and thermoelectric efficiency

We are also interested in the behavior of the nonequilibrium heat current and the thermoelectric efficiency η [50–55]. The formula for the heat current can be derived from the first law of thermodynamics, which for subsystem $\alpha = L, R$ reads $dU_\alpha = dW_\alpha + dQ_\alpha$. Here, dU_α is the energy flowing into the subsystem α , while dQ_α denotes the corresponding heat. The work done to the subsystem α is generally given by, $dW_\alpha = \mu_\alpha dN_\alpha$, where dN_α is the corresponding particle number change. The heat current associated with the left and right subsystem can be then defined as [51]

$$I_L^Q(V, \Delta T) = I^E(V, \Delta T) - \mu_L I(V, \Delta T)/e, \quad (9)$$

$$I_R^Q(V, \Delta T) = I^E(V, \Delta T) - \mu_R I(V, \Delta T)/e, \quad (10)$$

where $I^E(V, \Delta T)$ denotes the energy current given by

$$I^E(V, \Delta T) = -\frac{2\Gamma_R}{\hbar} \int_{-\infty}^{\infty} d\omega \omega A_L(\omega) \times [f_L(\omega) - f_R(\omega - eV)]. \quad (11)$$

In our setup, $T_R > T_L$, see Fig. 1, such that the electrons flow from the hot reservoir to the cold one performing the work $\dot{W}(V, \Delta T)$ per unit time. Such power output can be related to the heat currents through

$$P \equiv \dot{W}(V, \Delta T) = I_R^Q(V, \Delta T) - I_L^Q(V, \Delta T). \quad (12)$$

Then, the thermoelectric efficiency of such a heat engine can be defined as the ratio of the power to the heat extracted from the hot reservoir,

$$\eta(V, \Delta T) = \frac{\dot{W}(V, \Delta T)}{I_R^Q(V, \Delta T)} = 1 - \frac{I_L^Q(V, \Delta T)}{I_R^Q(V, \Delta T)}. \quad (13)$$

III. RESULTS AND DISCUSSION

In this section we present and discuss the numerical results obtained for the differential conductance, Seebeck effect, heat current and thermoelectric efficiency in far-from-equilibrium conditions. For the considered system we assume the Coulomb correlations $U = 0.2$, the coupling to the left lead $\Gamma_L = 0.02$ in units of half bandwidth, while the weak coupling to the right lead is assumed to be $\Gamma_R = \Gamma_L/10$. In NRG calculations we keep at least 4^5 states in the iterative procedure [56].

We note that in experimentally relevant scenarios, a voltage drop imposed across the junction would result in a change of the orbital level, depending on capacitive couplings to the

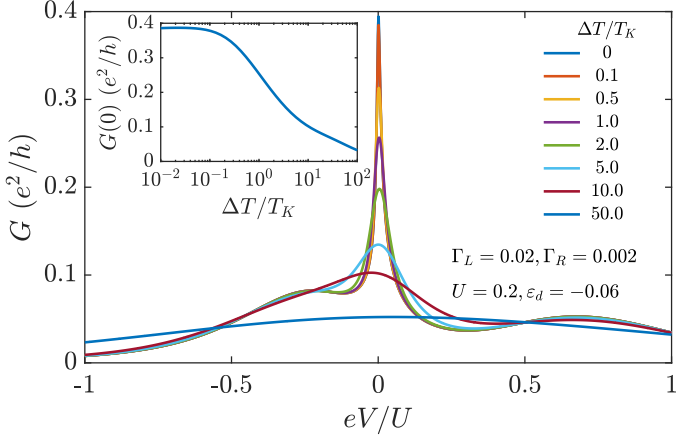


FIG. 2. The differential conductance plotted as a function of the bias voltage V for different values of the temperature gradient ΔT , as indicated. The inset shows the evolution of the zero-bias conductance as a function of ΔT . The parameters are: $U = 0.2$, $\Gamma_L = 0.02$, $\Gamma_R = 0.002$, $T = 0$, in units of band half-width, and $\varepsilon_d = -0.3U$. The Kondo temperature can be estimated from the Haldane's formula, which for assumed parameters yields $T_K/U \approx 8.26 \times 10^{-3}$. The Kondo energy scale in the applied bias potential, defined as the half-width at half-maximum of the $G(V)$ curve, is found to be $eV_K/U \approx 1.45 \times 10^{-2}$.

contacts and to the gate voltage. However, to get a better understanding of the transport properties, we first assume that the position of the orbital level does not change as the bias voltage is tuned. This would correspond to immediately counterbalancing the voltage drop on the molecule by an appropriate tuning of the gate voltage. Nevertheless, further on, assuming exemplary parameters of the junctions, we also present the results for the case when the orbital level depends on the transport voltage.

A. Electronic transport under finite potential and temperature gradient

Let us first analyze the behavior of the differential conductance $G \equiv dI(V, \Delta T)/dV$ as a function of the bias voltage calculated for different temperature gradients ΔT . This dependence is presented in Fig. 2. The figure was generated for $\varepsilon_d = -0.3U$, i.e., in the local moment regime, where the system exhibits the Kondo effect caused by the strong coupling to the left contact. The relevant Kondo temperature for the left subsystem can be estimated from the Haldane's formula [57], which yields $T_K \approx 8.26 \times 10^{-3}U = 8.26 \times 10^{-2}\Gamma_L$. Note that because $\Gamma_R = \Gamma_L/10$, the Kondo temperature associated with the right contact is exponentially suppressed and thus negligible. The presence of Kondo correlations is reflected in a pronounced zero-bias peak visible in the differential conductance, see Fig. 2. Note that because of asymmetric couplings, the maximum of conductance at zero bias is much reduced compared to $2e^2/h$. With increasing the bias voltage, the conductance decreases and shows smaller resonances corresponding to $eV \approx \varepsilon_d$ and $eV \approx \varepsilon_d + U$. When the thermal gradient increases (note that the base system temperature is assumed to be $T = 0$), one observes a gradual suppression of the zero-bias anomaly, until the whole bias dependence of G does

not show any Kondo correlation effects for $\Delta T \gg T_K$. The evolution of the Kondo peak with increasing ΔT is explicitly presented in the inset of Fig. 2. The conductance drops to a half of its maximum value when $\Delta T \approx 2T_K$. This reflects the fact that the actual system temperature, which can be associated with an average of the left and right contact temperatures, is equal to $\Delta T/2$. We also note that for $\Delta T \ll T_K$ one can quantify the Kondo resonance by V_K , which characterizes the Kondo energy scale in the applied bias potential, defined as the half-width at half-maximum of the $G(V)$ curve. For V_K we find $eV_K \approx 1.45 \times 10^{-2}U = 1.45 \times 10^{-1}\Gamma_L$. These results are in agreement with the previous works [32,58,59].

B. Nonequilibrium thermopower

In this section we focus on the analysis of the behavior of thermopower, both S_n and S_d , cf. Eqs. (7) and (8), under finite temperature and voltage gradients. However, to get a better understanding of thermoelectric transport, we first start with the case of $V \rightarrow 0$, while nonequilibrium settings are imposed only by increasing ΔT . The more general case of having both finite ΔT and V will be examined afterwards.

1. Thermopower under finite temperature gradient

The nonequilibrium (S_n) and differential (S_d) Seebeck coefficients as a function of temperature gradient ΔT and orbital level position ε_d , for the case when the nonlinear response regime is triggered by a large temperature gradient, are presented in Fig. 3. Before analyzing the behavior of the thermopower in greater detail, let us first briefly discuss different regimes for the energy of the orbital level ε_d , and what it implies. The local moment regime, $-1 \lesssim \varepsilon_d/U \lesssim 0$, denotes the value of orbital energy, in which the singly occupied level is held below the Fermi energy (of the left electrode in our case) and the doubly occupied state is above the Fermi level. This is the regime where the molecule is occupied by an unpaired electron and the system can exhibit the Kondo effect. As can be inferred from the name, the empty/fully occupied regime, $\varepsilon_d/U \gtrsim 0$, $\varepsilon_d/U \lesssim -1$, refers to the case where the preferred configuration is having the orbital level completely empty or fully occupied. On the other hand, when $\varepsilon_d/U \approx -1$ or $\varepsilon_d/U \approx 0$, we reach a mixed valence/resonant tunneling regime where the orbital level is in the vicinity of the Fermi level of the electrode (depending on its hybridization Γ_L).

The colormaps for S_n and S_d as presented in Figs. 3(a) and 3(c) show a similar behavior but with interesting deviations. We note that for $V \rightarrow 0$ both thermopowers are odd functions of ε_d across the particle-hole symmetry point, $\varepsilon_d = -U/2$ [see also Fig. 3(b)], and decay to zero when the temperature gradient $\Delta T \rightarrow 0$ [see also Fig. 3(d)]. Moreover, both S_n and S_d are generally negative (positive) for $\varepsilon_d > -U/2$ ($\varepsilon_d < -U/2$), indicating a dominant role of the electron (hole) processes. When inside the local moment regime, both S_n and S_d survive to even lower values of temperature gradient $\Delta T/\Gamma_L \approx 10^{-2}$, compared to $\Delta T/\Gamma_L \approx 10^{-1}$, as in the case of empty/fully occupied regime. This is due to the presence of Kondo correlations when the orbital level is singly occupied. Additionally, in this transport regime both thermopowers change sign twice as a function of ΔT . The first sign change occurs when $1 \lesssim \Delta T/\Gamma_L \lesssim 10$, whereas the second one

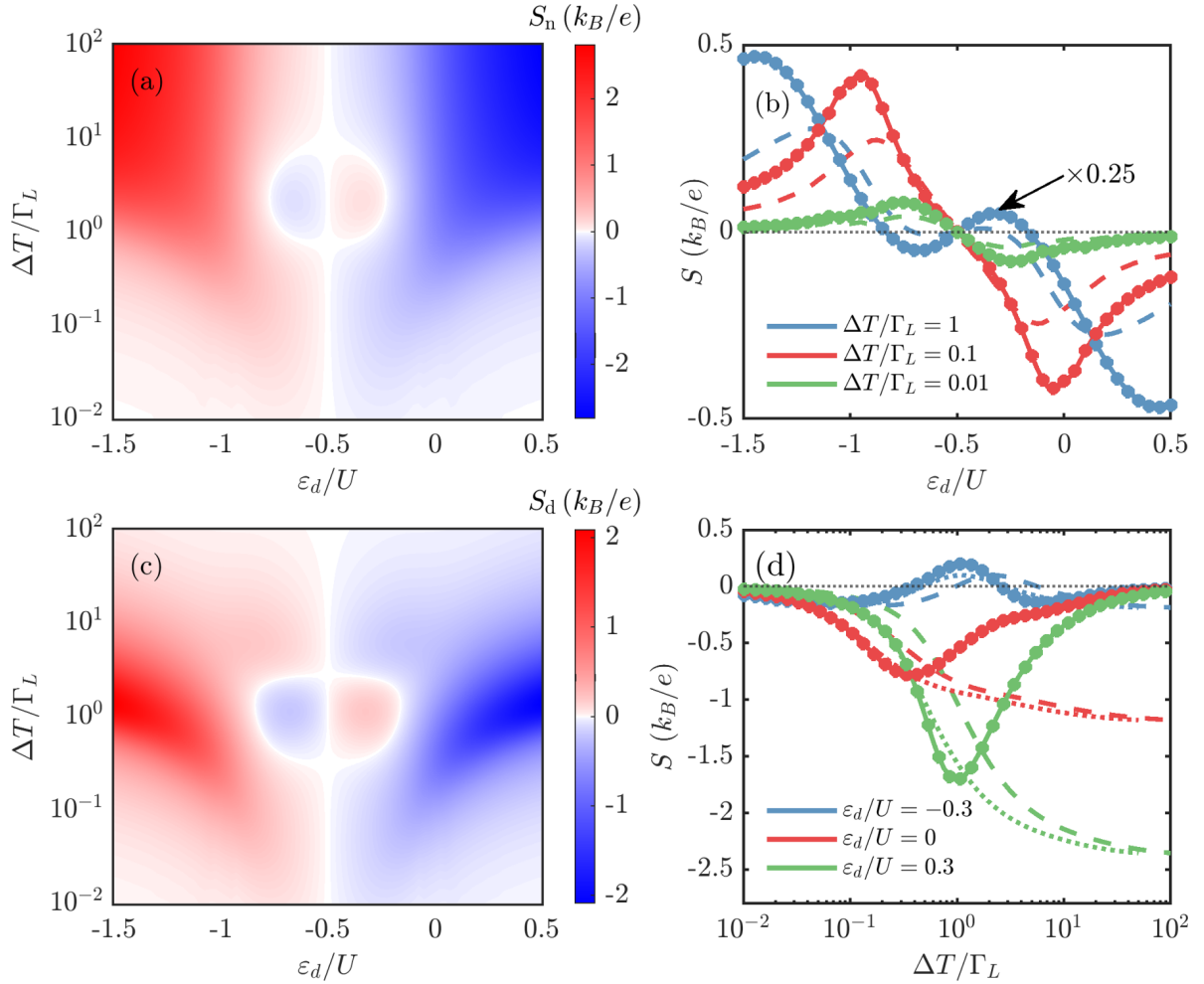


FIG. 3. (a) The nonequilibrium Seebeck coefficient S_n and (c) the differential Seebeck coefficient S_d calculated as a function of the orbital energy ε_d and the temperature gradient ΔT at potential bias $V \rightarrow 0$ for parameters the same as in Fig. 2. Note the logarithmic scale in temperature gradient. (b) The horizontal cross sections of (a) and (c), i.e., the dependence of S_n (dashed) and S_d (solid) as a function of ε_d for various ΔT , whereas (d) presents the vertical cross sections of (a) and (c), i.e., the dependence of S_n (dashed) and S_d (solid) on ΔT for various ε_d . The colored circles show the linear response thermopower $S_{\text{lin}}(T = \Delta T)$ and the colored dotted lines in (d) show the rescaled nonequilibrium thermopower $S_n(2\Delta T)$.

develops when $1/10 \lesssim \Delta T/\Gamma_L \lesssim 1$, see Figs. 3(a) and 3(c). The sign changes of thermopower in the linear response can be assigned to the corresponding behavior of the transmission coefficient (in our case the spectral function of the left subsystem) [10,22]. The Sommerfeld expansion indicates that it is the slope of $\mathcal{T}(\omega) \propto A_L(\omega)$ at the Fermi level, which determines the sign of the Seebeck coefficient [10]. Of course, this strictly holds in the low-temperature regime; however, it also allows for shedding some light onto the nonequilibrium behavior where in turn the dependence of S is determined by the whole integral in Eq. (4). Therefore, for the sake of completeness, in Fig. 4 we present the energy dependence of the normalized spectral function of the left subsystem calculated for different values of the orbital level position, as indicated. In the local moment regime, a pronounced Kondo peak can be seen at the Fermi energy accompanied by two Hubbard resonances at $\omega = \varepsilon_d$ and $\omega = \varepsilon_d + U$. On the other hand, in the mixed valence regime a resonant peak, with position around $\omega = 0$, renormalized by the coupling strength, develops, which moves to positive energies when

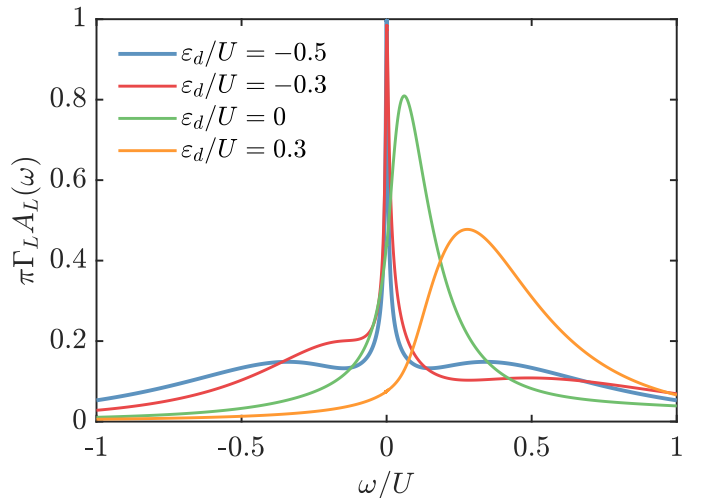


FIG. 4. The normalized spectral function $\pi\Gamma_L A_L(\omega)$ of the left subsystem calculated for various orbital energy ε_d , as indicated. The other parameters are the same as in Fig. 2.

raising the orbital level, see the case of $\varepsilon_d/U = 0.3$ in Fig. 4. Having that in mind, one can qualitatively understand the sign changes in the local moment regime. When lowering the temperature, the first sign change corresponds to change of slope of $A_L(\omega)$ around the Hubbard peak, whereas the second sign change has been found to indicate the onset of the Kondo effect. Note, however, that the value of temperature gradient corresponding to the sign change does not correspond to the Kondo temperature of the system but just indicates the emergence of Kondo correlations [10].

The differences between S_n and S_d become evident for higher values of the temperature gradient ΔT . Specifically, beyond the local moment regime, S_n starts to saturate above $\Delta T/\Gamma_L \gtrsim 1$, whereas S_d reaches maximum around $\Delta T/\Gamma_L \approx 1$ and then becomes suppressed with increasing ΔT , decaying to zero for $\Delta T/\Gamma_L \gtrsim 10$. This can be explicitly seen in Fig. 3(d), which presents the vertical cross-sections of Figs. 3(a) and 3(c). The difference in the high temperature behavior of S_n and S_d highlights the fundamental difference in the definitions of both thermopowers. The differential Seebeck coefficient S_d corresponds essentially to a response function and can justifiably show a vanishing response when the temperature gradient gets high enough. On the other hand, the nonequilibrium Seebeck coefficient S_n indicates the magnitude of the potential difference developed across the junction with a finite ΔT , which even at high temperature gradient has to remain finite. There is also a noticeable difference in the Φ -like shape visible in Figs. 3(a) and 3(c), drawn by the points of sign-change for each thermopower, which originates from the differences in the ΔT behavior of both S_n and S_d and can be understood from the below discussion of the cross sections of the colormaps.

The fact that S_n and S_d for $V \rightarrow 0$ and $\Delta T \rightarrow 0$ should recover the linear response thermopower S_{lin} justifies the comparison of $S_n(\Delta T)$ and $S_d(\Delta T)$ to $S_{\text{lin}}(T)$. The cross sections in Figs. 3(b) and 3(d) compare S_n and S_d as a function of ε_d and ΔT , respectively, along with the linear response thermopower S_{lin} calculated for the system with global temperature $T = \Delta T$, denoted as colored circles.

We note that the dependence of the differential Seebeck coefficient S_d over the temperature gradient ΔT shows good agreement with the behavior of the linear response Seebeck effect S_{lin} with the global temperature T even at large temperature gradients. This is not surprising due to the fact that for $\mu_L = 0$ and $T_L = 0$, Eq. (4) gives a formally similar expression for $S_{\text{lin}}(T)$ and $S_d(\Delta T)$. It is also interesting to note that, although S_n deviates from this behavior at large temperatures, the $S_n(\Delta T)$ dependence when rescaled by 2 in ΔT , i.e., $S_n(2\Delta T)$ [see the dashed lines in Fig. 3(d)] agrees well with the linear response behavior for low values of ΔT , see Fig. 3(d).

To further understand the behavior of the Seebeck coefficients in Fig. 3, one can separately focus on the three regimes. Since for $V \rightarrow 0$ thermopower is an odd function across the particle-hole symmetry point, we pick representative values of ε_d for $\varepsilon_d > -U/2$. In the local moment regime, see the case of $\varepsilon_d/U = -0.3$ in Fig. 3(d), S_n first starts decreasing with raising ΔT until $\Delta T \approx T_K$ and then it increases to reach a sign change occurring around $\Delta T/\Gamma_L \approx 1$. Further increase of ΔT , however, gives rise to another sign change and the

thermopower becomes again positive for large temperature gradients. Such behavior is consistent with the linear-response considerations of Kondo-correlated systems [10,22]. Here, however, we demonstrate that it extends to nonlinear response regime. The above-described behavior is absent when the orbital level is tuned out of the Kondo regime. For resonant conditions, i.e., $\varepsilon_d = 0$, S_n grows only in a monotonic fashion with increasing ΔT . The same can be observed for the empty orbital case ($\varepsilon_d/U = 0.3$), but now the value of S_n gets enhanced for $\Delta T/\Gamma_L \gtrsim 1$, compared to the case of $\varepsilon_d = 0$.

2. Thermopower for finite temperature gradient and bias voltage

After analyzing the influence of the nonlinear temperature gradient on the Seebeck coefficient at linear potential bias, we will now proceed with the examination of the thermopower in the presence of both finite bias voltage and temperature gradient. Figure 5 presents the nonequilibrium and differential Seebeck coefficients calculated for finite potential and temperature gradients for different values of the orbital level energy, as indicated.

Let us first focus on the case when at low voltages the system is in the local moment regime. This is presented in Figs. 5(a) and 5(b) for the particle-hole symmetry point ($\varepsilon_d/U = -0.5$), and in Figs. 5(c) and 5(d) when detuned out of the symmetry point ($\varepsilon_d/U = -0.3$). From the linear response studies, one can expect the thermopower at the particle-hole symmetry point to vanish, since S can be related to the slope of the spectral function $\frac{\partial A_L(\omega)}{\partial(\omega)}$ around the Fermi energy of the left lead in our case. In our system, where the potential bias is applied asymmetrically (only on the right lead), we are essentially shifting the system out of the symmetry point with an applied bias potential. This results in a nonzero Seebeck effect for a finite potential bias even in the case of $\varepsilon_d = -U/2$, see the first row of Fig. 5. As can be seen, in the nonlinear response regime for $\varepsilon_d = -U/2$, both S_n and S_d become finite and are odd functions of the applied bias voltage. More specifically, we observe positive Seebeck coefficients for negative applied bias voltage and vice versa. When the temperature gradient is of the order of the Kondo temperature, there is a new region of sign change present in the thermopower when the potential bias is between the range $0.2 \lesssim |eV/U| \lesssim 0.4$, i.e., the system is in the Coulomb blockade. This sign change, visible in both S_n and S_d at nonequilibrium settings, is due to the Kondo correlations. The sign changes of the differential Seebeck coefficient $S_d(V)$ at low temperature gradient ΔT can be inferred directly from the slope of the spectral function. From Eq. (2), when $|eV| \gg \Delta T$, the thermal response $\frac{\partial I}{\partial \Delta T}$ does not change considerably, resulting in the sign of S_d to be entirely dependent on $G = \frac{\partial I}{\partial V}$, cf. Eq. (8). This mandates the sign of S_d to roughly follow the sign of the function $h(eV) = -(\frac{\partial A_L(\omega=eV)}{\partial \omega})^{-1}$. When the bias voltage increases further, the Fermi levels of the leads are too far apart to show any effect of Kondo correlations on transport. In other words, the system leaves the Coulomb blockade regime for $|eV/U| \gtrsim 0.5$. For the case of the orbital level detuned out of the p-h symmetry point, we observe that the dependence of thermopower becomes generally asymmetric with respect to the bias reversal. For $\varepsilon_d/U = -0.3$, the sign changes corresponding to the Kondo

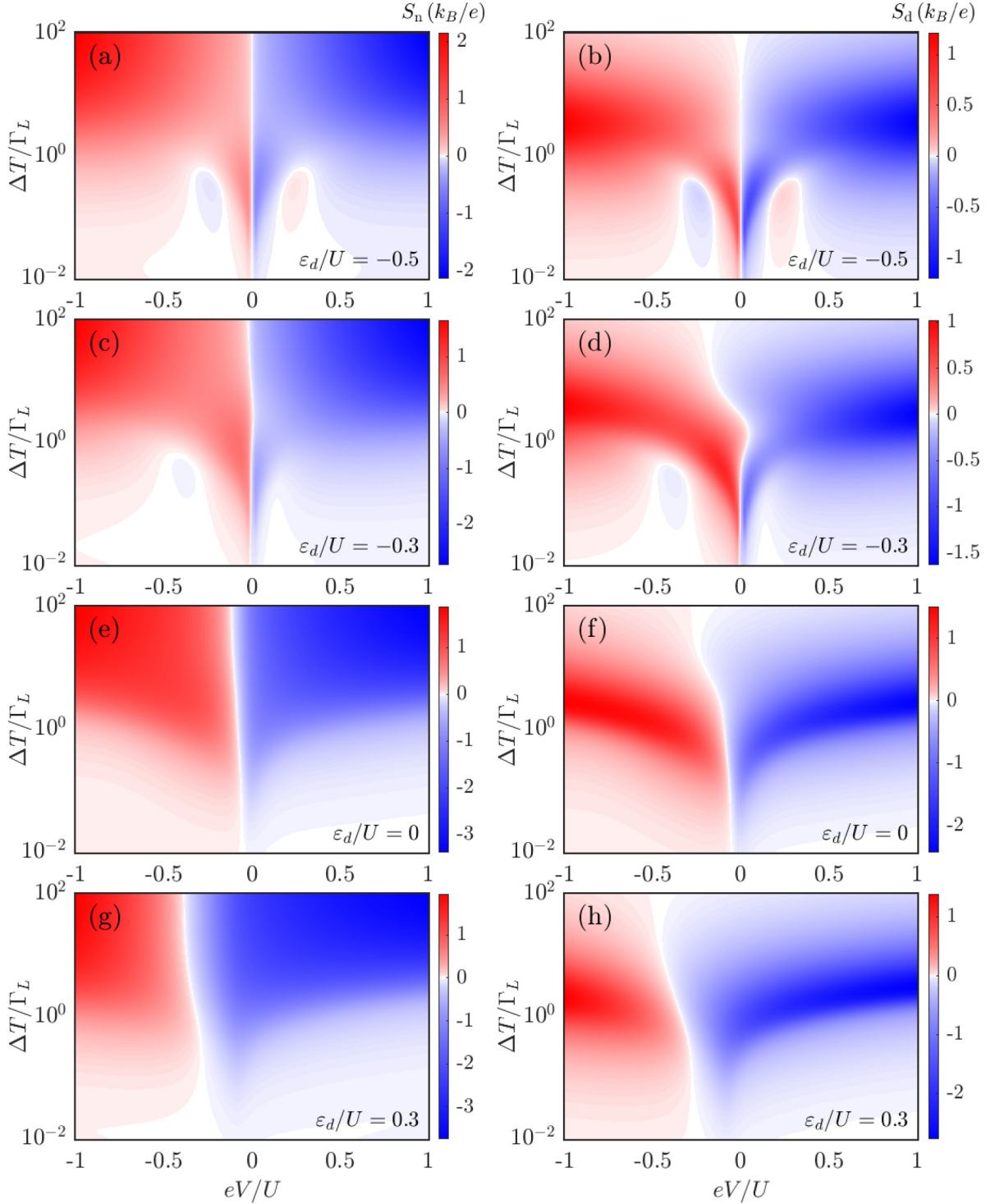


FIG. 5. (Left column) The nonequilibrium Seebeck coefficient S_n and (right column) the differential Seebeck coefficient S_d calculated as a function of the temperature gradient ΔT and the applied bias voltage V . (a) and (b) present the case of the particle-hole symmetry point $\varepsilon_d/U = -0.5$, (c) and (d) show the local moment regime with $\varepsilon_d/U = -0.3$, (e) and (f) display the resonant tunneling regime $\varepsilon_d/U = 0$, whereas (g) and (h) present the empty orbital regime with $\varepsilon_d/U = 0.3$.

correlations are present only for negative bias voltage, where the regime of sign change moves to slightly more negative bias voltage, $-0.5 \lesssim eV/U \lesssim -0.25$. Interestingly, there is a new sign change, seen mostly in the temperature dependence of S_d for small positive bias voltages, which develops around $\Delta T/\Gamma_L \approx 1$, see Fig. 5(d).

All the features discussed in the case when at low voltages the system is in the local moment regime are nicely exemplified in Fig. 6, which presents the relevant vertical cross sections of Fig. 5. One can clearly see the development of a finite Seebeck effect with increasing the potential bias in the case of $\varepsilon_d/U = -0.5$, where a small sign change

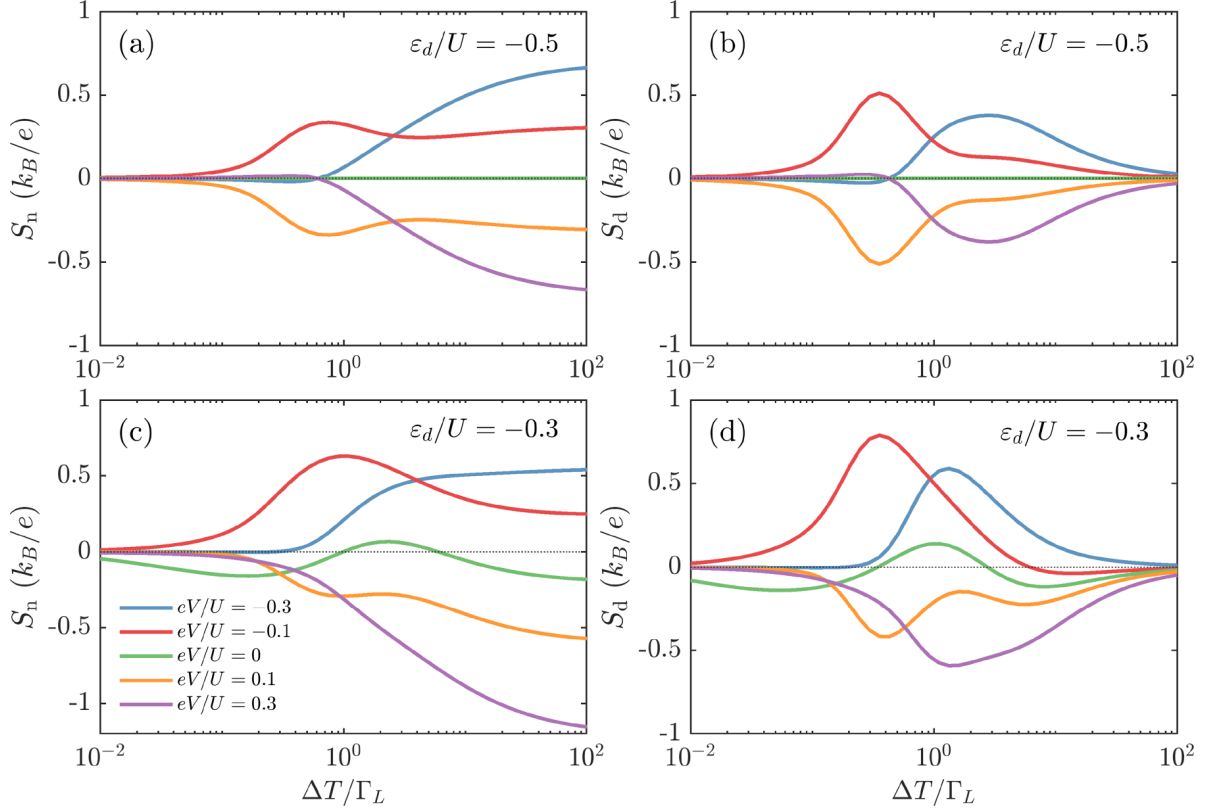


FIG. 6. The temperature gradient dependence of (left column) the nonequilibrium and (right column) the differential Seebeck coefficients for different values of the bias voltage applied to the system, as indicated. (a) and (b) present the case of $\varepsilon_d/U = -0.5$, while (c) and (d) display the case of $\varepsilon_d/U = -0.3$, respectively. This figure corresponds to the vertical cross sections of Figs. 5(a)–5(d).

for $|eV|/U = 0.3$ can be observed. Note also the symmetry with respect to the bias reversal. On the other hand, even larger and generally nonzero for any value of V thermopower develops for $\varepsilon_d/U = -0.3$. Here, one can explicitly see the sign changes of both S_n and S_d in the low bias voltage regime, which then disappear when the bias voltage increases.

The case when at equilibrium the orbital level is outside the local moment regime is presented in Figs. 5(e) and 5(f) for $\varepsilon_d = 0$ and in Figs. 5(g) and 5(h) for the empty orbital case $\varepsilon_d/U = 0.3$. Now, we generally observe only one sign change visible in the Seebeck coefficients S_n and S_d as a function of the applied bias voltage. Moreover, there is also a sign change as a function of thermal gradient for selected value of V . In the case of $\varepsilon_d/U = 0$, the sign change is close to zero voltage and the offset from $V = 0$ can be explained by renormalization of the orbital level by charge fluctuations with the strongly coupled lead, which give rise to a resonance in $A_L(\omega)$ slightly shifted with respect to the Fermi energy, cf. Fig. 4. When the potential bias V is positive, both Seebeck coefficients, S_n and S_d , are found to be negative. Moreover, in the regions of negative voltages, the magnitude of voltage required to change the sign of the thermopower increases with raising the temperature gradient. We observe a similar behavior in the case of $\varepsilon_d/U = 0.3$, but the sign change of the Seebeck effect with respect to the potential bias is offset by the value of ε_d in the negative voltage direction, see the last row of Fig. 5.

C. Nonequilibrium heat current and the thermoelectric efficiency

Figure 7 presents the bias voltage and temperature gradient dependence of the heat current I_R^Q associated with the right subsystem, the power P generated by the device together with the thermoelectric efficiency, cf. Eq. (13), calculated for several values of the dot level position, as indicated. First of all, we note the general tendency to increase the heat current by raising V or ΔT , which is irrespective of the level position ε_d . Moreover, for large bias voltages, there is a saturation and a slight decrease of I_R^Q with increasing ΔT . The same can be observed for the power generated by this device. Up to $eV \sim U/2$, the increase of the temperature gradient gives rise to an enhancement of the power. However, for larger voltages, there is a nonmonotonic dependence of P with respect to ΔT . The efficiency of the system is presented in the right column of Fig. 7. One can clearly identify an optimal choice of both ΔT and V , for which η becomes maximized. The parameter space with maximum η strongly depends on the transport regime. Interestingly, in the local moment regime, see Figs. 7(c) and 7(f), the maximum efficiency is obtained just around the Kondo regime. On the other hand, out of the Coulomb blockade and Kondo regime, the maximum efficiency occurs for larger voltages $eV/U \gtrsim 0.5$, see the case of $\varepsilon_d = 0$ and $\varepsilon_d/U = 0.3$ in Figs. 7(i) and 7(l). We also note that the Carnot efficiency for our system where $T_L \rightarrow 0$ is $\eta_C = 1$. Consequently, we predict that the efficiency of the considered

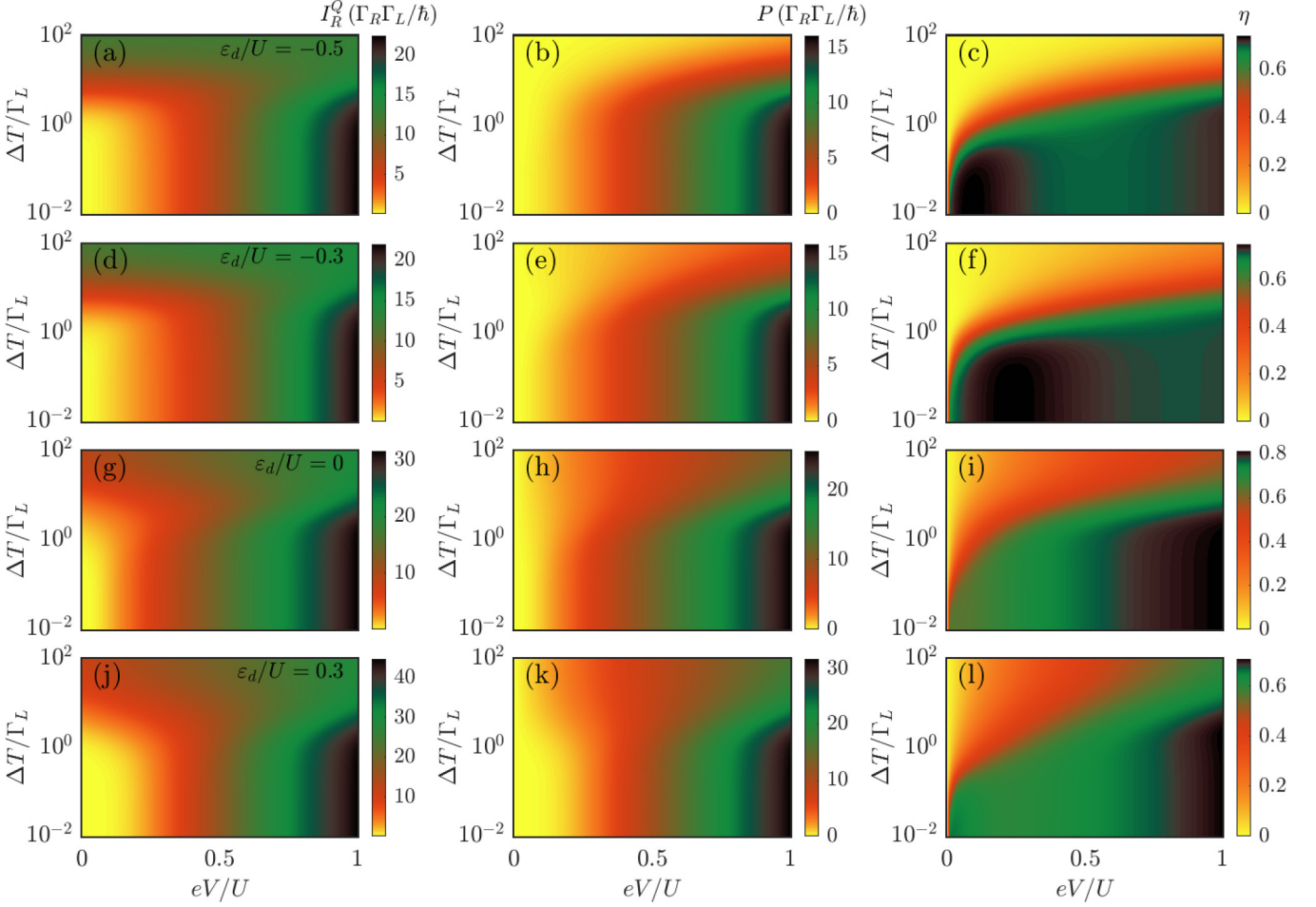


FIG. 7. (Left column) The heat current I_R^Q , (middle column) the power $P \equiv I_R^Q - I_L^Q$, as well as (right column) the thermoelectric efficiency η calculated as a function of the applied bias voltage V and the temperature gradient ΔT for different values of orbital energy ε_d . The first row is determined for $\varepsilon_d/U = -0.5$, the second one for $\varepsilon_d/U = -0.3$, the third row is for $\varepsilon_d = 0$, while the last one is calculated for $\varepsilon_d/U = 0.3$. The other parameters are the same as in Fig. 2.

device can reach up to $\eta/\eta_C \approx 0.8$, depending on the transport regime.

D. Realistic junction

To make the discussion of nonequilibrium thermopower more appealing to experimental realizations, in this section we relax the condition of voltage-independent orbital level and include the voltage drops assuming realistic junction parameters. An electrical circuit diagram of the considered system is shown in Fig. 8. The tunnel junctions are characterized by the capacitances C_L and C_R , and the gate capacitance is denoted by C_g with gate voltage V_g . The formula for the current flowing through such system can be written as

$$I(V, \Delta T) = -\frac{2e\Gamma_R}{\hbar} \int_{-\infty}^{\infty} d\omega A_L(\omega, v_g - v) \times [f_L(\omega) - f_R(\omega - eV)], \quad (14)$$

where $v_g = C_g V_g / e$ and $v = V C_R / e$ are the dimensionless gate and bias voltage drops [38]. For the junction capacitances, we assume $C_L/C_R = 2$ and $C_g/C_R = 0.1$, while the charging energy $E_C = e^2/2C$, with $C = C_L + C_R + C_g$, is equal to $E_C = U/2$.

The current, differential conductance, and differential Seebeck effect as a function of the bias voltage V and the dimensionless gate voltage v_g calculated for different temperature gradients are shown in Fig. 9. At low bias voltages, v_g

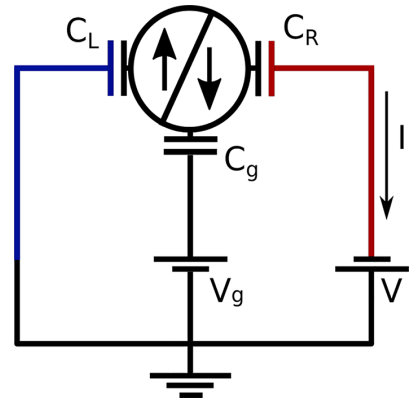


FIG. 8. The schematic shows an equivalent electrical circuit diagram for the asymmetrically coupled molecular junction along with the implementation of the bias potential V and the gate potential V_g . The capacitances associated with the left, right, and the gate electrodes are represented as C_L , C_R , and C_g , respectively.

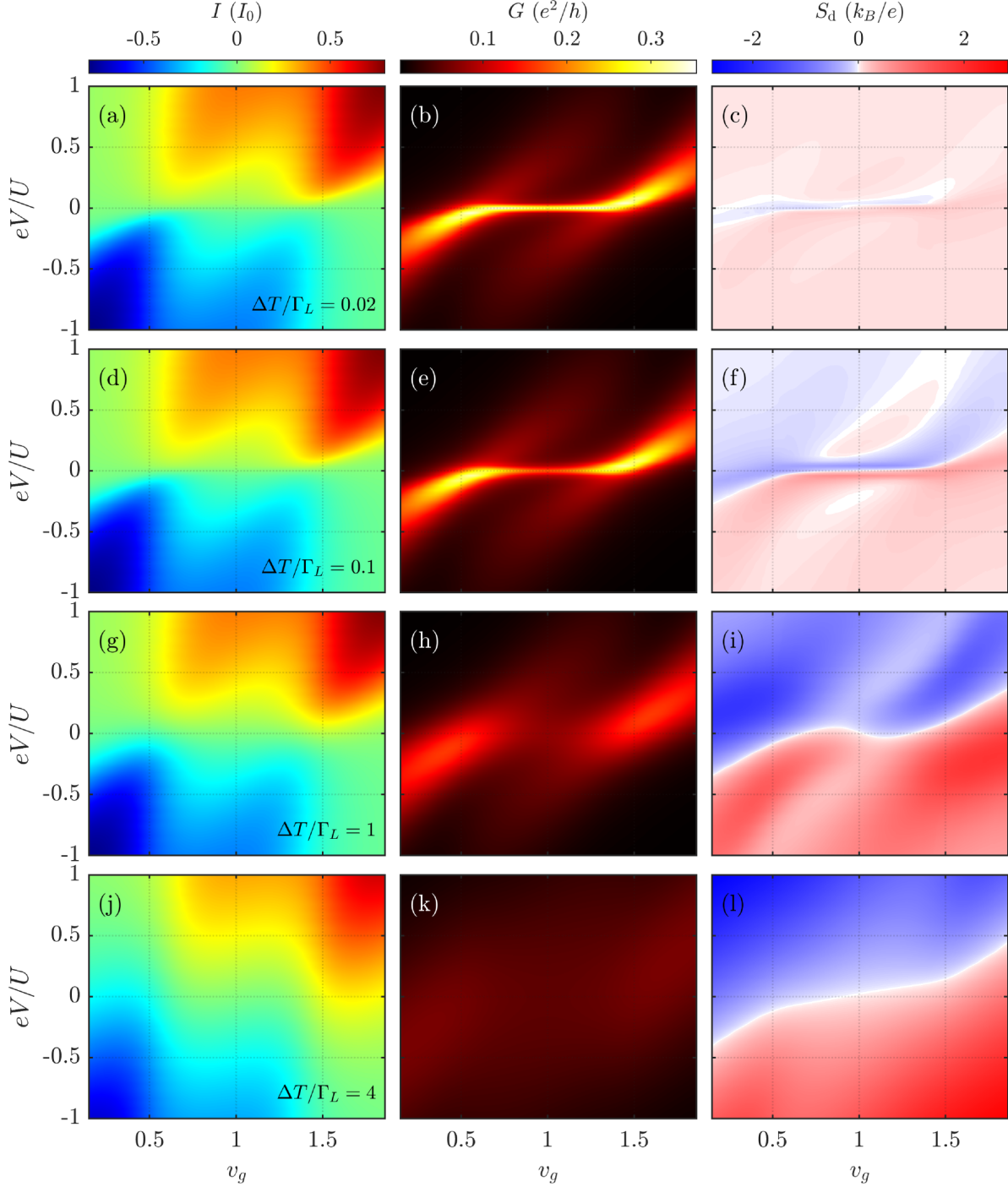


FIG. 9. (First column) The current I in units of $I_0 = 2e\Gamma_R/\hbar$, (second column) the differential conductance G , and (third column) the differential Seebeck coefficient S_d calculated as a function of the applied bias voltage V and the effective gate voltage v_g . For the capacitances we assume $C_L/C_R = 2$ and $C_g/C_R = 0.1$ and the other parameters are the same as in Fig. 2. Each row corresponds to different temperature gradient ΔT , as indicated.

sets the corresponding transport regimes: $v_g \lesssim 0.5$ ($v_g \gtrsim 1.5$) defines the empty (fully occupied) orbital regime, whereas the local moment regime is realized for $0.5 \lesssim v_g \lesssim 1.5$. Let us first analyze the case of the lowest temperature gradient, shown in the first row of Fig. 9, which corresponds to the situation when $\Delta T < T_K$. In Fig. 9(a) one can see a clear Coulomb diamond structure. On the other hand, the differential conductance exhibits then a pronounced zero-bias Kondo peak in the singly occupied orbital regime, i.e., $0.5 \lesssim v_g \lesssim 1.5$. Note, that the behavior of the differential

conductance is typical for tunnel junctions with asymmetric couplings to the contacts. Alternatively, one could also think of an adatom probed by a scanning tunneling microscope tip, which would correspond to a weakly coupled lead. At low temperatures, the differential thermopower is generally relatively small, however, one can still recognize sign change at low bias voltage regime, see Fig. 9(c).

When the thermal gradient becomes comparable to the Kondo temperature, the thermal response gets enhanced. This is presented in the second row of Fig. 9. Although the current

is hardly affected, the differential conductance shows a suppression of the Kondo resonance at zero bias voltage. Moreover, the differential Seebeck coefficient is increased at low bias voltages. In addition, in the Kondo regime one can clearly see a sign change of S_d as a function of positive bias voltage.

With increasing the temperature gradient even more, see the case of $\Delta T/\Gamma_L = 1$ in Fig. 9, the Coulomb diamond structure becomes smeared, and so does the conductance, which now only shows broad resonances due to resonant tunneling processes. The differential thermopower, on the other hand, is now much enlarged and it generally displays two regimes of either negative or positive values. Note, however, that the wavy line along which S_d changes sign strongly depends on both V and v_g , which is due to the voltage dependence of the orbital level. Finally, for larger temperature gradients, $\Delta T/\Gamma_L > 1$, see the last row of Fig. 9, most of the features are smeared. The differential conductance is suppressed by the thermal fluctuations, whereas the differential Seebeck effect again shows two regimes with different signs, but now separated by a line that monotonously depends on v_g .

IV. SUMMARY

In this paper we have studied the nonequilibrium thermoelectric transport properties of a molecular junction comprising a single-orbital molecule (or a quantum dot) asymmetrically attached to external electrodes. For such setup, we have determined the nonequilibrium electric and heat currents flowing through the system by using the perturbation theory with respect to the weakly coupled contact, while the strongly coupled subsystem was solved by using

the numerical renormalization group method. This allowed us to accurately take into account the electronic correlations that result in the development of the Kondo effect between the molecule and strongly coupled lead. In particular, we have determined the temperature gradient and bias voltage dependence of the nonlinear S_n and differential S_d Seebeck coefficients. First, we have performed the calculations assuming that the orbital level position is independent of the applied bias. Then, assuming realistic junction parameters, we have also considered the case when this condition is relaxed. In particular, we have shown that both S_n and S_d exhibit sign changes at nonequilibrium conditions, which are due to Kondo correlations. Up to now, such Kondo-related sign changes have been mostly observed in the linear response regime [10]. In addition, we have also determined the nonequilibrium heat currents, the power generated by the device, when it works as a heat engine, and the corresponding thermoelectric efficiency. We have found transport regimes characterized by a considerable efficiency of up to 80% of the Carnot efficiency. We believe that our results shed light on the thermopower of strongly-correlated molecular junctions in out-of-equilibrium settings and will foster further efforts in the examination of such systems.

ACKNOWLEDGMENTS

This work was supported by the Polish National Science Centre from funds awarded through the decision Nos. 2017/27/B/ST3/00621 and No. 2021/41/N/ST3/02098. We also acknowledge the computing time at the Poznań Supercomputing and Networking Center.

-
- [1] A. Dhar, Heat transport in low-dimensional systems, *Adv. Phys.* **57**, 457 (2008).
 - [2] Y. Dubi and M. Di Ventra, Thermoelectric effects in nanoscale junctions, *Nano Lett.* **9**, 97 (2009).
 - [3] Y. Dubi and M. Di Ventra, *Colloquium: Heat flow and thermoelectricity in atomic and molecular junctions*, *Rev. Mod. Phys.* **83**, 131 (2011).
 - [4] G. Benenti, G. Casati, K. Saito, and R. S. Whitney, Fundamental aspects of steady-state conversion of heat to work at the nanoscale, *Phys. Rep.* **694**, 1 (2017).
 - [5] G. Mazza, M. Gandolfi, M. Capone, F. Banfi, and C. Giannetti, Thermal dynamics and electronic temperature waves in layered correlated materials, *Nat. Commun.* **12**, 6904 (2021).
 - [6] G. D. Mahan and J. O. Sofo, The best thermoelectric, *Proc. Natl. Acad. Sci. USA* **93**, 7436 (1996).
 - [7] M. Krawiec and K. I. Wysokiński, Thermoelectric effects in strongly interacting quantum dot coupled to ferromagnetic leads, *Phys. B: Condens. Matter* **378-380**, 933 (2006).
 - [8] R. Franco, J. Silva-Valencia, and M. S. Figueira, Thermopower and thermal conductance for a Kondo correlated quantum dot, *J. Magn. Magn. Mater.* **320**, e242 (2008).
 - [9] J. Liu, Q.-f. Sun, and X. C. Xie, Enhancement of the thermoelectric figure of merit in a quantum dot due to the Coulomb blockade effect, *Phys. Rev. B* **81**, 245323 (2010).
 - [10] T. A. Costi and V. Zlatić, Thermoelectric transport through strongly correlated quantum dots, *Phys. Rev. B* **81**, 235127 (2010).
 - [11] T. K. T. Nguyen, M. N. Kiselev, and V. E. Kravtsov, Thermoelectric transport through a quantum dot: Effects of asymmetry in Kondo channels, *Phys. Rev. B* **82**, 113306 (2010).
 - [12] U. Eckern and K. I. Wysokiński, Two- and three-terminal far-from-equilibrium thermoelectric nano-devices in the Kondo regime, *New J. Phys.* **22**, 013045 (2020).
 - [13] P. A. Erdman, F. Mazza, R. Bosisio, G. Benenti, R. Fazio, and F. Taddei, Thermoelectric properties of an interacting quantum dot based heat engine, *Phys. Rev. B* **95**, 245432 (2017).
 - [14] M. A. Sierra, R. López, and D. Sánchez, Fate of the spin- $\frac{1}{2}$ Kondo effect in the presence of temperature gradients, *Phys. Rev. B* **96**, 085416 (2017).
 - [15] A. Svilans, M. Leijnse, and H. Linke, Experiments on the thermoelectric properties of quantum dots, *C. R. Phys.* **17**, 1096 (2016).
 - [16] A. Svilans, M. Josefsson, A. M. Burke, S. Fahlvik, C. Thelander, H. Linke, and M. Leijnse, Thermoelectric Characterization of the Kondo Resonance in Nanowire Quantum Dots, *Phys. Rev. Lett.* **121**, 206801 (2018).
 - [17] B. Dutta, D. Majidi, A. García Corral, P. A. Erdman, S. Florens, T. A. Costi, H. Courtois, and C. B. Winkelmann, Direct probe of the Seebeck coefficient in a Kondo-correlated single-quantum-dot transistor, *Nano Lett.* **19**, 506 (2019).
 - [18] D. Prete, P. A. Erdman, V. Demontis, V. Zannier, D. Ercolani, L. Sorba, F. Beltram, F. Rossella, F. Taddei, and S. Roddaro, Thermoelectric conversion at 30 K in InAs/InP nanowire quantum dots, *Nano Lett.* **19**, 3033 (2019).

- [19] C. Hsu, T. A. Costi, D. Vogel, C. Wegeberg, M. Mayor, H. S. J. van der Zant, and P. Gehring, Magnetic-Field Universality of the Kondo Effect Revealed by Thermocurrent Spectroscopy, *Phys. Rev. Lett.* **128**, 147701 (2022).
- [20] J. Kondo, Resistance minimum in dilute magnetic alloys, *Prog. Theor. Phys.* **32**, 37 (1964).
- [21] A. C. Hewson, *The Kondo Problem to Heavy Fermions*, Cambridge Studies in Magnetism (Cambridge University Press, Cambridge, 1993).
- [22] I. Weymann and J. Barnaś, Spin thermoelectric effects in Kondo quantum dots coupled to ferromagnetic leads, *Phys. Rev. B* **88**, 085313 (2013).
- [23] K. P. Wójcik and I. Weymann, Thermopower of strongly correlated T-shaped double quantum dots, *Phys. Rev. B* **93**, 085428 (2016).
- [24] T. A. Costi, Magnetic field dependence of the thermopower of Kondo-correlated quantum dots: Comparison with experiment, *Phys. Rev. B* **100**, 155126 (2019).
- [25] T. A. Costi, Magnetic field dependence of the thermopower of Kondo-correlated quantum dots, *Phys. Rev. B* **100**, 161106(R) (2019).
- [26] A. Manaparambil and I. Weymann, Spin Seebeck effect of correlated magnetic molecules, *Sci. Rep.* **11**, 9192 (2021).
- [27] V. Talbo, J. Saint-Martin, S. Retailleau, and P. Dollfus, Non-linear effects and thermoelectric efficiency of quantum dot-based single-electron transistors, *Sci. Rep.* **7**, 14783 (2017).
- [28] K. G. Wilson, The renormalization group: Critical phenomena and the Kondo problem, *Rev. Mod. Phys.* **47**, 773 (1975).
- [29] R. Bulla, T. A. Costi, and T. Pruschke, Numerical renormalization group method for quantum impurity systems, *Rev. Mod. Phys.* **80**, 395 (2008).
- [30] We used the open-access Budapest Flexible DM-NRG code, <http://www.phy.bme.hu/~dmnrg/>; O. Legeza, C. P. Moca, A. I. Tóth, I. Weymann, G. Zaránd, [arXiv:0809.3143](https://arxiv.org/abs/0809.3143).
- [31] A. Manaparambil, A. Weichselbaum, J. von Delft, and I. Weymann, Nonequilibrium spintronic transport through Kondo impurities, *Phys. Rev. B* **106**, 125413 (2022).
- [32] F. Schwarz, I. Weymann, J. von Delft, and A. Weichselbaum, Nonequilibrium Steady-State Transport in Quantum Impurity Models: A Thermofield and Quantum Quench Approach Using Matrix Product States, *Phys. Rev. Lett.* **121**, 137702 (2018).
- [33] J. Bauer, J. I. Pascual, and K. J. Franke, Microscopic resolution of the interplay of Kondo screening and superconducting pairing: Mn-phthalocyanine molecules adsorbed on superconducting Pb(111), *Phys. Rev. B* **87**, 075125 (2013).
- [34] C. Xu, C.-I. Chiang, Z. Han, and W. Ho, Nature of Asymmetry in the Vibrational Line Shape of Single-Molecule Inelastic Electron Tunneling Spectroscopy with the STM, *Phys. Rev. Lett.* **116**, 166101 (2016).
- [35] M. Gruber, A. Weismann, and R. Berndt, The Kondo resonance line shape in scanning tunnelling spectroscopy: Instrumental aspects, *J. Phys.: Condens. Matter* **30**, 424001 (2018).
- [36] M. Žonda, O. Stetsovych, R. Korytár, M. Ternes, R. Temirov, A. Raccanelli, F. S. Tautz, P. Jelínek, T. Novotný, and M. Švec, Resolving ambiguity of the Kondo temperature determination in mechanically tunable single-molecule Kondo systems, *J. Phys. Chem. Lett.* **12**, 6320 (2021).
- [37] Y. Xing, H. Chen, B. Hu, Y. Ye, W. A. Hofer, and H.-J. Gao, Reversible switching of Kondo resonance in a single-molecule junction, *Nano Res.* **15**, 1466 (2022).
- [38] S. Csonka, I. Weymann, and G. Zarand, An electrically controlled quantum dot based spin current injector, *Nanoscale* **4**, 3635 (2012).
- [39] D. Pérez Daroca, P. Roura-Bas, and A. A. Aligia, Enhancing the nonlinear thermoelectric response of a correlated quantum dot in the Kondo regime by asymmetrical coupling to the leads, *Phys. Rev. B* **97**, 165433 (2018).
- [40] P. Tulewicz, K. Wrześniewski, S. Csonka, and I. Weymann, Large Voltage-Tunable Spin Valve Based on a Double Quantum Dot, *Phys. Rev. Appl.* **16**, 014029 (2021).
- [41] P. W. Anderson, A poor man's derivation of scaling laws for the Kondo problem, *J. Phys. C: Solid State Phys.* **3**, 2436 (1970).
- [42] H. Haug and A.-P. Jauho, *Quantum Kinetics in Transport and Optics of Semiconductors* (Springer, Berlin, 2008).
- [43] R. Barnard, *Thermoelectricity in Metals and Alloys* (Taylor & Francis, London, 1972).
- [44] M. Krawiec and K. I. Wysokiński, Thermoelectric phenomena in a quantum dot asymmetrically coupled to external leads, *Phys. Rev. B* **75**, 155330 (2007).
- [45] M. Leijnse, M. R. Wegewijs, and K. Flensberg, Nonlinear thermoelectric properties of molecular junctions with vibrational coupling, *Phys. Rev. B* **82**, 045412 (2010).
- [46] J. Azema, P. Lombardo, and A.-M. Daré, Conditions for requiring nonlinear thermoelectric transport theory in nanodevices, *Phys. Rev. B* **90**, 205437 (2014).
- [47] J.-H. Jiang and Y. Imry, Enhancing Thermoelectric Performance Using Nonlinear Transport Effects, *Phys. Rev. Appl.* **7**, 064001 (2017).
- [48] P. W. Anderson, Localized magnetic states in metals, *Phys. Rev.* **124**, 41 (1961).
- [49] A. Dorda, M. Ganahl, S. Andergassen, W. von der Linden, and E. Arrigoni, Thermoelectric response of a correlated impurity in the nonequilibrium Kondo regime, *Phys. Rev. B* **94**, 245125 (2016).
- [50] S. Hershfield, K. A. Muttalib, and B. J. Nartowt, Nonlinear thermoelectric transport: A class of nanodevices for high efficiency and large power output, *Phys. Rev. B* **88**, 085426 (2013).
- [51] K. Yamamoto and N. Hatano, Thermodynamics of the mesoscopic thermoelectric heat engine beyond the linear-response regime, *Phys. Rev. E* **92**, 042165 (2015).
- [52] M. A. Sierra and D. Sánchez, Nonlinear heat conduction in coulomb-blockaded quantum dots, *Mater. Today: Proc.* **2**, 483 (2015).
- [53] H. Karbaschi, J. Lovén, K. Courteaut, A. Wacker, and M. Leijnse, Nonlinear thermoelectric efficiency of superlattice-structured nanowires, *Phys. Rev. B* **94**, 115414 (2016).
- [54] G. Gómez-Silva, P. A. Orellana, and E. V. Anda, Enhancement of the thermoelectric efficiency in a T-shaped quantum dot system in the linear and nonlinear regimes, *J. Appl. Phys.* **123**, 085706 (2018).
- [55] N.-X. Yang, Q. Yan, and Q.-F. Sun, Linear and nonlinear thermoelectric transport in a magnetic topological insulator nanoribbon with a domain wall, *Phys. Rev. B* **102**, 245412 (2020).
- [56] M. Yoshida, M. A. Whitaker, and L. N. Oliveira, Renormalization-group calculation of excitation properties for impurity models, *Phys. Rev. B* **41**, 9403 (1990).
- [57] F. D. M. Haldane, Scaling Theory of the Asymmetric Anderson Model, *Phys. Rev. Lett.* **40**, 416 (1978).


- [58] A. V. Kretinin, H. Shtrikman, D. Goldhaber-Gordon, M. Hanl, A. Weichselbaum, J. von Delft, T. Costi, and D. Mahalu, Spin-1/2 Kondo effect in an InAs nanowire quantum dot Unitary limit, conductance scaling, and Zeeman splitting, [Phys. Rev. B](#) **84**, 245316 (2011).
- [59] D. P. Daroca, P. Roura-Bas, and A. A. Aligia, Relation between width of zero-bias anomaly and Kondo temperature in transport measurements through correlated quantum dots: Effect of asymmetric coupling to the leads, [Phys. Rev. B](#) **98**, 245406 (2018).

9.2 Spin-resolved nonequilibrium thermopower of asymmetric nanojunctions [E]

Spin-resolved nonequilibrium thermopower of asymmetric nanojunctions

Anand Manaparambil^{*} and Ireneusz Weymann

*Institute of Spintronics and Quantum Information, Faculty of Physics, Adam Mickiewicz University,
Uniwersytetu Poznańskiego 2, 61-614 Poznań, Poland*

 (Received 31 July 2023; revised 20 January 2024; accepted 16 February 2024; published 4 March 2024)

The spin-resolved thermoelectric transport properties of correlated nanoscale junctions, consisting of a quantum dot/molecule asymmetrically coupled to external ferromagnetic contacts, are studied theoretically in the far-from-equilibrium regime. One of the leads is assumed to be strongly coupled to the quantum dot resulting in the development of the Kondo effect. The spin-dependent current flowing through the system, as well as the thermoelectric properties, are calculated by performing a perturbation expansion with respect to the weakly coupled electrode, while the Kondo correlations are captured accurately by using the numerical renormalization group method. In particular, we determine the differential and nonequilibrium Seebeck effects of the considered system in different magnetic configurations and uncover the crucial role of spin-dependent tunneling on the device performance. Moreover, by allowing for the spin accumulation in the leads, which gives rise to finite spin bias, we shed light on the behavior of the nonequilibrium spin Seebeck effect. In particular, we predict new sign changes of the spin-resolved Seebeck effect in the nonlinear response regime, which stem from the interplay of exchange field and finite voltage and temperature gradients.

DOI: [10.1103/PhysRevB.109.115402](https://doi.org/10.1103/PhysRevB.109.115402)

I. INTRODUCTION

Quantum transport through nanojunctions containing quantum dots or molecules has been under tremendous research interest due to promising applications of such nanostructures in nanoelectronics, spintronics, and spin caloritronics [1–4]. Due to the strong electron-electron interactions and a characteristic discrete density of states, these systems can exhibit large thermoelectric figure-of-merit and are excellent candidates for nanoscale heat engines [5–10]. As far as more fundamental aspects are concerned, correlated nanoscale systems enable exploration of fascinating many-body phenomena in a controllable fashion, which is hardly possible in bulk materials. One such phenomena is the Kondo effect [11,12], which can drastically change the system’s transport properties at low temperatures by giving rise to a universal enhancement of the conductance to its maximum [13,14]. In addition to voltage-biased setups’ investigations, the emergence of Kondo correlations can be also probed in the presence of a temperature gradient, where thermoelectric transport properties reveal the important physics [6–8]. In fact, the thermopower of quantum dot and molecular systems has been shown to contain the signatures of the Kondo phenomenon. More specifically, the sign changes in the temperature dependence of the Seebeck coefficient with the onset of Kondo correlations have been identified in both theoretical [15] and experimental [16–18] studies.

Further interesting properties arise when the junction’s electrodes are ferromagnetic and the tunneling processes become spin-dependent [1,3,4,19]. In the presence of a

finite temperature gradient, one can then observe an intricate interplay of heat, charge, and spin, which gives rise to the emergence of the spin Seebeck effect [20,21]. Besides this fundamental phenomenon, which is of interest for spin caloritronics [2], ferromagnetic nanojunctions allow for the exploration of competition between the Kondo correlations and the so-called ferromagnet-induced exchange field, which acts as a local magnetic field that can suppress the Kondo effect [22–25]. Such competition has already been revealed in theoretical studies on thermoelectric properties of various strongly correlated molecular and quantum dot systems with ferromagnetic contacts [26–34]. Most of these investigations, however, concerned the case of the linear response regime. As far as fully out-of-equilibrium settings are concerned, there have already been some efforts to understand nonlinear thermopower of nonmagnetic junctions [35–40], while the spin-dependent thermoelectric properties of ferromagnetic nanojunctions remain to a large extent unexplored.

The primary goal of this work is therefore to analyze the spin-resolved nonequilibrium thermopower of correlated nanoscale junctions, in which the interplay between the Kondo and exchange field is relevant. In particular, we study thermoelectric characteristics of nanojunctions that exhibit asymmetry in the couplings to ferromagnetic metallic leads. Such asymmetric couplings can be encountered especially in molecular junctions [41–46], and can be also present in artificial heterostructures with quantum dots by appropriately adjusting the gate voltages [47–49]. We thus consider a quantum dot/molecule strongly coupled to one ferromagnetic lead and weakly coupled to the other nonmagnetic or ferromagnetic lead kept at different potentials and temperatures, as displayed in Fig. 1. To determine the current flowing through such system, we perform a perturbation

^{*} anaman@amu.edu.pl

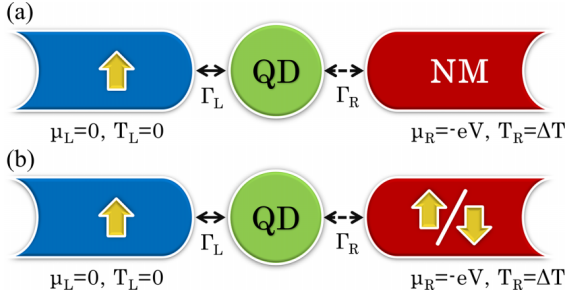


FIG. 1. The schematic of the considered asymmetric tunnel junction with embedded quantum dot/molecule strongly coupled to a cold ferromagnetic left lead and weakly coupled to a hot (a) nonmagnetic or (b) ferromagnetic right lead. The right lead is subject to voltage and temperature gradients, while the left lead is grounded and kept at zero temperature. The device in (b) can be in two magnetic configurations: the parallel (P) and antiparallel (AP) one, as indicated by the arrows.

expansion with respect to the weak coupling, while the properties of the strongly coupled subsystem, in which the Kondo correlations may arise, are obtained with the aid of the numerical renormalization group (NRG) method [50,51]. This allows us to accurately explore the signatures of the interplay between the spin-resolved transport and the Kondo correlations in the Seebeck coefficient. Furthermore, we study how different magnetic configurations of the system affect the differential and nonequilibrium Seebeck effects of the system. In particular, we show that the Seebeck coefficient exhibits new sign changes as a function of the bias voltage, which can be associated with the Kondo resonance split by exchange field. These sign changes are found to extend to the temperature gradients on the order of the Kondo temperature. Moreover, we provide a detailed analysis of the nonequilibrium spin Seebeck coefficient and demonstrate that it exhibits new sign changes in the nonlinear response regime, which stem from the interplay of spin-resolved tunneling and finite voltage and temperature gradients.

The paper is organized as follows: The system Hamiltonian and the theoretical framework are described in Sec. II. The numerical results and their discussion are presented in Sec. III, where we first analyze the exchange field effects on nonequilibrium thermopower, then, we consider the role of different magnetic configurations and, finally, we present the behavior of the nonlinear spin Seebeck effect. The summary and concluding remarks can be found in Sec. IV.

II. THEORETICAL DESCRIPTION

A. Model and Hamiltonian of the system

We consider a nanoscale junction with an embedded quantum dot/molecule, which is schematically shown in Fig. 1. The quantum dot is assumed to be strongly coupled to the left ferromagnetic lead and weakly coupled to the right lead, which can be either nonmagnetic [Fig. 1(a)] or ferromagnetic [Fig. 1(b)]. In the case of two ferromagnetic electrodes, we will distinguish two magnetic configurations: the parallel (P) one when the leads magnetic moments point in the same direction and the antiparallel (AP) one, when the orientation

of magnetic moments is opposite, see Fig. 1(b). It is assumed that there are finite temperature and voltage gradients applied to the system, with $T_L = 0$ and $\mu_L = 0$, whereas $T_R = \Delta T$ and $\mu_R = -eV$, as shown in Fig. 1, where T_α and μ_α are the temperature ($k_B \equiv 1$) and the chemical potential of lead α .

With the assumption of weak coupling between the quantum dot and right contact the system Hamiltonian can be simply written as

$$H = H_L + H_R + H_T. \quad (1)$$

H_L describes the strongly coupled left subsystem, consisting of the quantum dot and the left lead, and it is given by

$$H_L = \varepsilon_d \sum_{\sigma} n_{\sigma} + U n_{\uparrow} n_{\downarrow} + \sum_{k\sigma} \varepsilon_{Lk\sigma} c_{Lk\sigma}^{\dagger} c_{Lk\sigma} + \sum_{k\sigma} t_{Lk\sigma} (d_{\sigma}^{\dagger} c_{Lk\sigma} + c_{Lk\sigma}^{\dagger} d_{\sigma}), \quad (2)$$

where $n_{\sigma} = d_{\sigma}^{\dagger} d_{\sigma}$, with d_{σ}^{\dagger} (d_{σ}) being the creation (annihilation) operator on the quantum dot for an electron of spin σ , $c_{\alpha k\sigma}$ ($c_{\alpha k\sigma}^{\dagger}$) annihilates (creates) an electron in the lead α with momentum k , spin σ and energy $\varepsilon_{\alpha k\sigma}$. The quantum dot is modeled by a single orbital of energy ε_d and Coulomb correlations U . The hopping matrix elements between the quantum dot and lead α are denoted by $t_{\alpha k\sigma}$ and give rise to the level broadening $\Gamma_{\alpha\sigma} = \pi \rho_{\alpha\sigma} |t_{\alpha k\sigma}|^2$, which is assumed to be momentum independent, where $\rho_{\alpha\sigma}$ is the density of states of lead α for spin σ .

The second part of the Hamiltonian describes the right lead and is given by

$$H_R = \sum_{k\sigma} (\varepsilon_{Rk\sigma} - \mu_R) c_{Rk\sigma}^{\dagger} c_{Rk\sigma}, \quad (3)$$

while the last term of H accounts for the hopping between the left and right subsystems

$$H_T = \sum_{k\sigma} t_{Rk\sigma} (d_{\sigma}^{\dagger} c_{Rk\sigma} + c_{Rk\sigma}^{\dagger} d_{\sigma}). \quad (4)$$

In the following, we use the lowest-order perturbation theory in H_T to study the spin-dependent electric and thermoelectric properties of the system.

B. Method and nonlinear transport coefficients

The electric current flowing through the system in the spin channel σ in the lowest-order perturbation with respect to the coupling to the right lead can be expressed as [52,53]

$$I_{\sigma}(V, \Delta T) = -\frac{e\Gamma_{R\sigma}}{\hbar} \int_{-\infty}^{\infty} d\omega A_{L\sigma}(\omega) \times [f_L(\omega) - f_R(\omega - eV)], \quad (5)$$

where $f_{\alpha}(\omega) = [1 + \exp(\omega/T_{\alpha})]^{-1}$ is the Fermi-Dirac distribution function, while $A_{L\sigma}(\omega)$ denotes the spin-resolved spectral function of the left subsystem. The total current flowing through the system under potential bias V and temperature gradient ΔT is thus $I(V, \Delta T) = \sum_{\sigma} I_{\sigma}(V, \Delta T)$. Since we treat the coupling to the right lead as a perturbation, we expect the next-order contributions, e.g., $I_{\sigma} \sim \Gamma_{R\sigma}^2$, to be much smaller, and assume that these do not affect the main behavior of the system.

The spectral function of the left subsystem $A_{L\sigma}(\omega)$ is calculated by means of the NRG method [50,51,54], which allows us to include all the correlation effects between the quantum dot strongly coupled to the left contact in a fully nonperturbative manner. The spectral function $A_{L\sigma}(\omega)$ is determined as the imaginary part of the Fourier transform of the retarded Green's function of the left subsystem Hamiltonian, H_L , $G_\sigma(t) = -i\Theta(t)\langle\{d_\sigma(t), d_\sigma^\dagger(0)\}\rangle$. For the purpose of NRG calculations, the conduction band of the left lead can be discretized logarithmically with discretization parameter Λ and mapped onto a tight binding chain (Wilson chain) with couplings that decay as $\Lambda^{-n/2}$, where n is the site number in the chain. This mapping transforms H_L into a tight-binding Hamiltonian with each quantum dot spin σ coupled to the first site of the chain with an effective coupling $\sqrt{2\Gamma_{L\sigma}/\pi}$. The new Hamiltonian is then solved iteratively, while keeping a relevant number of the lowest energy eigenstates N_K . In our calculations, we use $\Lambda = 2$, the iteration number $N = 60$ and the kept states N_K at least 2^{10} . To obtain the spectral function, the data is collected in logarithmic bins that are then appropriately broadened to obtain a smooth function [55]. We note that in general the spectral function also depends on temperature, however, to shed light on the Kondo correlations in thermoelectric transport behavior, we assume that the left lead temperature is well below the Kondo temperature, T_K . Hence, the spectral function for $T_L \ll T_K$ is essentially equivalent to the zero-temperature spectral function.

For the further analysis, it is convenient to express the coupling constants $\Gamma_{\alpha\sigma}$ by using the spin polarization of the lead α , p_α , as $\Gamma_{L\sigma} = (1 + \sigma p_L)\Gamma_L$ and $\Gamma_{R\sigma} = (1 + \sigma p_R)\Gamma_R$ for the parallel magnetic configuration, with $\Gamma_{R\sigma} = (1 - \sigma p_R)\Gamma_R$ in the case of the antiparallel configuration of the system. Here, $\Gamma_\alpha = (\Gamma_{\alpha\uparrow} + \Gamma_{\alpha\downarrow})/2$. Furthermore, in the case when the right lead is nonmagnetic, $p_R = 0$, while for both ferromagnetic leads we for simplicity assume $p_L = p_R \equiv p$.

As far as thermoelectric coefficients are concerned, the differential Seebeck coefficient can be expressed as [56]

$$S_d = -\left(\frac{dV}{dT}\right)_I = -\left(\frac{\partial I}{\partial T}\right)_V \bigg/ \left(\frac{\partial I}{\partial V}\right)_{\Delta T}. \quad (6)$$

Furthermore, the extension of the conventional Seebeck coefficient to the nonlinear response regime is referred to as the nonequilibrium Seebeck coefficient S_n , and it can be defined as [39,47,49,57–59]

$$S_n = -\left(\frac{\Delta V}{\Delta T}\right)_{I(V+\Delta V, \Delta T)=I(V,0)}. \quad (7)$$

The above definitions will be used to describe thermoelectric transport in different configurations of the system, respectively.

III. NUMERICAL RESULTS AND DISCUSSION

In this section we present the main numerical results and their discussion. In our considerations we assume that the left lead is always ferromagnetic, while the right electrode can be either nonmagnetic or ferromagnetic, cf. Fig. 1. For the studied setup, the strong coupling to the left contact may give rise to the Kondo effect [12,13]. However, it is crucial to realize that the presence of the spin-dependent hybridization

results in a local exchange field on the quantum dot, which can split the dot orbital level when detuned from the particle-hole symmetry point, and thus suppress the Kondo resonance. The magnitude of such exchange field can be estimated from the perturbation theory, which at zero temperature gives [60],

$$\Delta\varepsilon_{\text{exch}} = \frac{2p_L\Gamma_L}{\pi} \ln \left| \frac{\varepsilon_d}{\varepsilon_d + U} \right|. \quad (8)$$

The presence of the exchange field and its detrimental effect on the Kondo phenomenon has been confirmed by various experiments on electronic transport measurements in quantum dot and molecular systems [23,24,61,62].

We start our considerations with the analysis of electric transport properties, revealing the effects of the exchange field. Further on, we study the nonlinear thermoelectric response, first for the case of nonmagnetic right lead and then for the case of two ferromagnetic leads. In numerical calculations, we use the following parameters: $U = 0.2$, $\Gamma_L = 0.02$, $\Gamma_R = 0.002$, in units of band halfwidth, and $p = 0.4$ for the ferromagnetic leads. For the assumed parameters, the Kondo temperature of the left subsystem for $\varepsilon_d = -U/2$ is equal to [60,63], $T_K \approx 0.035\Gamma_L$. We notice that one could, in principle, expect that the coupling to the right contact should also give rise to the Kondo correlations. However, due to exponential dependence of T_K on the ratio of Coulomb correlations and coupling strength, the estimated right-lead Kondo temperature is completely negligible. Thus, it is fully justifiable to assume that the Kondo correlations result only from the coupling to the left lead.

To begin with, it is instructive to analyze the properties of the left subsystem itself as described by its local density of states. The spectral function for each individual spin channel is shown in Fig. 2. First of all, one can see that for $\varepsilon_d = -U/2$, there is a pronounced Kondo peak at the Fermi level for each spin component. However, when detuned from the particle-hole symmetry, a finite exchange-induced splitting emerges, cf. Eq. (8), which suppresses the Kondo effect when $|\Delta\varepsilon_{\text{exch}}| \gtrsim T_K$. Because of that, each spin component of the spectral function displays a slightly detuned from Fermi energy side peak, constituting the split Kondo resonance. In addition, the Hubbard resonances at $\omega \approx \varepsilon_d$ and $\omega \approx \varepsilon_d + U$ become affected as well: although their position is only slightly modified, their magnitude gets strongly spin-dependent.

The splitting of the Kondo resonance is directly visible in the differential conductance of the system, which is displayed in Fig. 3. This figure presents the bias voltage dependence of the differential conductance in different magnetic configurations for various temperature gradients, as indicated. More specifically, G corresponds to the case when the right lead is nonmagnetic [cf. Fig. 1(a)], while G^P (G^{AP}) presents the case of both ferromagnetic leads in the parallel (antiparallel) alignment [cf. Figs. 1(b)–1(c)]. When the orbital level is detuned out of the particle-hole symmetry point, the splitting of the Kondo resonance may emerge depending on the magnetic configuration of the system. The behavior of the differential conductance at low bias voltage is displayed in the insets of Fig. 3.

Let us begin the discussion with the case of nonmagnetic right lead, presented in Fig. 3(a). First of all, one can note a

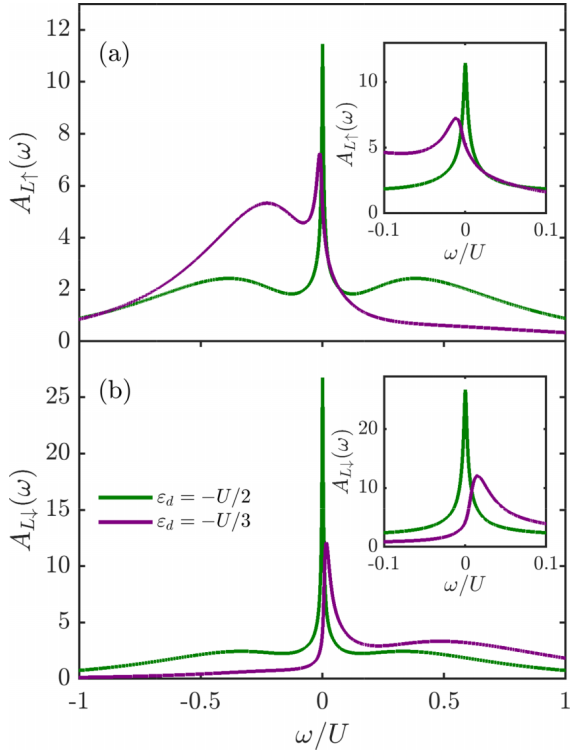


FIG. 2. The energy dependence of the spectral functions for the individual spin channels, (a) $A_{L\uparrow}(\omega)$ and (b) $A_{L\downarrow}(\omega)$ calculated for the strongly coupled left subsystem with orbital energies as indicated. The zoomed Kondo and split-Kondo peaks are shown in the insets. The other parameters are: $U = 0.2$, $\Gamma_L = 0.02$, in units of band half width, and $p = 0.4$.

large asymmetry of the differential conductance with respect to the bias reversal. Moreover, for small temperature gradients, $\Delta T \lesssim T_K$, the split zero-bias anomaly due to the Kondo effect is visible. To qualitatively understand this behavior, it is helpful to inspect the behavior of the spectral function around the Fermi energy, see the insets of Fig. 2. One can note that the split Kondo peak in $A_{L\uparrow}(\omega < 0)$ has a smaller weight compared to the split Kondo peak in $A_{L\downarrow}(\omega > 0)$. Because, for low temperature gradients, for $eV > 0$ ($eV < 0$), we probe the density of states of the left subsystem for negative (positive) energies, the above-mentioned asymmetry in $A_{L\sigma}(\omega)$ gives rise to highly asymmetric behavior of the differential conductance, see Fig. 3(a), with the peak in the negative voltage regime more pronounced than the other. Interestingly, when the tunneling to the right lead becomes spin dependent, in the case of parallel configuration one observes a rather symmetric behavior of G^P , with nicely visible split zero-bias anomaly, see Fig. 3(b). This is due to the fact that the increased tunneling rate of spin-down electrons due to larger density of states becomes now reduced since the spin-down electrons are the minority ones in the right lead. On the other hand, the tunneling of spin-up electrons to the right is enlarged. As a consequence, the unequal contributions of the currents in each spin channel become now equalized and the differential conductance in the parallel configuration exhibits split-Kondo resonance with the side peaks of comparable height. On the other hand, when the magnetization of the right lead is flipped, the asymmetric behavior visible in Fig. 3(a) is even further

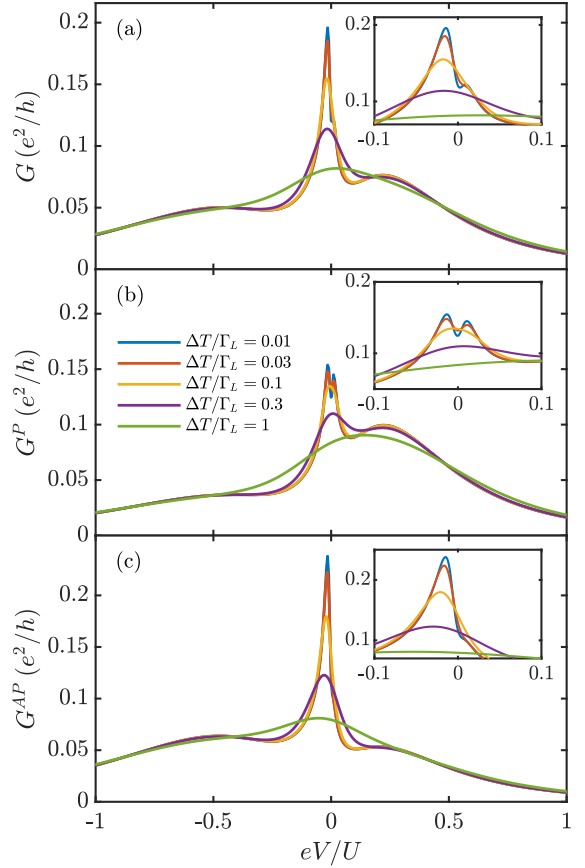


FIG. 3. The differential conductance for the quantum dot strongly coupled to ferromagnetic left lead and weakly coupled to (a) nonmagnetic right lead, ferromagnetic right lead in (b) the parallel, and (c) antiparallel magnetic configuration. The insets show the closeup of the differential conductance behavior for respective configurations. The parameters are the same as in Fig. 2 with $\varepsilon_d = -U/3$, $\Gamma_R = 0.002$, and different temperature gradients, as indicated.

magnified, see Fig. 3(c). This can be understood by invoking similar arguments as above, keeping in mind that now the rate of spin-up tunneling to the right lead is smaller than that for the spin-down electrons. With increase in the temperature gradient, the Kondo-related behavior gets smeared and finally disappears when $\Delta T \gtrsim T_K$, $|\Delta\varepsilon_{\text{exch}}|$.

A. Effects of exchange field on nonequilibrium thermopower

In this section, we focus on the case where the right lead is nonmagnetic, see Fig. 1(a). In such a setup it will be possible to observe clear signatures of ferromagnet-induced exchange field on the thermoelectric properties of the system subject to temperature and voltage gradients. We first study the case of the linear response in potential bias with nonlinear temperature gradient in Sec. III A 1, while in Sec. III A 2 the discussion is extended to the case of nonlinear response regime in both ΔT and V .

1. Zero-bias thermoelectrics with finite temperature gradient

Figure 4 displays the zero-bias differential conductance G , the differential Seebeck coefficient S_d and the nonlinear

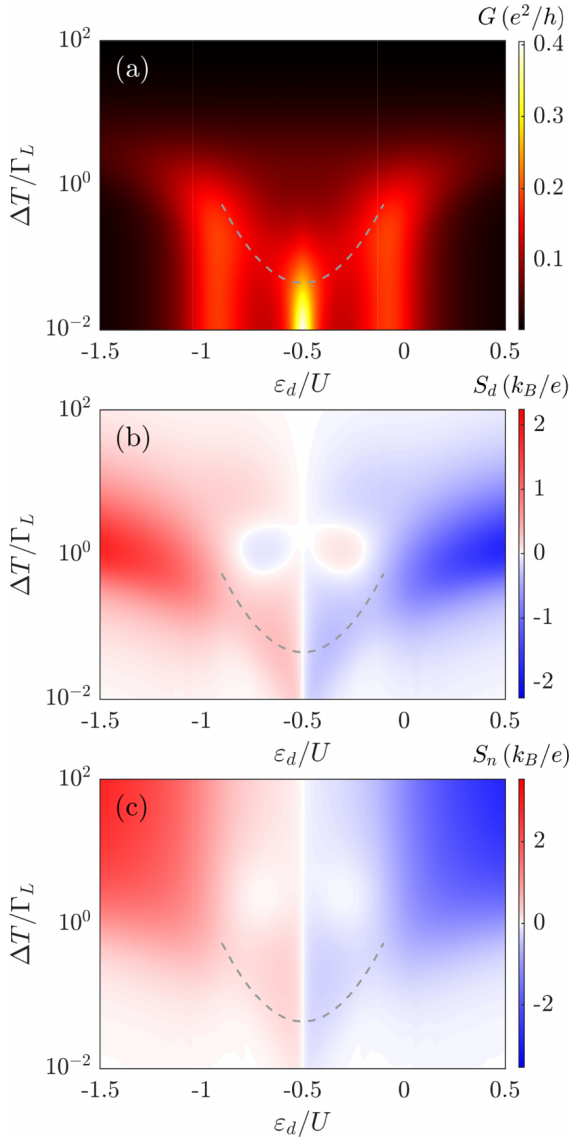


FIG. 4. (a) The differential conductance G , (b) the differential Seebeck coefficient S_d , and (c) the nonequilibrium Seebeck coefficient S_n of the quantum dot strongly coupled to left ferromagnetic lead and weakly attached to the right nonmagnetic lead plotted as a function of the orbital energy ε_d and the temperature gradient ΔT . The dashed lines show the Kondo temperature for the corresponding parameters. The system is assumed to be in the linear response regime with respect to the bias voltage. The other parameters are the same as in Fig. 3.

Seebeck coefficient S_n calculated as a function of orbital level ε_d and finite temperature gradient ΔT . For low temperature gradients, the conductance shows considerable increase near three values of ε_d . The peaks for $\varepsilon_d \approx 0$ and $\varepsilon_d \approx -U$ correspond to the Hubbard resonances, whereas the maximum at $\varepsilon_d = -U/2$ is due to the Kondo effect. In fact, in the local moment regime, $-1 \lesssim \varepsilon_d/U \lesssim 0$, the Kondo resonance is suppressed by the exchange field once $|\Delta\varepsilon_{\text{exch}}| \gtrsim T_K$, i.e., for values of ε_d away from the particle-hole symmetry point, cf. Eq. (8). With the increase in the temperature gradient, the Kondo resonance dies out when $\Delta T > T_K$, see the dashed line

in the figure, and the Hubbard peaks get suppressed when $\Delta T > \Gamma_L$, see Fig. 4(a).

In the case of differential and nonlinear Seebeck coefficients presented in Figs. 4(b) and 4(c), respectively, we can see an overall antisymmetric behavior across the particle-hole symmetry point $\varepsilon_d = -U/2$. The sign of the Seebeck coefficient here corresponds to the dominant charge carriers in transport, holes for $\varepsilon_d < -U/2$ and particles for $\varepsilon_d > -U/2$. The differential Seebeck coefficient shows two sign changes in the local moment regime as a function of the temperature gradient. Typically, in the linear response regime, the sign change at the lower temperature gradient corresponds to the Kondo correlations and is seen around the Kondo temperature T_K [15]. However, in our system the exchange field suppresses and splits the Kondo resonance, such that the signatures of the Kondo correlations are seen at $\Delta T \approx \Gamma_L$, which is much larger than $\Delta T \approx T_K$. In the case of nonlinear Seebeck coefficient, we do not find the corresponding sign changes because S_n can deviate considerably from the linear response Seebeck coefficient at large ΔT [33]. Additionally, one can see that both Seebeck coefficients decay with decreasing ΔT . This behavior can be captured using the Sommerfeld expansion for the linear response Seebeck coefficient

$$S(T) \propto \frac{T}{A(\omega=0, T)} \left. \frac{\partial A}{\partial \omega} \right|_{\omega=0}. \quad (9)$$

We also note that both Seebeck coefficients can possess finite values at even lower ΔT inside the local moment regime than outside of it, due to the additional contribution associated with the Kondo effect.

2. The case of nonlinear potential bias and temperature gradients

Let us now inspect the behavior of the nonequilibrium thermoelectric coefficients as a function of both potential bias and temperature gradient shown in Fig. 5, focusing on V and ΔT range where Kondo correlations are important. The first row of the figure corresponds to the case of particle-hole symmetry, $\varepsilon_d = -U/2$, while the second row presents the results for $\varepsilon_d = -U/3$. Consider the first case. Figure 5(a) depicts the bias and temperature gradient dependence of the differential conductance G . There exist a prominent peak at low ΔT centered at $V = 0$, this is the zero-bias conductance peak characteristic of the Kondo effect. As the temperature gradient increases, the Kondo peak dies out and becomes smeared when $\Delta T \gtrsim T_K$. It is important to note that the increase in the temperature of the right lead does not suppress the Kondo resonance in the strongly correlated left subsystem. Finite T_R rather obscures the characteristics of the Kondo effect by smearing the transport window defined by $[f_L(\omega) - f_R(\omega - eV)]$, cf. Eq. (5). The differential and nonlinear Seebeck coefficients, shown in Figs. 5(b) and 5(c), exhibit a sign change with respect to the bias voltage reversal. Moreover, while S_d exhibits considerable values around the Kondo peak and becomes suppressed as ΔT grows, S_n gets enhanced when $\Delta T \gtrsim (\Gamma_L/U)|eV|$.

When the orbital level is detuned out of the particle-hole symmetry point, one can observe an interesting interplay between the exchange field and Kondo effect, and its signatures present in the nonlinear thermoelectric coefficients. First,

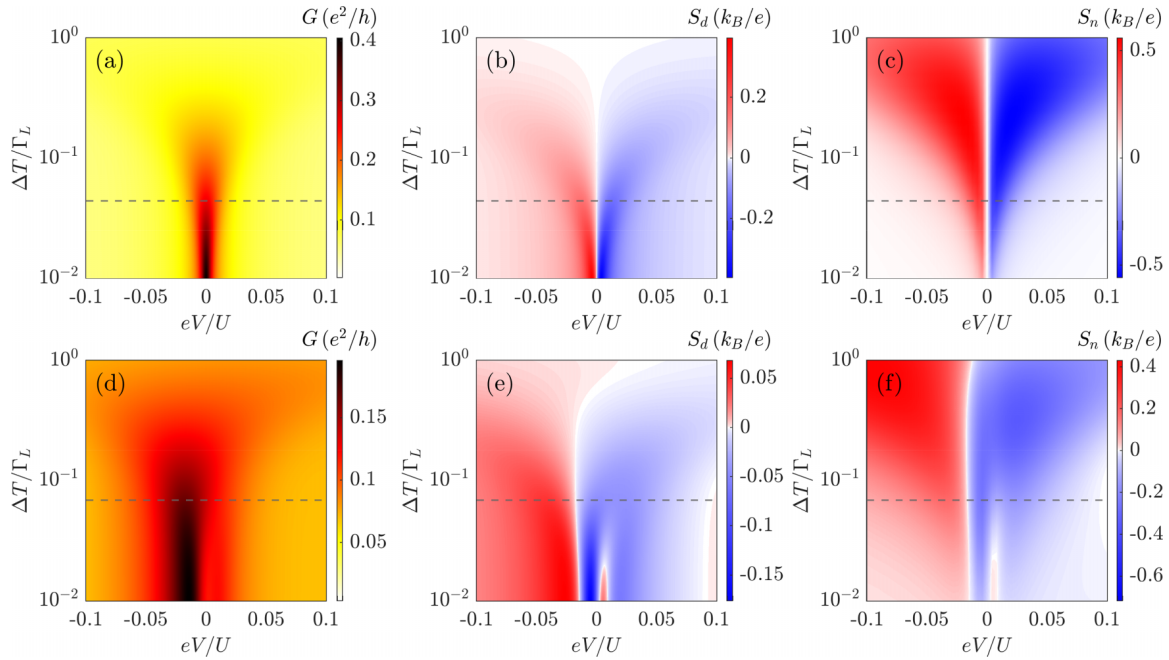


FIG. 5. (a), (d) The differential conductance G , (b), (e) the differential Seebeck coefficient S_d and (c), (f) the nonequilibrium Seebeck coefficient S_n as a function of the potential bias V and the temperature gradient ΔT . The first row corresponds to the particle-hole symmetry point $\varepsilon_d = -U/2$, while the second row shows the case of $\varepsilon_d = -U/3$. The dashed horizontal lines indicate the Kondo temperature T_K for the corresponding ε_d . The other parameters are the same as in Fig. 3.

Fig. 5(d) shows the splitting of the Kondo peak due to the exchange field present in the strongly correlated subsystem. As observed in the discussions of Fig. 3(a), the split Kondo peaks are not symmetric, with the more prominent one in the $eV < 0$ regime and both dying off at large ΔT . Interestingly, the differential and nonlinear Seebeck coefficients also capture the signatures of the exchange field shown by the split Kondo peak. In fact, there exist additional sign changes in the nonlinear response regime with respect to V . More specifically, at low ΔT , there is a sign change at low bias voltages, followed by another one, roughly located around the split-Kondo peak, see Figs. 5(e) and 5(f). These sign changes correspond to the additional energy scale in the system, namely the exchange field $\Delta\varepsilon_{\text{exch}}$. They occur at slightly different absolute values of eV , which is due to the fact that the Kondo resonance exhibits an asymmetric splitting, cf. Fig. 2. With increasing the temperature gradient, we observe that the right split Kondo peak in the conductance dies out first, accordingly the regime of positive values of the Seebeck coefficients corresponding to the right peak disappears around $\Delta T \approx 0.03\Gamma_L$. Moreover, we also note that the overall sign change of the thermopower as a function of the bias voltage is now shifted to negative values of eV , as compared to the case of particle-hole symmetry, see Fig. 5.

B. Effects of different magnetic configurations on nonequilibrium thermopower

In this section we study the case where the quantum dot is coupled to both ferromagnetic leads with spin polarization $p = 0.4$. The magnetic moments of the external leads are assumed to be aligned either in parallel or antiparallel. The

focus is on the effects of different magnetic configurations on nonequilibrium thermoelectric transport properties.

1. The case of zero bias with nonlinear temperature gradient

The zero-bias thermoelectric properties of the system with two ferromagnetic leads are shown in Fig. 6. The differential conductance for the parallel G^P and antiparallel G^{AP} configuration of the lead magnetizations is shown in Figs. 6(a) and 6(b). The qualitative behavior of both conductances is similar to the case of nonmagnetic lead on the right, where G shows a region of high conductance around $\varepsilon_d = -U/2$ due to the Kondo effect. Similarly to the previous case, the exchange field suppresses the linear response conductance for values of ε_d away from the particle-point symmetry. Around $\varepsilon_d \approx 0, -U$, there is an increase in the conductance corresponding to the contribution from the Hubbard peaks. It is interesting to note that the conductance in the case of parallel configuration is smaller than that in the antiparallel configuration around the Kondo resonance, cf. the discussion of Fig. 3, while this situation is reversed for the resonances at $\varepsilon_d \approx 0, -U$.

The Seebeck coefficients S_d^P and S_n^P shown in Figs. 6(c) and 6(e) for the parallel configuration display very interesting features corresponding to various energy scales. These coefficients show antisymmetric behavior across $\varepsilon_d = -U/2$ and sign changes as a function of temperature gradient in the local moment regime $-1 \lesssim \varepsilon_d/U \lesssim 0$. Let us first consider the linear response in ΔT for S_d^P . In this regime one can relate the Seebeck coefficient to the conductance through the Mott's formula. Thus, the changes of G^P as a function of orbital level are reflected in the corresponding dependence of the thermopower, which shows sign changes as ε_d is detuned

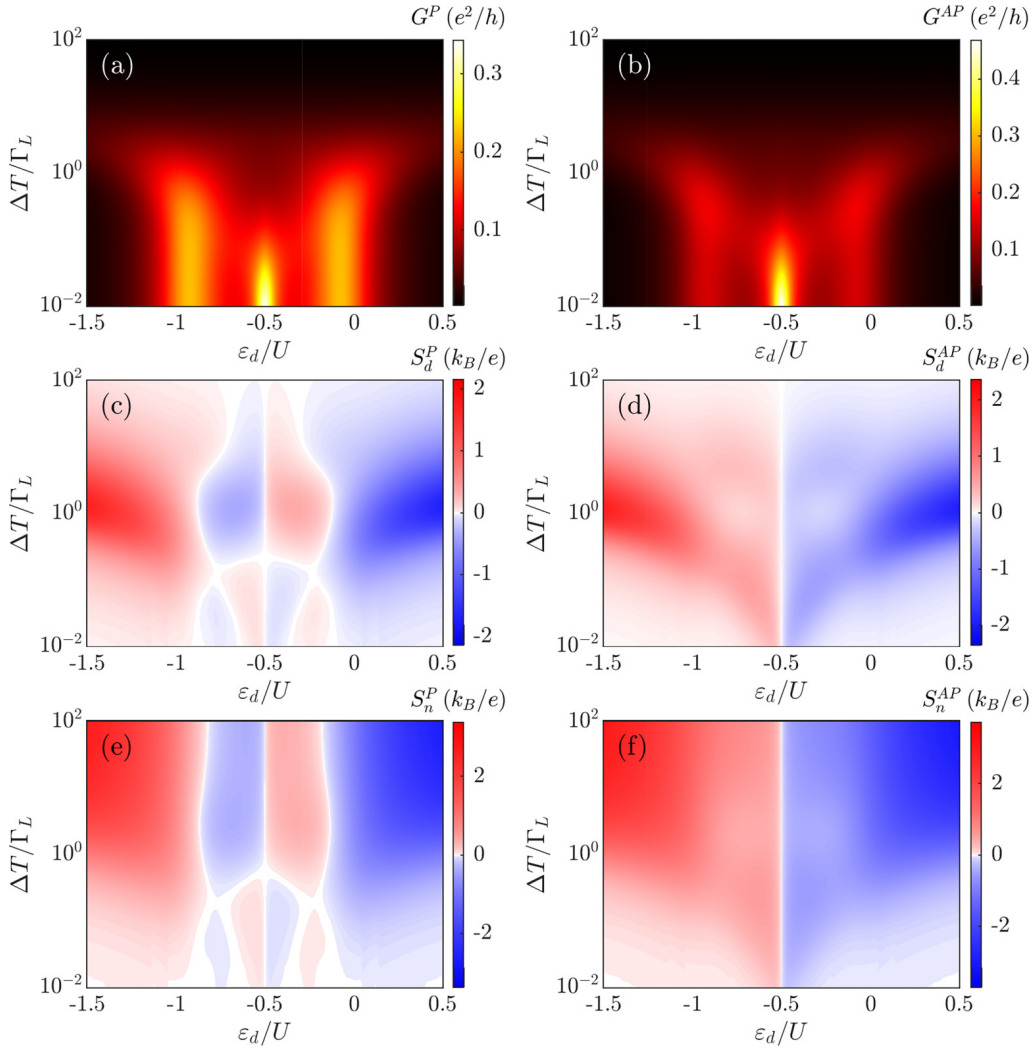


FIG. 6. (a), (b) The differential conductance G , (c), (d) the differential Seebeck coefficient S_d and (e), (f) the nonequilibrium Seebeck coefficient S_n in (first column) the parallel (P) and (second column) antiparallel (AP) configuration calculated as a function of ΔT and ε_d assuming linear response in voltage. The spin polarizations of both leads are equal to $p = 0.4$ and the other parameters are the same as in Fig. 3.

from the particle-hole symmetry point. The first sign change occurs when detuning is large enough to induce the exchange field that suppresses the Kondo effect. Further sign change occurs at the onset of conductance increase (as function of ε_d) due to the Hubbard resonance. This behavior extends to higher ΔT as long as the thermal gradient is smaller than the Kondo energy scale (or $\Delta\varepsilon_{\text{exch}}$). Otherwise, another sign change occurs as a function of ΔT , see Fig. 6(c). Very similar dependence can be observed in Fig. 6(e), which shows the nonequilibrium Seebeck coefficient S_n^P . The main difference can be seen for large ΔT , where S_n^P takes considerable values while S_d^P decreases, as explained earlier.

The situation is completely different in the case of the antiparallel configuration, where one does not see any additional sign changes, neither in S_d^{AP} nor in S_n^{AP} , other than the ones present across $\varepsilon_d = -U/2$, see Figs. 6(d) and 6(f). This can be understood by realizing that the interplay of exchange field with spin-dependent tunneling to the right contact hinders the splitting of the Kondo resonance as a function of the bias voltage. Consequently, one only observes a single resonance displaced from $V = 0$, cf. Fig. 3(c), which results in much

more regular dependence of the differential and nonequilibrium Seebeck coefficients.

2. The case of nonlinear potential bias and temperature gradient

The nonequilibrium thermoelectric properties of the quantum dot coupled to both ferromagnetic leads are shown in Fig. 7. The first row corresponds to the case of parallel configuration of the leads' magnetizations. The differential conductance depicted in Fig. 7(a) exhibits the split Kondo anomaly, with side peaks of similar magnitude located at roughly the same distance from the zero bias. Both peaks die off with the temperature gradient around $\Delta T \approx 0.05\Gamma_L$, i.e. when thermal gradient exceeds the Kondo temperature.

At low ΔT the differential and nonequilibrium Seebeck coefficients exhibit similar bias voltage dependence to the case presented in Figs. 5(e) and 5(f), see Figs. 7(b) and 7(c). Now, however, the region of negative Seebeck coefficient is smaller. This can be attributed to the fact that the split Kondo resonance is more symmetric across the bias reversal in the case of parallel magnetic configuration, cf. Fig. 3(b). Unlike

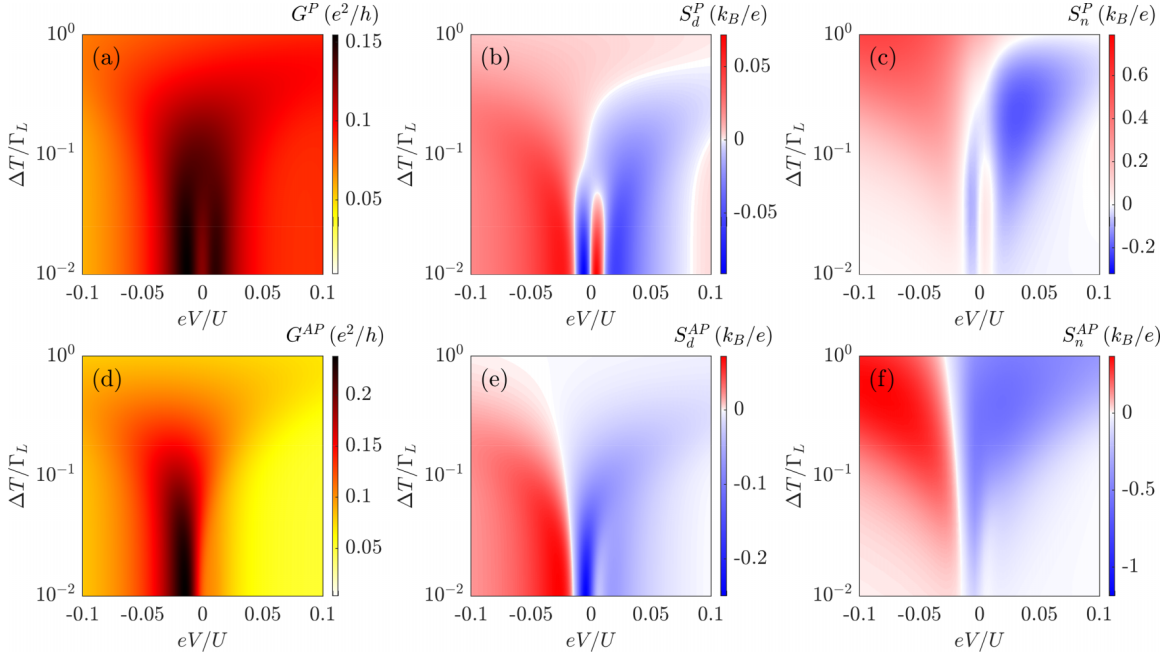


FIG. 7. (a), (d) The differential conductance G , (b), (e) the differential Seebeck coefficient S_d and (c), (f) the nonequilibrium Seebeck coefficient S_n as a function of the bias voltage and temperature gradient in the case of $\varepsilon_d = -U/3$. The first (second) row corresponds to the parallel (antiparallel) magnetic configuration of the system. The other parameters are the same as in Fig. 6.

in the case of nonmagnetic right lead, the sign changes at finite bias corresponding to the split Kondo peak persist as long as $\Delta T \lesssim T_K$ and disappear around comparable temperature gradient.

The case of antiparallel magnetic configuration of the system is presented in the second row of Fig. 7. Consistent with the discussion of Fig. 3(c), the differential conductance exhibits two conductance peaks but with a large difference in their magnitudes. The peak in the negative bias regime is far more pronounced than the miniscule peak one can observe in the positive regime. Just as in the case of other configurations, the peaks die out with increasing the temperature gradient but the negative bias peak survives till larger temperature gradients $\Delta T \approx 0.2\Gamma_L$, whereas the positive bias peak vanishes at temperature gradients as low as $\Delta T \approx 0.02\Gamma_L$.

The Seebeck coefficients S_d^{AP} and S_n^{AP} , shown in Figs. 7(e) and 7(f), respectively, demonstrate a similar behavior to the other configurations only at very low temperature gradients. However, now, instead of sign changes, one only observes suppression of the Seebeck coefficients at the corresponding values of the bias voltage associated with the exchange field. These suppressions extend to temperature gradients of the order of $\Delta T \approx 0.03\Gamma_L$, see Figs. 7(e) and 7(f).

C. Finite spin accumulation and the associated nonequilibrium spin Seebeck effect

In this section we consider the case when ferromagnetic contacts are characterized by slow spin relaxation, which can result in a finite spin accumulation [64,65]. Such a spin accumulation will induce a spin bias across the quantum dot. Here, we assume that the spin accumulation and the resulting spin-dependent chemical potential occurs only in the right

lead. Thus, we define the induced spin bias as, $eV_s/2 = \mu_{R\uparrow} - \mu_{R\downarrow}$ (keeping $\mu_L = 0$). The nonequilibrium spin bias across the quantum dot enables the spin chemical potentials to be tuned separately and thus the thermal bias induced transport can be different in the separate spin channels. The system can then exhibit interesting spin caloritronic properties, such as the spin Seebeck effect. The spin Seebeck coefficient S_s quantifies the magnitude and the direction of the spin current induced in the presence of a thermal bias [20]. Analogous to the differential Seebeck effect S_d , the differential spin Seebeck coefficient S_s in the nonlinear response regime can be defined as

$$S_s = -\left(\frac{dV_s}{d\Delta T}\right)_{I_s} = -\left(\frac{\partial I_s}{\partial \Delta T}\right)_{V_s} / \left(\frac{\partial I_s}{\partial V_s}\right)_{\Delta T}, \quad (10)$$

where $I_s = I_{\uparrow}(\mu_{R\uparrow}, \Delta T) - I_{\downarrow}(\mu_{R\downarrow}, \Delta T)$ is the net spin current flowing through the system. This quantity acts as a response over the spin current as a function of both the spin bias V_s and the temperature gradient ΔT . In addition to the net spin current, there can also exist a charge current $I = \sum_{\sigma} I_{\sigma}(\mu_{R\sigma}, \Delta T)$ flowing across the system originating solely from the thermal and the spin biases. We define the Seebeck coefficient that estimates the charge current in the presence of the spin bias as the charge Seebeck coefficient S [64]. The charge Seebeck coefficient S can thus be defined based on the response of charge current I as

$$S = -\left(\frac{dV_s}{d\Delta T}\right)_I = -\left(\frac{\partial I}{\partial \Delta T}\right)_{V_s} / \left(\frac{\partial I}{\partial V_s}\right)_{\Delta T}. \quad (11)$$

We first discuss the case of linear response in the spin bias V_s with large and finite temperature gradient ΔT , focusing on the differential spin Seebeck coefficient S_s and the charge Seebeck coefficient S . It is pertinent to note that the

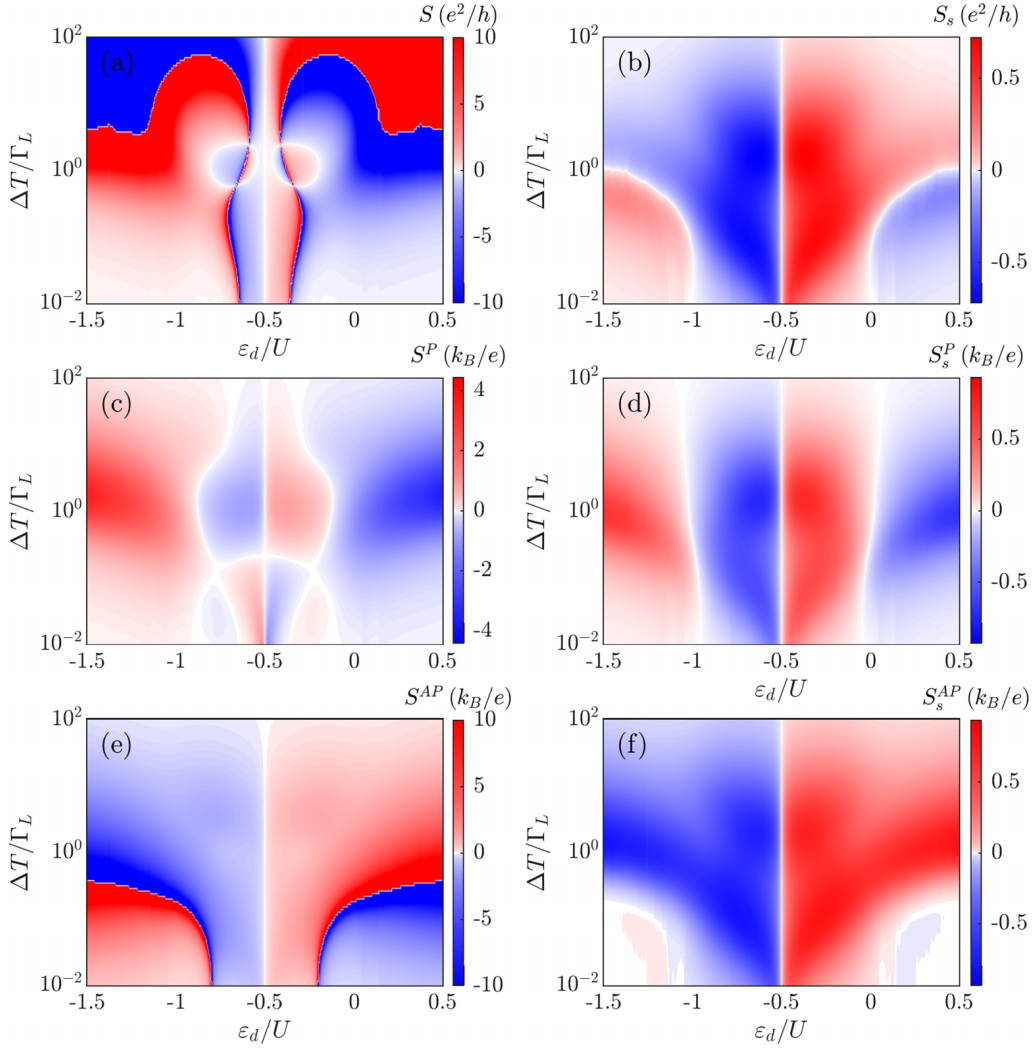


FIG. 8. The charge Seebeck (first column) and the spin Seebeck (second column) coefficients under nonlinear temperature gradient ΔT and linear response spin bias V_s as a function of the orbital level energy ε_d and ΔT . The first row corresponds to the case of nonmagnetic right lead, while the second (third) row presents the case of ferromagnetic right lead in the parallel (antiparallel) magnetic configuration of the system. The other parameters are the same as in Fig. 6.

nonequilibrium equivalent of the spin Seebeck coefficient $S_{s,n}$ tends to remain undefined in our considerations, since the magnitude of the spin bias fails to compensate for the thermally induced spin current in (*parts of*) the regimes considered. Hence in this paper, we limit our discussions to the differential spin Seebeck coefficient $S_s \equiv S_{s,d}$ in the case of different configurations. We further investigate the dependence of S_s and S on large and finite spin bias under applied temperature gradient.

1. The case of zero spin bias with nonlinear temperature gradient

Figure 8 shows the behavior of the charge Seebeck coefficients S , S^P , S^{AP} and the spin Seebeck coefficients S_s , S_s^P , S_s^{AP} for the case of nonmagnetic right lead, as well as the case of ferromagnetic lead in the parallel and antiparallel magnetic configurations, respectively. The first row of Fig. 8 shows the case of right lead with spin polarization $p = 0$, but with finite spin accumulation occurring from the spin-resolved transport through the quantum dot. Figure 8(a) displays the charge Seebeck S coefficient, which behaves similarly to the

differential Seebeck effect S_d presented in Fig. 4 except some points of divergences. At temperature gradients smaller than Γ_L , there exist two additional sign changes, both in the local moment regime symmetric across the particle-hole symmetry point. The points of sign change spread out of the local moment regime for thermal biases $\Delta T \gtrsim 3\Gamma_L$. The sign changes of the Seebeck effect are also accompanied by large divergences in the magnitude of S . The additional sign changes and divergences originate from the behavior of the denominator in the definition of S , cf. Eq. (11). The denominator in Eq. (11), which can be represented as, $G^{cs} = (\partial I / \partial V_s)_{\Delta T}$, is the differential mixed conductance [64] that estimates the charge current in the presence of a spin bias, which can be either negative or positive, resulting in its zero crossing points causing the divergence. From a physical perspective, tuning the temperature gradient in these specific regimes will result in extraordinary changes in the induced charge current. Note that the colormaps in Figs. 8(a) and 8(e) have been truncated for readability.

The charge Seebeck coefficient for the parallel configuration [see Fig. 8(c)] nicely recreates the behavior seen in

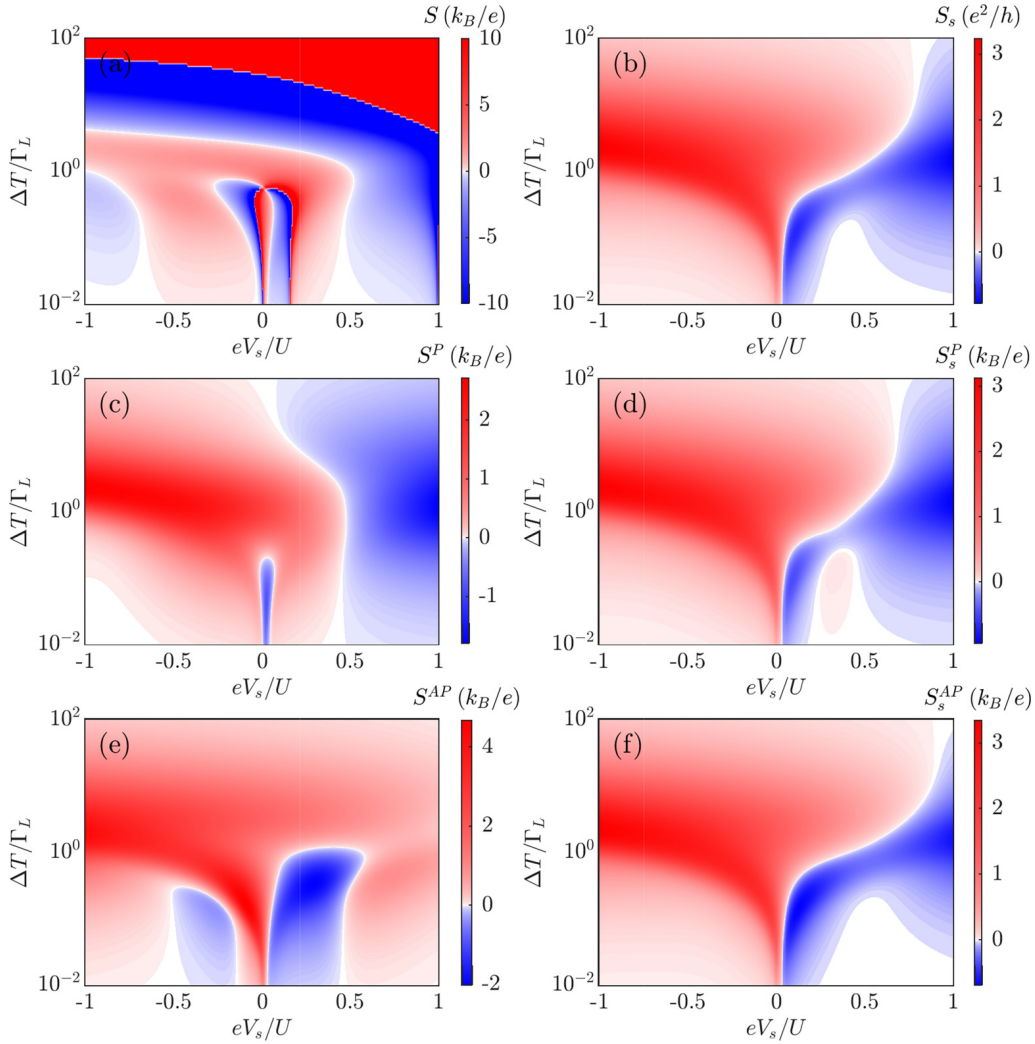


FIG. 9. The charge Seebeck (first column) and the spin Seebeck (second column) coefficients for the orbital level $\varepsilon_d = -U/3$ as a function of the applied spin bias V_s and ΔT . The first row corresponds to the case of nonmagnetic right lead, while the second (third) row presents the case of ferromagnetic right lead in the parallel (antiparallel) magnetic configuration of the system. The other parameters are the same as in Fig. 6.

Fig. 6(c). In the case of the parallel configuration, the relative scaling of the couplings in each spin channel on the right and left is the same, resulting in a non-negative G^{cs} and, thus, no divergences. Similarly, the charge Seebeck effect in the antiparallel configuration shown in Fig. 8(e) presents the behavior resembling the Seebeck coefficient discussed in Fig. 6(d), but overlaid by the divergences associated with G^{cs} . In this case, the additional sign changes start from inside the local moment regime at very low temperature gradients and move out of the local moment regime monotonously around $\Delta T \approx 10^{-1}\Gamma_L$.

The differential spin Seebeck coefficient S_s shown in Figs. 8(b), 8(d), and 8(f) for different lead configurations behave antisymmetrically across the particle-hole symmetry point ($\varepsilon_d = -U/2$). As can be seen, there exists a pronounced spin Seebeck coefficient in the local moment regime for all the configurations that dies off at $\Delta T \gtrsim 10\Gamma_L$. Such regions of considerable spin Seebeck effect have been observed in the linear response studies of symmetrically coupled quantum dots as a function of the global temperature T [27,33]. In addition to the sign change at the particle-hole symmetry

point, at very low ΔT , S_s changes sign when moving out of the local moment regime (i.e., at $\varepsilon_d \approx -U, 0$). In the case of the nonmagnetic right lead, the region of sign change outside the local moment regime extends up to $\Delta T \approx \Gamma_L$, whereas for the antiparallel configuration the sign change extends only up to $\Delta T \approx 0.2\Gamma_L$. On the other hand, the sign change of the spin Seebeck coefficient in the local moment regime survives at thermal gradients even greater than $\Delta T \approx 10^2\Gamma_L$ for the parallel configuration.

2. The case of nonlinear spin bias and temperature gradient

The dependence of the nonlinear charge and spin Seebeck effects is shown in Fig. 9 for the case of orbital energy level $\varepsilon_d = -U/3$. The first column in Fig. 9 focuses on the charge Seebeck effect for various magnetic configurations of the system. For the case of nonmagnetic right lead, the charge Seebeck coefficient S changes sign multiple times as a function of eV_s at temperature gradients below $\Delta T \approx 0.5\Gamma_L$, see Fig. 9(a). Two among these sign changes (around $eV_s \approx 0.001U$ and $eV_s \approx 0.15U$) correspond to the zeros in the

mixed conductance G^{cs} , which can be identified from the divergence in S around the sign changes. The other two sign changes (around $eV_s \approx -0.05U$ and $eV_s \approx 0.03U$) originate from the zeros of the thermal response $-(\partial I/\partial \Delta T)_{V_s}$, i.e., the numerator in the definition of the charge Seebeck coefficient, cf. Eq. (10). As the temperature gradient increases, the regions of sign change introduced by G^{cs} and the thermal response become larger in the spin bias regime until around $\Delta T \approx \Gamma_L/3$ for the sign change associated with the mixed conductance, and until $\Delta T \approx \Gamma_L/2$ for the sign change associated with the thermal response. With further increase in the temperature gradient, the regions of sign change disappear. This happens around $\Delta T \gtrsim \Gamma_L/2$ for the sign change caused by the mixed conductance, and for $\Delta T \gtrsim 0.8\Gamma_L$ in the case of the sign change due to the thermal response. The remaining two sign changes at $eV_s \approx -U/2$ and $eV_s \approx U/2$ can be associated with the Hubbard resonances. The region of these sign changes disappears above temperature gradient $\Delta T \gtrsim 4\Gamma_L$. On the other hand, at $eV_s \approx 0$ and very large temperature gradients (around $\Delta T \gtrsim 10\Gamma_L$), there exists another sign change that originates from the zeros of G^{cs} . For positive eV_s , this sign change moves to lower ΔT , while for negative eV_s , the sign change moves to higher ΔT , see Fig. 9(a).

Figure 9(c) shows the charge Seebeck coefficient S^P corresponding to the system in the parallel magnetic configuration of ferromagnetic leads. We observe that there are two sign changes as a function of the spin bias eV_s . At low temperatures, $\Delta T \lesssim 0.01\Gamma_L$, the region of sign change appears between $eV_s \approx 0.005U$ and $eV_s \approx 0.5U$. One can identify that these sign changes originate solely from the thermal response of the current under spin bias. As can be seen in Fig. 9(c), the position of the sign changes in eV_s hardly depends on temperature gradient as long as it is lower than $\Delta T \approx 0.5\Gamma_L$. On the other hand, once $\Delta T \gtrsim 0.5\Gamma_L$, the negative region of S^P around $eV_s \approx 0.005U$ disappears. However, unlike in the previous case of S , the sign change around $eV_s \approx U/2$, which is due to the contribution from the Hubbard resonance, survives for large temperature gradients ΔT . This sign change moves closer to $V_s \approx 0$ when the temperature gradient ΔT is increased $\Delta T \gtrsim \Gamma_L$, see Fig. 9(c).

The charge Seebeck coefficient for the antiparallel configuration S^{AP} does not exhibit any sign change in the local moment regime apart from the particle-hole symmetry point $\varepsilon_d = -U/2$, as shown in Fig. 8(e). However, as a function of the spin bias eV_s , two new regions of sign change form in the dependence of S^{AP} . More specifically, one sign change occurs in the negative spin bias regime around $eV_s \approx -0.15U$, and the other one in the positive regime for $eV_s \approx 0.03U$. As can be seen in the figure, the negative values of the charge Seebeck effect extend until $|eV_s| \gtrsim U/2$. Furthermore, with increasing ΔT , the corresponding sign changes move further apart into the negative and positive spin bias regimes, respectively. On the other hand, for $\Delta T \gtrsim \Gamma_L$, S^{AP} becomes positive for all values of eV_s considered, see Fig. 8(e).

It is important to emphasize that the sign changes observed in the charge Seebeck coefficient as a function of spin bias eV_s do not correspond to the sign changes seen in the Seebeck coefficient as a function of eV , as discussed and presented in Figs. 5 and 7. This is associated with the fact that the generated current as a function of voltage V scans through each of

the split Kondo resonances shown in Fig. 2 separately, resulting in the split peaks seen in the differential conductance and the corresponding sign changes in the Seebeck coefficients. However, as a function of the spin bias eV_s , the signatures from the split Kondo resonance cannot be identified directly in the generated current I . This is because for finite spin bias, $\mu_{R\uparrow} - \mu_{R\downarrow} = eV_s$, both split Kondo peaks contribute simultaneously, and the total current I is rescaled by relative couplings of the separate spin channels $\Gamma_{R\sigma}$. Hence, the sign changes in the charge Seebeck coefficient are solely resulting from the sign changes in the thermal response and the mixed charge conductance.

The spin Seebeck coefficient in the nonlinear spin bias regime is presented in the second column of Fig. 9. Figures 9(b), 9(d), and 9(f) show the case of the nonmagnetic right lead as well as ferromagnetic right lead in the parallel and antiparallel magnetic configuration of the nanojunction, respectively. As can be seen, the behavior of the spin Seebeck coefficient is qualitatively comparable for almost all configurations. From the discussion of the linear V_s case shown in Fig. 8, we observe that the differential spin Seebeck coefficient for $eV_s \approx 0$ does not change sign as a function of thermal gradient for all three configurations. Thus, for negative eV_s , S_s is positive irrespective of magnetic arrangement, see the right column of Fig. 9. On the other hand, for positive spin bias eV_s , one observes a sign change around $eV_s \approx 0.02U$, which moves to higher eV_s with increasing ΔT above $\Delta T \approx \Gamma_L$. Moreover, with further increasing eV_s , there is a region of suppressed S_s around $eV_s \approx 0.2U$, which extends to $eV_s \approx U/2$. Interestingly, one can note that the spin Seebeck effect in this region changes sign in the case of parallel configuration, thus introducing another sign change as a function of spin bias, see Fig. 9(d). This region disappears once $\Delta T \gtrsim 0.2\Gamma_L$.

IV. CONCLUDING REMARKS

In this paper we have analyzed the nonequilibrium spin-resolved thermoelectric properties of a ferromagnetic nanojunction consisting of a quantum dot/molecule asymmetrically coupled to external ferromagnetic leads. The considerations have been carried out by performing perturbative expansion with respect to the weakly coupled electrode, while the properties of quantum dot strongly coupled to ferromagnetic lead were extracted by numerical renormalization group method. The emphasis has been put on the signatures of the interplay between spin-resolved tunneling and strong electron correlations in the nonequilibrium spin-dependent thermopower of the system. In particular, we have determined the bias voltage and temperature gradient dependence of the differential and nonequilibrium Seebeck coefficients in different magnetic configurations of the system. We have observed new signatures in the Seebeck effect corresponding to the Kondo resonance and the regions where the ferromagnetic contact induced exchange field suppresses the Kondo effect, both in the potential bias and the temperature gradient. More specifically, we have demonstrated that the Seebeck coefficient exhibits new sign changes as a function of bias voltage, which are associated with the split Kondo resonance. These sign changes, depending on the transport region, extend to the temperature gradients on the order of the Kondo

temperature or of the temperature associated with the energy scale of the exchange field. Furthermore, we have investigated the influence of the spin accumulation in the leads, that gives rise to finite spin bias, on the Seebeck and spin Seebeck coefficients. The nonlinear charge Seebeck coefficient and the spin Seebeck coefficient showed points of sign changes in the presence of finite spin and thermal bias, indicating an intricate interplay of Kondo correlations with spin-resolved tunneling processes at nonequilibrium settings.

We believe that our work sheds new light on the spin-resolved nonequilibrium thermopower of correlated nanoscale junctions and, thus, provides a better understanding of thermoelectrics under finite temperature and voltage gradients. We also hope that our findings will foster further theoretical and experimental investigations of spin thermoelectric properties in fully nonequilibrium conditions.

As an outlook, we would like to notice that it would be of importance to explore the nonequilibrium thermoelectric

transport properties of nanoscale systems strongly coupled to both left and right leads. Accurate treatment of correlations in such setups would however require resorting to more sophisticated numerical techniques, such as recently developed hybrid method of NRG and time-dependent density matrix renormalization group [66,67]. While addressing such a problem goes beyond the scope of the present paper, it definitely provides an important objective for future research endeavor.

ACKNOWLEDGMENT

This work was supported by the Polish National Science Centre from funds awarded through the decision No. 2017/27/B/ST3/00621. We also acknowledge the computing time at the Poznań Supercomputing and Networking Center.

-
- [1] I. Žutić, J. Fabian, and S. Das Sarma, Spintronics: Fundamentals and applications, *Rev. Mod. Phys.* **76**, 323 (2004).
- [2] G. E. W. Bauer, E. Saitoh, and B. J. van Wees, Spin caloritronics, *Nat. Mater.* **11**, 391 (2012).
- [3] D. D. Awschalom, L. C. Bassett, A. S. Dzurak, E. L. Hu, and J. R. Petta, Quantum spintronics: Engineering and manipulating atom-like spins in semiconductors, *Science* **339**, 1174 (2013).
- [4] A. Hirohata, K. Yamada, Y. Nakatani, I.-L. Prejbeanu, B. Diény, P. Pirro, and B. Hillebrands, Review on spintronics: Principles and device applications, *J. Magn. Magn. Mater.* **509**, 166711 (2020).
- [5] G. D. Mahan and J. O. Sofo, The best thermoelectric, *Proc. Natl. Acad. Sci. USA* **93**, 7436 (1996).
- [6] A. Dhar, Heat transport in low-dimensional systems, *Adv. Phys.* **57**, 457 (2008).
- [7] Y. Dubi and M. Di Ventra, Thermoelectric effects in nanoscale junctions, *Nano Lett.* **9**, 97 (2009).
- [8] Y. Dubi and M. Di Ventra, *Colloquium: Heat flow and thermoelectricity in atomic and molecular junctions*, *Rev. Mod. Phys.* **83**, 131 (2011).
- [9] G. Benenti, G. Casati, K. Saito, and R. S. Whitney, Fundamental aspects of steady-state conversion of heat to work at the nanoscale, *Phys. Rep.* **694**, 1 (2017).
- [10] M. Josefsson, A. Svilans, A. M. Burke, E. A. Hoffmann, S. Fahlvik, C. Thelander, M. Leijnse, and H. Linke, A quantum-dot heat engine operating close to the thermodynamic efficiency limits, *Nat. Nanotechnol.* **13**, 920 (2018).
- [11] J. Kondo, Resistance minimum in dilute magnetic alloys, *Prog. Theor. Phys.* **32**, 37 (1964).
- [12] A. C. Hewson, *The Kondo Problem to Heavy Fermions*, Cambridge Studies in Magnetism (Cambridge University Press, Cambridge, 1993).
- [13] D. Goldhaber-Gordon, H. Shtrikman, D. Mahalu, D. Abusch-Magder, U. Meirav, and M. A. Kastner, Kondo effect in a single-electron transistor, *Nature (London)* **391**, 156 (1998).
- [14] S. M. Cronenwett, T. H. Oosterkamp, and L. P. Kouwenhoven, A tunable Kondo effect in quantum dots, *Science* **281**, 540 (1998).
- [15] T. A. Costi and V. Zlatić, Thermoelectric transport through strongly correlated quantum dots, *Phys. Rev. B* **81**, 235127 (2010).
- [16] A. Svilans, M. Josefsson, A. M. Burke, S. Fahlvik, C. Thelander, H. Linke, and M. Leijnse, Thermoelectric characterization of the Kondo resonance in nanowire quantum dots, *Phys. Rev. Lett.* **121**, 206801 (2018).
- [17] B. Dutta, D. Majidi, A. García Corral, P. A. Erdman, S. Florens, T. A. Costi, H. Courtois, and C. B. Winkelmann, Direct probe of the Seebeck coefficient in a Kondo-correlated single-quantum-dot transistor, *Nano Lett.* **19**, 506 (2019).
- [18] C. Hsu, T. A. Costi, D. Vogel, C. Wegeberg, M. Mayor, H. S. J. van der Zant, and P. Gehring, Magnetic-field universality of the Kondo effect revealed by thermocurrent spectroscopy, *Phys. Rev. Lett.* **128**, 147701 (2022).
- [19] J. Barnaś and I. Weymann, Spin effects in single-electron tunnelling, *J. Phys.: Condens. Matter* **20**, 423202 (2008).
- [20] K. Uchida, S. Takahashi, K. Harii, J. Ieda, W. Koshibae, K. Ando, S. Maekawa, and E. Saitoh, Observation of the spin Seebeck effect, *Nature (London)* **455**, 778 (2008).
- [21] H. Adachi, K.-I. Uchida, E. Saitoh, and S. Maekawa, Theory of the spin Seebeck effect, *Rep. Prog. Phys.* **76**, 036501 (2013).
- [22] J. Martinek, M. Sindel, L. Borda, J. Barnaś, J. König, G. Schön, and J. von Delft, Kondo effect in the presence of itinerant-electron ferromagnetism studied with the numerical renormalization group method, *Phys. Rev. Lett.* **91**, 247202 (2003).
- [23] A. N. Pasupathy, R. C. Bialczak, J. Martinek, J. E. Grose, L. A. K. Donev, P. L. McEuen, and D. C. Ralph, The Kondo effect in the presence of ferromagnetism, *Science* **306**, 86 (2004).

- [24] K. Hamaya, M. Kitabatake, K. Shibata, M. Jung, M. Kawamura, K. Hirakawa, T. Machida, T. Taniyama, S. Ishida, and Y. Arakawa, Kondo effect in a semiconductor quantum dot coupled to ferromagnetic electrodes, *Appl. Phys. Lett.* **91**, 232105 (2007).
- [25] I. Weymann, Finite-temperature spintronic transport through Kondo quantum dots: Numerical renormalization group study, *Phys. Rev. B* **83**, 113306 (2011).
- [26] M. Krawiec and K. I. Wysokiński, Thermoelectric effects in strongly interacting quantum dot coupled to ferromagnetic leads, *Phys. Rev. B* **73**, 075307 (2006).
- [27] I. Weymann and J. Barnaś, Spin thermoelectric effects in Kondo quantum dots coupled to ferromagnetic leads, *Phys. Rev. B* **88**, 085313 (2013).
- [28] Ł. Karwacki, P. Trocha, and J. Barnaś, Spin-dependent thermoelectric properties of a Kondo-correlated quantum dot with Rashba spin-orbit coupling, *J. Phys.: Condens. Matter* **25**, 505305 (2013).
- [29] K. P. Wójcik and I. Weymann, Thermopower of strongly correlated T-shaped double quantum dots, *Phys. Rev. B* **93**, 085428 (2016).
- [30] Ł. Karwacki and P. Trocha, Spin-dependent thermoelectric effects in a strongly correlated double quantum dot, *Phys. Rev. B* **94**, 085418 (2016).
- [31] K. P. Wójcik and I. Weymann, Strong spin Seebeck effect in Kondo T-shaped double quantum dots, *J. Phys.: Condens. Matter* **29**, 055303 (2017).
- [32] G. Górski and K. Kucab, Effect of assisted hopping on spin-dependent thermoelectric transport through correlated quantum dot, *Phys. B* **545**, 337 (2018).
- [33] A. Manaparambil and I. Weymann, Spin Seebeck effect of correlated magnetic molecules, *Sci. Rep.* **11**, 9192 (2021).
- [34] P. Majek, K. P. Wójcik, and I. Weymann, Spin-resolved thermal signatures of Majorana-Kondo interplay in double quantum dots, *Phys. Rev. B* **105**, 075418 (2022).
- [35] M. A. Sierra and D. Sánchez, Strongly nonlinear thermovoltage and heat dissipation in interacting quantum dots, *Phys. Rev. B* **90**, 115313 (2014).
- [36] A. Svilans, M. Leijnse, and H. Linke, Experiments on the thermoelectric properties of quantum dots, *C. R. Phys.* **17**, 1096 (2016).
- [37] M. A. Sierra, R. López, and D. Sánchez, Fate of the spin- $\frac{1}{2}$ Kondo effect in the presence of temperature gradients, *Phys. Rev. B* **96**, 085416 (2017).
- [38] A. Khedri, T. A. Costi, and V. Meden, Nonequilibrium thermoelectric transport through vibrating molecular quantum dots, *Phys. Rev. B* **98**, 195138 (2018).
- [39] U. Eckern and K. I. Wysokiński, Two- and three-terminal far-from-equilibrium thermoelectric nano-devices in the Kondo regime, *New J. Phys.* **22**, 013045 (2020).
- [40] A. Manaparambil and I. Weymann, Nonequilibrium Seebeck effect and thermoelectric efficiency of Kondo-correlated molecular junctions, *Phys. Rev. B* **107**, 085404 (2023).
- [41] J. Bauer, J. I. Pascual, and K. J. Franke, Microscopic resolution of the interplay of Kondo screening and superconducting pairing: Mn-phthalocyanine molecules adsorbed on superconducting Pb(111), *Phys. Rev. B* **87**, 075125 (2013).
- [42] C. Xu, C.-L. Chiang, Z. Han, and W. Ho, Nature of asymmetry in the vibrational line shape of single-molecule inelastic electron tunneling spectroscopy with the STM, *Phys. Rev. Lett.* **116**, 166101 (2016).
- [43] M. Gruber, A. Weismann, and R. Berndt, The Kondo resonance line shape in scanning tunnelling spectroscopy: Instrumental aspects, *J. Phys.: Condens. Matter* **30**, 424001 (2018).
- [44] N. Xin, J. Guan, C. Zhou, X. Chen, C. Gu, Y. Li, M. A. Ratner, A. Nitzan, J. F. Stoddart, and X. Guo, Concepts in the design and engineering of single-molecule electronic devices, *Nat. Rev. Phys.* **1**, 211 (2019).
- [45] M. Žonda, O. Stetsovych, R. Korytár, M. Ternes, R. Temirov, A. Raccanelli, F. S. Tautz, P. Jelínek, T. Novotný, and M. Švec, Resolving ambiguity of the Kondo temperature determination in mechanically tunable single-molecule Kondo systems, *J. Phys. Chem. Lett.* **12**, 6320 (2021).
- [46] Y. Xing, H. Chen, B. Hu, Y. Ye, W. A. Hofer, and H.-J. Gao, Reversible switching of Kondo resonance in a single-molecule junction, *Nano Res.* **15**, 1466 (2022).
- [47] M. Krawiec and K. I. Wysokiński, Thermoelectric phenomena in a quantum dot asymmetrically coupled to external leads, *Phys. Rev. B* **75**, 155330 (2007).
- [48] T. K. T. Nguyen, M. N. Kiselev, and V. E. Kravtsov, Thermoelectric transport through a quantum dot: Effects of asymmetry in Kondo channels, *Phys. Rev. B* **82**, 113306 (2010).
- [49] D. Pérez Daroca, P. Roura-Bas, and A. A. Aligia, Enhancing the nonlinear thermoelectric response of a correlated quantum dot in the Kondo regime by asymmetrical coupling to the leads, *Phys. Rev. B* **97**, 165433 (2018).
- [50] K. G. Wilson, The renormalization group: Critical phenomena and the Kondo problem, *Rev. Mod. Phys.* **47**, 773 (1975).
- [51] R. Bulla, T. A. Costi, and T. Pruschke, Numerical renormalization group method for quantum impurity systems, *Rev. Mod. Phys.* **80**, 395 (2008).
- [52] S. Csonka, I. Weymann, and G. Zarand, An electrically controlled quantum dot based spin current injector, *Nanoscale* **4**, 3635 (2012).
- [53] P. Tulewicz, K. Wrześniewski, S. Csonka, and I. Weymann, Large voltage-tunable spin valve based on a double quantum dot, *Phys. Rev. Appl.* **16**, 014029 (2021).
- [54] We used the open-access Budapest Flexible DM-NRG code, <http://www.phy.bme.hu/~dmnrg/>; O. Legeza, C. P. Moca, A. I. Tóth, I. Weymann, G. Zarand, Manual for the flexible DM-NRG code, [arXiv:0809.3143](https://arxiv.org/abs/0809.3143) (unpublished).
- [55] A. Weichselbaum and J. von Delft, Sum-rule conserving spectral functions from the numerical renormalization group, *Phys. Rev. Lett.* **99**, 076402 (2007).
- [56] A. Dorda, M. Ganahl, S. Andergassen, W. von der Linden, and E. Arrigoni, Thermoelectric response of a correlated impurity in the nonequilibrium Kondo regime, *Phys. Rev. B* **94**, 245125 (2016).
- [57] M. Leijnse, M. R. Wegewijs, and K. Flensberg, Nonlinear thermoelectric properties of molecular junctions with vibrational coupling, *Phys. Rev. B* **82**, 045412 (2010).
- [58] J. Azema, P. Lombardo, and A.-M. Daré, Conditions for requiring nonlinear thermoelectric transport theory in nanodevices, *Phys. Rev. B* **90**, 205437 (2014).
- [59] P. A. Erdman, F. Mazza, R. Bosisio, G. Benenti, R. Fazio, and F. Taddei, Thermoelectric properties of an interacting quantum dot based heat engine, *Phys. Rev. B* **95**, 245432 (2017).

- [60] J. Martinek, Y. Utsumi, H. Imamura, J. Barnaś, S. Maekawa, J. König, and G. Schön, Kondo effect in quantum dots coupled to ferromagnetic leads, *Phys. Rev. Lett.* **91**, 127203 (2003).
- [61] J. R. Hauptmann, J. Paaske, and P. E. Lindelof, Electric-field-controlled spin reversal in a quantum dot with ferromagnetic contacts, *Nat. Phys.* **4**, 373 (2008).
- [62] M. Gaass, A. K. Hüttel, K. Kang, I. Weymann, J. von Delft, and Ch. Strunk, Universality of the Kondo effect in quantum dots with ferromagnetic leads, *Phys. Rev. Lett.* **107**, 176808 (2011).
- [63] F. D. M. Haldane, Scaling theory of the asymmetric Anderson model, *Phys. Rev. Lett.* **40**, 416 (1978).
- [64] R. Świrkowicz, J. Barnaś, and M. Wilczyński, Transport through a quantum dot subject to spin and charge bias, *J. Magn. Magn. Mater.* **321**, 2414 (2009).
- [65] R. Świrkowicz, M. Wierzbicki, and J. Barnaś, Thermoelectric effects in transport through quantum dots attached to ferromagnetic leads with noncollinear magnetic moments, *Phys. Rev. B* **80**, 195409 (2009).
- [66] F. Schwarz, I. Weymann, J. von Delft, and A. Weichselbaum, Nonequilibrium steady-state transport in quantum impurity models: A thermofield and quantum quench approach using matrix product states, *Phys. Rev. Lett.* **121**, 137702 (2018).
- [67] A. Manaparambil, A. Weichselbaum, J. von Delft, and I. Weymann, Nonequilibrium spintronic transport through Kondo impurities, *Phys. Rev. B* **106**, 125413 (2022).

9.3 Giant tunnel magnetoresistance induced by thermal bias [F]



Research article

Giant tunnel magnetoresistance induced by thermal bias

Anand Manaparambil*, Ireneusz Weymann

Institute of Spintronics and Quantum Information, Faculty of Physics, Adam Mickiewicz University, ul. Uniwersytetu Poznańskiego 2, 61-614 Poznań, Poland

ARTICLE INFO

Keywords:

Tunnel magnetoresistance
Kondo effect
Exchange field
Spintronic transport
Thermal bias
Spin-valves

ABSTRACT

We analyze the spin-resolved transport and, in particular, the tunnel magnetoresistance of an asymmetric ferromagnetic tunnel junction with an embedded quantum dot or molecule subject to thermal and voltage bias in the nonlinear response regime. We demonstrate that such system exhibits a *giant* tunnel magnetoresistance effect that can be tuned by gate and bias voltages. Large values of magnetoresistance are associated with the interplay between the Kondo correlations and the ferromagnetic-contact-induced exchange field. In particular, we show that the nonequilibrium current in the parallel and antiparallel magnetic configuration of the system changes sign at different values of the voltage and thermal bias. This gives rise to giant values of magnetoresistance, the sign of which can be controlled by the applied sources.

1. Introduction

Quantum dots, due to their charge quantization and strong electronic interactions, provide a reliable and tunable platform for manipulation and control of single electron charges and spins [1–3]. A single or coupled quantum dots separating two ferromagnetic leads constitute the so-called quantum dot spin valve, the transport properties of which can be controlled by changing the alignment of magnetic moments of external ferromagnetic electrodes [4]. In fact, this is a grass-root device for single-spin electronics, bringing interesting possibilities for spintronic applications [5–10]. Moreover, the interplay of the Kondo effect [11–13], a many-body screening phenomenon, along with the exchange field induced by the spin-resolved tunneling from the ferromagnetic leads [14–16], enables an additional tunability exhibited by such nanoscale spin valves [17–24]. Although the electrical control of the transport properties of quantum dot spin valves has been under rigorous studies [21–23], the transport induced by a finite temperature gradient and the extra control offered by the thermal bias remains to be explored [25], especially, as far as strong electron correlations are concerned [10,26].

In this paper we therefore study the behavior of the spin-resolved transport and, especially, the tunnel magnetoresistance of a strongly-correlated quantum dot spin valve, which is subject to nonlinear voltage and temperature gradients. In particular, we consider an asymmetric junction, in which the coupling of the quantum dot to one of the leads is much stronger than the other coupling. At low temperature gradients this gives rise to strong electron correlations effects, such as the Kondo effect and its interplay with the ferromagnet-induced exchange field. To capture those effects we make use of the versatile

numerical renormalization group (NRG) method [27,28]. In particular, while the quantum dot strongly coupled to one of the leads is treated nonperturbatively, we perform the perturbation expansion with respect to tunneling processes to the weakly coupled electrode. By calculating the spin-resolved currents in the nonlinear response regime, we demonstrate that an appropriate choice of the bias voltage and temperature gradient gives rise to a giant tunnel magnetoresistance effect that can also be tuned by the gate voltage. More specifically, we show that the thermally induced currents change sign at different bias voltage depending on the magnetic configuration of the system. Thus, our study demonstrates that the combination of applied voltage and temperature gradient can provide an extra knob to tune the spin-dependent tunneling processes in the system. This is of great importance for possible spintronics applications.

2. Theoretical description

The Hamiltonian H of the system consists of the strongly coupled left lead and the quantum dot, described by H_L , the weakly coupled right lead, H_R , and the term describing tunnel coupling between the left and right parts, H_T . The Hamiltonian of the left part is given by [29]

$$H_L = \varepsilon_d (n_\uparrow + n_\downarrow) + U n_\uparrow n_\downarrow + \sum_{k\sigma} \varepsilon_{k\sigma} c_{Lk\sigma}^\dagger c_{Lk\sigma} + \sum_{k\sigma} t_{Lk\sigma} (d_\sigma^\dagger c_{Lk\sigma} + d_\sigma c_{Lk\sigma}^\dagger), \quad (1)$$

where $n_\sigma = d_\sigma^\dagger d_\sigma$ is the number operator for an electron on the quantum dot with spin σ , with d_σ (d_σ^\dagger) being the annihilation (creation) operator

* Corresponding author.

E-mail address: anaman@amu.edu.pl (A. Manaparambil).<https://doi.org/10.1016/j.jmmm.2023.171272>

Received 3 August 2023; Received in revised form 13 September 2023; Accepted 17 September 2023

Available online 21 September 2023

0304-8853/© 2023 The Author(s). Published by Elsevier B.V. This is an open access article under the CC BY-NC-ND license (<http://creativecommons.org/licenses/by-nc-nd/4.0/>).

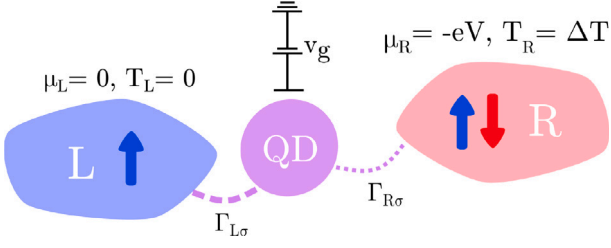


Fig. 1. The schematic of a quantum dot strongly coupled to a cold ferromagnetic lead ($T_L = 0, \mu_L = 0$) on the left and weakly coupled to a hot ferromagnetic lead ($T_R = \Delta T, \mu_R = -eV$) via the spin-dependent hybridization functions $\Gamma_{L\sigma}$ and $\Gamma_{R\sigma}$, respectively. The quantum dot energy level is tuned by the gate voltage v_g .

for the same. The annihilation (creation) operator for an electron in the lead $\alpha \in \{L, R\}$ with spin σ and momentum k is represented as $c_{ak\sigma}$ ($c_{ak\sigma}^\dagger$). The $t_{Lk\sigma}$ are the tunneling matrix elements between the quantum dot and the left lead.

The potential bias across the quantum dot is achieved solely by changing the chemical potential of the right lead $\mu_R = -eV$. Thus, the Hamiltonian of the right lead can be expressed as

$$H_R = \sum_{k\sigma} \epsilon_{k\sigma} c_{Rk\sigma}^\dagger c_{Rk\sigma} - eV \sum_{k\sigma} c_{Rk\sigma}^\dagger c_{Rk\sigma}. \quad (2)$$

The tunneling processes between the left (quantum dot strongly coupled to left lead) and right part (weakly coupled right lead) are described using the tunneling Hamiltonian H_T

$$H_T = \sum_{k\sigma} t_{Rk\sigma} (d_\sigma^\dagger c_{Rk\sigma} + d_\sigma c_{Rk\sigma}^\dagger), \quad (3)$$

where $t_{Rk\sigma}$ are the tunneling matrix elements between the quantum dot and the right lead. The total Hamiltonian is thus $H = H_L + H_R + H_T$. The tunnel matrix elements give rise to the broadening of the quantum dot energy levels, which can be expressed as, $\Gamma_{\alpha\sigma} = \pi \rho_{\alpha\sigma} |t_{\alpha\sigma}|^2$, where $\rho_{\alpha\sigma}$ is the spin-dependent density of states of lead α and we assumed momentum and spin independent tunnel matrix elements $t_{ak\sigma} \equiv t_{\alpha\sigma}$.

The current flowing through the system in the lowest-order perturbation with respect to Γ_R , i.e. the total coupling to the right lead, is given by $I = I_\uparrow + I_\downarrow$, with [21,23,26,30]

$$I_\sigma = -\frac{e\Gamma_{R\sigma}}{\hbar} \int_{-\infty}^{\infty} d\omega A_{L\sigma}(\omega) [f_L(\omega) - f_R(\omega - eV)]. \quad (4)$$

Here, $f_\alpha(\omega) = [1 + e^{\omega/T_\alpha}]^{-1}$ denotes the Fermi-Dirac distribution function with $k_B \equiv 1$, whereas $A_{L\sigma}(\omega)$ is the spin-resolved spectral function of the left subsystem. We assume a bias independent dot energy level ϵ_d , this setup can be experimentally realized by immediately tuning the gate voltage v_g according to the applied bias. The transport through each spin channel depends on the magnetic configuration of the system, for the parallel configuration the coupling strength is given by, $\Gamma_{\alpha\sigma} = (1 + \sigma p_\alpha) \Gamma_\alpha$, while for the antiparallel configuration one has, $\Gamma_{R\sigma} = (1 - \sigma p_R) \Gamma_R$, with $\Gamma_\alpha = (\Gamma_{\alpha\uparrow} + \Gamma_{\alpha\downarrow})/2$ and we introduced the spin polarization of lead α , p_α . Thus, we assume that the magnetization of the left lead is fixed, while the system changes the magnetic configuration by flipping the magnetic moment of the right lead, see Fig. 1. The difference in the resistance of the junction while changing the magnetic configuration can be described by the tunnel magnetoresistance (TMR), which is defined as [31]

$$\text{TMR} = \frac{I^P - I^{AP}}{I^{AP}}, \quad (5)$$

where I^P (I^{AP}) is the current flowing through system in the case of parallel (antiparallel) magnetic configuration.

3. Numerical results and discussion

In the calculations, we use the following parameters: $\Gamma_L = 0.02$, $\Gamma_R = 0.002$, $U = 0.2$, in units of band halfwidth, and $p = p_L = p_R = 0.4$.

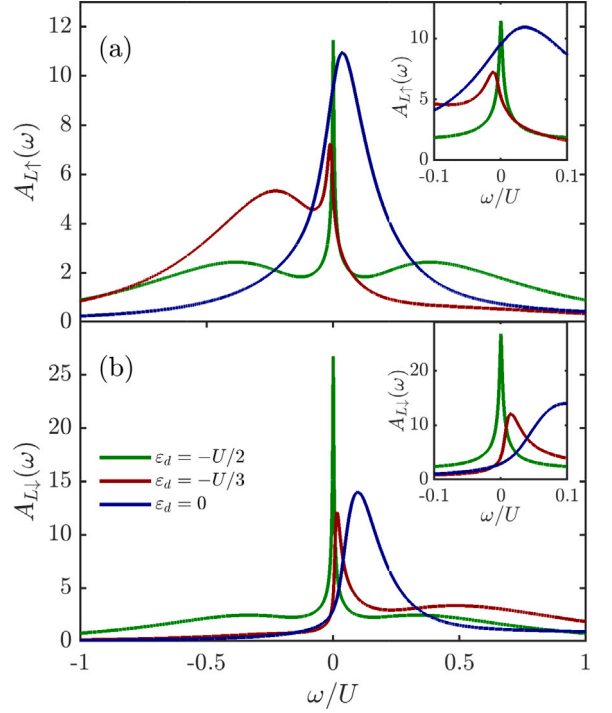


Fig. 2. The spin-resolved spectral function $A_{L\sigma}(\omega)$ for $\sigma = \uparrow$ [$\sigma = \downarrow$] is shown in panel (a) [panel (b)] for the representative energy levels ϵ_d . The insets show the behavior of the spectral function around $\omega = 0$.

The spectral functions are determined by NRG calculations with 2^{10} kept states [32]. The corresponding results are shown in Fig. 2. In particular, we focus on the local moment regime with particle-hole symmetry $\epsilon_d = -U/2$ (green curves in Fig. 2), detuned out of the symmetry point $\epsilon_d = -U/3$ (red curves in Fig. 2) and the resonant tunneling regime $\epsilon_d = 0$ (blue curves in Fig. 2). We observe the Kondo resonance formed around $\omega \approx 0$ for both the energy levels $\epsilon_d = -U/2, -U/3$ in the local moment regime. For the particle-hole symmetry point, the Kondo peak can be observed exactly at $\omega = 0$ in the spectral functions for both spin components. On the other hand, for the case of $\epsilon_d = -U/3$, the Kondo peak moves into the negative regime for the spin- \uparrow and towards the positive frequencies for the spin- \downarrow spectral function. Finally, the $\epsilon_d = 0$ case shows no Kondo peak, but just hybridized peak with broadening approximately given by Γ_L around the orbital energy level.

We begin our analysis by studying the current in the parallel and antiparallel magnetic configurations as well as the TMR in the case of finite temperature gradient, while keeping $V \rightarrow 0$. These transport coefficients are presented in Fig. 3. Note that we use the logarithmic colormap scale to show the currents in the full parameter space, since the current for small ΔT is very low. Moreover, it is important to emphasize that in the considered case, the nonlinear current flows exclusively due to the thermal gradient applied to the system. As one can see in the figure, the current is antisymmetric across the particle-hole symmetry point $\epsilon_d = -U/2$. For the antiparallel configuration, I^{AP} is positive (negative) for $\epsilon_d > -U/2$ ($\epsilon_d < -U/2$), see Fig. 3(b), which is associated with the type of the charge carriers (either electrons or holes) for finite ΔT . Interestingly, in the parallel configuration the above rule is not strictly obeyed and we observe sign changes of the current as a function of temperature gradient for a fixed value of the orbital level position. These sign changes are present in the local moment regime, see Fig. 3(a), and are associated with the presence of the exchange field. Such a field can suppress the Kondo effect and strongly influence the local density of states of the left subsystem. Consequently, the temperature gradient dependence of the current

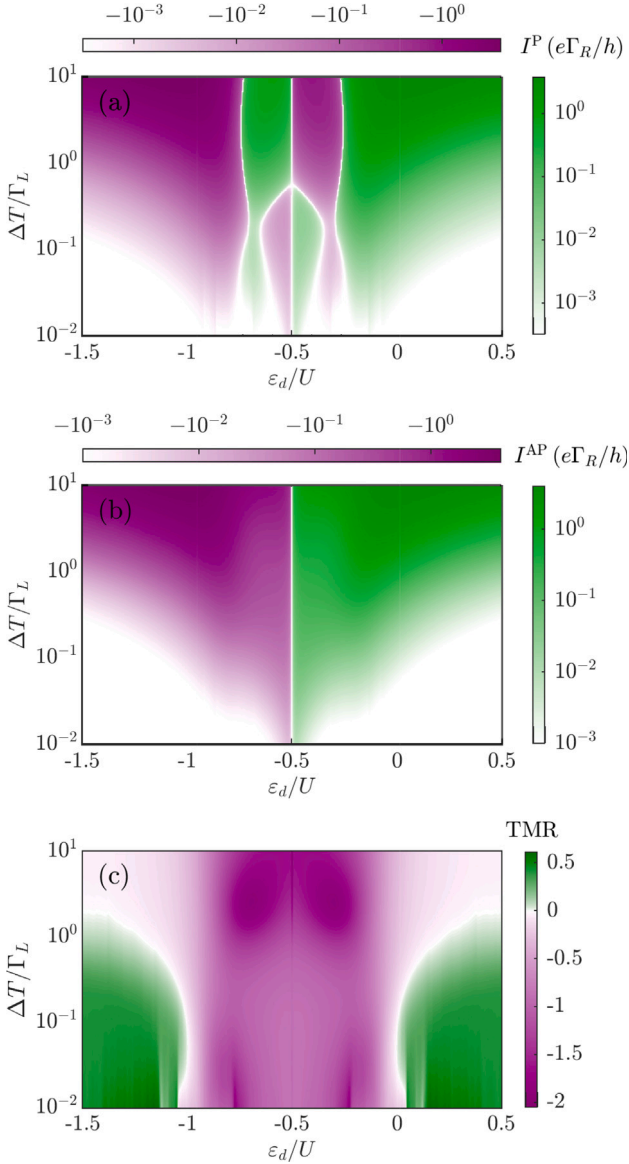


Fig. 3. The current in (a) the parallel configuration I^P , (b) the antiparallel configuration I^{AP} as well as (c) the tunnel magnetoresistance of a quantum dot in the linear response potential bias regime $V \rightarrow 0$ as a function of the orbital energy ε_d and the temperature gradient ΔT . The other parameters are: $\Gamma_L = 0.02$, $\Gamma_R = 0.002$, $U = 0.2$, in units of band halfwidth, and $p = p_L = p_R = 0.4$.

may then become nonmonotonic. Thus, the observed large difference between the two magnetic configurations is related to the effects of the exchange field and its competition with Kondo correlations. In fact, it has already been demonstrated experimentally that the exchange field can be switched off by flipping the system's magnetic configuration from the parallel to the antiparallel one [16]. Here, we observe a similar behavior but in the presence of nonlinear temperature gradient. The difference between the two magnetic configurations is directly reflected in the behavior of the TMR, which is shown in Fig. 3(c). As can be seen, tunnel magnetoresistance can take both positive and negative values, depending on the transport regime and the value of ΔT . More specifically, in the local moment regime, $-1 \lesssim \varepsilon_d/U \lesssim 0$, where for low temperature gradients the interplay of exchange field and Kondo correlations is relevant, the current in the parallel configuration is smaller than that in the antiparallel configuration and the TMR takes negative values. The negative TMR becomes magnified even more when $\Delta T \gtrsim \Gamma_L$. On the other hand, in the empty (or doubly-occupied)

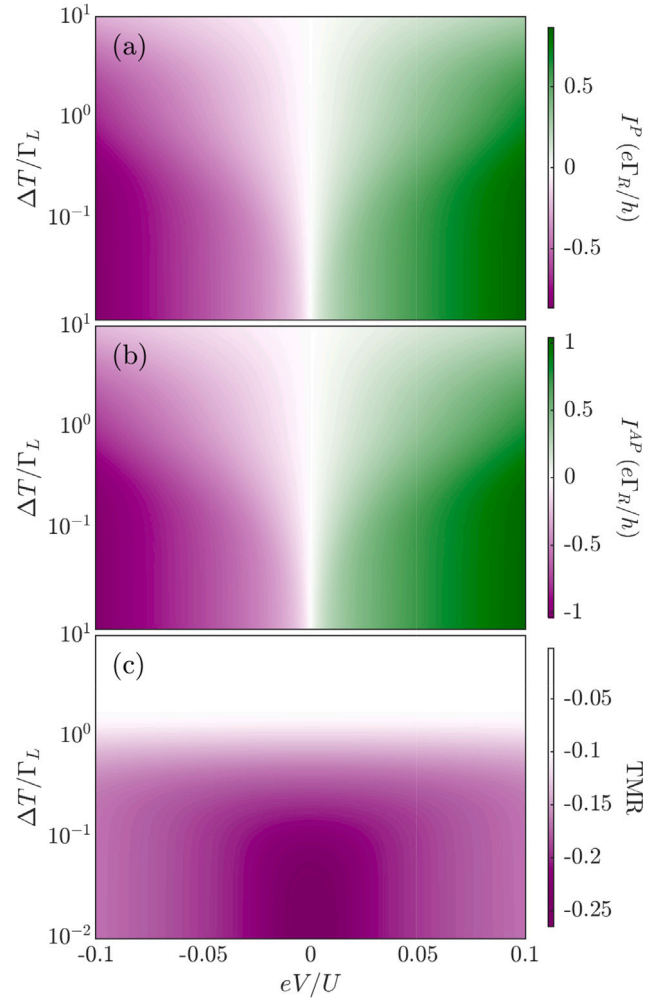


Fig. 4. (a) The current I^P in the parallel configuration, (b) the current I^{AP} in the antiparallel configuration and (c) the TMR for a quantum dot with orbital energy $\varepsilon_d = -U/2$ plotted as a function of the applied potential bias V and temperature gradient ΔT . The other parameters are the same as in Fig. 3.

orbital regime the TMR is positive for $\Delta T \lesssim \Gamma_L$, which is characteristic of elastic cotunneling regime [33,34]. However, once $\Delta T \gtrsim \Gamma_L$, one finds suppressed TMR and the difference between the two magnetic configurations becomes hardly visible, see Fig. 3(c).

The spin-resolved transport behavior is even more interesting in the presence of both temperature and voltage gradients. Below, we present and discuss the corresponding dependence of the currents in the parallel and antiparallel configurations and the resulting TMR for three different values of the orbital level position. The linear bias voltage regime corresponds thus to the cross-sections of Fig. 3. Let us first analyze the case of quantum dot at the particle-hole symmetry point ($\varepsilon_d = -U/2$), which is presented in Fig. 4. Due to the absence of the exchange field in this situation, we do not observe remarkable features of the TMR. The TMR shows an overall negative value in this regime, which decays out with increasing the bias voltage $|V|$ and temperature gradient ΔT . Remarkable features of the TMR arise in the local moment regime when detuned out of the particle-hole symmetry point, as shown in Fig. 5. This figure was generated assuming $\varepsilon_d = -U/3$, such that the effects of exchange field are present in the system. As can be seen in Fig. 5(c), the TMR changes sign when crossing $V = 0$ at very low temperature gradients, and the sign change moves to the positive potential regime with increasing ΔT . This behavior is due to the sign change of I^{AP} as a function of V and ΔT , see Fig. 5(b). Near the points of sign change, due to the suppression of I^{AP} , we observe

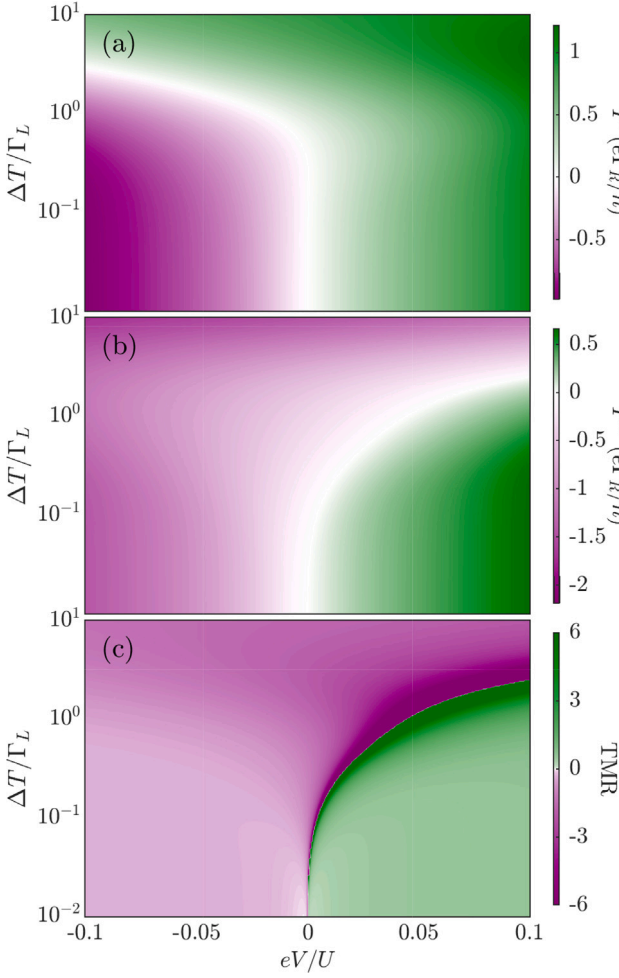


Fig. 5. (a) The current I^P in the parallel configuration, (b) the current I^{AP} in the antiparallel configuration and (c) the TMR for a quantum dot with orbital energy $\varepsilon_d = -U/3$ plotted as a function of the applied potential bias V and temperature gradient ΔT . The other parameters are the same as in Fig. 3.

very large values of the TMR. Such *giant* tunnel magnetoresistance can be easily tuned by either changing the temperature gradient or the bias voltage. It could be also tuned by shifting the position of the quantum dot orbital level with a gate voltage, since this would affect the exchange field and the corresponding sign change in the current. Moreover, it is important to note that small changes in the parameter space result in huge changes in the TMR, since in the vicinity of the sign change of I^{AP} one can obtain either positive *giant* TMR or inverted *giant* TMR, see Fig. 5(c). We would like to emphasize that this is a fully nonequilibrium effect that requires a finite temperature gradient applied to the system. However, once finite ΔT is generated, the TMR could be then controlled purely by electrical means. An additional regime of inverted TMR is observed for the empty orbital case $\varepsilon_d = 0$, which is shown in Fig. 6(c). This region exists in the negative bias regime and increases with increasing temperature gradient to become positive around $\Delta T \approx 0.5 \Gamma_L$. This sign change of TMR in the negative bias regime is not accompanied by a *giant* values of the TMR, since the current in the antiparallel configuration does not change sign then, see Fig. 6(b). However, for positive bias voltage, both currents change sign with increasing ΔT (see Fig. 6), and this happens for different values of the temperature gradient, such that again giant values of TMR are observed, similar to the case of $\varepsilon_d = -U/3$ presented in Fig. 5.

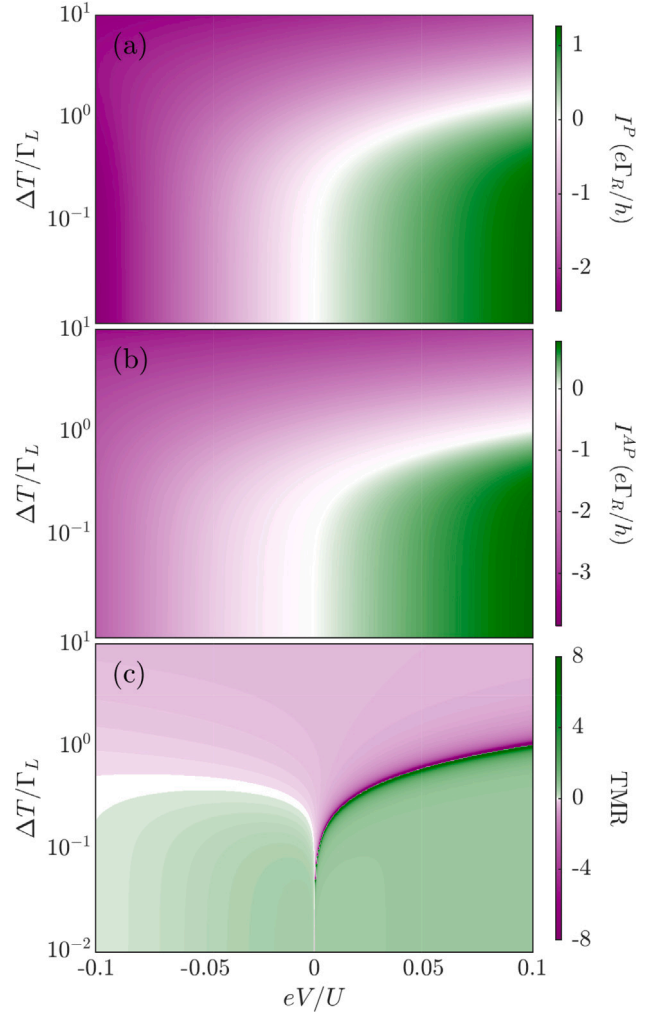


Fig. 6. (a) The current I^P in the parallel configuration, (b) the current I^{AP} in the antiparallel configuration and (c) the TMR for a quantum dot with orbital energy $\varepsilon_d = 0$ plotted as a function of the applied potential bias V and temperature gradient ΔT . The other parameters are the same as in Fig. 3.

4. Summary

We have studied the spin-resolved transport through a quantum dot/molecule asymmetrically coupled to the ferromagnetic leads under finite potential and thermal biases. In our studies we accurately took into account the interplay between the exchange field and the Kondo effect, while performing a perturbation expansion in the weakly coupled lead. We determined the nonequilibrium currents in the parallel and antiparallel configurations of the system, which allowed us to find the corresponding TMR. In the considered device, we have predicted a *giant* TMR effect of both signs, depending on the parameter space, in the out-of-equilibrium settings. This is in particular associated with a sign change of the current in the antiparallel configuration at finite bias voltage and temperature gradient. Moreover, we have shown that the TMR is tunable with respect to the orbital energy level, applied potential and thermal biases. Our system can be thus considered as a highly tunable magnetoresistive device with high values of the TMR, which should be of importance for spintronics applications.

Declaration of competing interest

The authors declare that they have no known competing financial interests or personal relationships that could have appeared to influence the work reported in this paper.

Data availability

Data will be made available on request.

Acknowledgments

This work was supported by the Polish National Science Centre, Poland from funds awarded through the decision No. 2017/27/B/ST3/00621. We also acknowledge the computing time at the Poznań Supercomputing and Networking Center.

References

- [1] I. Žutić, J. Fabian, S. Das Sarma, Spintronics: Fundamentals and applications, *Rev. Modern Phys.* 76 (2) (2004) 323–410, <http://dx.doi.org/10.1103/RevModPhys.76.323>.
- [2] A. Ardavan, G.A.D. Briggs, Quantum control in spintronics, *Philos. Trans. R. Soc. Lond. Ser. A* 369 (1948) (2011) 3229–3248, <http://dx.doi.org/10.1098/rsta.2011.0009>.
- [3] D.D. Awschalom, L.C. Bassett, A.S. Dzurak, E.L. Hu, J.R. Petta, Quantum spintronics: Engineering and manipulating atom-like spins in semiconductors, *Science* 339 (6124) (2013) 1174–1179, <http://dx.doi.org/10.1126/science.1231364>.
- [4] J. Barnaś, I. Weymann, Spin effects in single-electron tunnelling, *J. Phys.: Condens. Matter* 20 (42) (2008) 423202.
- [5] W. Rudziński, J. Barnaś, Tunnel magnetoresistance in ferromagnetic junctions: Tunneling through a single discrete level, *Phys. Rev. B* 64 (8) (2001) 085318, <http://dx.doi.org/10.1103/PhysRevB.64.085318>.
- [6] C.A. Merchant, N. Marković, Electrically tunable spin polarization in a carbon nanotube spin diode, *Phys. Rev. Lett.* 100 (15) (2008) 156601, <http://dx.doi.org/10.1103/PhysRevLett.100.156601>.
- [7] J. Barnaś, I. Weymann, Spin effects in single-electron tunnelling, *J. Phys.: Condens. Matter* 20 (42) (2008) 423202, <http://dx.doi.org/10.1088/0953-8984/20/42/423202>.
- [8] G. Michałek, B.R. Bulka, Tunnel magnetoresistance in quantum dots in the presence of singlet and triplet, *J. Phys.: Condens. Matter* 23 (17) (2011) 175305, <http://dx.doi.org/10.1088/0953-8984/23/17/175305>.
- [9] A. Hirohata, K. Yamada, Y. Nakatani, I.-L. Prejbeanu, B. Diény, P. Pirro, B. Hillebrands, Review on spintronics: Principles and device applications, *J. Magn. Magn. Mater.* 509 (2020) 166711, <http://dx.doi.org/10.1016/j.jmmm.2020.166711>.
- [10] H.R. Saeedi, A. Ahmadi Fouladi, F. Mofid Nakhaei, A. Pahlavan, Spin-polarized currents through a triangle quantum dot junction driven by voltage and temperature gradient, *Micro Nanostruct.* 174 (2023) 207474, <http://dx.doi.org/10.1016/j.micrna.2022.207474>.
- [11] J. Kondo, Resistance minimum in dilute magnetic alloys, *Progr. Theoret. Phys.* 32 (1) (1964) 37–49, <http://dx.doi.org/10.1143/PTP.32.37>.
- [12] A.C. Hewson, *The Kondo Problem To Heavy Fermions*, Cambridge Studies in Magnetism, Cambridge University Press, 1993, <http://dx.doi.org/10.1017/CBO9780511470752>.
- [13] D. Goldhaber-Gordon, H. Shtrikman, D. Mahalu, D. Abusch-Magder, U. Meirav, M.A. Kastner, Kondo effect in a single-electron transistor, *Nature* 391 (6663) (1998) 156–159, <http://dx.doi.org/10.1038/34373>.
- [14] J. Martinek, Y. Utsumi, H. Imamura, J. Barnaś, S. Maekawa, J. König, G. Schön, Kondo effect in quantum dots coupled to ferromagnetic leads, *Phys. Rev. Lett.* 91 (12) (2003) 127203, <http://dx.doi.org/10.1103/PhysRevLett.91.127203>.
- [15] J. Martinek, M. Sindel, L. Borda, J. Barnaś, J. König, G. Schön, J. von Delft, Kondo effect in the presence of itinerant-electron ferromagnetism studied with the numerical renormalization group method, *Phys. Rev. Lett.* 91 (24) (2003) 247202, <http://dx.doi.org/10.1103/PhysRevLett.91.247202>.
- [16] A.N. Pasupathy, R.C. Bialczak, J. Martinek, J.E. Grose, L.A.K. Donev, P.L. McEuen, D.C. Ralph, The Kondo effect in the presence of ferromagnetism, *Science* 306 (5693) (2004) 86–89, <http://dx.doi.org/10.1126/science.1102068>.
- [17] K. Hamaya, S. Masubuchi, M. Kawamura, T. Machida, M. Jung, K. Shibata, K. Hirakawa, T. Taniyama, S. Ishida, Y. Arakawa, Spin transport through a single self-assembled InAs quantum dot with ferromagnetic leads, *Appl. Phys. Lett.* 90 (5) (2007) 053108, <http://dx.doi.org/10.1063/1.2435957>.
- [18] K. Hamaya, M. Kitabatake, K. Shibata, M. Jung, M. Kawamura, K. Hirakawa, T. Machida, T. Taniyama, S. Ishida, Y. Arakawa, Electric-field control of tunneling magnetoresistance effect in a $x\text{N-NiInAsNi-z77de}$ quantum-dot spin valve, *Appl. Phys. Lett.* 91 (2) (2007) 022107, <http://dx.doi.org/10.1063/1.2759264>.
- [19] K. Hamaya, M. Kitabatake, K. Shibata, M. Jung, M. Kawamura, K. Hirakawa, T. Machida, T. Taniyama, S. Ishida, Y. Arakawa, Kondo effect in a semiconductor quantum dot coupled to ferromagnetic electrodes, *Appl. Phys. Lett.* 91 (23) (2007) 232105, <http://dx.doi.org/10.1063/1.2820445>.
- [20] K. Hamaya, M. Kitabatake, K. Shibata, M. Jung, M. Kawamura, S. Ishida, T. Taniyama, K. Hirakawa, Y. Arakawa, T. Machida, Oscillatory changes in the tunneling magnetoresistance effect in semiconductor quantum-dot spin valves, *Phys. Rev. B* 77 (8) (2008) <http://dx.doi.org/10.1103/PhysRevB.77.081302>, 081302(R).
- [21] S. Csonka, I. Weymann, G. Zarand, An electrically controlled quantum dot based spin current injector, *Nanoscale* 4 (12) (2012) 3635–3639, <http://dx.doi.org/10.1039/C2NR30399J>.
- [22] A. Bordoloi, V. Zannier, L. Sorba, C. Schönenberger, A. Baumgartner, A double quantum dot spin valve, *Commun. Phys.* 3 (135) (2020) 1–7, <http://dx.doi.org/10.1038/s42005-020-00405-2>.
- [23] P. Tulewicz, K. Wrześniewski, S. Csonka, I. Weymann, Large voltage-tunable spin valve based on a double quantum dot, *Phys. Rev. A* 16 (1) (2021) 014029, <http://dx.doi.org/10.1103/PhysRevApplied.16.014029>.
- [24] A. Manaparambil, A. Weichselbaum, J. von Delft, I. Weymann, Nonequilibrium spintronic transport through Kondo impurities, *Phys. Rev. B* 106 (12) (2022) 125413, <http://dx.doi.org/10.1103/PhysRevB.106.125413>.
- [25] G.E.W. Bauer, E. Saitoh, B.J. van Wees, Spin caloritronics, *Nature Mater.* 11 (5) (2012) 391–399, <http://dx.doi.org/10.1038/nmat3301>.
- [26] A. Manaparambil, I. Weymann, Nonequilibrium seebeck and spin seebeck effects in nanoscale junctions, 2023, <http://dx.doi.org/10.48550/arXiv.2307.10393>, arXiv [arXiv:2307.10393](https://arxiv.org/abs/2307.10393).
- [27] K.G. Wilson, The renormalization group: Critical phenomena and the Kondo problem, *Rev. Modern Phys.* 47 (4) (1975) 773–840, <http://dx.doi.org/10.1103/RevModPhys.47.773>.
- [28] R. Bulla, T.A. Costi, T. Pruschke, Numerical renormalization group method for quantum impurity systems, *Rev. Modern Phys.* 80 (2) (2008) 395–450, <http://dx.doi.org/10.1103/RevModPhys.80.395>.
- [29] P.W. Anderson, Localized magnetic states in metals, *Phys. Rev.* 124 (1) (1961) 41–53, <http://dx.doi.org/10.1103/PhysRev.124.41>, URL <https://link.aps.org/doi/10.1103/PhysRev.124.41>.
- [30] A. Manaparambil, I. Weymann, Nonequilibrium Seebeck effect and thermoelectric efficiency of Kondo-correlated molecular junctions, *Phys. Rev. B* 107 (8) (2023) 085404, <http://dx.doi.org/10.1103/PhysRevB.107.085404>.
- [31] M. Julliere, Tunneling between ferromagnetic films, *Phys. Lett. A* 54 (3) (1975) 225–226.
- [32] O. Legeza, C.P. Moca, A.I. Tóth, I. Weymann, G. Zarand, We used the open-access Budapest Flexible DM-NRG code, 2008, <http://www.phy.bme.hu/~dmnr/ arXiv:0809.3143> (unpublished).
- [33] I. Weymann, J. König, J. Martinek, J. Barnaś, G. Schön, Tunnel magnetoresistance of quantum dots coupled to ferromagnetic leads in the sequential and cotunneling regimes, *Phys. Rev. B* 72 (11) (2005) 115334, <http://dx.doi.org/10.1103/PhysRevB.72.115334>.
- [34] I. Weymann, Finite-temperature spintronic transport through Kondo quantum dots: Numerical renormalization group study, *Phys. Rev. B* 83 (11) (2011) 113306, <http://dx.doi.org/10.1103/PhysRevB.83.113306>.

Appendices

Appendix A

List of Scientific Achievements

A.1 Complete list of Publications

1. Anand Manaparambil & Ireneusz Weymann. *Spin Seebeck effect of correlated magnetic molecules*. Sci. Rep., vol. 11, no. 9192, 28 Apr. 2021, pp. 1-15, doi: [10.1038/s41598-021-88373-7](https://doi.org/10.1038/s41598-021-88373-7).
2. Anand Manaparambil, Andreas Weichselbaum, Jan von Delft & Ireneusz Weymann. *Nonequilibrium spintronic transport through Kondo impurities* (Editor's suggestion). Phys. Rev. B, vol. 106, no. 12, 14 Sept. 2022, p. 125413, doi:[10.1103/PhysRevB.106.125413](https://doi.org/10.1103/PhysRevB.106.125413).
3. Anand Manaparambil & Ireneusz Weymann. *Nonequilibrium Seebeck effect and thermoelectric efficiency of Kondo-correlated molecular junctions*. Phys. Rev. B, vol. 107, no. 8, 7 Feb. 2023, p. 085404, doi:[10.1103/PhysRevB.107.085404](https://doi.org/10.1103/PhysRevB.107.085404).
4. Anand Manaparambil & Ireneusz Weymann. *Giant tunnel magnetoresistance induced by thermal bias*. J. Magn. Magn. Mater., vol. 587, 1 Dec. 2023, p. 171272, doi:[10.1016/j.jmmm.2023.171272](https://doi.org/10.1016/j.jmmm.2023.171272).
5. Anand Manaparambil & Ireneusz Weymann. *Spin-resolved nonequilibrium thermopower of asymmetric nanojunctions*. Phys. Rev. B, vol. 109, no. 11, 4 Mar. 2024, p. 115402, doi:[10.1103/PhysRevB.109.115402](https://doi.org/10.1103/PhysRevB.109.115402).
6. Anand Manaparambil, Andreas Weichselbaum, Jan von Delft & Ireneusz Weymann. **Nonequilibrium steady-state thermoelectrics of Kondo-correlated quantum dots**. arXiv:2409.03102, 4 Sep. 2024, doi:[10.48550/arXiv.2409.03102](https://doi.org/10.48550/arXiv.2409.03102).
7. Anand Manaparambil, Cătălin Pașcu Moca, Gergely Zarand & Ireneusz Weymann. *Underscreened Kondo compensation in a superconductor*. To be submitted.
8. Anand Manaparambil, Kacper Wrześniewski & Ireneusz Weymann. *Temporal dynamics of the Kondo compensation in YSR phases*. Manuscript under preparation.

A.2 List of Seminars and Conferences

1. “Kondo cloud of a partially screened impurity coupled to s-wave superconductor”, DPG Spring Meeting of the Condensed Matter Section 2024, 17-24 March 2024, Berlin, Germany (Oral).
2. “Screening clouds in Superconductors”, American Physical Society March meeting 2024, 4-8 March 2024, Minneapolis, USA (Oral).
3. “Nonequilibrium Kondo effect under finite thermal bias”, American Physical Society March meeting 2024, 4-8 March 2024, Minneapolis, USA (Poster).
4. “Underscreened Kondo cloud in superconductor”, CMD30-FisMat 2023, 4-8 September 2023, Milan, Italy (Oral).
5. “Underscreened Kondo cloud in superconductor”, Sympozyjum Młodych Naukowców 2023, 18-20 September 2023, Warsaw, Poland (Oral).
6. “Nonequilibrium Kondo effect under finite thermal bias: An accurate treatment of electronic correlations”, Physics of Magnetism 23, 26-30 June 2023, Poznan, Poland (Invited talk).
7. "Nonequilibrium Kondo effect in a Quantum Dot coupled to Ferromagnetic leads", American Physical Society March Meeting, 5-10 March 2023, Las Vegas, USA (Oral).
8. "Nonequilibrium thermoelectrics of a Kondo-correlated molecular junction", American Physical Society March Meeting, 5-10 March 2023, Las Vegas, USA (Poster).
9. "Nonequilibrium spintronic and thermoelectric transport through quantum impurities", Quantum Many Body Theory Department at Jagiellonian University, 23 January 2023, Krakow, Poland (Invited Seminar).
10. “Nonequilibrium Seebeck coefficient of a correlated molecular junction”, International Conference on Strongly Correlated Electron Systems (SCES-2022), 24- 29, July 2022, Amsterdam, Netherlands (Poster).
11. “Nonequilibrium spintronic transport through Kondo impurities”, Condensed Matter Division conference of the European Physical Society, 21-26 August 2022, Manchester, UK (Oral).
12. “Nonequilibrium spintronic transport using hybrid renormalization group approach”, School on Tensor Networks based approaches to Quantum Many-Body Systems, 5-9 September 2022, Vienna, Austria (Poster).
13. "Interplay of exchange field and Kondo effect in quantum impurity systems out of equilibrium", International conference on Strongly Correlated Electron Systems (SCES - 2020), 27 September - 2 October 2021 (Oral).

14. "Spin-resolved thermoelectric properties of correlated magnetic molecules", Multiscale Phenomena in Condensed Matter Conference for young researchers (Young MULTIS 2021) , 5-7 July 2021 (Oral).
15. "Non-equilibrium steady state transport through quantum dot spinvalves", Physics of Magnetism 2021 (PM '21), 28 June 2021 – 2 July 2021 (Poster).
16. "Nonequilibrium spin-resolved transport through correlated quantum dots: An accurate treatment by renormalization group methods", Condensed Matter and Quantum Materials 2021 (CMQM -2021), 21-23 June 2021, (Oral).
17. "Nonequilibrium spin-resolved transport through correlated quantum dots: An accurate treatment by renormalization group methods", Chair of Theoretical Solid State Physics, Ludwig-Maximilians-University (LMU), Munich, 2020 (Seminar).

A.3 Experience in Scientific Projects

1. Co-investigator in the NCN Opus grant No: 2017/27/B/ST3/00621,
Project title: *Nonequilibrium phenomena and dynamics in nanoscale systems*
(PI: Prof. Ireneusz Weymann).
2. Principal investigator in the NCN Preludium grant No: 2021/41/N/B/ST3/02098,
Project title: *Kondo cloud in magnetic molecules coupled to superconductors*.
3. Co-investigator in the NCN Opus grant No: 2022/45/B/ST3/02826,
Project title: *Critical phenomena and transport in correlated hybrid nanostructures*
(PI: Prof Ireneusz Weymann).

A.4 List of Research visits

1. One-week research visit to Budapest University of Economics and Technology, Hungary - 2023.
2. One-month research visit to University of Oradea, Romania - 2023.
3. One-month research visit to Brookhaven National Laboratory, USA - 2022.
4. One-week research visit to Ludwig Maximilians Universitat, Munich, Germany - 2022.
5. Two-week research visit to Ludwig Maximilians Universitat, Munich, Germany- 2021.

A.5 List of Awards

1. The National Science Center of Poland (NCN) - Preludium Grant recipient for the project titled “Kondo cloud in magnetic molecules coupled to superconductors”.
2. Awarded the NAWA-STER travel grant for one-month internship to Brookhaven National Laboratory, USA.
3. Awarded the ID-UB action 003 - travel grant for a research visit to LMU, Munich.
4. Second best poster presented in Physics of Magnetism 2021 (PM’21).

A.6 Other Scientific Activities

1. Technical assistance in organizing the conference - Physics of Magnetism’21.
2. Technical assistance in organizing the conference - International symposium on spintronics and quantum information 2024.
3. Technical assistance in organizing the conference - Physics of Magnetism’23.

Appendix B

Statements concerning the Author's contributions

Anand Manaparambil
Faculty of Physics and Astronomy
Adam Mickiewicz University, Poznań

Poznań, 07 October 2024

Hereby, I declare that my contribution to the following publications is as follows

1. Anand Manaparambil & Ireneusz Weymann.
Spin Seebeck effect of correlated magnetic molecules.
Sci. Rep., vol. 11, no. 9192, 28 Apr. 2021, pp. 1-15.
doi: 10.1038/s41598-021-88373-7.

I performed all the numerical calculations and prepared the figures. I contributed extensively to the text in the manuscript.

2. Anand Manaparambil, Andreas Weichselbaum, Jan von Delft & Ireneusz Weymann.
Nonequilibrium spintronic transport through Kondo impurities.
Phys. Rev. B, vol. 106, no. 12, 14 Sept. 2022, p. 125413.
doi:10.1103/PhysRevB.106.125413.

I adapted the numerical method, performed all the calculations, prepared the figures, contributed towards the interpretation of the results, and extensively towards the preparation of the manuscript.

3. Anand Manaparambil, Andreas Weichselbaum, Jan von Delft & Ireneusz Weymann.
Nonequilibrium steady-state thermoelectrics of Kondo-correlated quantum dots.
ArXiv: 2409.03102 (2024).
doi:10.48550/arXiv.2409.03102.

I adapted the numerical method, performed all the calculations, prepared the figures, and contributed extensively towards the interpretation of the results and the preparation of the manuscript.

4. Anand Manaparambil & Ireneusz Weymann.
Nonequilibrium Seebeck effect and thermoelectric efficiency of Kondo-correlated molecular junctions.
Phys. Rev. B, vol. 107, no. 8, 7 Feb. 2023, p. 085404.
doi:10.1103/PhysRevB.107.085404.

I performed all the numerical calculations, interpreted the results, prepared the figures. and contributed extensively towards the manuscript preparation.

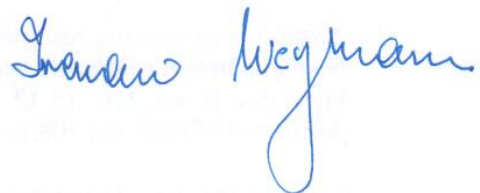
5. Anand Manaparambil & Ireneusz Weymann.
Spin-resolved nonequilibrium thermopower of asymmetric nanojunctions.
Phys. Rev. B, vol. 109, no. 11, 4 Mar. 2024, p. 115402.
doi:10.1103/PhysRevB.109.115402.

I performed all the numerical calculations, interpreted the results, prepared the figures. and contributed extensively towards the manuscript preparation.

6. Anand Manaparambil & Ireneusz Weymann.
Giant tunnel magnetoresistance induced by thermal bias.
J. Magn. Magn. Mater., vol. 587, 1 Dec. 2023, p. 171272.
doi:10.1016/j.jmmm.2023.171272.

I performed all the numerical calculations, interpreted the results, prepared the figures. and contributed extensively towards the manuscript preparation.

Signature: Anand Manaparambil



Prof. Ireneusz Weymann
Faculty of Physics and Astronomy
Adam Mickiewicz University, Poznań

Poznań, 07 October 2024

Hereby, I declare that my contribution to the following publications,

1. Anand Manaparambil & Ireneusz Weymann.
Spin Seebeck effect of correlated magnetic molecules.
Sci. Rep., vol. 11, no. 9192, 28 Apr. 2021, pp. 1-15.
doi: 10.1038/s41598-021-88373-7.
2. Anand Manaparambil, Andreas Weichselbaum, Jan von Delft & Ireneusz Weymann.
Nonequilibrium spintronic transport through Kondo impurities.
Phys. Rev. B, vol. 106, no. 12, 14 Sept. 2022, p. 125413.
doi:10.1103/PhysRevB.106.125413.
3. Anand Manaparambil, Andreas Weichselbaum, Jan von Delft & Ireneusz Weymann.
Nonequilibrium steady-state thermoelectrics of Kondo-correlated quantum dots.
ArXiv: 2409.03102 (2024).
doi:10.48550/arXiv.2409.03102.
4. Anand Manaparambil & Ireneusz Weymann.
Nonequilibrium Seebeck effect and thermoelectric efficiency of Kondo-correlated molecular junctions.
Phys. Rev. B, vol. 107, no. 8, 7 Feb. 2023, p. 085404.
doi:10.1103/PhysRevB.107.085404.
5. Anand Manaparambil & Ireneusz Weymann.
Spin-resolved nonequilibrium thermopower of asymmetric nanojunctions.
Phys. Rev. B, vol. 109, no. 11, 4 Mar. 2024, p. 115402.
doi:10.1103/PhysRevB.109.115402.
6. Anand Manaparambil & Ireneusz Weymann.
Giant tunnel magnetoresistance induced by thermal bias.
J. Magn. Magn. Mater., vol. 587, 1 Dec. 2023, p. 171272.
doi:10.1016/j.jmmm.2023.171272.

was in the formulation of the research problem, supervising the projects, helping in the interpretation of the results and in finalizing the manuscripts for publication.

Signature: 

Andreas Weichselbaum, Ph.D., Dr. habil.
Brookhaven National Laboratory
Upton, NY 11973, USA

Upton, Sep. 26, 2024

I hereby declare that my contribution to the following publications,

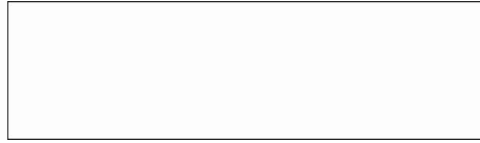
1. Anand Manaparambil, Andreas Weichselbaum, Jan von Delft & Ireneusz Weymann. ***Non-equilibrium spintronic transport through Kondo impurities.***
Phys. Rev. B, 106 , pp. 125413 (2022).
[doi:10.1103/PhysRevB.106.125413](https://doi.org/10.1103/PhysRevB.106.125413)
2. Anand Manaparambil, Andreas Weichselbaum, Jan von Delft & Ireneusz Weymann.
Nonequilibrium steady-state thermoelectrics of Kondo-correlated quantum dots.
ArXiv: 2409.03102 (2024).
[doi:10.48550/arXiv.2409.03102](https://doi.org/10.48550/arXiv.2409.03102)

was to suggest these research topics and to co-supervise Anand Manaparambil throughout these projects either via visits of his, virtual meetings, or written communication. The papers above were extensively iterated by all authors via gitlab.

Signature:  _____



LUDWIG-
MAXIMILIANS-
UNIVERSITÄT
MÜNCHEN



Munich, 04 October 2024

Hereby, I declare that my contribution to the publications listed below was in the formulation of the research problem, helping in the interpretation of the results and in finalizing the manuscripts for publications:

Anand Manaparambil, Andreas Weichselbaum, Jan von Delft & Ireneusz Weymann.
Nonequilibrium spintronic transport through Kondo impurities.
Phys. Rev. B, 106 , pp. 125413 (2022).
doi:10.1103/PhysRevB.106.125413

Anand Manaparambil, Andreas Weichselbaum, Jan von Delft & Ireneusz Weymann.
Nonequilibrium steady-state thermoelectrics of Kondo-correlated quantum dots.
arXiv: 2409.03102 (2024).
doi:10.48550/arXiv.2409.03102


Jan von Delft

Prof. Dr. Jan von Delft
Lehrstuhl für Theoretische Festkörperphysik
Theresienstraße 37 - D-80333 München

Tel.: +49-89-2180-4527
Sekretariat:+49-89-2180-4528
Fax: +49-89-2180-4155

e-mail:vondelft@theorie.physik.uni-münchen.de
<http://www.theorie.physik.uni-münchen.de/lsvondelft>

